IN -34
027443

NASA Contractor Report 202334

Experimental Investigation of Unsteady Shock Wave Turbulent Boundary Layer Interactions About a Blunt Fin
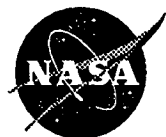
Paul J. Barnhart
NYMA Inc.
Brook Park, Ohio

and

Isaac Greber
Case Western Reserve University
Cleveland, Ohio

April 1997

National Aeronautics and
Space Administration

EXPERIMENTAL INVESTIGATION OF UNSTEADY

SHOCK WAVE TURBULENT BOUNDARY LAYER INTERACTIONS

ABOUT A BLUNT FIN

by

PAUL J. BARNHART

and

ISAAC GREBER

EXPERIMENTAL INVESTIGATION OF UNSTEADY
SHOCK WAVE TURBULENT BOUNDARY LAYER INTERACTIONS
ABOUT A BLUNT FIN

Abstract

by

PAUL J. BARNHART

A series of experiments were performed to investigate the effects of Mach

number variation on the characteristics of the unsteady shock wave/turbulent

boundary layer interaction generated by a blunt fin. A single blunt fin hemi-

cylindrical leading edge diameter size was used in all of the experiments which

covered the Mach number range from 2.0 to 5.0. The measurements in this

investigation included surface flow visualization, static and dynamic pressure

measurements, both on centerline and off-centerline of the blunt fin axis.

Surface flow visualization and static pressure measurements showed that

the spatial extent of the shock wave/turbulent boundary layer interaction increased

with increasing Mach number. The maximum static pressure, normalized by the

incoming static pressure, measured at the peak location in the separated flow

region ahead of the blunt fin was found to increase with increasing Mach number.

The mean and standard deviations of the fluctuating pressure signals from the

dynamic pressure transducers were found to collapse to self-similar distributions as

a function of the distance perpendicular to the separation line. The standard deviation of the pressure signals showed initial peaked distributions, with the maximum standard deviation point corresponding to the location of the separation line at Mach number 3.0 to 5.0. At Mach 2.0 the maximum standard deviation point was found to occur significantly upstream of the separation line.

The intermittency distributions of the separation shock wave motion were found to be self-similar profiles for all Mach numbers. The intermittent region length was found to increase with Mach number and decrease with interaction sweepback angle. For Mach numbers 3.0 to 5.0 the separation line was found to correspond to high intermittencies, or equivalently to the downstream locus of the separation shock wave motion. The Mach 2.0 tests, however, showed that the intermittent region occurs significantly upstream of the separation line.

Power spectral densities measured in the intermittent regions were found to have self-similar frequency distributions when compared as functions of a Strouhal number for all Mach numbers and interaction sweepback angles. The maximum zero-crossing frequencies were found to correspond with the peak frequencies in the power spectra measured in the intermittent region.

TABLE OF CONTENTS

Page

LIST OF FIGURES

LIST OF TABLES

LIST OF SYMBOLS

C_f skin friction coefficient

c_P specific heat at constant pressure

D blunt fin leading edge hemi-cylindrical diameter

f frequency

f_C zero-crossing frequency

G power spectral density function

i $\sqrt{-1}$

L_T intermittent region length

M Mach number

P pressure

$\overline{P}$ mean pressure

r turbulent recovery factor

Re Reynolds number

S separation line

T temperature or time period

t time

u velocity

U freestream velocity

V shock wave velocity

$\overline{V}$ mean shock velocity

x,y	cartesian coordinate system
z	coordinate normal to boundary layer surface
r,ω	polar coordinate system
l,λ	orthonormal coordinate system
α	skewness
β	kurtosis
γ	ratio of specific heats
γ_{xy}^2	coherence
Γ	intermittency
δ	boundary layer thickness
δ^*	boundary layer displacement thickness
ϵ	error estimate
θ	boundary layer momentum thickness
Λ	integral length scale
Π	boundary layer wake strength parameter
ρ	autocorrelation or denstiy
ρ_{xy}	cross-correlation
σ	standard deviation
τ	time delay
Υ	threshold
φ	probability density function
Ω	integral time scale

Subscripts

0	freestream or incoming
1	first or upstream
2	second or downstream
D	downstream
e	boundary layer edge
P	pressure or port
S	separation line or sampling or starboard or test section static
T	wind tunnel total
U	upstream
V	shock velocity
aw	adiabatic wall
w	wall
Γ	intermittency

Superscritps

+	rise event or downstream
-	fall event or upstream
*	complex conjugate

CHAPTER I

INTRODUCTION

Shock wave/turbulent boundary layer interactions are found in virtually any application employing supersonic flows. Examples include supersonic and hypersonic flight vehicles and associated propulsion systems including inlets and nozzles. These interactions involve complex flow phenomenon, including boundary layer separation, which are still poorly understood. As a result, most of the knowledge to date pertaining to shock wave/turbulent boundary layer interactions has resulted from experiments using simple geometries.

Many experimental investigations, covering a wide range of basic geometries and Mach numbers, exist in the literature. An extensive compilation of these experiments can be found in reference 1. The majority of the existing experimental work has been performed using simple geometries. The premise has been that by first understanding shock wave/turbulent boundary layer interactions for elementary configurations, interactions occurring in real applications would then be modeled as extensions of the elementary interactions.

Some of the commonly tested basic geometries include swept and unswept compression ramps, cylinders, and blunt fins. These are juncture type geometries which are used to simulate shock wave/turbulent boundary layer interactions

produced by deflected control surfaces, engine inlets, and wing-body junctures. Other commonly tested geometries include glancing and incident interactions generated by sharp fins at angles of attack. Flow separation is often produced by these shock wave/turbulent boundary layer interactions, particularly in the juncture type geometries. In some cases, the flow separations are found to be highly unsteady.

Experimental measurements of unsteady flow separations in shock wave/turbulent boundary layer interactions have shown that large fluctuating pressure loads, in excess of 185 dB, are possible.[2] The characteristic frequencies of the of the unsteady separation can occur within the structural resonance frequencies.[3] As a result, high cycle fatigue becomes a concern in the design of aerostructures.

Most of the existing data measured in shock wave/turbulent boundary layer interactions is in the form of mean quantities. Schlieren and shadowgraph photography have been used for non-intrusive flowfield imaging. Surface flow tracing using oil-flow or kerosene/lampblack techniques have provided length scale information. Mean pressure distributions on test surfaces and pitot pressure measurements in the flowfield have been used to interpret the general structure of shock wave/turbulent boundary layer interactions. None of these commonly used techniques, however, provide information on the unsteady characteristics of the interactions. A brief listing of experiments measuring unsteady quantities in shock wave/turbulent boundary layer interactions follows.

The first quantitative experiments measuring fluctuating pressures in the separated flowfield upstream of a forward facing step at Mach numbers 3 and 4.5 were performed by Kistler.[4] Dolling and Bogdonoff[5] performed fluctuating pressure measurements characterizing the unsteady flowfield produced by a hemi-cylindrical blunt fin at Mach 3. Dolling and Smith[6] measured fluctuating pressures in the shock wave/turbulent boundary layer interaction produced by a cylinder at Mach 5. Erengil and Dolling have performed fluctuating pressure measurements in unswept[7] and swept[8] compression ramp interactions at Mach 5. Gibson and Dolling[9] performed unsteady pressure measurements in a glancing shock wave/turbulent boundary layer interaction at Mach 5.

The references cited above do not comprise a complete list, but are still representative of the experimental measurements of the unsteady characteristics in shock wave/turbulent boundary layer interactions. The above citations do, however, show that the majority of the published unsteady measurement data come from experiments at the University of Texas at Austin. These experiments were all performed at Mach 5. There is currently little unsteady data available at other Mach numbers. Additionally, since the vast majority of the unsteady data comes from a single experimental facility, there is no independent check of facility effects on the unsteady behavior of shock wave/turbulent boundary layer interactions.

The principle objective of this investigation is to determine the effects of Mach number on the characteristics of the unsteady shock wave/turbulent

boundary layer interaction generated by a blunt fin. Figure 1 shows the geometry

and flowfield sketch of the basic shock wave/turbulent boundary layer interaction

used in this experimental investigation. The unsteady characteristics are

determined through fluctuating pressure measurements made at the surface, ahead

of the blunt fin leading edge, upstream of and within the separated flow region.

Additionally, since almost all of the existing unsteady pressure measurements in

the literature are only located along the centerline upstream of the blunt fin

leading edge, unsteady pressure measurements are made in this investigation both

on centerline and off-centerline about the blunt fin in the shock wave/turbulent

boundary layer interaction. A secondary objective is to provide unsteady

measurements suitable for direct comparison with existing data from other

experimental facilities in an effort to identify any facility effects inherent in

unsteady measurements.

CHAPTER II

EXPERIMENTAL TECHNIQUE AND EQUIPMENT

2.1 OVERVIEW

The experimental configuration examined in this investigation is the blunt fin induced unsteady shock wave turbulent boundary layer interaction. A blunt fin with a leading edge hemi-cylindrical diameter, D, protrudes from a flat plate and is aligned in the free stream flow direction. A supersonic boundary layer which develops on the flat plate interacts with the detached bow shock generated by the blunt fin. In the shock wave boundary layer interaction which ensues, an unsteady lambda-shock develops around the base of the blunt fin. The boundary layer separates and a pair of horseshoe vortices are developed which spiral off downstream. Figure 1 shows the basic near field interaction elements. The spatial extent of the separating flowfield interaction near the blunt fin has been found to scale primarily with D, the blunt fin leading edge diameter.[10]

Other investigators have examined the characteristics of the separation shock wave motion ahead of the blunt fin. Previously, Dolling[11] has used a protruding cylinder to determine the shock wave motion using high speed surface pressure transducers mounted in the flat plate, directly ahead of a cylinder, along the centerline parallel with the incoming Mach 5.0 free stream flow. From

5

analysis of the simultaneous pressure transducer signals, Dolling has found that the extent of the separation shock wave motion is on the order of the cylinder (or blunt fin leading edge) diameter, D. The streamwise motion of the separation shock wave ahead of the cylinder was found to be essentially random. The separated flow region was found to extend approximately $2.5D$ ahead of the blunt fin leading edge. The frequency of the separation shock wave oscillation was found to be on the order of 1 kHz in a Mach 5.0 free stream flow.

Nearly all of the previous experiments have been performed along the centerline of the blunt fin (or cylinder). Only one other work exists which examines the unsteady flow separation ahead of and to the side of the blunt fin. Gonsalez[12] did measure high speed wall pressure fluctuations in the separated region to the side of the blunt fin centerline. Although Gonsalez's work was primarily a comparison of sweepback effects in unsteady shock wave induced boundary layer separations for a variety of geometries, his blunt fin data will be used as an important source of comparison for this work.

Gonsalez and Dolling have examined some of the parametric effects in the blunt fin interaction. Particularly, Gonsalez's experiments encompassed a range of blunt fin leading edge diameters, while the incoming boundary layer was the same. Other experiments conducted by Dolling have examined the effects of different incoming boundary layer heights. However, as a result of facility limitations, all of Dolling's experiments have been done at an incoming Mach number of 5.0. There is only one other set of experiments[13] which include

simultaneous high speed wall pressure measurements performed at a different

Mach number. These measurements are only made along the blunt fin centerline,

but the incoming Mach number is 3.0 rather than 5.0.

The objective of this investigation was to examine the blunt fin induced

unsteady shock wave boundary layer separation over a range of incoming Mach

numbers. The experimental program focused on the simultaneous measurement of

high speed wall pressure fluctuations about a blunt fin, both along the centerline as

well as off-centerline. A single blunt fin leading edge diameter, D, was used.

For the purpose of direct comparison with the results from other experiments, the

interaction measurements were taken at incoming Mach numbers of 2.0, 3.0, 4.0,

and 5.0. This set of experiments provided information on how the incoming

Mach number is a parameter in the interaction characteristics. Additionally, direct

comparisons will be available at Mach numbers 3.0 and 5.0, and these

comparisons should provide an indication as to the extent to which facility effects

influence the characteristics of the interaction.

2.2 1x1 SUPERSONIC WIND TUNNEL

The supersonic wind tunnel used in this experiment is shown in Figure 2.

The wind tunnel is an open circuit continuous run type. Air is supplied upstream

of the plenum chamber at either 380 kPa or 960 kPa absolute, and is throttled

down to a desired tunnel stagnation pressure in the plenum. The exhaust system

maintains a constant pressure of 13 kPa absolute downstream of the tunnel

subsonic diffuser. In this manner, a required pressure differential for supersonic operation is established across the nozzle and test section of the wind tunnel. The wind tunnel is of a fixed nozzle construction with interchangeable nozzle blocks for test section design Mach numbers of 1.3, 1.6, 2.0, 2.5, 3.0, 3.5, 4.0, 5.0, and 6.0. Skebe[14] provides a more detailed description of the wind tunnel.

For Mach numbers of 4.0 and below the 380 kPa air supply system is typically used. The total temperature, although not controlled, is typically 295 Kelvin. For wind tunnel operation at Mach 5.0 and above the 960 kPa air supply system must be used. At the higher Mach numbers the static temperatures in the test section can fall below the liquefaction point for air, and hence electric resistance heaters are used to raise the total temperature of the air supply. During the Mach 5.0 tests the total temperature was maintained at 345 Kelvin or above, assuring that there would be no possibility of liquefaction in the test section. The air supply system used air dryers to remove water vapor, insuring that condensation would not occur in the test section.

2.3 BLUNT FIN MODEL

The test section in the 1x1 supersonic wind tunnel has a square crossectional area measuring 30.5 by 30.5 centimeters, or 1.0 by 1.0 foot, hence the name. The length of the test section is 66.0 centimeters. A sketch of the configuration used in the experiment is shown in Figure 3.

A blunt fin is used to create the separation shock wave interaction in the

test section. Two different size blunt fins are used in the experiment. The first has a circular leading edge diameter of 1.90 cm and is stationary. The second blunt fin has a 2.54 cm circular leading edge diameter and is capable of moving 5.08 cm forward by remote control. With the moving blunt fin the interaction region can be accurately positioned over the transducers mounted in the test section sidewall. Each blunt fin is 15.2 cm high, spanning half the test section, and is effectively semi-infinite.

The test section sidewall is equipped with a series of static pressure taps and a large circular cut-out into which fit a series of instrumented circular insert plates. Three insert plates are used in the experiment. The first is blank and is used for surface flow visualization. The second is fitted with 114 static pressure taps and is used for the steady-state static pressure surveys. The third circular insert plate has another off-center circular cut-out into which fits an instrumented plug containing the dynamic pressure transducers. All of the insert plates rotate co-incidentally about the blunt fin circular leading edge.

2.4 INSTRUMENTATION

During the course of the experimental program a number of quantities were recorded. These measurements fall into three broad categories: wind tunnel conditions, interaction pressures, and flow visualization. The most important wind tunnel conditions monitored were the plenum total pressure, P_T, and total temperature, T_T. The incoming test section static pressure, P_S, was also recorded.

From these measurements the wind tunnel operating conditions (Mach number, unit Reynolds number, and flow velocity, among others) were constantly computed, displayed, and monitored on the operator's console in the control room.

2.4.1 Static pressure measurements

Steady state pressure data were measured in the wind tunnel by using small (1.0 mm) holes drilled into the test surface. A 1.6 mm flexible plastic tube, approximately 2.0 m long, was then used to attach the static pressure line to a set of solid-state pressure transducers. The solid-state pressure transducers, manufactured by PSI, were part of the ESP data acquisition system described in more detail in a subsequent section.

A variety of pressure data were measured about the wind tunnel sidewall and blunt fin root juncture where the unsteady shock wave turbulent boundary layer interaction takes place. The first series of measurements was a survey of the static pressure distribution on the tunnel sidewall about the blunt fin leading edge. This was accomplished by the use of a specially instrumented circular insert plate. Figures 4 through 7 show the locations of the static pressure taps which were machined into the plate. The taps were arranged in such a way as to permit detailed spatial pressure distribution measurements by sequential rotations of the circular insert plate orientation about the blunt fin leading edge axis.

The 10 rows of taps on the left side of the plate as shown in Figure 4 all

have the same radial distributions. By rotating the circular insert plate 10 degrees

clockwise and counter-clockwise the angular resolution of the static tap

distribution was effectively tripled. This set of orientations provided a suitable

array of measurements to determine the static pressure field on the wind tunnel

sidewall covering 180 degrees about the blunt fin leading edge. The other rows of

static pressure taps on the right side of the plate in Figure 4 indicated by section

lines A, B, C, and D had the same equally spaced tap locations along radii, but

each row slightly farther offset from the center of the plate. By orientating the

circular insert plate so that each of these rows were subsequently positioned along

the same direction, rotation by 30 degree increments, a very detailed radial

pressure distribution was measured ahead of the blunt fin.

2.4.2 Dynamic pressure measurements

The fluctuating pressure measurements, also referred to as dynamic

pressure measurements, were made using surface mounted Kulite miniature

pressure transducers. Model XCQ-062-50A absolute pressure transducers having

a range of 0.0 to 345 kPa were used in the dynamic pressure measurements. The

dynamic pressure transducers had a body size of 1.59 mm.

The dynamic pressure measurements were made using the hardware shown

in Figures 8 and 9. The dynamic pressure transducers were mounted in various

locations among the arrangement of three parallel rows of threaded holes shown in

the transducer plug in Figure 9. The dynamic pressure transducers were mounted

protruding from the end of specially machined threaded screws which fit into the threaded holes in the transducer plug. The holes which did not contain transducers were filled with blanks. The transducers were mounted flush with the surface of the transducer plug. The back of the transducer plug was capped, and the transducer leads were passed through a vacuum tight connector. The volume within the transducer plug and cap was effectively sealed down to a hard vacuum from atmospheric leakage during the wind tunnel tests. This assured that ambient air did not jet into the wind tunnel past the transducers during testing.

The circular insert plate shown in Figure 8 had a large hole bored through, offset from the center of rotation, into which the transducer plug was mounted. both the circular insert plate and transducer plug were capable of independent rotations, thus permitting a wide variety of positionings for the dynamic pressure transducers within the unsteady shock wave turbulent boundary layer interaction region. Once the transducers were positioned about the blunt fin, the interaction region could be translated over the transducers by the actuation of a movable fin. Figures 10 and 11 show the design of the blunt fin used in the dynamic pressure measurements and the rail mount which permitted the fin to move forward up to 5.08 cm. When the fin was in the fully retracted position, the blunt fin leading edge axis was coincident with the circular insert plate center of rotation. The blunt fin was actuated by a hydraulic piston and could be accurately positioned within 0.13 mm. The location of the blunt fin was recorded from the calibrated output voltage of a linear translation potentiometer attached to the rear of the fin.

The top trailing edge of the blunt fin, as seen in Figure 10, was cut away as a safety feature. This minimized side loads on the fin should one side 'unstart' without affecting the flowfield ahead of and about the blunt fin leading edge. A pressure tap was also machined into the blunt fin leading edge along the centerline approximately 2.5 cm below the top of the fin. This pressure tap recorded the stagnation pressure on the blunt fin and was monitored during testing as another indicator of wind tunnel free stream conditions.

2.4.3 Flow visualization

Schlieren photography and surface flow visualization techniques were also used in the test program. For the flow visualization experiments a blank (non-instrumented) circular insert plate was used. Surface flow tracing was attempted using varying viscosity oil mixtures and florescent dye suspensions. In one series of tests a relatively viscous oil mixture was applied to the wind tunnel sidewall ahead of and around the base of the blunt fin. The wind tunnel was then run for 10 to 20 minutes. The flow of the oil was viewed through a plexiglass window on a video camera. Once the oil had appeared to stabilize into a fixed pattern the wind tunnel was shut down and the resulting flow was photographed through the window under black-light exposure, thus causing the florescent dye to glow. This image approximated the mean surface streamline field in the shock wave turbulent boundary layer interaction.

Another oil and dye mixture was also used to record an image of the

surface streamline traces. A series of tests were run using a low viscosity oil/kerosene mixture with dye in suspension in an attempt to reproduce the kerosene/lampblack method used in blow-down wind tunnels. A series of trial runs were conducted varying the oil/kerosene mixture ratio until the desired image resolution was achieved. The wind tunnel was run for as brief a time as possible, approximately 2 to 3 minutes. After the wind tunnel was shut down, the blank circular insert plate was removed from the test section sidewall. A very thin layer of oil and dye mixture was left on the insert plate. This image was saved by placing a sheet of standard photocopier paper over the plate and letting the oil and dye mixture soak into the paper fibers. The resulting images showed very fine resolution surface streamline traces in the shock wave turbulent boundary layer interaction region about the root of the blunt fin.

The other flow visualization technique used in the experimental program was Schlieren photography. In one series of tests the Schlieren image was taken across the interaction region perpendicular to the blunt fin parallel to the wind tunnel sidewall. For these tests color Schlieren was used to help enhance the flowfield structure. In another test the same Schlieren image was recorded using a high speed black and white film camera running at approximately 2,000 frames per second. With this test it was possible to capture some of the unsteady shock wave turbulent boundary layer interaction motion.

2.4.4 Data acquisition

Nearly all of the data recorded during the experiment consisted of pressure measurements. The static pressure measurements were recorded by a solid-state pressure measurement system developed at the NASA Lewis Research Center, known as the ESP system. This system could measure and record 256 simultaneous pressures. The ESP system is controlled by IBM-PC class minicomputer. The system is self calibrating, and automatically re-calibrates every 20 minutes. The measured pressure data was transferred and stored on a Micro-VAX computer located within the wind tunnel control room. The raw data from the Micro-VAX was permanently archived onto ½ inch magnetic tape for later reduction and analysis.

The dynamic pressure measurements were recorded by an entirely different method than that used for the static pressure measurements. Figure 12 shows a schematic of the data acquisition system developed for the dynamic pressure measurement tests. Although only one dynamic pressure transducer is shown in Figure 12 the system was able to measure up to 8 transducers simultaneously.

An instrumentation rack containing 8 signal conditioners and amplifiers was located next to the wind tunnel test section. The signal conditioners provided the excitation voltage for the dynamic pressure transducers and also adjusted the output voltage so that the signal was always positive over the operating range of the transducers. The output from the signal conditioners was then passed to amplifiers, which were used as pre-amps to amplify the signal voltage to

approximately 1 volt at atmospheric pressures. This was done to minimize the effects of spurious noise which may have affected the signal over the long cable run from the wind tunnel to the control room.

Within the control room, the signal was then passed to another set of amplifiers which were used to amplify the signal further. The analog-to-digital (A/D) converter used, discussed below, was capable of digitizing a 0 to 10 volt signal. Depending on the particular pressure level being measured by the dynamic pressure transducers, the amplifiers in the control room were set to amplify the input signal level into the A/D board as high as possible without exceeding the maximum level of 10 volts. This in turn resulted in the maximum resolution of the dynamic pressure signal once it was digitized.

The high frequency content of the signal from the amplifiers in the control room was then removed by a set of low-pass analog filters. This was done to prevent high frequency aliasing which could have resulted due to the finite sampling rate of the A/D board. The low-pass filtering cut-off frequency, typically 50 kHz, was set to no more than half of the A/D sampling rate. Since it was necessary to alter the order in which the dynamic pressure transducers were measured, a simple patch board was used to set which transducer signal was sent to the digitizing channels in the Masscomp computer.

The Masscomp computer, a scientific workstation designed for high-speed data acquisition, was used for analog-to-digital conversion of the dynamic pressure transducer signals and subsequent data storage. Since it was critical for the test

program to measure simultaneous pressure fluctuations, the signals from all the transducers had to be captured at the same moment prior to digitizing. The sample-and-hold (S/H) board in the Masscomp was used to store up to 8 of the incoming signals from the transducers at the same moment. The A/D board was then triggered to sequentially convert the stored voltage in each channel held on the S/H board.

The A/D board had a maximum conversion frequency of 1 megahertz, and a 12 bit digital resolution. However, since the signals on the S/H board had to be sequentially digitized by the A/D board, the effective simultaneous sampling rate had to be lower than the maximum A/D conversion frequency, and was also slower as more channels were simultaneously measured. Table 1 shows the maximum sampling rate possible with the S/H and A/D system as the number of transducers simultaneously measured increased. Since the available main memory on the Masscomp computer was finite, the total times of recorded dynamic pressure data for each measurement decreased as the number of pressures simultaneously sampled increased. Also listed in Table 1 are the total time measurements at the maximum sampling rates. Longer measurement times were possible by simply decreasing the sampling frequency, but this also decreased the temporal resolution of the signal.

A series of programs were written in Fortran to perform the tasks of driving the S/H and A/D boards, acquiring, and storing data on the Masscomp computer. All data was initially stored in the computer main memory, and then

written to files in Unix binary format on the Masscomp hard disk drive. For final

archiving of the data, the binary data files were copied off to standard 60 Mb 1/4

inch magnetic tape cartridges.

Over 1250 separate dynamic pressure measurements were made during the

experimental program. Each of the Unix binary data files exceeded 1.6 Mb of

disk storage. As a result more than 2 Gb (gigabytes) of dynamic pressure data

was recorded.

2.5 TEST CONDITIONS

The experimental program covered the Mach number range from 2.0 to

5.0. The basic wind tunnel conditions for the experiments are given in Table 2.

The total pressures chosen for the tests were such that the wind tunnel operation

was stable and the unit Reynolds number was approximately constant (about

10,000,000/m) over the range of Mach numbers examined. For the Mach 2.0

tests, two total pressures were used for different measurements, the static pressure

tests used the larger total pressure condition, and the dynamic pressure tests used

the lower total pressure.

Table 2 also lists the measured test section free stream Mach numbers.

The wind tunnel nozzle blocks were designed for the nominal Mach numbers

listed, but calculations using the blunt fin stagnation pressure and the tunnel total

pressure measurements show slight deviations from the nominal design Mach

number. Since these deviations are small, the nominal Mach number shall be used

in subsequent discussions for simplicity. The reader is cautioned to note the slight differences from the actual Mach numbers that were measured in the tests.

2.6 EXPERIMENTAL ERRORS

The experimental data measured in this investigation consisted of static pressures, dynamic pressures, transducer spatial locations, and recording times. An estimation of the errors inherent in all of these measurements is necessary to establish the accuracy of the data subsequently presented. For any measurement, χ, let ϵ_χ be the error associated with the measurement of χ. The confidence interval of the measurement, $\langle \chi \rangle$, can then be determined by $\langle \chi \rangle = \chi \pm \epsilon_\chi$. An estimation of the measurement errors follows.

The manufacturer of the solid state pressure transducers provides an estimate of the static pressure errors. For the transducers used, the quoted error for the static pressure measurements is $\epsilon_P = 0.145$ kPa. The manufacturer of the dynamic pressure transducers also provides an estimate of the linearity of the transducers. The dynamic pressure transducers were used to measure pressure fluctuations, ΔP. The error for these fluctuating pressure measurements was taken to be $\epsilon_{\Delta P} = 0.104$ kPa.

The signals from the dynamic pressure transducers were also time averaged to calculate a mean pressure, $\overline{P}$. A number of factors influenced the error estimate for the mean pressures recorded with the dynamic pressure transducers. The first is the fact that the static pressure measurement transducers were used to

calibrate the dynamic pressure transducers. Since a simple two point linear calibration was used, the error estimate for the mean of the dynamic pressure transducers could be estimated as $\epsilon_{\bar{P}} = 0.290$ kPa. However, other factors increased this measurement error. The dynamic pressure transducers were found to have a zero-drift, which was sensitive to temperature changes. It was not possible to estimate the zero-drift errors, but rather a bound was determined by examination of the variations of the mean pressure calculations from many dynamic pressure measurements. Including this zero-drift effect, and the errors inherent in the calibration procedures, the mean pressure error estimate for the dynamic pressure transducers was determined to be $\epsilon_{\bar{P}} = 0.62$ kPa.

The dynamic pressures were recorded at discrete time intervals. An estimate of the errors in recorded times can determined from the clock cycle used in the A/D conversion process. The clock cycle was 1 MHz. The associated time error was determined to be $\epsilon_t = 0.000001$ sec. The errors associated with transducer positions x,y was determined to be typically $\epsilon_{x,y} = 0.65$ mm.

CHAPTER III

DATA REDUCTION AND ANALYSIS

3.1 DYNAMIC DATA

The vast majority of the experimental data collected in this investigation consists of time series, or dynamic, pressure measurements. These dynamic measurements in their raw form, $P(t)$, are of limited use. It is therefore necessary to apply time series analysis techniques in an effort to characterize the interaction in terms of quantities other than $P(t)$. However, before describing the data reduction and analysis techniques, it is beneficial to describe in some detail the characteristics of the dynamic pressure data.

Figure 13 shows a typical pressure signal measured from a dynamic pressure transducer. The plot in Figure 13 is only a short sample of the complete signal. For this particular reading, there were 3 other pressure transducers which were measured simultaneously along with the signal shown in Figure 13. A reading is any recorded signal from one or more dynamic pressure transducers. For more than one transducer, the pressure signals were recorded simultaneously in a reading.

Although the pressure signal in Figure 13 is shown as a continuous measurement in time, the data was actually recorded discretely. Figure 14 shows

the discrete data points, P_n, which were recorded for the same pressure signal shown in Figure 13. The index n represents the number of the particular pressure measurement P_n in the series which approximates the dynamic pressure signal $P(t)$. The discrete pressure measurements were taken at equal time intervals, $\Delta t = 1/f_s$, where f_s is the sampling frequency. In Figure 14 the sampling frequency was 200 kHz.

A record is a subset of an entire discrete pressure signal series. A record is typically taken to be 1024 data points. Figure 14 shows a single record for one pressure transducer signal in a typical reading. The complete pressure signal from the reading shown in Figure 14 consists of 200 records, or 204800 discrete data points. The total number of discrete data points for all 4 dynamic pressure transducers measured simultaneously in the reading is therefore 819200. A record is the basic length of a dynamic pressure signal segment which is processed by the spectral analyses as described below.

3.2 STATISTICAL ANALYSIS

Basic statistical concepts can be directly applied to the dynamic data measurements. By very simple algebraic operations a long sequence of discrete pressure measurements, approximating the continuous pressure signal, can be reduced to time independent scalar quantities. These scalar quantities, the mean, standard deviation, and higher moments, can be used as gross descriptors of the fluctuating pressure signals over long periods of time. Statistical quantities,

although simple and useful, do not describe the time or frequency characteristics of the dynamic pressure signal. For quantitative description of the temporal characteristics of the dynamic data, spectral analysis techniques must be used.

3.2.1 Mean and standard deviation

The average or the mean pressure, $\overline{P}$, of the discrete dynamic data series can easily be found from the following equation.

$$\overline{P} = \frac{1}{N} \sum_{j=1}^{N} P_j \qquad (3\text{-}1)$$

In the above, N is the total number of discrete data points used to determine the mean. In all instances the entire pressure signal in a reading is used to define the mean and other statistical quantities.

The standard deviation about the mean pressure, σ_P, is a measure of the extent of the data scatter of the pressure signal. The standard deviation can be found from the following equation.

$$\sigma_P = \sqrt{\frac{1}{N} \sum_{j=1}^{N} (P_j - \overline{P})^2} \qquad (3\text{-}2)$$

Although the standard deviation provides a simple measure of the width of data

scatter about the mean, it does not provide any information on the distribution of the scatter.

3.2.2 Probability density function

To characterize the scatter of data about the mean pressure, the probability density function, $\varphi(P)$, must be determined. Using the probability density function (PDF), the mean pressure can be defined by the following relation.

$$\overline{P} = \int\limits_{-\infty}^{\infty} P\,\varphi(P)\,dP \tag{3-3}$$

The PDF defines the exact distribution of scatter about the mean. The PDF in Equation 3-3 has units of inverse pressure, and must satisfy the following constraint.

$$\int\limits_{-\infty}^{\infty} \varphi(P)\,dP = 1 \tag{3-4}$$

Additionally, the PDF can be used to determine the standard deviation from the following relation.

$$\sigma_P^2 = \int\limits_{-\infty}^{\infty} (P - \overline{P})^2\,\varphi(P)\,dP \tag{3-5}$$

Equations 3-3 and 3-5 are not typically used, since most data are discrete, and

Equations 3-1 and 3-2 are very easy to implement.

Determining the PDF is usually done numerically. For a random scatter of data about the mean pressure, there is an analytic form of the PDF.

$$\varphi(P) = \frac{1}{\sqrt{2\pi}\,\sigma_P}\exp\left[-\frac{(P-\overline{P})^2}{2\,\sigma_P^{\,2}}\right] \tag{3-6}$$

This form of the PDF is called a Gaussian, or normal, distribution. It is convenient to represent the Gaussian PDF in a non-dimensional form.

$$\varphi(\xi)\,\sigma_P = \frac{1}{\sqrt{2\pi}}\exp\left[-\frac{\xi^2}{2}\right] \tag{3-7}$$

$$\xi = \frac{P-\overline{P}}{\sigma_P} \tag{3-8}$$

The variable ξ is a convenient non-dimensional argument for the PDF, since it represents the pressure referenced to the mean, normalized by the standard deviation. All probability density functions are presented in the non-dimensional form, $\varphi(\xi)\,\sigma_P$, in this and subsequent discussions.

To construct the PDF from a dynamic pressure measurement, the discrete

pressure data series, P_n, is plotted referenced to the mean pressure, $\overline{P}$, normalized by the standard deviation, σ_p, as in Equation 3-8. This new variable, ξ, becomes the abscissa for the PDF. To determine the PDF numerically, the ξ abscissa is divided into 50 sub-intervals over the total range from -3 to 3. The number of data points which fall within each sub-interval is then accumulated. The PDF defined at each sub-interval mid-point is then just the ratio of the accumulated points in the sub-interval to the total number of points in all sub-intervals, times the number of intervals divided by the total interval range (50/6).

Figure 15 shows an example of the results of this technique. The data sequence in Figure 14 is re-plotted in the top plot of Figure 15 as the abscissa ξ. The bottom plot shows the resulting PDF constructed by accumulating data points in 50 sub-intervals over the total range $-3 < \xi < 3$. The open-circle symbols define the PDF for the complete data sequence of 204800 points, although only the first record (1024 data points) in the reading is shown in the top plot for clarity. A Gaussian PDF is also shown in the bottom plot of Figure 15 for comparison as a continuous line.

3.2.3 Skewness and kurtosis

There are two additional statistical quantities, higher moments about the mean, which are useful in characterizing the distribution of fluctuating pressure data. The skewness, α_p, or third moment, is defined as follows.

$$\alpha_P = \frac{\frac{1}{N}\sum_{j=1}^{N}(P_j - \overline{P})^3}{\sigma_P^3} \qquad (3\text{-}9)$$

The kurtosis, β_P, or fourth moment, is defined as follows.

$$\beta_P = \frac{\frac{1}{N}\sum_{j=1}^{N}(P_j - \overline{P})^4}{\sigma_P^4} \qquad (3\text{-}10)$$

Skewness and kurtosis are useful in characterizing the shape of the probability distribution function. Note that the skewness and kurtosis are non-dimensional numbers, as opposed to the standard deviation, which has units of pressure.

The skewness is a measure of the asymmetry of the PDF. A PDF with a positive α_P has a tail trailing off in the positive ζ direction and a corresponding peak shifted to the negative ζ. This characteristic is clearly seen in Figure 15, and for the signal shown, $\alpha_P = 1.330$.

The kurtosis is a measure of the flatness of the PDF. A Gaussian probability density function has a kurtosis of 3. A PDF with a sharper peak will have a kurtosis greater than 3, and a PDF with a flatter peak will have a kurtosis less than 3. For the PDF in Figure 15, $\beta_P = 5.574$, indicative of the observed sharper peak relative to that for a Gaussian PDF.

3.3 SPECTRAL ANALYSIS

Temporal characterization of dynamic pressure signals is typically accomplished by techniques which are broadly classified as spectral analysis. Spectral analysis involves the transformation of the pressure signal from the time domain to the frequency domain. As a result, the temporal characteristics of the original pressure signal are re-interpreted in terms of the frequency content of the pressure signal. In spectral analysis, the transformation of a signal from the time domain to the frequency domain is performed by the Fourier transform.

3.3.1 Fourier transforms

The Fourier transform is a classic integral operator, where the transform kernel is a complex exponential of the product of time and frequency. The Fourier transform of a fluctuating pressure signal is defined as follows.

$$\hat{P}(f) = \int_{-\infty}^{\infty} P(t)\, e^{-i2\pi ft} dt \qquad (3\text{-}11)$$

The Fourier transform, $\hat{P}(f)$, of the pressure signal is a function of frequency, f, and has units of pressure times time. The inverse-Fourier transform reconstructs the original pressure signal, $P(t)$, from the transformed pressure signal, $\hat{P}(f)$. The inverse-Fourier transform is also in integral operator and is defined as

follows.

$$P(t) = \int_{-\infty}^{\infty} \hat{P}(f)\, e^{i2\pi ft} df \qquad (3\text{-}12)$$

Equations 3-11 and 3-12 comprise the Fourier transform pair for a continuous

pressure signal.

There are two problems which occur with experimental data when

attempting to apply Equation 3-11 to compute the Fourier transform of a measured

pressure signal. First, the pressure signal is not measured over an infinite time

range, and second, the pressure signal data is not continuous but discrete. The

first problem is overcome by introducing the finite-Fourier transform.

$$\hat{P}(f) = \int_{0}^{T} P(t)\, e^{-i2\pi ft} dt \qquad (3\text{-}13)$$

In Equation 3-13, T, is the time interval over which the pressure signal, $P(t)$, is

measured. Overcoming the second problem, discrete data, requires converting the

integral transformation in Equation 3-13 into a discrete summation.

The pressure signal can be represented as a series of N data points recorded

over the time interval T.

$$P_n = P(t_n) = P(n\Delta t) \qquad n = 0,1,2,\ldots,N-1 \tag{3-14}$$

Using the discretization in Equation 3-14, the Fourier transform defined in Equation 3-13 can be written as follows.

$$\hat{P}(f) = \Delta t \sum_{n=0}^{N-1} P_n \exp\left[-i2\pi f n \Delta t\right] \tag{3-15}$$

Equation 3-15 calculates a continuous Fourier transform from a discrete data representation of the pressure signal. However, it is inconsistent to express a Fourier transform of a signal at any arbitrarily precise frequency when the data for the signal is only defined at discrete time intervals.

This inconsistency is corrected by introducing a discretization of the frequency variable.

$$f_k = \frac{k}{T} = \frac{k}{N\Delta t} \qquad k = 0,1,2,\ldots,N-1 \tag{3-16}$$

Using the discretization in Equation 3-16, a discrete Fourier transform can be

properly defined as follows.

$$\hat{P}(f_k) = \Delta t \sum_{n=0}^{N-1} P_n \exp\left[-i\frac{2\pi kn}{N}\right] \tag{3-17}$$

There is one more change of variable which is usually introduced for

computational convenience.

$$\hat{P}_k = \frac{\hat{P}(f_k)}{\Delta t} \tag{3-18}$$

Recall that the units for the Fourier transform of the pressure signal were pressure

times time. Using Equation 3-18 reduces the Fourier transform of the pressure

signal to a variable with units of just pressure. This substitution is typically

performed for computational convenience, where the Fourier transform of the

signal has the same dimensionality as the original signal.

A consistent discrete finite-Fourier transform pair may now be defined for

manipulation of the experimental discrete pressure signal data.

$$\hat{P}_k = \sum_{n=0}^{N-1} P_n \exp\left[-i\frac{2\pi kn}{N}\right] \qquad k=0,1,2,\dots,N-1 \qquad (3\text{-}19)$$

$$P_n = \frac{1}{N}\sum_{k=0}^{N-1} \hat{P}_k \exp\left[i\frac{2\pi kn}{N}\right] \qquad n=0,1,2,\dots,N-1 \qquad (3\text{-}20)$$

Equations 3-19 and 3-20 are used to compute the Fourier transform and inverse Fourier transform for all spectral analyses presented in this investigation. Computation of the Fourier transform series, $\hat{P}_k$, or the inverse Fourier transform series, P_n, is usually performed by one of many standard fast Fourier transform (FFT) algorithms.

The Cooley-Tukey FFT algorithm[15] was used to calculate the Fourier transforms required by data reduction and analysis. The Cooley-Tukey FFT requires that the length of the data samples, N, be an integer power of 2. Typical calculations used 1024 data points as the basic data sample length. This was the number of points used to define a data record. A complete pressure signal was typically made up of 200 records. Any calculation requiring a Fourier transformation was performed on one data record at a time, the results accumulated, the next record processed, and so on until the complete pressure signal was analyzed. The results from each record analyzed were then averaged

over all of the records to define the computed quantity over the entire signal length. The data reduction and analyses that required Fourier transforms were the computation of spectra and correlations.

3.3.2 Power spectral density

A useful descriptor of the general frequency content of a fluctuating pressure signal is the power spectral density (PSD) function. The power spectral density function, $G(f)$, is defined as follows.

$$G(f) = \frac{2}{T} \left| \hat{P}(f) \right|^2 \tag{3-21}$$

$$G(f) = \frac{2}{T} \int_0^T \int_0^T P(\eta) P(\mu) \, e^{-i2\pi f(\mu - \eta)} \, d\mu \, d\eta \tag{3-22}$$

The PSD as defined in Equations 3-21 and 3-22 exists for positive frequencies only. The PSD can be computed by the FFT of the discrete pressure signal as follows.

$$G(f_k) = \frac{2}{N\Delta t} \left| \hat{P}(f_k) \right|^2 \qquad k = 0,1,2,\ldots,\frac{N}{2} \tag{3-23}$$

Equation 3-23 was used to calculate the PSD from the discrete pressure signal data for each record in a pressure signal reading. The PSD was then ensemble averaged at each discrete frequency, f_k, over all of the records in a pressure signal reading. Note that the units of the PSD are pressure squared per hertz.

In Equation 3-23 the PSD is calculated only up to the Nyquist frequency, $f_{k=N/2}$. For indices of k greater than $N/2$, Equation 3-23 calculates the PSD in the negative frequency range. Since the PSD is defined for positive frequencies only, Equation 3-23 can be applied up to the Nyquist frequency only. For a discretely sampled pressure signal, the Nyquist frequency is one half the sampling frequency, f_s.

For a pressure signal with a mean value of zero, the integral over all positive frequencies of the PSD also defines the variance of the pressure signal.

$$\int_0^\infty G(f)\, df = \sigma_P^2 \qquad (3\text{-}24)$$

Equation 3-24 provides a very useful normalization. Since assessing the frequency content of a fluctuating pressure signal does not depend on the value of the mean pressure, all computations using the FFT were done on data from pressure signals with the mean pressure subtracted.

Using Equation 3-24, a non-dimensionalized PSD can be defined by

$G(f)f/\sigma_P^2$. This form of the PSD will be used in subsequent descriptions and comparisons. Figure 16 shows the power spectral density function, $G(f)$, for the sample pressure signal presented in Figure 13. Figure 16 plots the PSD verses frequency on log-log axes. As expected for a turbulent flow, the PSD shows the typical rapid fall-off at higher frequencies, with the PSD decreasing nearly 8 orders of magnitude over the frequency range shown. The plot in Figure 16, however, does not easily convey information on the relative frequency contributions in the pressure signal, and comparisons of differences in PSD are difficult in this format.

Figure 17 shows the same pressure signal data, but a normalized power spectral density function, $G(f)f/\sigma_P^2$, is used instead of a simple PSD. In Figure 17 the relative frequency content is easily discerned. The frequency content of the pressure signal is broad band with a maximum at approximately 1 kHz. This presentation of spectral data is very useful for comparing the content of different pressure signals since the normalization eliminates the relative differences in the magnitude of the fluctuating signals as well as enhancing the high frequency contributions.

3.4 CORRELATIONS

In contrast to using power spectral density functions to describe the frequency characteristics of a pressure signal, correlation functions can be used to describe the characteristics of various time scales in the pressure signal. In

general, a correlation function is defined as the time averaged product of two fluctuating quantities separated by a time delay. A pressure signal can be correlated to itself producing an autocorrelation function, or two simultaneously measured pressure signals (from separate transducers) can be correlated to each other producing a cross-correlation function.

3.4.1 Autocorrelation

The autocorrelation function of a pressure signal is found from a normalized autocovariance, $R(\tau)$, which is defined by the following relation.

$$R(\tau) = \frac{1}{T} \int_0^T P(t)\, P(t-\tau)\, dt \qquad (3\text{-}25)$$

Equation 3-25 is the time average of a pressure signal multiplied by the same signal offset by a time delay τ. Equation 3-25, however, is not convenient to use for numerical calculation of the autocovariance function. Instead, $R(\tau)$, is usually determined from a power spectral density function.

The power spectral density function, $G(f)$, can also be defined in terms of an autocovariance function, as opposed to the definition given in Equation 3-21.

$$G(f) = 4 \int_0^T R(\tau) \, e^{-i2\pi f \tau} d\tau \qquad\qquad (3\text{-}26)$$

From Equation 3-26, the autocovariance function can be found by an inverse-Fourier transform of the power spectral density function. Using a discrete inverse FFT, the autocovariance function can be calculated by the following.

$$R(\tau_n) = \frac{1}{4(N-n)\Delta t} \sum_{k=0}^{2N-1} G(f_k) \exp\left[i \frac{2\pi kn}{N} \right] \qquad n = 0,1,2,\ldots,N\text{-}1 \qquad (3\text{-}27)$$

In Equation 3-27 the discrete PSD, $G(f_k)$, is calculated from Equation 3.23 for a pressure data record of N data points padded with an additional N zeros. Thus the FFT operates on $2N$ data points in this instance rather than N data points as defined in Equation 3-19. This technique of zero padding is covered in detail in reference 15.

The autocorrelation function, $\rho(\tau)$, is simply the autocovariance function normalized by the autocovariance at a time delay of zero.

$$\rho(\tau) = \frac{R(\tau)}{R(0)} \qquad\qquad (3\text{-}28)$$

Figure 18 shows an example of the autocorrelation function for the sample

pressure signal of Figure 13. The autocorrelation function is always unity for

zero time delay, and Figure 18 shows a very steep drop off for small time delays.

The autocorrelation is very nearly zero for the rest of the time delay range shown.

This behavior is typical of a pressure signal which has random fluctuations about

the mean and is comprised of broad band frequency content.

3.4.2 Cross-correlation

The cross-correlation function, $\rho_{xy}(\tau)$, is similar to the autocorrelation, but

instead of a single pressure signal, two separate pressure signals are used. The

first pressure signal is denoted by the subscript x, and the second pressure signal

is denoted by y. However, since two separate pressure signals are used the

computations to determine the cross-correlation are slightly different from those

used to determine the autocorrelation.

The cross-correlation function, $\rho_{xy}(\tau)$, is calculated from the cross-

covariance function, $R_{xy}(\tau)$, as shown below.

$$\rho_{xy}(\tau) = \frac{R_{xy}(\tau)}{\sqrt{R_{xx}(0)}\sqrt{R_{yy}(0)}} \tag{3-29}$$

In Equation 3-29, the cross-covariance functions, $R_{xx}(\tau)$ and $R_{yy}(\tau)$, reduce to

the autocovariance function, $R(\tau)$, for pressure signals x and y respectively. The Fourier transform of the cross-covariance also defines the cross-spectral density function, $G_{xy}(f)$, as follows.

$$G_{xy}(f) = 4 \int_0^T R_{xy}(\tau) \, e^{-i2\pi f\tau} d\tau \qquad (3\text{-}30)$$

The cross-covariance in turn may be calculated from the inverse-Fourier transform of Equation 3-30, in the same manner that the autocovariance function was determined from the inverse-Fourier transform of the power spectral density function in Equation 3-26.

The cross-spectral density function, $G_{xy}(f)$, is calculated from the two pressure signals, x and y, by the following relation.

$$G_{xy}(f) = \frac{2}{T} \int_0^T \int_0^T P_x(\eta) P_y(\mu) \, e^{-i2\pi f(\mu - \eta)} d\mu \, d\eta \qquad (3\text{-}31)$$

For discrete pressure signal data, the discrete cross-spectral density is calculated as follows.

$$G_{xy}(f_k) = \frac{2}{N\Delta t} \hat{P}_x^*(f_k) \, \hat{P}_y(f_k) \qquad\qquad (3\text{-}32)$$

Equation 3-27 is then used to calculate the cross-covariance by the discrete inverse FFT of the cross-spectral density.

The cross-correlation function, $\rho_{xy}(\tau)$, is a useful indicator of one pressure signal leading or lagging another pressure signal. The cross-correlation also shows if the two pressure signals are in phase or out of phase. The cross-correlation function is bounded within the range of $+1$ to -1 for all time delays.

3.4.3 Coherence

One other spectral function can be calculated from the Fourier transforms of two pressure signals. The coherence function, $\gamma_{xy}^2(f)$, is defined by the following.

$$\gamma_{xy}^2(f) = \frac{|G_{xy}(f)|^2}{G_{xx}(f) \, G_{yy}(f)} \qquad\qquad (3\text{-}33)$$

The cross-spectral density, $G_{xy}(f)$, in Equation 3-33 does not use zero padding. The cross-spectral densities, $G_{xx}(f)$ and $G_{yy}(f)$, reduce to the power spectral density, $G(f)$, for the pressure signals x and y respectively. The coherence

function, $\gamma_{xy}^2(f)$, is bounded between 0 and 1 for all frequencies, and indicates at what frequencies and to what extent the two pressure signals correlate.

3.5 BOX-CAR TECHNIQUES

When analyzing a pressure signal measurement taken in the intermittent region where the separation shock wave is observed, very large pressure changes are recorded as the shock wave passes over the transducer. The pressure signal is characterized by two distinct regimes. The first regime is the natural turbulent pressure fluctuations measured in the incoming boundary layer flow when the separation shock wave is downstream of the transducer. The second regime measures large pressure oscillations in the separated boundary layer when the separation shock wave is upstream of the transducer.

Figure 19 shows a single record of a typical pressure signal reading from a transducer in the intermittent region. The large pressure rises correspond the measurements at times when the separation shock wave has moved upstream of the transducer. The portion of the pressure signal between the rises corresponds to measurements of the incoming boundary layer fluctuations when the separation shock wave is downstream of the transducer. From this measurement it is possible to construct a relatively simple algorithm to determine the time periods when the separation shock wave is either upstream or downstream of the transducer.

A two-threshold algorithm is used which converts the pressure signal into a

bimodal signal, valued at either 1 or 0, indicating the position of the separation

shock wave as either upstream or downstream of the transducer. The resulting

bimodal signal when plotted appears as a series of step functions, or box-cars.

Thus this type of analysis is called a box-car technique. The resulting box-car

output signal is also shown in Figure 19.

In Figure 19 three lines are drawn across the pressure signal, labeled: $\overline{P}_0$,

Υ_1, and Υ_2. The first level, $\overline{P}_0$, is the mean pressure measured in the incoming

boundary layer. The next two levels, Υ_1 and Υ_2, are the low and high thresholds

for determining the box-car signal. If the pressure signal is below Υ_1 the box-car

output is 0. If the pressure signal rises above Υ_2 the box-car output becomes 1,

and remains 1 until the pressure signal falls below both Υ_2 and Υ_1. The low and

high thresholds are set at $\Upsilon_1 = \left(\overline{P} + 3\sigma_P\right)_0$, and $\Upsilon_2 = \left(\overline{P} + 6\sigma_P\right)_0$. The box-car signal

can be processed to yield additional information on the dynamics of the separation

shock wave motion.

3.5.1 Intermittency and zero-crossing frequency

Intermittency is defined as the fraction of time the separation shock wave is

upstream of a pressure transducer. The intermittency, Γ, can be directly

computed from the box-car signal by the following relation.

$$\Gamma = \frac{1}{T}\sum_{j=1}^{M}\left(t_j^- - t_j^+\right)$$

(3-34)

The rise and fall times in the box-car signal are denoted by t^+ and t^-. The total number of shock wave passages is denoted by M.

The zero-crossing frequency, f_c, is the number of shock wave passages in a single direction per unit time and is calculated by the following.

$$\frac{1}{f_c} = \frac{1}{M} \sum_{j=1}^{M} \left(t_{j+1}^+ - t_j^+ \right)$$
(3-35)

Figure 19 also indicates the location of a pair of rise and fall times on the box-car signal.

3.5.2 Shock position and velocity

For a series of pressure transducers located in the intermittent region, a series of nested box-car signals can be constructed from the simultaneous pressure measurements. It is then possible to determine the instantaneous position of the separation shock wave as it moves across the transducers. From the recorded time delays as the shock wave moves over each transducer, and the known transducer spacings, it is possible to calculate the separation shock wave velocity history. From the velocity history it is also possible to calculate the mean shock wave velocities moving in the upstream and downstream directions, as well as the standard deviations, other statistical quantities, spectra, and correlations.

CHAPTER IV

RESULTS AND DISCUSSION

4.1 INCOMING BOUNDARY LAYERS

As a precursor to the general discussion of results, it is necessary to quantify the upstream boundary conditions in the interaction. The characteristics of the incoming boundary layers may in part determine the characteristics of the unsteady shock wave turbulent boundary layer interaction. The incoming boundary layers can be described by mean velocity profiles and fluctuating wall pressure signals. The wall pressure signals in turn can be characterized by power spectral density and autocorrelation functions. Analysis of the autocorrelations provides information on the incoming boundary layer turbulent integral time and length scales. The incoming boundary layer location is taken to be at the start of the test section.

4.1.1 Velocity profiles

The incoming turbulent boundary layer mean velocity profiles are accurately described using a wall-wake function developed by Sun and Childs.[16] This modified law-of-the-wall-law-of-the-wake function provides an analytic representation of a compressible, turbulent boundary layer mean velocity profile in

the form $u/u_e = f(z/\delta; C_f, \Pi, M_e)$. The parameters in the wall-wake function are

the skin friction coefficient, C_f, the coefficient of the wake function, Π, and the

boundary layer edge Mach number, M_e. These three parameters control the

terms in the wall-wake function which model; the inner law-of-the-wall profile,

the outer law-of-the-wake profile, and compressibility effects, respectively. A

wall-wake function is uniquely determined by these three parameters.

The exact form of the wall-wake function used is given below.

$$
\left.
\begin{aligned}
\frac{u}{u_e} &= \frac{1}{\sqrt{\sigma}} \sin\left\{ \sin^{-1}\sqrt{\sigma}\left[1 + \frac{1}{K}\frac{u_\tau}{u_e^*}\left(\ln\eta + 2\sqrt{1-\eta} - 2\ln(1+\sqrt{1-\eta}) \right) \right.\right. \\
&\qquad\qquad\qquad\qquad\qquad\left.\left. - \frac{\Pi}{K}\frac{u_\tau}{u_e^*}\left(2 - W(\eta)\right) \right] \right\} \\
\frac{u_\tau}{u_e^*} &= \left[\frac{C_f}{2}\frac{\sigma}{1-\sigma} \right]^{1/2} \frac{1}{\sin^{-1}\sqrt{\sigma}} \\
\sigma &= \frac{\dfrac{\gamma-1}{2}M_e^2}{1 + \dfrac{\gamma-1}{2}M_e^2} \\
W(\eta) &= 1 - \cos\pi\eta \\
\eta &= \frac{z}{\delta}
\end{aligned}
\right\} \quad (4\text{-}1)
$$

In Equation 4-1 the law-of-the-wall constant is taken to be, $K = 0.4$. Equation 4-1

can be used in two basic ways. In the first, the parameters δ, C_f, and Π are

known and the velocity profile is then directly determined. In the second, the

velocity profile is known and the parameters δ, C_f, and Π are then determined

by a least-squares curve fit. Typically the boundary layer edge velocity, u_e, and

Mach number, M_e, are known independently.

Other investigators have measured the incoming boundary layer velocity

profiles in the 1x1 supersonic wind tunnel at Mach numbers 2.0, 2.5, 3.0, 3.5,

and 4.0. The incoming boundary layer velocity profiles for Mach 5.0 have not

been measured as of this date. The incoming boundary layer velocity profile

data[17] was calculated from pitot pressure measurements. This data was then used

in a least-squares curve fit using Equation 4-1 to determine the boundary layer

thickness, δ, the skin friction coefficient, C_f, and the coefficient of the wake

function, Π, for the Mach number range from 2.0 to 4.0. The details of the

least-squares curve fitting techniques used are found in reference 18. The

resulting incoming boundary layer velocity profile wall-wake curve fits, and the

corresponding experimental measurements, are shown in Figures 20 through 22

for Mach number 2.0, 3.0, and 4.0. The least-squares determined values for δ,

C_f, and Π are provided in Table 3.

Since no experimental velocity profile data was available for Mach 5.0, the

wall-wake function was evaluated using extrapolations to the parameters δ, C_f,

and Π determined from the experimental data at Mach numbers 2.0, 2.5, 3.0,

3.5, and 4.0. A linear function was generated for each extrapolation by a least-

squares curve fit. The extrapolated values are also included in Table 3 for Mach

5.0. Figure 23 shows the resulting incoming boundary layer profile defined by

the wall-wake function for Mach 5.0.

The displacement thickness, δ^*, and the momentum thickness, θ, for the incoming boundary layers were determined from the wall-wake functions and the following definitions.

$$\frac{\delta^*}{\delta} = \int_0^1 \left[1 - \frac{\rho}{\rho_e} \frac{u}{u_e} \right] d\left(\frac{z}{\delta} \right) \qquad (4\text{-}2)$$

$$\frac{\theta}{\delta} = \int_0^1 \frac{\rho}{\rho_e} \frac{u}{u_e} \left[1 - \frac{u}{u_e} \right] d\left(\frac{z}{\delta} \right) \qquad (4\text{-}3)$$

In order to evaluate the above integrals, however, it is necessary to determine the density profile. This is accomplished by first starting with the Croco-Busemann approximation for a turbulent boundary layer.

$$T \approx T_w + \left(T_{aw} - T_w \right) \frac{u}{u_e} - \frac{ru^2}{2c_p} \qquad (4\text{-}4)$$

The adiabatic wall temperature is defined by the relation below.

$$T_{aw} = T_e\left(1 + r\frac{\gamma-1}{2}M_e^2\right) \tag{4-5}$$

Assuming an adiabatic wall, then the following relations can be written.

$$\frac{T}{T_e} = 1 + r\frac{\gamma-1}{2}M_e^2\left[1 - \left(\frac{u}{u_e}\right)^2\right] = \left(\frac{\rho}{\rho_e}\right)^{-1} \tag{4-6}$$

Equation 4-6 determines the density profile as a function of the velocity profile, which in turn is already defined by the wall-wake function. The turbulent recovery factor, r, was assumed to be 0.89. Equation 4-6 was used with the wall-wake functions to evaluate the integrals in Equations 4-2 and 4-3. The resulting displacement and momentum thicknesses are also included in Table 3.

4.1.2 Spectra

The fluctuating wall pressures were measured for the incoming boundary layers at Mach numbers 2.0, 3.0, 4.0, and 5.0. The power spectral density functions were calculated and are shown in Figures 24 through 27. All of the PSD show broad band frequency content. The Mach 2.0 pressure signal indicates a slight dominant frequency at approximately 1 kHz. This frequency peak is not observed at the other Mach numbers.

The PSD at Mach numbers 3.0 to 5.0 show very similar characteristics.

Each PSD has a maximum frequency contribution of approximately 0.3 between 1

and 2 kHz. The PSD for Mach 4.0 and 5.0 appear to have slight dominant

frequencies below 1 kHz, however, the resolution of the spectra is very coarse in

this frequency range. The PSD for Mach 5.0 also shows relatively higher

contributions at the high-end frequencies near 40 kHz.

The probability density functions for the incoming boundary layer pressure

signals were found to be Gaussian for all Mach numbers. The standard deviation

of the pressure signal normalized by the mean pressure, σ_P / P_0, can be found in

Table 4 for Mach numbers 2.0, 3.0, 4.0, and 5.0. Note that the ratio of σ_P / P_0

shows a factor of 2 increase from Mach 2.0 to Mach 5.0.

4.1.3 Integral scales

The autocorrelation functions for the incoming boundary layer pressure

signals for Mach numbers 2.0, 3.0, 4.0, and 5.0 are shown in Figures 28 through

31. All of the autocorrelations show the same basic characteristic of a rapid fall-

off to zero within a time delay of less than 1 ms. The Mach 2.0 autocorrelation

does show a slight oscillatory behavior for longer time delays. The other Mach

number autocorrelations do not exhibit this characteristic.

An integral time scale of the turbulent pressure fluctuations can be

determined from the autocorrelation function by integration over all time delays.

This can be expressed analytically as follows.

$$\Omega = \int_{0}^{\infty} \rho(\tau)\,d\tau \qquad\qquad (4\text{-}7)$$

Instead of using Equation 4-7 to determine the integral time scale, Ω, the

autocorrelation can often be approximated by an exponential function which

satisfies Equation 4-7.

$$\rho(\tau) = \exp\left[-\frac{\tau}{\Omega}\right] \qquad\qquad (4\text{-}8)$$

Equation 4-8 was used to least-squares curve fit the autocorrelation functions to

determine the integral time scales, Ω, for each Mach number. Table 4 lists the

values of Ω for each Mach number.

An integral length scale of the turbulent pressure fluctuations can be found

by employing Taylor's hypothesis.

$$\Lambda = U\Omega \qquad\qquad (4\text{-}9)$$

The integral length scale, Λ, is also listed in Table 4 for each Mach number. In

Equation 4-9 the turbulent bulk velocity, U, is taken to be the free stream flow

velocity.

Using an analysis based on the integral length scale, Taylor[19] developed a theoretical function describing the one-dimensional turbulent energy spectrum, $E(f)$. This theoretical function is given as follows.

$$\frac{E(f)U}{u'^2\Lambda} = \frac{4}{1 + 4\pi^2 f^2 \dfrac{\Lambda^2}{U^2}} \qquad (4\text{-}10)$$

It is proposed that by direct analogy Equation 4-10 can be applied to the PSD, $G(f)$, of a turbulent pressure signal, and with the use of Equation 4-9, the following relation is developed.

$$\frac{G(f)}{\sigma_P^2 \Omega} = \frac{4}{1 + 4\pi^2 f^2 \Omega^2} \qquad (4\text{-}11)$$

To verify the validity of Equation 4-11, the PSD from the incoming boundary layer pressure signals for each Mach number have been plotted in Figure 32, along with Equation 4-11.

The PSD for Mach numbers 2.0 and 3.0 agree very well with the theoretical relation of Equation 4-11, as can be seen in Figure 32. The PSD for

Mach numbers 4.0 and 5.0 show slightly less consistent agreement with the theory of Equation 4-11, particularly at the higher frequencies. The overall agreement of the PSD with the theoretical form of the spectra, however, is very encouraging.

The average integral time scale, Ω, for all Mach numbers is approximately 0.1 ms. By using this value, and plotting Equation 4-11 as a normalized power spectral density function, Figure 33 shows the expected theoretical PSD for all Mach numbers. Comparing Figure 33 with the experimental results in Figures 24 through 27 indicates that the observed incoming boundary layer PSD are indeed consistent with the theoretical PSD given in Equation 4-11.

4.2 FLOW VISUALIZATION

An initial series of experiments were conducted in an effort to provide qualitative flow visualization information about the unsteady shock wave/turbulent boundary layer interaction. Two basic techniques were used. In the first, schlieren photography was employed in an attempt to resolve the shock wave structure ahead of the blunt fin. In the second, surface flow tracing visualization methods were applied in an effort to resolve the surface flow patterns in the unsteady shock wave/turbulent boundary layer interaction region about the blunt fin. Two slightly different surface flow visualization techniques, fluorescent oil and "kerosene/lampblack", were used.

In the fluorescent oil flow visualization experiments a 1.9 cm blunt fin was used. This same size blunt fin was also used in the schlieren photography

experiments. For both of these techniques it was necessary to use a glass sidewall in the test section in order to record the test results photographically. As a result of safety requirements there were no experiments performed at Mach 5.0 with these flow visualization methods. For the "kerosene/lampblack" surface flow visualization technique, it was not necessary to use a glass sidewall in the test section, therefore experiments at Mach 5.0 were conducted. Additionally, for the "kerosene/lampblack" technique, and all other experiments in this investigation, a 2.54 cm blunt fin was used.

4.2.1 Schlieren photography

Figure 34 shows a schlieren photograph of the Mach 2.0 interaction. The optical path of the schlieren system was perpendicular to the blunt fin. The outline of the blunt fin can be seen in Figure 34 blocking the majority of the circular optical path. The detached shock wave is clearly visible ahead of the blunt fin hemi-cylindrical leading edge as the strong, vertical line in Figure 34. Note that the flow is from right to left in the photograph. For a linear dimensional reference, the height of the blunt fin is 15.2 cm.

The technique of schlieren photography resolves density gradients in the flow through which the optical beam passes. As a result, the two-dimensional image recorded on a photographic film is an integration of the density gradients across the entire test section. Using schlieren photography to image three-dimensional flows must be done with care. The detached shock wave ahead of the

blunt fin wraps around the leading edge, and the dark vertical line in Figure 34 corresponds to the strongest density gradient roughly tangent to the curved shock wave surface. Thus, for this geometry, schlieren photography records an image approximating the flowfield along the blunt fin centerline.

In typical schlieren systems[20] a gray scale photographic image is generated by placing a knife edge at the focus of the optical system. The knife edge blocks a portion of the light path which has been displaced by changes in the index of refraction which are caused by changes in fluid density. The blocked light paths create darker regions in the photographic image. For the schlieren photography performed in these experiments, false color images were made by replacing the knife edge by a color filter made up of very fine colored bands. Rather than blocking a light path which has been refracted, the light path passed through a different colored band. The resulting image formed on the photographic film shows density gradients as differing colors, not just differing intensities.

Figure 34 is a photocopy of a false color schlieren photograph. One of the advantages of using false color over gray scale schlieren is the ability for false color to enhance the visualization of boundary layers. Although much of the visible contrast is lost when photocopying, the incoming boundary layer is seen in Figure 34 as the darker, horizontal band in the lower right of the image. In the region near the root of the blunt fin is a bright, diagonal feature which is the resulting image of the unsteady separation shock wave. Since the separation shock wave is moving over a distended region, a sharp density gradient cannot be

imaged with the same clarity as the detached shock wave about the blunt fin

leading edge, which is seen above and is stationary.

Figures 35 and 36 show schlieren photographs for Mach numbers 3.0 and

4.0 respectively. Each of these figures show the same elements as found in

Figure 34 at Mach 2.0. There are notable differences, however, between the

Mach numbers. As the Mach number increases from 2.0 to 4.0, the detached

shock wave ahead of the blunt fin moves closer to the fin leading edge. As the

Mach number increases, so does the thickness of the incoming boundary layer. In

Figures 34 to 36 the separation shock wave shows some change in rough location

and angle, however, since the image is blurred by shock wave motion, more

accurate descriptions are not possible from these photographs.

4.2.2 Fluorescent oil technique

Figure 37 shows the resulting surface flow pattern in the shock

wave/turbulent boundary layer interaction about the blunt fin at Mach 2.0 using

the fluorescent oil technique. In this method, the test section surface around the

blunt fin root was painted with an oil, in which fluorescent dye was suspended.

The wind tunnel was started, and the test section was monitored by video camera

as the resulting flow sheared the oil film into a stable pattern. The wind tunnel

was then stopped, and the oil film was exposed under black light, fluorescing the

dye. The image was photographed by a camera aligned along the blunt fin leading

edge hemi-cylindrical axis. The top surface of the blunt fin was also painted with

fluorescent oil, enhancing the blunt fin outline in contrast to the surface below.

The most prominent feature in Figure 37 is the crescent shaped coalescence of oil ahead of the blunt fin. This coalescence of surface streamlines ahead of the blunt fin indicates the presence of boundary layer separation, and this line of coalescence is called the primary separation line. In Figure 37 at Mach 2.0, the primary separation line is seen as a rather broad region of accumulated oil. Figures 38 and 39 show the surface flow visualization for Mach numbers 3.0 and 4.0 respectively. A notable difference over the Mach number range shown is that the primary separation line is more sharply defined in the Mach 3.0 and 4.0 flows than in the Mach 2.0 flow. An additional line of coalescence is seen downstream of the primary separation line, ahead of the blunt fin, in the Mach 3.0 and 4.0 flows which is not observed in the Mach 2.0 flow.

The flowfield behind the separation line and ahead of the blunt fin is complex, unsteady, and can depend significantly on the state of the incoming boundary layer. Other investigators have found differences in surface flow trace patterns behind the primary separation line for the blunt fin induced shock wave/turbulent boundary layer interaction. All experiments to date, however, show pronounced primary separation lines. Fomison[21] performed oil flow visualization with different diameter blunt fins, and he concluded that a secondary separation line exists downstream of the primary separation line and ahead of the blunt fin. Sedney[22] found up to three separation lines in experiments using circular cylinders. Brusniak[23] found a surface flow feature similar to the

secondary coalescence line observed in Figures 38 and 39. Brusniak concluded

that this feature was not a secondary separation line, and he noted that

experiments in the same facility, using different incoming boundary layer

thicknesses, did not show this feature at all. The interpretation of surface flow

visualization techniques in this particular shock wave/turbulent boundary layer

interaction is still a source of discussion, particularly when trying to determine

mean flow structures in the separated region ahead of the blunt fin. Given the

disparity in observations between experiments, the feature observed in Figures 38

and 39 will simply be referred to as a secondary coalescence line, with no proof

or refutation of a secondary separation line implied.

4.2.3 "Kerosene/lampblack" technique

In addition to the fluorescent oil surface flow visualization technique,

another surface flow tracing method was used. The kerosene/lampblack technique

is usually applied in blow-down supersonic wind tunnels where rapid starting is

possible. In this method, a test surface is coated with a fine, dark powder,

typically lampblack, in a suspension of kerosene. Once the wind tunnel is started

the kerosene and lampblack mixture flows into a pattern approximating the wall

shear flowfield. The kerosene is quickly evaporated, freezing the resulting pattern

of dried lampblack, which can then be lifted off the test surface with a wide piece

of cellophane tape.

Since the wind tunnel used in this investigation was not a blow-down

facility, slight modifications to the "kerosene/lampblack" technique were

necessary. A mixture of oil and kerosene with powdered dye in suspension was

applied to the test surface, and once the kerosene was evaporated from the

mixture, a very thin layer of oil/dye traced the wall shear flowfield. The pattern

was then transferred, by soaking into a piece of paper, forming a permanent

record.

The resulting images of the wall shear flowfield on the surface beneath the

shock wave/turbulent boundary layer interaction are shown in Figures 40 through

43 for Mach numbers 2.0, 3.0, 4.0, and 5.0 respectively. In each of the figures,

ahead of the outline of the blunt fin, can be seen the primary separation line trace,

as well as a fine tracing of the overall interaction detail and extent. The results of

this surface flow visualization technique are significantly clearer than the results

obtained using the fluorescent oil technique, although both methods show the same

interaction features. Using this surface flow visualization technique, however,

does not prominently indicate the same secondary coalescence line found with the

fluorescent oil technique in Figures 38 and 39.

The primary separation line, henceforth referred to as simply the separation

line, S, is particularly important in describing the location and characteristics of

the unsteady shock wave/turbulent boundary layer interaction. Other investigators

have shown that the separation line corresponds to the farthest downstream

location of the unsteady shock wave motion. Because of the significance of the

separation line in relation to the unsteady shock wave motion, it is desirable to

find a mathematical representation of the curve S. Given the basic shape of the separation line traces in Figures 40 through 43, it is expected that a functional relation in polar coordinates can be determined for S.

Figure 44 shows the polar coordinate system, (r, ω), used to describe the interaction region. The separation line traces in Figures 40 through 43 were digitized in terms of the radial coordinate to the separation line, $-r_s(\omega)$. A polynomial curve fit of the form, $-r_s(\omega) = a + b\omega^2 + c\omega^4$, was then determined for each Mach number separation line. The resulting curve fits for the Mach 2.0, 3.0, 4.0, and 5.0 separation lines are shown together in Figure 45 for comparison. In Figure 45 the cartesian coordinate system, (x, y), has been non-dimensionalized by the blunt fin leading edge diameter, D. The resulting scaled coordinates X/D and Y/D are used from this point on to present spatial results. Many other experiments have shown that the spatial scaling of the interaction is primarily dependent on D. The convention of using a lower case variable (x) for a dimensional coordinate and an uppercase ratio (X/D) for a non-dimensional, scaled coordinate will be adhered to for consistency.

The separation lines in Figure 45 show a clear Mach number dependency, with higher Mach numbers resulting in greater upstream and lateral extent. It is also possible that these differences are due in part, or totally, to differences in the incoming boundary layers. It should be noted that the locations of the Mach 2.0 and 3.0 separation lines correspond to similar measurements made by other investigators, at other Mach numbers, and with other diameter blunt fins. No

known previous investigations have shown a Mach number trend for the separation line location. The locations of the Mach 4.0 and 5.0 separation lines found in this investigation appear to deviate from previous findings. The following equation can be used to reconstruct the separation line trace.

$$\frac{-R_S(\omega)}{D} = \frac{A}{D} + \frac{B}{D}\omega^2 + \frac{C}{D}\omega^4 \qquad (4\text{-}12)$$

The scaled constants for the curve fit in Equation 4-12 are given in Table 5. Note that in Equation 4-12, the polar angle, ω, is defined in radians, not degrees.

4.3 STATIC PRESSURES

The wall static pressure distributions were measured beneath the shock wave/turbulent boundary layer interaction about the blunt fin. The static pressure measurements were taken in two basic forms. In the first set, detailed pressure measurements were made along the interaction centerline ahead of the blunt fin leading edge. In the second set, the entire wall static pressure field ahead of, and around, the leading edge of the blunt fin was measured with less spatial detail, but in greater spatial extent.

The static pressure measurements along the blunt fin centerline are shown in Figure 46 for Mach numbers 2.0, 3.0, 4.0, and 5.0. The pressure data is presented in normalized form, P/P_0, where P_0 is the static pressure of the incoming flow. The coordinate ahead of the blunt fin is scaled by the blunt fin

diameter, D, and the leading edge of the blunt fin corresponds to $X/D = -0.5$. As can be seen in Figure 46 the pressure distributions have the same characteristic shapes with differences primarily in pressure level as a function of Mach number.

Each of the pressure distributions, for all Mach numbers, is seen to rise above the incoming levels at values of X/D between -4.0 and -3.5. This pressure rise is caused by the separation shock wave ahead of the blunt fin, and this is generally the region in which the unsteady separation shock wave motion is observed. There is, however, a trend in the location of the initial pressure rise with Mach number. By careful examination of Figure 46 it can be seen that the initial pressure rise is further upstream with increasing Mach number. The Mach 2.0 data is an apparent exception. The Mach 2.0 initial pressure rise is first seen slightly ahead of the Mach 3.0 pressure rise.

Following the initial pressure rise, a region of relatively constant static pressure is observed between X/D values of -3.0 and -2.0. The relative levels of static pressure show a clear trend of higher pressures corresponding to higher Mach numbers. The local maximum normalized pressure levels of 1.7, 1.9, 2.5, and 2.9 are found for Mach numbers 2.0, 3.0, 4.0, and 5.0 at approximately the same X/D location of -2.2. This region in the pressure distribution, where separated flow is found ahead of the blunt fin, is typically referred to as a pressure plateau.

Following these plateau maxima, the pressure distributions fall to local minima between X/D locations of -1.5 and -1.0 for all Mach numbers. The

pressure levels in this region are relatively constant, and show only a modest Mach number dependence. The pressure levels in the local minima are nearly coincident for Mach 2.0 and 3.0 and again for Mach 4.0 and 5.0.

The pressure distributions along the interaction center line in Figure 46 rapidly rise to peaks just ahead of the blunt fin leading edge. The maximum pressure levels of the peaks are very dependent on Mach number, with the peak value increasing with increasing Mach number. The pressure levels of the peaks, however, are lower that the normal shock wave stagnation pressures by factors ranging from 1.4 at Mach 2.0 to 2.5 at Mach 5.0. Other investigators have concluded that the pressure peak just ahead of the root of the blunt fin is a result of flow reattachment.

The static pressure field beneath the shock wave/turbulent boundary layer was also measured over a wide extent about the blunt fin leading edge. The resulting data is presented in the form of contour plots of normalized pressure, P/P_0. Figures 47 through 50 show the static pressure field contour plots for Mach numbers 2.0, 3.0, 4.0, and 5.0 respectively. These figures show both pressure isobars and gray scale shading for the pressure levels measured about the blunt fin. An outline of the blunt fin is also included for reference. In each figure, the contour levels shown are the same, permitting direct comparison of the extent and pressure levels in the interaction over the Mach number range.

The maximum normalized pressure level shown in the contour plots is 3.0, which is significantly less than the peak pressure levels measured on the blunt fin

centerlines in Figure 46. As a result, the high pressure levels near the blunt fin leading edge are not resolved. However, this choice of limiting pressure level enhances resolution in the pressure plateau region ahead of the blunt fin where the unsteady shock wave and separated flow are located.

From Figures 47 through 50 the extent of the static pressure distribution about the blunt fin can be seen. Both the intensity (darkness of gray scale) and spatial extent of the interaction can be seen to increase with increasing Mach number. The intensity of the pressure plateau can be seen to wrap around the blunt fin to a greater extent as the Mach number increases from 2.0 to 5.0. Additionally, the initial pressure rise in the interaction is seen to occur farther upstream as the Mach number is increased. For a visualization aid, Figure 51 is included. In this figure the Mach 3.0 pressure field is shown as a mesh surface, with the vertical height proportional to the pressure level.

4.4 DYNAMIC PRESSURES

As previously mentioned an enormous amount of raw pressure signal data has been recorded in this investigation. The raw pressure data is nearly useless in attempting an interpretation of results. It has therefore been necessary to perform a series of data reduction analyses on the raw pressure signal data in order to make interpretation of the results tractable. The results of these data analyses are presented in three broad sections; statistics, box-car methods, and spectra. Each of these sections are detailed below.

When appropriate, results for all Mach numbers measured (2.0, 3.0, 4.0, and 5.0) are presented. There are instances, however, when the results of the analyses do not show any dependence on Mach number. When such instances arise, the Mach 3.0 data will be shown as a representative set of the general results observed for all Mach numbers. The Mach 3.0 data has been chosen simply for the fact that it comprises the most complete set of measured data. No other bias is implied.

Before discussing the specific results from the data reduction analyses, it is useful to indicate the dynamic pressure measurement locations which were used in the experiments. Figures 52 through 55 show the dynamic pressure transducer locations relative to both the blunt fin and the separation line determined from the surface flow visualization experiments for Mach 2.0, 3.0, 4.0, and 5.0 respectively. The dynamic pressure transducer locations were arranged in rows parallel to the incoming flow direction, on and offset from, the blunt fin centerline. The offset rows were positioned in Y/D increments of -1.

Figure 56 shows a new coordinate system which is useful in presenting results of the measurements in the shock wave/turbulent boundary layer interaction. In addition to the cartesian coordinates, (x,y), and the polar coordinates, (r,ω), the orthonormal coordinates, (l,λ), enables the comparison of measurements relative to the separation line S. The dimension l is a measure of the distance perpendicular to the separation line surface trace. The angle λ is a measure of the sweepback of the separation line at the origin of the l dimension.

The orthonormal coordinate system is related to the polar coordinate system by the following equation.

$$
\left.
\begin{aligned}
r\cos\omega - l\cos\lambda &= r_s(\omega)\cos\omega \\
r\sin\omega - l\sin\lambda &= r_s(\omega)\sin\omega
\end{aligned}
\right\}
\qquad (4\text{-}13)
$$

The function $r_s(\omega)$, the radial distance to the separation line S, has already been defined by Equation 4-12. Note that the sweepback angle, λ, is the angle of the tangent to the separation line, and λ can be determined by finite differences using the function $r_s(\omega)$. Applying Equation 4-13 to determine the orthonormal coordinates, (l,λ), requires solving a coupled set of nonlinear equations. A multi-variable Newton-Raphson iteration scheme was employed to solve Equation 4-13. Additionally, the relations defining the transformation between cartesian and polar coordinates are $x = r\cos\omega$ and $y = r\sin\omega$. Thus, with the use of the multi-variable Newton-Raphson solution technique for Equation 4-13, a mapping from cartesian coordinates, (x,y), to orthonormal coordinates, (l,λ), was developed.

In the presentation of results, rather than using the actual orthonormal dimension l, the scaled coordinate L/D is used. Negative values of L/D correspond to locations upstream of the separation line S, and positive values of L/D correspond to locations downstream from the separation line. In describing

the physical location of a measurement in the following presentation of results, three scaled coordinates, X/D, Y/D, and L/D, are variously used corresponding to the streamwise, cross-stream, and separation line normal coordinates respectively.

4.4.1 Statistics

The reductions of the dynamic pressure data into simple, time-independent statistical quantities are presented in this section. The interaction surface pressure distributions are described by mean pressures, standard deviations, skewness and kurtosis, and probability density functions of the measured dynamic pressure signals. For all results presented in these sections, the dynamic pressure signals were recorded at a sampling frequency of 200 kHz. The dynamic pressure transducer signals were low-pass filtered at 50 kHz.

4.4.1.1 Mean pressures

The mean pressure values of the dynamic pressure signals measured were calculated by Equation 3-1. The resulting mean pressure levels along the blunt fin centerline are shown in Figures 57 through 60 for Mach numbers 2.0, 3.0, 4.0, and 5.0 respectively. The mean pressures presented are normalized by the incoming static pressure, $\overline{P}/P_0$. Also shown in the figures as the solid line are the pressure distributions measured by the static pressure transducers. These static pressure distributions along the blunt fin centerline were previously presented in Figure 46. The mean pressures determined from the dynamic pressure signals

agree well with the static pressure distributions at Mach numbers 2.0 and 3.0.

The mean pressures determined from the dynamic pressure transducers show relative errors when compared with the static pressure measurements at Mach numbers 4.0 and 5.0. The nature of these relative errors is a result of zero-drift in the calibrations of the dynamic pressure transducers. The dynamic pressure transducers which were used in this investigation have an inherent zero-drift, which is particularly sensitive to temperature variations. This zero-drift is typically not a significant effect, unless the pressures being measured are very low. At the high Mach numbers (4.0 and 5.0) the static pressures are indeed low, and the zero-drift is seen in the mean pressure results. The calculations of the mean pressure are the only results in which the zero-drift is apparent. All other reduction analyses involve differences from the mean pressure and are not influenced by zero-drift effects. The measurement of small changes in pressure were unaffected by zero-drift since the calibration slopes did not change. Despite this shortcoming, the mean pressures measured by the dynamic pressure transducers are consistent with the static pressure measurements at both Mach 4.0 and 5.0.

The off-centerline mean pressures are shown in Figure 61 for Mach 3.0. The centerline results are shown as symbols corresponding to the transducer row at Y/D of 0, while the off-centerline measurements are shown as different sets of symbols corresponding to Y/D values of -1, -2, and -3. In Figure 61 each of the mean pressure measurements along streamwise, X/D, rows is shifted downstream

as the transducer rows are located at greater cross-stream, Y/D, locations. The pressure profiles appear to have the same characteristic distribution, with the downstream shift in X/D resulting from the sweeping back of the interaction region around the blunt fin.

In contrast to Figure 61, where the mean pressure data is plotted against the streamwise coordinate, X/D, Figures 62 through 65 show the mean pressures plotted against the separation line normal coordinate, L/D, for Mach numbers 2.0, 3.0, 4.0, and 5.0 respectively. In these figures the mean pressure data, both centerline and off-centerline, are seen to collapse to a representative distribution that is predominantly independent of cross-stream, Y/D, location. The results for the higher Mach numbers again show relative errors resulting from transducer calibration zero-shift. As a result of the collapse of data found in Figures 62 through 65 it can be concluded that the comparison of measurements located at various cross-stream positions should be done using the orthonormal coordinate L/D.

4.4.1.2 Standard deviations

The standard deviations of the pressure signals measured along the centerline ahead of the blunt fin at Mach 3.0 are shown in Figure 66 in the upper plot. Also shown in Figure 66 are the mean pressures along the blunt fin centerline, as well as the static pressure measurements (shown as the solid line), in the lower plot. In Figure 66 the standard deviations presented are normalized by

the incoming static pressure, σ_P / P_0. Also note that the scales used for the mean pressures and standard deviations are not the same. For reference, the location of the separation line trace S is shown in Figure 66 as the vertical line which crosses both plots.

In Figure 66 the standard deviation distribution is seen to rise from the incoming boundary layer level to an initial peak value just upstream of the separation line position. This initial rise in the standard deviation is seen to correspond with the initial rise in the mean pressure distribution. Following the initial peak, the standard deviation distribution falls to an intermediate level downstream of the separation line. This intermediate level in the standard deviation distribution corresponds to the position of the pressure plateau observed in the mean pressure distribution.

Proceeding downstream in Figure 66, the standard deviation distribution rises from the intermediate level to a second peak. This second peak in the standard deviation distribution is slightly greater than the initial peak. The second peak in the standard deviation distribution is seen to correspond to the decrease in the mean pressure distribution downstream of the pressure plateau region. The standard deviation distribution decreases once again to the intermediate level downstream of the second peak. This region of decreasing standard deviation, downstream from the second peak, corresponds to the beginning of the local minima region found in the mean pressure distribution at an X/D location of -1.5. This is also the approximate location at which the secondary coalescence line was

observed in the surface flow visualization experiments. Both the standard deviation and mean pressure distributions show rapid rises to the maximum levels just upstream of the blunt fin leading edge in Figure 66.

The standard deviation distributions, both on centerline and off-centerline, are shown in Figures 67 through 70 for Mach numbers 2.0, 3.0 4.0, and 5.0 respectively. In each of these figures, the data is seen to collapse when plotted as a function of the orthonormal coordinate, L/D. The maximum values of both the initial and second peaks in the standard deviation distributions are seen to decrease with increasing distance, Y/D, from the interaction centerline for all Mach numbers. The intermediate level between the peaks in the standard deviation distributions is also seen to decrease with increasing distance from the interaction centerline for all Mach numbers.

A comparison of the centerline standard deviation distributions for Mach numbers 2.0, 3.0, 4.0, and 5.0 is shown in Figure 71. For Mach numbers 3.0, 4.0, and 5.0 the initial peaks in the standard deviation distributions are all located at approximately L/D of 0, or equivalently, at the separation line S location. For these Mach numbers, the levels of the peaks are also nearly the same, with σ_P / P_0 approximately 0.25 for Mach 3.0, 4.0, and 5.0. The initial rises in the standard deviations for Mach numbers 3.0, 4.0, and 5.0 also appear to be coincident.

The centerline standard deviation distribution for Mach 2.0, however, does not follow the trends found for Mach numbers 3.0, 4.0, and 5.0 in Figure 71.

The initial peak in the standard deviation distribution occurs substantially forward of the separation line, at an L/D location of -0.8. Additionally, the maximum level of the initial peak in the Mach 2.0 standard deviation distribution is less than half the value found for Mach numbers 3.0, 4.0, and 5.0.

From the above observations, there is a clear distinction between Mach 2.0 and Mach numbers 3.0, 4.0, and 5.0 in the behavior of the unsteady shock wave/turbulent boundary layer interaction near the location of the separation line. This is the region where the unsteady separation shock wave motion is observed. Downstream of the separation line the second peaks in the standard deviation distributions appear to show consistent trends for all Mach numbers. The downstream location and level of the second peaks are seen to increase with increasing Mach number in Figure 71. The region downstream from the separation line does not show inconsistent behavior between Mach numbers, in contrast to the upstream region.

4.4.1.3 Skewness and kurtosis

While the standard deviation provides a measure of the magnitude of the pressure fluctuations measured about the mean pressure, the skewness indicates asymmetry in the pressure fluctuations about the mean pressure. The skewness of a pressure signal, α_p, is a non-dimensional coefficient. A pressure signal with symmetric pressure fluctuations about the mean pressure has a skewness of zero. Figure 72 shows the skewness distribution for Mach 3.0, both on centerline and

off-centerline. The incoming measurements show $\alpha_p = 0$, indicating that the pressure fluctuations are symmetric about the mean pressure. Between L/D of -1 and approximately 0, the measured pressure signals have large, positive skewness. This indicates that there is an asymmetry in the pressure fluctuations, which results from the motion of the separation shock wave super-imposing high pressure oscillations on the incoming boundary layer pressure fluctuations. This is the region where intermittent motion of the separation shock wave is observed. This region also corresponds to the initial rise in the standard deviation distribution, as seen in Figure 68.

Slightly negative skewness is seen in Figure 72 just upstream and downstream of the separation line location, at L/D of 0. This results from the separation shock wave motion also, but at these positions the separation shock wave pressure rise dominates the transducer signal for most of the time. Occasionally, the shock wave moves downstream of the transducer, and the lower pressure in the incoming boundary layer is measured. This region corresponds to the decrease from the initial peak in the standard deviation distribution observed in Figure 68. Downstream of the separation line the skewness distribution returns to zero, approximately between L/D of 0 and 1. This corresponds to the location of the intermediate level in the standard deviation distribution observed in Figure 68. At the most downstream end of the skewness distribution, there is a very slight positive skewness, which corresponds to the second peak in the standard deviation distribution. Figure 72 indicates that the pressure fluctuations are symmetrical in

the incoming boundary layer and downstream of the separation line, but are highly asymmetrical in the region of the separation shock wave motion.

The kurtosis provides a measure of the tendency of a fluctuating pressure signal to form a peaked or flat probability density function. The kurtosis of a pressure signal, β_p, is also a non-dimensional coefficient. A pressure signal with a random distribution of pressure fluctuations about the mean pressure will have $\beta_p = 3$. Figure 73 shows the kurtosis distribution, both on centerline and off-centerline, for Mach 3.0. Upstream of the separation line the kurtosis is observed to be very large, indicating very peaked probability density functions. Downstream of the separation line the kurtosis is approximately 3, indicating random pressure fluctuations about the mean pressure, or gaussian probability density functions.

4.4.1.4 Probability density functions

Instead of using the skewness and kurtosis coefficients to describe the behavior of the fluctuating pressure signal about the mean pressure, an alternative is to use probability density functions. Figure 74 shows a series of normalized probability density functions, $\varphi(\xi)\,\sigma_p$, along the interaction centerline, near the separation line trace, for Mach 3.0. The abscissa in Figure 74, $\xi = \dfrac{P - \overline{P}}{\sigma_p}$, is a normalization of the pressure variation in terms of standard deviations from the mean pressure. In Figure 74, 5 different probability density functions (PDF) are shown, corresponding to 5 different locations in the shock wave/turbulent

boundary layer interaction. For reference a small, inset plot in the upper right corner of Figure 74 shows the locations of the 5 PDF on the standard deviation distribution. For ease of comparison, the 5 PDF are plotted on the same axes in Figure 74, but following the first PDF, each of the subsequent 4 PDF are shifted upward 0.2 on the ordinate.

The first PDF, plotted as circle symbols, is located just upstream of the initial rise in the standard deviation distribution, where the standard deviation of the pressure signal is only slightly higher than the incoming boundary layer level. A gaussian PDF is also shown for comparison in Figure 74 plotted as a solid line without symbols. The first PDF is distorted from a gaussian distribution due to the occurrence, although very infrequent, of high pressure spikes in the pressure signal, which result from the separation shock wave moving up to, or ahead of, the pressure transducer.

The second PDF, plotted as square symbols, is located approximately half way up the initial peak in the standard deviation distribution. This PDF is very distorted from a gaussian distribution. The narrow peak in the PDF, although off of the limits of the plot, exceeds a value of 3. This portion of the PDF corresponds the pressure fluctuations measured in the incoming boundary layer and comprises most of the pressure signal. The second PDF shows a prominent tail running off to the right, indicating low probability, high pressure measurements, which again result from the passage of the separation shock wave over the transducer. This PDF has very large values of both skewness and

kurtosis.

The next PDF in Figure 74, plotted as diamond symbols, is positioned at the maximum point in the standard deviation distribution initial peak. This third PDF still shows a narrow, peaked probability corresponding to the measurement of the incoming boundary layer flow. The probability of measuring incoming boundary layer flow at this position is much smaller than the previous PDF. Most of the pressure signal measures the higher pressures behind the separation shock wave. This PDF shows the merging of two separate probability distribution functions, one narrow PDF corresponding to the lower pressure in the incoming boundary layer flow when the separation shock wave is downstream of the transducer, the other broader PDF corresponding to higher pressure in the separated flow when the separation shock wave is upstream of the transducer.

The fourth PDF, plotted as triangle symbols, is located downstream from the maximum of the initial peak in the standard deviation distribution. At this location, the PDF has regained gaussian characteristics, with only a small tail on the left side of the PDF. This is indicative of very small probabilities for measuring lower pressures in the incoming boundary layer flow when the separation shock wave is downstream of the transducer. At this position, almost all of the pressure signal measures separated flow, resulting from the separation shock wave remaining upstream of this pressure transducer location nearly all of the time.

The last PDF in Figure 74, plotted as inverted-triangle symbols, is located

at the intermediate level in the standard deviation distribution. This PDF is essentially gaussian at this position in the unsteady shock wave/turbulent shock wave interaction. The pressure transducer at this location measures only the higher pressures in the separated flow region downstream of the unsteady separation shock wave. All of the probability density functions downstream of this location were found to be gaussian, or very nearly gaussian.

4.4.2 Box-Car

The results of the box-car analyses are presented in this section. The box-car technique can only be applied in the region of shock wave motion. This region of shock wave motion is located upstream of the separation line trace. The fluctuating pressure signal, recorded in the region of shock wave motion, can be reduced to a bimodal time series indicating the position of the shock wave motion relative to a dynamic pressure transducer. From the analysis of the box-car signal, the intermittency and zero-crossing frequency can be determined. By analyzing a number of box-car signals, recorded simultaneously, from different dynamic pressure transducers, the intermittent region length and mean shock velocity can be determined.

4.4.2.1 Intermittency

The intermittency, Γ, is a measure of the fraction of time the separation shock wave is upstream of a particular position in the shock wave/turbulent

boundary layer interaction. Figure 75 shows the intermittency distribution along the blunt fin centerline for Mach 3.0. The symbols indicate the intermittency calculated from the dynamic pressure transducer signals. The solid line is an error function least-squares curve fit to the data. As can be seen from Figure 75, the data closely matches the error function curve fit. The error function can be related the integral of the normal probability density function. Since the intermittency data closely matches an error function, it can be directly deduced that the location of the separation shock wave must be described by a gaussian probability density function. Thus, Figure 75 indicates that the separation shock wave position is randomly distributed about a mean shock wave position. The intermittency data is plotted as a function of the orthonormal dimension, L/D, and the data also shows that the shock wave region of motion is localized upstream of the separation line ($L/D = 0$).

Figure 76 shows the intermittency distributions, both on centerline and off-centerline, for Mach 3.0. The error function curve fit for the centerline distribution is again shown for reference as the solid line. In Figure 76 there is a general trend of increasing upstream shift in the location of the intermittent region relative to the separation line trace ($L/D = 0$) with increasing cross-stream distance, Y/D, from the interaction centerline. Additionally, there is a trend of decrease in the intermittent region length with increasing cross-stream distance from the centerline. The intermittent region length, L_Γ, is conveniently defined as follows.

$$\frac{L_T}{D} = \frac{L}{D}\bigg|_{\Gamma=0.95} - \frac{L}{D}\bigg|_{\Gamma=0.05} \tag{4-14}$$

The intermittent region length, determined by Equation 4-14, is shown in Figure 77 for Mach 3.0 as a function of the separation line sweepback angle λ. The locations of the 5% and 95% intermittency points were determined from error function least-squares curve fits. The sweepback angles of 0, 14.5, 29.5, and 42 degrees correspond the cross-stream coordinates, Y/D, of 0, -1, -2, and -3 respectively. Figure 77 shows that the intermittent region length decreases with increasing cross-stream distance, or equivalently, increasing separation line sweepback.

Figure 78 shows, for Mach 3.0, that the intermittent regions at different cross-stream distances, are self-similar. The intermittency distributions are shifted so that the locations of 95% intermittency coincide. This shifted orthonormal coordinate is defined below.

$$\frac{L'}{D} = \frac{L}{D} - \frac{L}{D}\bigg|_{\Gamma=0.95} \tag{4-15}$$

In Figure 78 this shifted orthonormal coordinate is scaled by the intermittent region length, L_T, instead of the blunt fin diameter, D. All of the intermittency distributions are seen to collapse onto the error function curve fit shown in Figure

78, thus indicating that the intermittent regions are self-similar throughout the shock wave/turbulent boundary layer interaction region measured.

Figure 79 shows the intermittency distributions along the interaction centerline for Mach numbers 2.0, 3.0, 4.0, and 5.0. Also shown in the figure are the error function least-squares curve fits for each Mach number data as the solid lines. In Figure 79 the intermittent region is shifted further downstream, relative to the separation line trace, with increasing Mach number. The Mach 3.0, 4.0, and 5.0 intermittency distributions are all located with the maximum intermittency corresponding closely with the separation line location ($L/D = 0$). Only a slight downstream shift in position with Mach number is seen for the Mach 3.0, 4.0, and 5.0 distributions. The Mach 2.0 intermittency distribution is observed to be located significantly upstream of the separation line trace position. For the Mach 2.0 distribution, the maximum intermittency does not correspond with the separation line location. This behavior was already observed in the standard deviation distributions. The reader is referred to Figure 71 for comparison.

The centerline intermittent region length as a function of Mach number is shown in Figure 80. The intermittent region length is seen to increase with increasing Mach number. These intermittent region lengths are also based on 5% to 95% intermittency locations, using the error function least-squares curve fits for numerical values. By shifting the intermittency distributions, and normalizing by the intermittent region length, the centerline intermittency distributions are also seen to be self-similar. Figure 81 shows the collapse of the measured

intermittency distributions, for all Mach numbers, on the interaction centerline. The error function least-squares curve fit is shown again for comparison.

The collapse of the data for varying incoming Mach number is comparable to collapse of the data for varying cross-stream location, shown in Figure 78. The intermittency distributions are observed to be self-similar along the variable sweepback of the interaction as well as self-similar over variations in incoming Mach number. The spatial locations of the intermittent region, relative to the separation line trace, and the intermittent region length scales, are seen to show dependencies with interaction sweepback and incoming Mach number.

4.4.2.2 Zero-crossing frequency

The zero-crossing frequency, f_c, is the inverse of the average time period between measured separation shock wave crossings over a dynamic pressure transducer. The zero-crossing frequency can be computed for shock wave crossings in the upstream and downstream directions. The zero-crossing frequency as a function of intermittency is shown in Figure 82 for the Mach 3.0 measurements along the interaction centerline. The data in the figure is plotted as triangle symbols for the upstream shock motions, and as inverted-triangles for the downstream shock motions. Figure 82 shows no bias in zero-crossing frequency for upstream or downstream shock motions.

The zero-crossing frequency is observed to be a symmetric function of intermittency, with the maximum zero-crossing frequency occurring at the 50%

intermittency point. Although Figure 82 shows relatively few data points on which to base this observation, numerous calculations of the zero-crossing frequency for various measurements have shown this symmetry. To aid the reader in visualizing the zero-crossing frequency with sparse data, the following functional relation is used.

$$f_c = a\left[\Gamma(1 - \Gamma) - \Gamma^2(1 - \Gamma)^2\right] \tag{4-16}$$

Equation 4-16 is shown in Figure 82 as the solid line. The single parameter a in Equation 4-16 was determined by a least-squares curve fit to the data. The particular fourth-order polynomial form of Equation 4-16 was chosen as the simplest single parameter relation in Γ which adequately describes the observed data. There is no theoretical basis for this choice for the functional dependence of intermittency on zero-crossing frequency.

Figure 83 shows the zero-crossing frequencies, both on centerline and off-centerline, for Mach 3.0. Least-squares curve fits using Equation 4-16 are also shown as solid lines in the figure for reference. There is a clear trend of increasing zero-crossing frequency with increasing interaction sweepback in Figure 83. The centerline maximum zero-crossing frequency is interpolated to be 0.6 kHz, while for the largest cross-stream measurements (greatest sweepback), the maximum zero-crossing frequency is interpolated to be nearly 0.9 kHz.

Figure 84 shows the zero-crossing frequencies measured along the interaction centerline for Mach numbers 2.0, 3.0, 4.0, and 5.0. The zero-crossing frequencies of Mach 3.0 and 4.0 are identical, while those for Mach 5.0 and 2.0 are found to be lower. Figure 85 shows the maximum zero-crossing frequency along the interaction centerline. There is no consistent trend in the maximum zero-crossing frequency with Mach number. For the Mach number range of 2.0 to 5.0, the maximum zero-crossing frequencies are found to be between 0.45 and 0.6 kHz, with the highest maximum zero-crossing frequencies at Mach numbers 3.0 and 4.0.

4.4.2.3 Mean shock velocity

The analysis of the box-car signals calculated from simultaneously measured dynamic pressure transducers permits the computation of the separation shock wave position and velocity histories. Four adjacent dynamic pressure transducers were simultaneously recorded in this investigation. The resulting computations of the separation shock wave velocity behavior are presented in this section. The separation shock wave velocity is described by the mean shock velocity, $\overline{V}$, measured along the orthonormal coordinate L/D. The mean shock velocity is the average of the calculated velocity history over the entire measured range of motion. The separation shock wave motion has been shown to be confined to the intermittent region in the interaction. The mean shock velocity is therefore associated with the entire intermittent region, not just a single location in

the interaction.

Figure 86 shows the normalized probability density function for the shock velocity calculated along the interaction centerline at Mach 3.0. Two PDF are shown in the figure, one for upstream shock motions, and one for downstream shock motions. A gaussian PDF is also shown as the solid line for reference. The upstream and downstream shock velocity PDF shown in Figure 86 are approximately the same. The shock velocity PDF are highly skewed, with high probabilities of low shock velocities, and low probabilities of high shock velocities. From Figure 86 is can be seen that the mean shock velocity, for either upstream or downstream motion, is significantly lower than the highest calculated velocities. Also note that the standard deviation of the shock velocity distribution about the mean shock velocity is approximately the same as the mean shock velocity. A shock velocity of zero has a probability of occurrence of zero. Shock velocities in excess of four times the mean shock velocity, although infrequent, are possible.

Figure 87 shows the mean shock velocity for the Mach 3.0 interaction. The upstream motion mean shock velocity is seen to be greater than the downstream motion mean shock velocity. The mean shock velocity is observed to be greater off-centerline of the interaction, with a nearly constant value of approximately 2% of the incoming freestream velocity U.

Figure 88 shows the mean shock velocity calculated on the interaction centerline over the Mach number range 2.0 to 5.0. A clear trend is observed for

Mach numbers 3.0, 4.0, and 5.0. The mean shock velocity decreases linearly as the Mach number decreases. At Mach 2.0, however, the mean shock velocity increases rather than continuing to decrease. The upstream motion mean shock velocity slightly exceeds the downstream mean shock velocity for Mach number 3.0, 4.0, and 5.0. The upstream and downstream motion mean shock velocities are the same for Mach 2.0.

4.4.3 Spectra

The spectral analysis of a dynamic pressure signal reveals the temporal characteristics of the pressure fluctuations by a representation of the frequency content of the signal. The normalized power spectral density function, $G(f)f/\sigma_P{}^2$, is a convenient comparative representation of the relative frequency content in a pressure signal. Also referred to as a power spectrum, $G(f)f/\sigma_P{}^2$, will be used to quantify the temporal characteristics of the dynamic pressure measurements throughout the unsteady shock wave/turbulent boundary layer interaction.

Figures 89 through 93 present a series of power spectra measured along the interaction centerline at Mach 3.0. Each figure in the series corresponds to a particular location in the shock wave/turbulent boundary layer interaction spanning the intermittent region. A small inset plot in the upper right corner of each figure shows the location of the power spectrum measurement as the circle symbol on the standard deviation distribution. Note for comparison that the locations of the

power spectra measurements in Figures 89 through 93 correspond to the same locations used in the description of the probability density functions shown in Figure 74.

Figure 89 shows the power spectrum measured upstream of the intermittent region at an L/D location of -0.76. The calculated intermittency for this location is effectively 0.0, however, a few infrequent shock wave crossings were recorded. The power spectrum shows a broad band frequency content with the maximum frequency contributions located at approximately 1 kHz. The power spectrum in Figure 89 should be compared to the power spectrum measured for the incoming boundary layer, shown in Figure 25. The two power spectra show very similar characteristics, with the incoming boundary layer power spectrum showing a peak frequency content at approximately 3 kHz. The power spectrum measured upstream of the intermittent region shows reduced high frequency and increased low frequency contributions compared to the power spectrum measured for the incoming boundary layer. The very infrequent passage of the separation shock wave over the dynamic pressure transducer upstream of the intermittent region, therefore, can still have significant effects in the resulting power spectrum measured.

Figure 90 shows the power spectrum measured within the intermittent region. The intermittency at this position was calculated to be 0.3. The power spectrum within the intermittent region shows considerable change from the power spectrum measured upstream of the intermittent region. In Figure 90 the power

spectrum still shows broad band frequency distribution, but the maximum

frequency content is at approximately 0.5 kHz. There is no significant frequency

contribution found above 3 kHz. Additionally, the peak region in the frequency

contribution corresponds closely to the maximum zero-crossing frequency

measured in the intermittent region.

Figure 91 shows the power spectrum measured at the maximum standard

deviation location in the intermittent region. This location also corresponds

closely to the location of the separation line trace. The intermittency calculated

for this position was 0.9. The power spectrum shown in Figure 91 is nearly

identical to the previous power spectrum shown. The power spectrum for any

location measured within the intermittent region, intermittencies between 0.05 and

0.95, showed effectively identical frequency distributions. Within the intermittent

region the power spectrum frequency content is dominated by the unsteady

separation shock wave motion.

Figure 92 shows the power spectrum measured just downstream of the

intermittent region. The peak frequency range has shifted to approximately 1 kHz

at this location. This power spectrum shows slightly higher high-end frequency

contributions in comparison to the power spectrum measured within the

intermittent region.

Figure 93 shows the last power spectrum measured downstream of the

intermittent region, at the location of the intermediate level in the standard

deviation distribution. It is interesting to note the similarity between this power

spectrum and the first one shown in Figure 89. Both power spectra show the same peak frequencies, and the only apparent distinction is that the power spectrum upstream of the intermittent region has slightly greater high-end frequency content than the downstream power spectrum.

For the purpose of direct comparison, Figure 94 shows all 5 power spectra in the same plot. Although somewhat difficult to distinguish individual spectrum, two distinct characteristic power spectra are seen. The two power spectra in the intermittent region, at L/D of -0.38 and -0.13, are essentially indistinguishable. The power spectra upstream, L/D of -0.76, and downstream, L/D of 0.37, of the intermittent region have nearly identical frequency distributions, with only a slight reduction seen in the high-end frequency content for the downstream spectrum compared to the upstream spectrum.

The power spectrum just downstream of the intermittent region, at L/D of 0.12, shows an enhanced high-end frequency contribution greater than that found in the intermittent region power spectrum, but less than the downstream spectrum. The low-end frequency contribution is seen to be identical to the intermittent region power spectrum.

Given the similar characteristics of the power spectra measured within the intermittent region, it is anticipated that self-similar power spectra would be found in the intermittent region located off-centerline also. Figure 95 shows power spectra measured within the intermittent region off-centerline in the Mach 3.0 interaction. After the centerline spectrum, at λ of 0.0 degrees, each subsequent

power spectrum shown in the figure are shifted upward 0.1 units on the ordinate. There is an observed similarity in the power spectra shown in Figure 95, however, a slight shift in the peak frequency range to higher frequencies with increasing sweepback angle is also apparent. This behavior corresponds to the observed increase in maximum zero-crossing frequency with increasing interaction sweepback angle seen in Figure 83. Figure 77 also showed the trend of decreasing intermittent region length with increasing sweepback. These observations, taken together, suggest that the power spectra measured in the intermittent region may be self-similar when represented as a function of a variable comprised of the product of frequency and a length scale. A Strouhal number is the appropriate non-dimensional group to use.

A Strouhal number for the power spectra in the intermittent region can be formed as $L_{\Gamma} f / U$. Figure 96 shows the power spectra in Figure 95 plotted as a function of the Strouhal number, $L_{\Gamma} f / U$, instead of the frequency. As can be seen in Figure 96 the power spectra measured within the interaction region, both on centerline and off-centerline, collapse to a self-similar frequency distribution as a function of the Strouhal number.

Given the success of using the Strouhal number, $L_{\Gamma} f / U$, in comparing power spectra measured at different cross-stream positions within the intermittent region at Mach 3.0, it is expected that power spectra measured within the intermittent region at different Mach numbers may also show self-similarity as a function of the Strouhal number. Figure 97 shows the power spectra measured

along the interaction centerline within the intermittent region at Mach numbers 2.0, 3.0, 4.0, and 5.0 plotted as a function of the Strouhal number. Again, the power spectra within the intermittent region are seen to be self-similar in frequency distribution as a function of $L_T f/U$. It is therefore concluded that any power spectra measured at any location within the intermittent region, at any Mach number, will exhibit the same self-similar frequency distribution as a function of Strouhal number.

4.4.4 Comparisons with other experiments

In order to establish that the results determined in this investigation are not in some way influenced by anomalies particular to the experimental facility used, it is necessary to make direct comparisons with similar measurements made in other wind tunnels. Unfortunately, there are relatively few experimental results available for direct comparison with the dynamic pressure measurements performed in this investigation of the blunt fin induced unsteady shock wave/turbulent boundary layer interaction. Only two other experimental investigations exist in which comparable dynamic pressure measurements were made. In the first, reference 12, dynamic pressure measurements were made at Mach 5.0 at the University of Texas at Austin. In the second, reference 13, dynamic pressure measurements were made at Mach 3.0 at Princeton University. In this section, data from both of these other experiments will be compared to the results found in this investigation.

The experiments conducted at the University of Texas at Austin (UTA) were performed in a blow down wind tunnel at an incoming Mach number of 5.0. The wind tunnel test section measured 15.2 cm by 17.8 cm. The tunnel sidewall boundary layer was used in the blunt fin induced shock wave/turbulent boundary layer interaction. The incoming boundary layer thickness was reported to be 1.50 cm. Figure 98 shows the power spectrum measured in the incoming boundary layer in the UTA experiments. Also shown for comparison in Figure 98 is the incoming boundary layer power spectrum measured in this investigation at Mach 5.0. The two power spectra are significantly different. The power spectrum for the UTA experiments shows a peak frequency range at approximately 30 kHz, compared to 3 kHz measured in this investigation. The rapid decrease in the UTA power spectrum at 50 kHz is a result of analog low-pass filtering of the dynamic pressure transducer signal.

The experiments conducted at Princeton University were performed in a blow down wind tunnel at Mach 3.0. The wind tunnel test section measured 20.3 cm by 20.3 cm, and the test section sidewall boundary layer was also used for the shock wave/turbulent boundary layer interaction. The incoming boundary layer thickness was reported to be 2.79 cm. Figure 99 shows the incoming boundary layer power spectrum measured in the Princeton experiments. The Mach 3.0 incoming boundary layer power spectrum measured in this investigation is also shown in Figure 99 for comparison. Again, there is significant difference between the two incoming boundary layer power spectra. The two spectra do

show comparable low-end frequency content, however, the Princeton power spectrum shows significantly greater high-end frequency content. The Princeton power spectrum does not show a clear peak frequency content range. The rapid decrease in the Princeton power spectra at 50 kHz is also due to analog low-pass filtering of the dynamic pressure transducer signal.

Despite the differences in the incoming boundary layer power spectra, the spectra measured within the intermittent region, along the centerline of the shock wave/turbulent boundary layer interaction, are found to be very similar. Figure 100 shows the intermittent region power spectrum measured in the Princeton experiments compared to the power spectrum measured in this investigation at Mach 3.0. The two power spectra are almost identical, differing only by a shift of the spectrum to higher frequencies for the Princeton data. The Princeton experiments used a 1.90 cm blunt fin, in contrast to the 2.54 cm blunt fin used in this investigation. As will be shown in subsequent paragraphs, the size of the blunt fin hemi-cylindrical leading edge diameter determines the maximum zero-crossing frequency measured in the intermittent region. The maximum zero-crossing frequency, in turn, corresponds to the peak frequency range in the power spectra measured in the intermittent region. The differences in the sizes of the blunt fins used between this investigation and the Princeton experiments accounts for the frequency shift observed between the two spectra of Figure 100.

A comparison of the power spectra measured in the intermittent region, along the interaction centerline, in this investigation at Mach 5.0 with data from

the University of Texas at Austin is provided in Figure 101. The power spectra

are shown as functions of the Strouhal number, $L_\Gamma f / U$. The experiments at

UTA used a range of blunt fin leading edge hemi-cylindrical diameters; 0.635 cm,

0.953 cm, 1.27 cm, and 1.90 cm. The UTA power spectrum shown in Figure

101 was measured using the 0.635 cm blunt fin. The power spectra, plotted as a

function of $L_\Gamma f / U$, were indistinguishable for the entire range of blunt fin sizes

used in the UTA experiments. The power spectra measured at UTA and in this

investigation at Mach 5.0 show similar frequency distributions. There is an

observed shift of the power spectrum to higher frequencies for the UTA data in

comparison to the measured spectra in this investigation. Also, the UTA data has

slightly greater high-end frequency content, which may be a result of the higher

frequency content measured in the incoming boundary layer power spectrum for

the UTA experiments.

In addition to the measured power spectra, the University of Texas at

Austin experimental results permit direct comparisons with other data. Figure 102

shows the maximum zero-crossing frequency, along the interaction centerline,

determined from the UTA experiments, compared with the results from this

investigation at Mach 5.0. The maximum zero-crossing frequency is plotted as a

function of the blunt fin leading edge hemi-cylindrical diameter, D. Data from

the UTA experiments is shown in Figure 102 as the circle symbols for the four

different size blunt fins tested. The maximum zero-crossing frequency measured

in this investigation is shown as the square symbol. Comparing the data from

both facilities shows a consistent trend of decreasing maximum zero-crossing

frequency with increasing blunt fin size. Additionally, the factor of 2 difference

in maximum zero-crossing frequencies between a 2.54 cm and a 1.90 cm blunt fin

corresponds to the frequency shift seen between the power spectra in Figure 100.

Figure 103 shows a comparison of the intermittent region lengths

determined in the UTA experiments with those determined in this investigation

along the interaction centerline. The data from the University of Texas at Austin

experiments at Mach 5.0 do not show a consistent trend in intermittent region

length with blunt fin size. All of the data from UTA show larger intermittent

region lengths than those determined in this investigation. The differences in the

determination of the intermittent region lengths between the two experiments can

account for the frequency shift observed between the two power spectra in Figure

101. It should be noted that the determination of the intermittent region length

from an error function curve fit to sparse experimental data is a possible source of

significant differences in the results between experiments and facilities.

Differences in intermittent region lengths can also be a result of differences in the

incoming boundary layer thicknesses between experimental facilities.

Figure 104 shows a comparison of the maximum standard deviation of the

pressure signal measured in the intermittent region, along the interaction

centerline, between the experiments in this investigation and the data from the

University of Texas at Austin. These maximum standard deviation measurements

correspond to the initial peaks in the standard deviation distributions previously

shown in Figure 71. The data from UTA at Mach 5.0 shows a strong trend of increasing maximum standard deviation with increasing blunt fin leading edge hemi-cylindrical diameter. The maximum standard deviation for the UTA data using a 0.635 cm blunt fin shows the closest agreement with the maximum standard deviation measured in this investigation at Mach 5.0.

The maximum standard deviation measurements found in this investigation are shown in Figure 104 as the circle symbols. The maximum standard deviation is observed to be nearly constant for Mach numbers 3.0, 4.0, and 5.0. The maximum standard deviation at Mach 2.0 is significantly lower than the corresponding measurements made at the higher Mach numbers. The reasons for this observed behavior in the maximum standard deviation of the pressure signal, measured in the intermittent region, as a function of Mach number are examined in the next section.

Figure 105 shows a comparison of the mean shock velocities determined in this investigation with those found in the UTA experiments. The data from UTA is shown as a range of mean shock velocity in Figure 105. The format of the data presentation from the UTA experiments did not permit identifying the particular blunt fin size used for a mean shock velocity data point. The range of mean shock velocities from the UTA experiments spans the mean shock velocities determined in this investigation at Mach 5.0. Although the upper limit of the UTA mean shock velocities is significantly higher (for some blunt fin diameters) than the mean shock velocities found in this investigation, the correspondence

between the two experimental facilities is consistent.

4.5 INTERMITTENCY VARIANCE THEORY

The distribution of the standard deviation of the measured pressure signal across the intermittent region can be described by a theory developed by Debieve and LaCharme[24]. The behavior of the pressure signal within the intermittent region can be modeled as the combination of two distinct flowfields, one consisting of the incoming boundary layer flow when the separation shock wave is downstream of the dynamic pressure transducer, and the second consisting of the separated flow when the shock wave is located upstream of the transducer. If the transition between these two flow regimes is assumed to be instantaneous and complete, then the variance of the pressure signal, the square of the standard deviation, can be determined from the following equation.

$$\left(\frac{\sigma_P}{P_0}\right)^2 = (1-\Gamma)\left(\frac{\sigma_P^-}{P_0}\right)^2 + \Gamma\left(\frac{\sigma_P^+}{P_0}\right)^2 + \Gamma(1-\Gamma)\left(\frac{\Delta P_\Gamma}{P_0}\right)^2 \qquad (4\text{-}17)$$

In Equation 4-17, σ_P^- and σ_P^+ are the standard deviations in the flow regimes upstream and downstream of the separation shock wave, respectively. The pressure rise across the intermittent region, ΔP_Γ, is defined by the following relation.

$$\frac{\Delta P_\Gamma}{P_0} = \left.\frac{\overline{P}}{P_0}\right|_{\Gamma=0.95} - 1 \qquad (4\text{-}18)$$

With the use of Equation 4-18, all of the variables in Equation 4-17 are known from experiment and analysis of the dynamic pressure data. It is therefore possible to compare the theoretical standard deviation distribution of Equation 4-17 with measurements made in this investigation.

Figures 106 through 109 show a comparison of the standard deviation distributions measured across the intermittent region, along the interaction centerline, to the theory of Equation 4-17 at Mach numbers of 2.0, 3.0, 4.0, and 5.0. In Figures 106 through 109 the standard deviation is plotted against the calculated intermittency. The experimental data is shown as circle symbols, and the theory of Equation 4-17 is shown as the solid line.

For each Mach number, the theory provides an approximation to the level of the experimental maximum standard deviation, however, the location of the maxima do not coincide. The experimental data show a linear increase in standard deviation from low values of intermittency to intermittencies close to one. The experimental maximum standard deviations are found to occur at intermittencies of nearly one. The theory of Equation 4-17 shows the maximum point to be at intermittencies of approximately 0.5, with the standard deviation distribution varying parabolically, not linearly.

For Mach numbers 3.0, 4.0, and 5.0, the experiment and theory both show

a maximum σ_P/P_0 of approximately 0.25 over the Mach number range. There

is an observed slight over-prediction of the maximum by the theory, which

increases with increasing Mach number. It should be noted that the value of the

maximum σ_P/P_0 is dominated by the last term in Equation 4-17, and is

determined by the mean pressure rise across the intermittent region. For Mach

numbers 3.0, 4.0, and 5.0 this pressure rise across the unsteady separation shock

wave is approximately one-half the incoming boundary layer pressure. This is

also typically the pressure rise across a shock wave required to separate a

turbulent supersonic boundary layer. This accounts for the experimentally

observed constant maximum standard deviation levels over the Mach number

range from 3.0 to 5.0.

The theory of Equation 4-17 is also useful in interpreting the experimental

observation that the maximum σ_P/P_0 for the Mach 2.0 interaction is less than

half that found for the higher Mach number experiments. As was previously

presented in Figure 79, the intermittent region for the Mach 2.0 measurements

was found to be located substantially farther upstream in comparison to the Mach

3.0 to 5.0 experiments. The static pressure distributions also showed lower mean

pressure distributions ahead of the blunt fin for the Mach 2.0 experiments

compared to those for Mach numbers 3.0 to 5.0 (see Figure 46). These two

effects result in a substantially lower mean pressure rise across the intermittent

region for the Mach 2.0 experiments, and the last term in Equation 4-17 predicts a

correspondingly lower maximum σ_P / P_0.

In an effort to assess the applicability of Equation 4-17 for modeling the standard deviation distribution in the intermittent region generated by the unsteady shock wave/turbulent boundary layer interaction ahead of a blunt fin, it is useful to compare the theory to experimental data in a slightly different format. Figure 110 shows the centerline standard deviation distribution, along the interaction centerline, as a function of the physical dimension X/D for the Mach 3.0 measurements. Also shown in the figure is the theoretical distribution predicted by Equation 4-17, transformed from a function of Γ to a function of X/D by using the least-squares error function curve fit to the intermittency calculations previously shown in Figure 79. When the results of the theory and experiment are compared in this form, the agreement is quite good. The theory predicts the relative levels and characteristic shape of the measured standard deviation distribution. The results of the theory do, however, show a significant upstream displacement relative to the experimental data.

4.6 LATERAL CORRELATIONS

A final series of measurements were conducted in an effort to determine the centerline symmetry of the separation shock wave motion. Wether the separation shock wave is characterized by an essentially random rippling motion around the blunt fin, or expands and contracts symmetrically, is the question of interest for this final section of the experimental program. To provide

measurements of the shock wave motion which would answer this question, a series of dynamic pressure transducers were arranged in a pair of lateral rows, equally spaced on either side on the interaction centerline. Figure 111 shows the location of the transducers, separation line trace, and blunt fin for the Mach 3.0 tests. The transducers were positioned in two groups of three adjacent locations along the X/D rows, each pair of groups at the same X/D positions, but at Y/D locations of either +1 or -1. For identification of the particular lateral measurement location, transducers located along the row at Y/D of -1 are identified as "port" (subscript P), while those locations at Y/D of +1 are identified as "starboard" (subscript S). By examining the lateral cross-correlation and coherence functions, the nature of the shock wave motion simultaneously measured port to starboard can be determined.

Before examining the lateral correlations of the pressure measurements, the longitudinal correlations should be determined. Figure 112 shows the longitudinal cross-correlation, $\rho_{UD}(\tau)$, measured in the Mach 3.0 incoming boundary layer. The two dynamic pressure transducers were positioned at adjacent locations 0.318 cm apart, and are designated by subscripts U and D for the upstream and downstream positions, respectively. The cross-correlation is approximately 0.8 for a zero time delay, and rapidly falls to essentially zero for positive and negative time delays. This cross-correlation indicates that the pressure fluctuations in the incoming boundary layer are essentially random. The longitudinal coherence function, $\gamma_{UD}^2(f)$, is shown in Figure 113. The coherence function shows that the

pressure signals measured simultaneously upstream and downstream posses a common dominant frequency range at approximately 10 kHz. The high-end frequency fluctuations in the pressure signals are essentially random in nature between the two transducers. The same is true of the low-end frequency content for the pressure signals.

The lateral cross-correlation, $\rho_{PS}(\tau)$, measured in the Mach 3.0 incoming boundary layer is shown in Figure 114. The lateral separation distance is 5.08 cm, which is much greater than the longitudinal cross-correlation transducer separation shown previously in Figure 52. The peak cross-correlation is approximately 0.1 at a time delay of zero, and essentially zero for all other times. Figure 114 indicates that there is no correlation of the pressure signals between the port and starboard transducers. Figure 115 shows the lateral coherence function, $\gamma_{PS}^{2}(f)$, for the Mach 3.0 incoming boundary layer. There are no dominant frequencies found in common between the port and starboard transducers. The pressure fluctuations measured by these laterally located pressure transducers are essentially independent of each other.

To determine if there are any common lateral pressure fluctuations measured as a result of the separation shock wave motion, the port and starboard transducers were located within the intermittent region. Figure 116 shows the resulting cross-correlation. There is a small peak in the cross-correlation at a time delay of zero. This peak is less than 0.2 and indicates a weak correlation between the pressure signals resulting from shock wave crossings over the pressure

transducers. This result suggests that the shock wave motion is predominantly random between the port and starboard transducers. If the separation shock wave expanded and collapsed symmetrically about the blunt fin, then a much higher cross-correlation would have been measured. Therefore, it is concluded that the separation shock wave motion is characterized by a rippling motion around the blunt fin. The coherence function shown in Figure 117 does not show any dominant frequency range in common between the port and starboard transducers. The frequency of the rippling shock wave motion is random, also showing no strong port to starboard correlation.

A final set of measurements were made in the separated flow, downstream of the intermittent region. The lateral cross-correlation and coherence functions are shown in Figures 118 and 119, respectively. From these measurements it is also concluded that the flow in the separated region about the blunt fin shows no lateral correlation, and is essentially random.

CHAPTER V

SUMMARY AND CONCLUSIONS

A series of experiments, covering the Mach number range from 2.0 to 5.0, were performed in an effort to determine the effects of Mach number variation on the characteristics of the unsteady shock wave/turbulent boundary layer interaction generated by a blunt fin. A single blunt fin hemi-cylindrical leading edge size was used in all of the experiments. The experiments included surface flow visualization, static pressure measurements, and dynamic pressure measurements.

Surface flow visualization techniques are successful in resolving the primary separation line. The location of the separation line is found to vary with Mach number. As the Mach number increases, the separation line is located farther upstream of the blunt fin. As the Mach number increases, the lateral extent of the separated region is also seen to increase. The separation line is found to form an arced trace, sweeping back around the blunt fin leading edge. The sweepback angle of the separation line is found to increase with increasing cross-stream distance from the blunt fin (and interaction) centerline.

Static pressure measurements confirm the observations on the extent of the interaction found from the surface flow visualization experiments. The initial increase in the static pressure is seen to occur farther upstream, and at larger

lateral (cross-stream) distances, as the Mach number increases from 3.0 to 5.0. The Mach 2.0 tests, however, deviate from this trend, and the initial pressure increase is seen to occur upstream of the location found in the Mach 3.0 tests. The static pressure distributions behind the separation line reach an initial peak approximately 2 diameters upstream of the blunt fin leading edge, along the centerline of the fin. The maximum pressure, normalized by the incoming static pressure, measured at the peak location is found to increase with increasing Mach number. Off-centerline, the peak pressure ratio is found to decrease with increasing cross-stream distance, or equivalently, increasing separation line sweepback angle. The locus of the peak pressures is also found to sweep backward about the blunt fin leading edge, approximately paralleling the separation line sweepback.

Extensive dynamic pressure data was recorded in this investigation. Since the pressure signal, in raw form, is of limited use, a series of analyses were applied to render useful information. These analyses fall into three main categories; statistical analysis, box-car analysis, and spectral analysis.

The results of the statistical analyses show that the mean and standard deviation of the pressure signals collapsed to self-similar distributions as a function of the distance perpendicular to the separation line, for measurements made both on the interaction centerline and off-centerline. The mean pressure increase at the location of the separation line is found to be approximately 1.5 times the incoming freestream static pressure. The standard deviation of the pressure signals show

initial peaked distributions, with the maximum standard deviation point corresponding closely to the location of the separation line at Mach numbers of 3.0, 4.0, and 5.0. The Mach 2.0 tests show that the maximum standard deviation point does not correspond to the separation line but occurs farther upstream. Additionally, the maximum standard deviation is found to be approximately 0.25 times the freestream static pressure for Mach numbers 3.0, 4.0, and 5.0. For the Mach 2.0 test the maximum standard deviation is found to be more than a factor of 2 lower.

An examination of the probability density functions sampled at locations spanning the initial standard deviation distribution peak show evidence of the unsteady separation shock wave motion. The farthest upstream measurements show gaussian PDF. As the locations progressed downstream toward the separation line, highly skewed PDF are observed. These skewed PDF indicated the occurrence of infrequent, high pressure increases measured as a result of the separation shock wave passing upstream of the transducer. At the maximum standard deviation point, approximately coincident with the separation line, the PDF are observed to show bimodal characteristics, resulting from the transducer measuring flowfields from both upstream and downstream of the separation shock wave for significant fractions of the total sampling time. Farther downstream from the initial standard deviation peak, where the standard deviation reach an intermediate level, the PDF are observed to return to gaussian distributions. These locations corresponded to positions in the separated flowfield, downstream

of the unsteady shock wave motion region.

The results of the box-car analyses show that the intermittency distributions, both on centerline and off-centerline, for all Mach numbers measured, were self-similar profiles. The intermittency distributions are well represented by error function curve fits, indicating that the unsteady separation shock wave position is randomly distributed over the intermittent region. For a given Mach number the intermittent region length is found to decrease with increasing interaction sweepback angle, or equivalently, increasing cross-stream distance. The intermittent region length, along the interaction centerline, is found to increase with increasing Mach number.

The location of the intermittent region relative to the separation line is found to shift progressively farther upstream with increasing interaction sweepback angle. For Mach numbers 3.0, 4.0, and 5.0 the intermittent region location, along the interaction centerline, is found to correspond closely with the separation line location, with a slight downstream shift in position observed with increasing Mach number. For these Mach numbers, the separation line corresponds to high intermittencies, or equivalently, to the downstream locus of the unsteady shock wave motion. For the Mach 2.0 tests, the location of the intermittent region is not found to correspond to the separation line position. Instead, for Mach 2.0, the downstream locus of the unsteady separation shock wave motion is found to occur approximately 0.8 blunt fin diameters upstream of the separation line position.

The box-car analyses also determined the zero-crossing frequency and

mean shock velocity of the unsteady separation shock wave motion. The maximum zero-crossing frequencies are found to occur at intermittencies of 0.5. The maximum zero-crossing frequency is found to increase with increasing interaction sweepback angle. The interaction centerline zero-crossing frequency does not show a consistent trend over the Mach number range, but rather is bounded between 0.45 kHz at Mach 2.0 and 6.0 kHz at Mach 3.0 and 4.0. The mean shock velocity, along the interaction centerline, shows the trend of decreasing velocity with decreasing Mach number from Mach 5.0 to 3.0. At Mach 2.0 the mean shock velocity is found to increase again.

Power spectral densities were calculated from the dynamic pressure signals measured at various locations in the unsteady shock wave/turbulent boundary layer interaction. The power spectra measured in the incoming boundary show similar frequency distributions for all Mach numbers. The power spectra measured upstream and downstream of the intermittent region are found to also have similar frequency content. The power spectra measured within the intermittent region show lower frequency content than either the upstream or downstream spectra. All power spectra measured within the intermittent region show a peak frequency range which corresponds to the maximum zero-crossing frequency. For a given Mach number, the power spectra measured within the intermittent region, both on centerline and off-centerline, are found to have self-similar frequency distributions when compared as functions of a Strouhal number. The power spectra, along the interaction centerline, are also found to be self-similar for all Mach numbers when

compared as functions of a Strouhal number.

Examination of the simultaneous pressure signals from two dynamic pressure transducers located within the intermittent region, separated by equal lateral distances on either side of the blunt fin centerline, show that the shock wave motion on either side of the interaction centerline is not symmetrically synchronized. This result indicates that the separation shock wave moves in a rippling motion, not a symmetric expanding and collapsing motion.

In an effort to assess facility effects, the results found in this investigation were compared with results from similar experiments conducted at the University of Texas at Austin, at Mach 5.0, and Princeton University, at Mach 3.0. The incoming boundary layer power spectra measured in all of the different facilities show significantly different frequency distributions. Despite the differences in the incoming boundary layer power spectra, however, the power spectra measured within the intermittent regions in each facility show similar frequency distributions. Comparing the maximum zero-crossing frequency, along the interaction centerline, with experiments at the University of Texas at Austin show a consistent trend of decreasing maximum zero-crossing frequency with increasing blunt fin leading edge hemi-cylindrical diameter. The intermittent region lengths calculated in this investigation are less than those found in the experiments at the University of Texas at Austin. Additionally, the experiments at the University of Texas at Austin show a factor of 2 decrease in the maximum standard deviation, along the interaction centerline, as the blunt fin size is decreased by a factor of 3.

The maximum standard deviations, normalized by the incoming static pressure, measured along the interaction centerline in this investigation are lower than those found in all of the University of Texas at Austin experiments.

There are two unresolved issues which have been identified in this investigation. The first is the discrepancy in the maximum standard deviations of the pressure signal measured between the University of Texas at Austin and the results presented here. The second is the observation of the intermittent region location upstream of the separation line in the Mach 2.0 tests. The facility used in this investigation has the capability of testing at Mach numbers 2.5 and 1.6 also. By performing additional experiments at these Mach numbers it may be possible to establish that the observations at Mach 2.0 are part of a general Mach number dependent phenomenon. Since the tests at the University of Texas at Austin showed significant dependence of the blunt fin size on the measured maximum standard deviation, it is also recommended that additional blunt fin sizes be tested in the facility used in this investigation in an effort to verify the effect of blunt fin size on maximum standard deviation measurements.

For the blunt fin induced shock wave/turbulent boundary layer interaction, the effects of unsteadiness are an important feature in the flowfield. The unsteady separation shock wave exhibits a significant range of motion in all of the tests performed in this investigation. The motion of the separation shock wave also produces locally large pressure fluctuations. From the results presented in this investigation, estimates of the unsteady pressure loads and frequencies can be used

in the design of efficient aerostructures employing this type of wing-body juncture. Neglecting the unsteady effects in this interaction could lead to the design of aerostructures which will be susceptible to high cycle fatigue failure.

Zero-frequency response surface flow visualization techniques are useful in developing an approximate estimation of the spatial extent of the shock wave/turbulent boundary layer interaction. Surface flow visualization techniques, however, produce a misleading steady-state image of a very unsteady flowfield. This investigation has shown that the primary separation line trace can be correlated to the farthest downstream location of the unsteady separation shock wave motion for Mach numbers 3.0 and greater. The Mach 2.0 tests did not show this correspondence, however, and the use of surface flow tracing methods alone is not recomended for the determination of the location of the unsteady separation shock wave motion.

The use of quasi-steady approximations is inherently incorrect in the computations of the blunt fin induced shock wave/turbulent boundary layer interaction. It has been experimentally observed that the pressure field in the vicinity of the separation shock wave motion is distinctly bimodal at any instant, with two separate flowfields measured upstream and downstream of the unsteady separation shock wave. The zero-frequency response static pressure measurements are thus a time average of a oscilating flowfield. Computations based on quasi-steady assumptions cannot properly compute the measured static pressure distribution from a stationary shock wave model.

REFERENCES

1   Settles, G. S. and Dodson, L. J., "Supersonic and Hypersonic Shock/Boundary-Layer Interaction Database", AIAA Journal, Vol. 32, No. 7, July 1994, pp. 1377-1383.

2   Dolling, D. S., "Fluctuating Loads in Shock Wave/Turbulent Boundary Layer Interaction: Tutorial and Update", AIAA Paper 93-0284, 1993.

3   Pozefsky, P., Blevins, R. D., and Langanelli, A. L., "Thermo-Vibro-Acoustic Loads and Fatigue of Hypersonic Flight Structures", AFWAL TR-89-3014, 1989.

4   Kistler, A. L., "Fluctuating Wall Pressure Under Separated Supersonic Flow", Journal of Acoustical Society od America, Vol. 36, March 1964, pp. 543-550.

5   Dolling, D. S. and Bogdonoff, S. M., "An Experimental Investigation of the Unsteady Behavior of Blunt Fin-Induced Shock Wave Trubulent Boundary Layer Interactions", AIAA Paper 81-1287, 1981.

6   Dolling, D. S. and Smith, D. R., "Unsteady Shock-Induced Turbulent Separation in Mach 5 Cylinder Interactions", AIAA Paper 88-0305, 1988.

7   Erengil, M. E. and Dolling, D. S., "Unsteady Wave Structure near Separation in a Mach 5 Compression Ramp Interaction", AIAA Journal, Vol. 29, No. 5, May 1991, pp. 728-735.

8   Erengil, M. E. and Dolling, D. S., "Effects of Sweepback on Unsteady Separation in Mach 5 Compression Ramp Interactions", AIAA Journal, Vol. 31, No. 2, February 1993, pp. 302-311.

9   Gibson, B. T. and Dolling, D. S., "Exploratory Study of Wall Pressure Fluctuations in a Mach 5, Sharp Fin-Induced Turbulent Interaction", AIAA Journal, Vol. 30, No. 9, September 1992, pp. 2188-2189.

10   Dolling, D. S., and Bogdonoff, S. M., "Blunt Fin-Induced Shock Wave/Turbulent Boundary-Layer Interaction", AIAA Journal, Vol. 20, No. 12, December 1982, pp. 1674-1680.

11   Dolling, D. S., and Brusniak, L., "Separation Shock Motion in Fin, Cylinder, and Compression Ramp-Induced Turbulent Interactions", AIAA Journal, Vol. 27, No. 6, June 1989, pp. 734-742.

12   Gonsalez, J. C., "Correlation of Interaction Sweepback Effects on Unsteady Shock-Induced Turbulent Separation", M.S. Thesis, The University of Texas at Austin, August 1993.

13   Evans, T., Poddar, K., and Smits, A. J., "Compilation of Wall Pressure Data for a Shock Wave Boundary Layer Interaction Generated by a Blunt Fin", MAE Report No. 1908 T, Gas Dynamics Laboratory, Department of Mechanical and Aerospace Engineering, Princeton University, December 1990.

14   Skebe, S. A., "Experimental Investigation of Two Dimensional Shock Boundary Layer Interaction.", Ph.D. Dissertation, Case Western Reserve University, August 1983.

15   Bendat, J. S., and Piersol, A. G., Random Data, 2nd Edition, John Wiley & Sons, Inc., 1986, pp. 377-379.

16   Sun, C. C., and Childs, M. E., "Successive Oblique Shock Wave-Turbulent Boundary Layer Interactions", NASA CR 2656, March 1976, pp. 14-17.

17   Davis, D. O., NASA-Lewis Research Center data currently unpublished.

18   Bevington, P. R., Data Reduction and Error Analysis for the Physical Sciences, McGraw-Hill, 1969, pp. 232-245.

19   Hinze, J. O., Turbulence, 2nd Edition, McGraw-Hill, 1975.

20   Liepmann, H. W., and Roshko, A., Elements of Gasdynamics, John Wiley & Sons, 1957, pp.157-162.

21   Fomison, N. R., and Stollery, J. L., "The Effects of Sweep and Bluntness on a Glancing Shock Wave Turbulent Boundary Layer Interaction", AGARD Conference Procedures 428, 1987.

22   Sedney, R., and Kitchens, C. W., "Separation Ahead of Protruberances in Supersonic Turbulent Boundary-Layers", AIAA Journal, vol. 15, no. 4, April 1977, pp. 546-552.

23 Brusniak, B. S., "Experimental Investigation of the Driving Mechanism of the Unsteady Separation Shock Motion in a Cylinder-Indiced Hypersonic Interaction", M. S. Thesis, The University of Texas at Austin, May 1991.

24 Debieve, J. F., and LaCharme, J. P., "A Shock Wave/Free Turbulence Interaction", Proceedings, IU-TAM Symposium, Turbulent Shear-Layer/Shock-Wave Interactions, Springer-Verlag, 1986, pp. 393-403.

TABLE 1

Maximum Sampling Frequency of Dynamic Pressure
Transducer Measurements

Number of Transducers	Maximum Sampling Frequency (kHz)	Total Measurement Time (ms)
1	850	963.7
2	330	2482.4
3	250	3268.6
4	200	4096.0
5	160	5120.0
6	140	5836.8
7	120	6809.6
8	110	7447.3

TABLE 2

Basic Wind Tunnel Test Conditions

Nominal Mach Number	Total Pressure P_T (kPa)	Unit Reynolds No. Re_x (1/m)	Measured Mach Number
5.0	689	13,900,000	4.99
4.0	345	14,100,000	3.94
3.0	207	15,000,000	2.94
2.0	138	17,000,000	1.97
	68.9	8,500,000	

TABLE 3

Incoming Boundary Layer Properties

Nominal Mach Number	2.0	3.0	4.0	5.0*
δ (cm)	2.81	3.03	3.62	3.89
δ^* (cm)	0.561	0.853	1.39	1.79
θ (cm)	0.202	0.183	0.188	0.162
C_f (x10^3)	1.04	0.907	0.792	0.651
Π	1.12	1.18	1.42	1.55
M_e	1.97	2.94	3.94	4.99
u_e (m/s)	512	618	676	765
Re_θ (x10^{-3})	17.2	27.4	26.5	22.5
$H = \delta^*/\theta$	2.78	4.66	7.39	11.0

* not measured; extrapolated values

TABLE 4

Incoming Boundary Layer Dynamic Characteristics

Nominal Mach Number	2.0	3.0	4.0	5.0
σ_P / P_0	0.00513	0.00523	0.00807	0.0119
Ω (ms)	0.133	0.0709	0.0987	0.118
Λ (cm)	6.81	4.38	6.67	9.02

TABLE 5

Separation Line Curve Fit Scaled Constants

Nominal Mach Number	2.0	3.0	4.0	5.0
A/D	2.765	2.866	3.209	3.437
B/D	0.2541	0.2899	0.5934	0.4862
C/D	0.1004	0.008043	0.03347	0.06133

BOW SHOCK

SEPARATION SHOCK

VORTEX
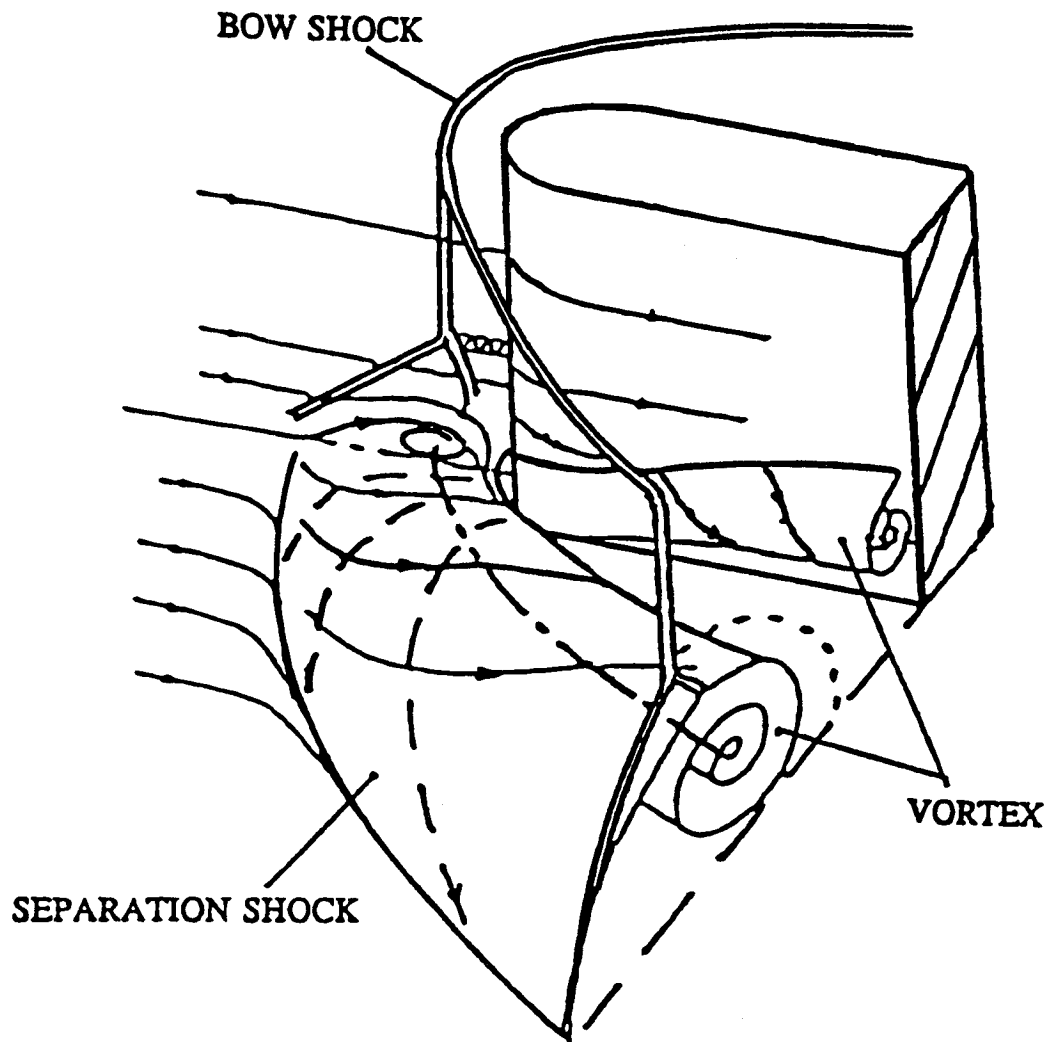
Figure 1   Blunt Fin Induced Shock Wave Turbulent Boundary Layer Interaction

119
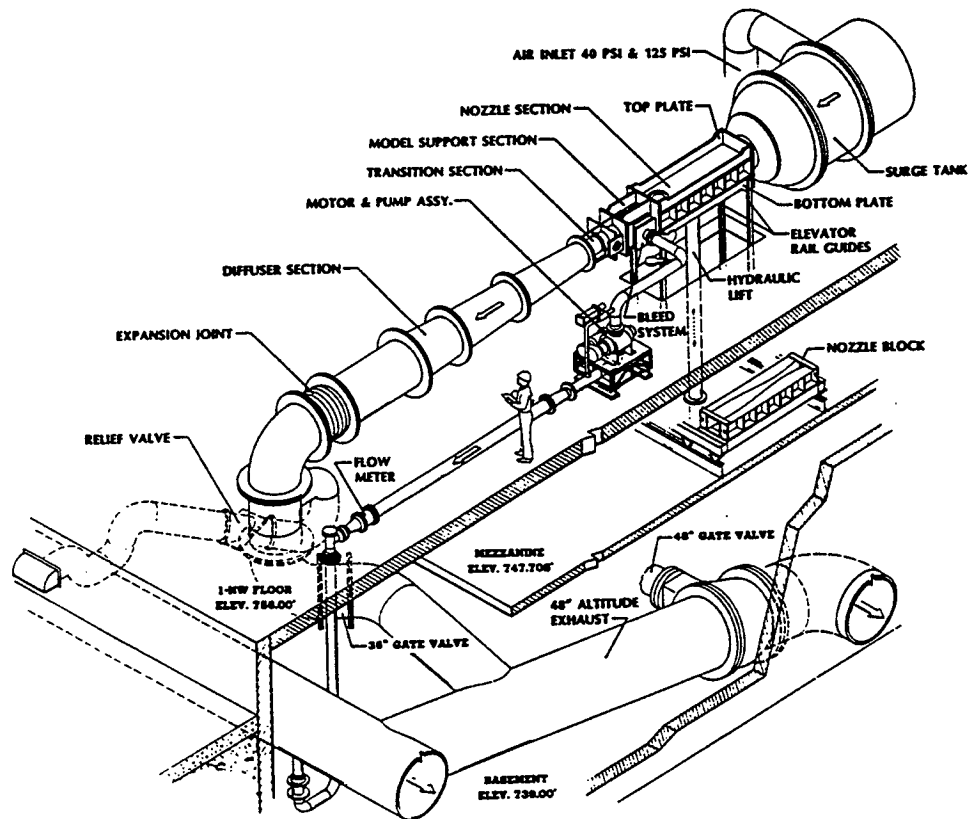
Figure 2   1x1 Supersonic Wind Tunnel

Circular Insert Plate

Transducer Plug

Blunt Fin

Flow

Sidewall
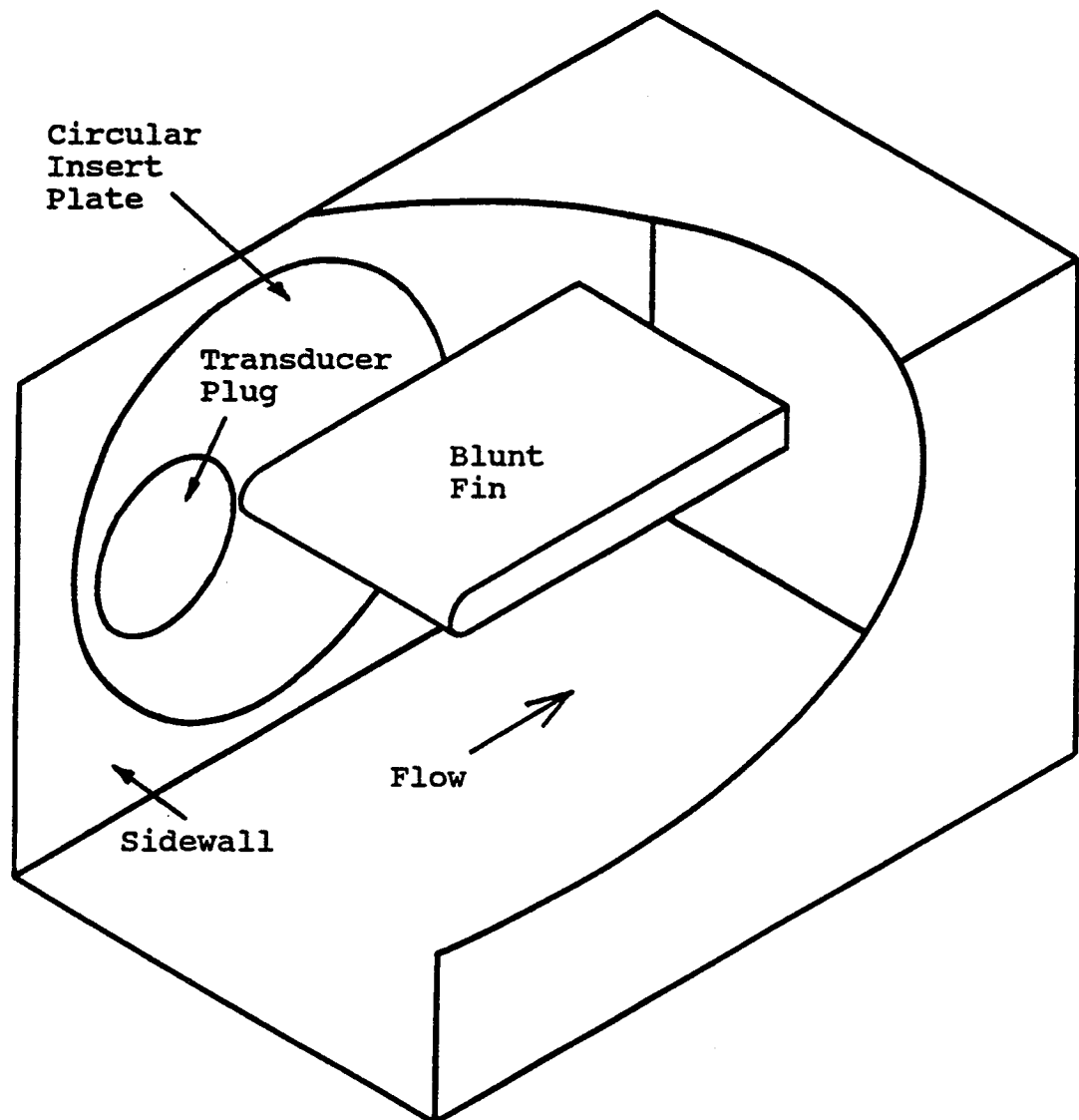
Figure 3 Test Section
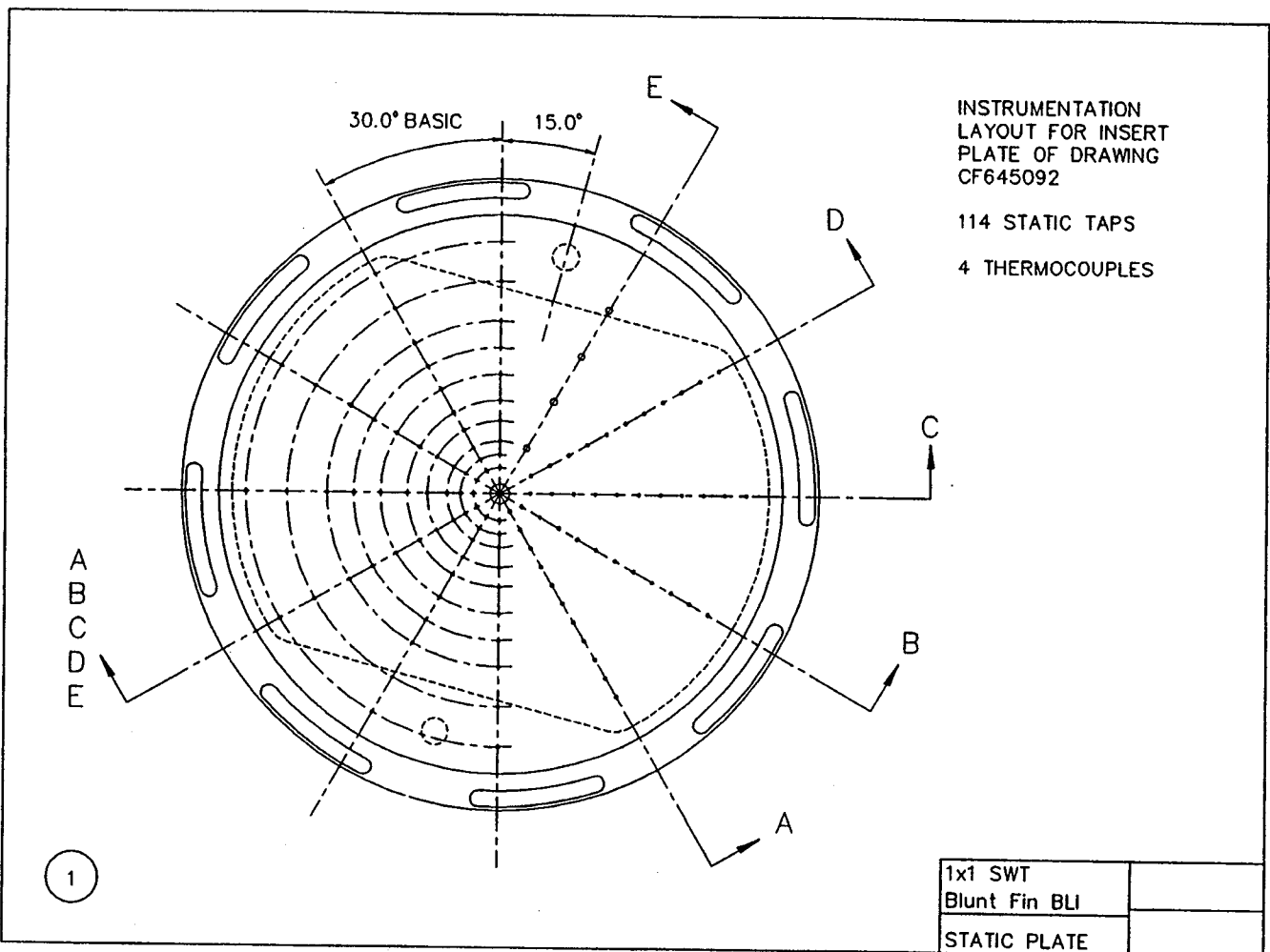
Figure 4 Circular Insert Plate for Static Pressure Measurements (Drawing 1 of 4)
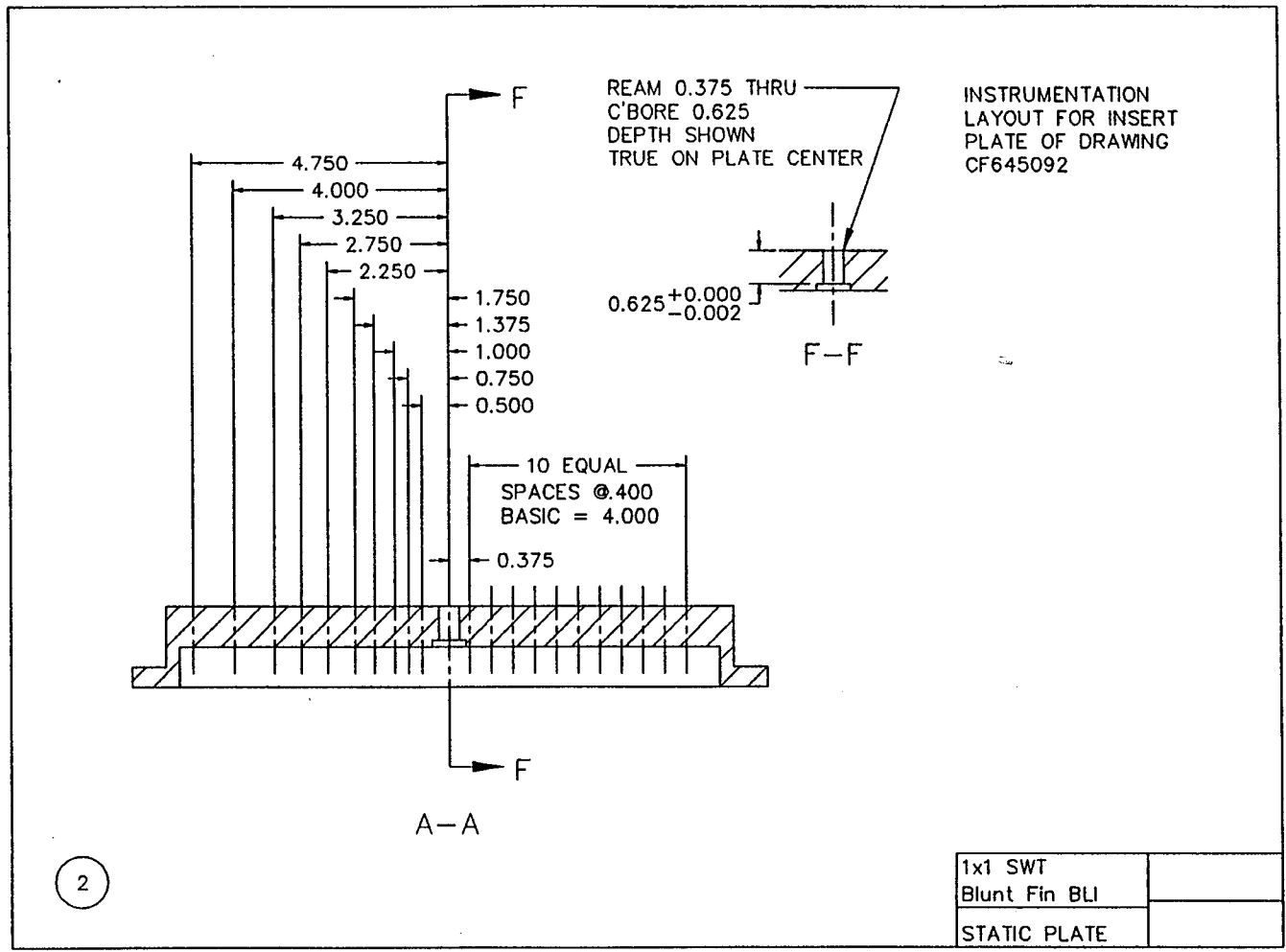
[dimensions: inch]

Figure 5   Circular Insert Plate for Static Pressure Measurements
(Drawing 2 of 4)

[dimensions: inch]

INSTRUMENTATION
LAYOUT FOR INSERT
PLATE OF DRAWING
CF645092

10 EQUAL
SPACES @.400
BASIC = 4.000

0.575

C—C

10 EQUAL
SPACES @.400
BASIC = 4.000

0.475

B—B

1x1 SWT
Blunt Fin BLI

STATIC PLATE

3
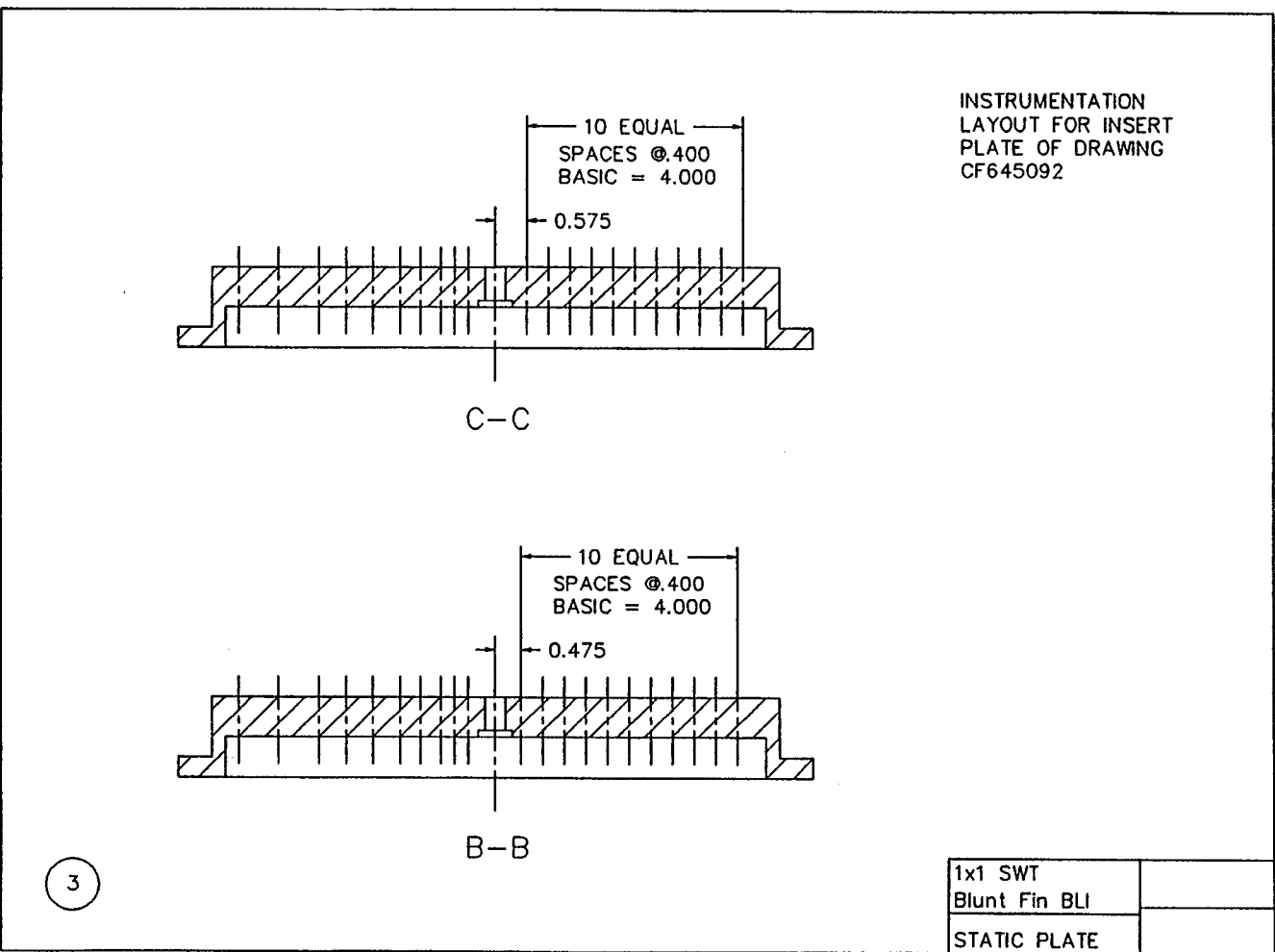
Figure 6   Circular Insert Plate for Static Pressure Measurements
(Drawing 3 of 4)

[dimensions: inch]

123
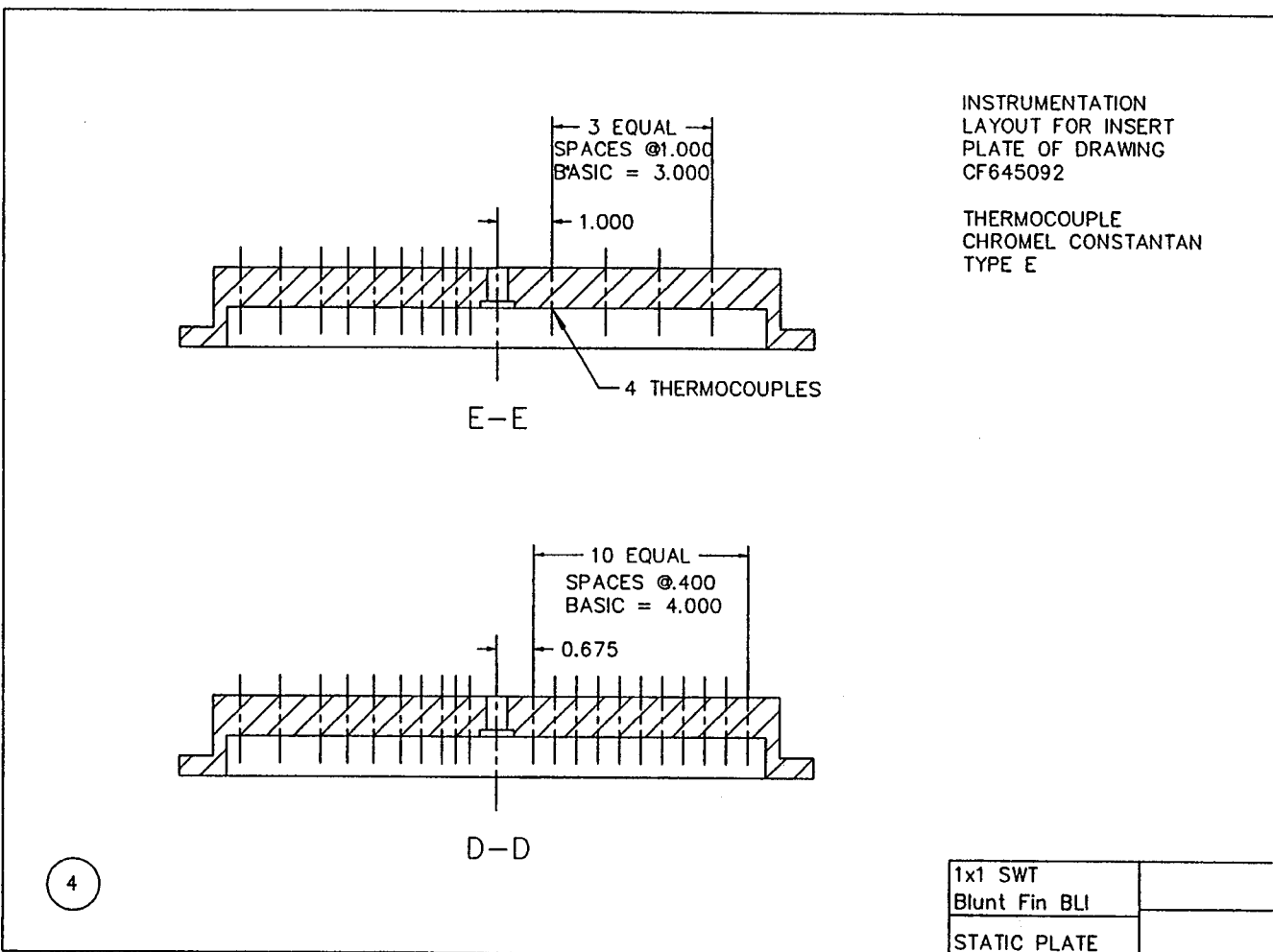
Figure 7

Circular Insert Plate for Static Pressure Measurements
(Drawing 4 of 4)

[dimensions: inch]

124

125
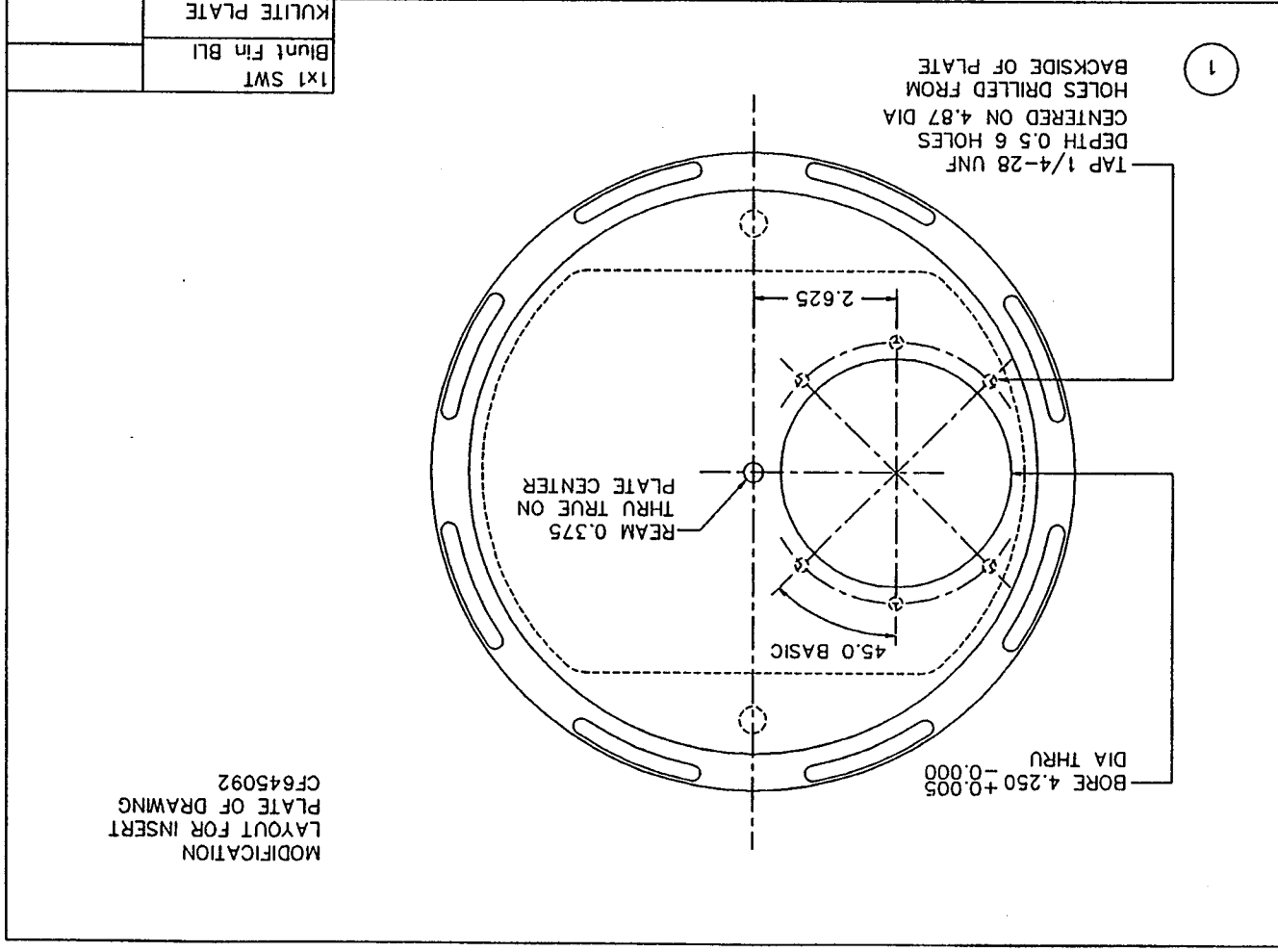
Figure 8   Circular Insert Plate for Dynamic Pressure Measurements

[dimensions: inch]

Figure 9   Dymanic Pressure Transducer Plug   [dimensions: inch]

TAP 10-32 UNF
DEPTH 0.8 4 HOLES
CENTERED ON 3.875 DIA
HOLES DRILLED FROM
BACKSIDE OF PLATE

60.0°BASIC

SURFACES MUST BE
PARALLEL, FLAT,
SQUARE AND TRUE TO
EACH OTHER WITHIN
0.005 FIR.

MATERIAL: BRASS

16/ALL OVER

1.500
1.000
1.000
1.500

A   A

0.25 R TYP

DRILL No 50 (.070)
THRU 81 HOLES
BOTTOM TAP 4-40 UNC
DEPTH AS SHOWN
BELLOW FROM BACKSIDE
OF PLATE

$4.250 ^{+0.000}_{-0.005}$ DIA

0.125

0.031

1.250

0.400
BOTTOM
TAP
DEPTH

0.500

30 EQUAL SPACES @.125
BASIC = 3.750

A—A

1

1x1 SWT	
Blunt Fin BLI	
KULITE INSERT	

126

Figure 10　Moveable Blunt Fin

[dimensions: inch]

SURFACES MUST BE
PARALLEL, FLAT,
SQUARE AND TRUE TO
EACH OTHER WITHIN
0.005 FIR.

MATERIAL: BRASS

16/ALL OVER

30°

6.000

1.750

9.375

A

A

TAP 3/8-16 UNC
DEPTH 0.70-0.80

R0.500

R0.250

1.000

8.500

1

$0.250^{+0.000}_{-0.002}$

0.250

0.750

0.125

0.125

$0.500^{+0.002}_{-0.000}$

A-A

1x1 SWT
Blunt Fin BLI

MOVABLE FIN 1"

127
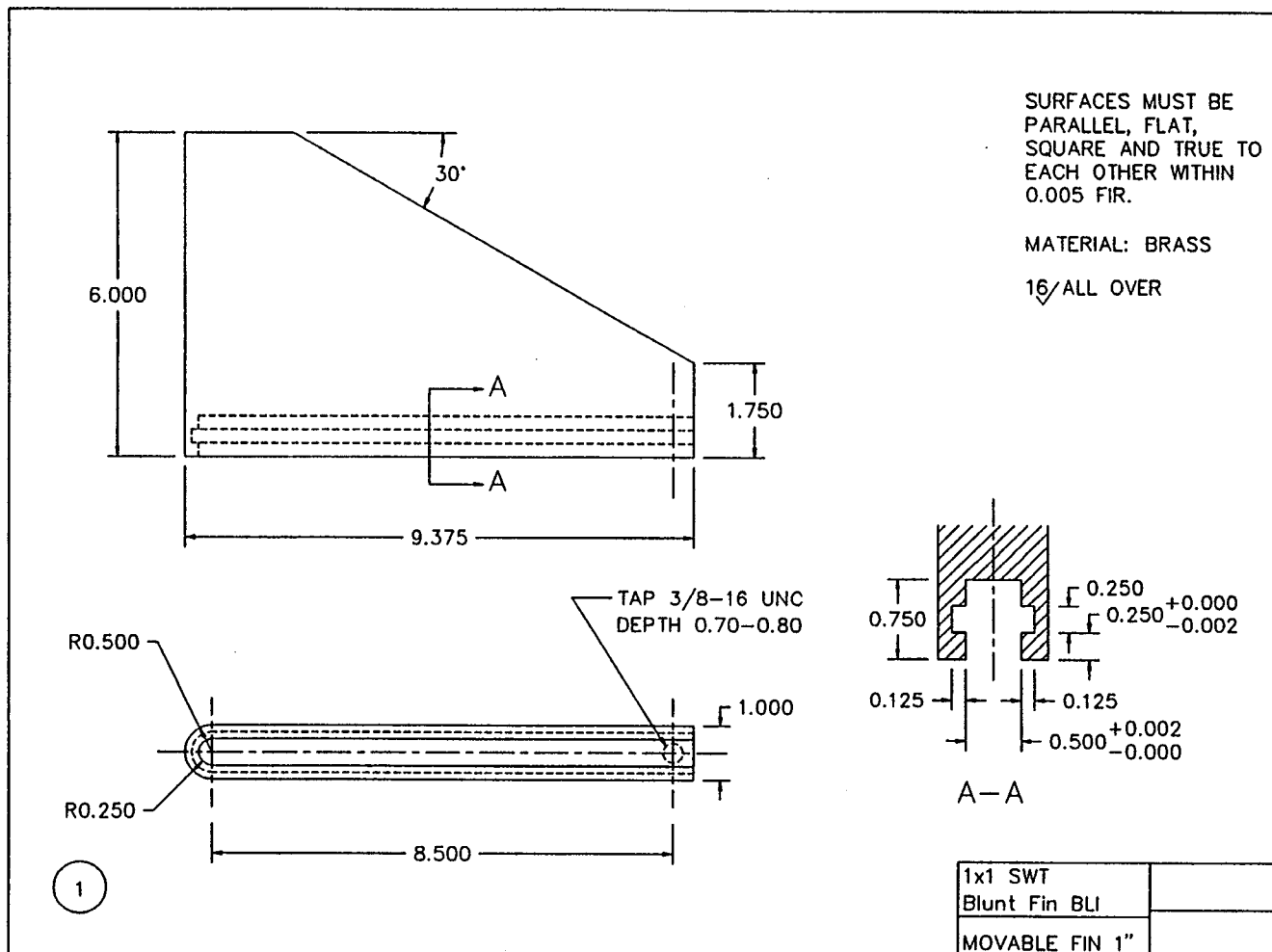
Figure 11   Moveable Blunt Fin Mounting Rail

[dimensions: inch]

TAP 5/16-18 UNC
THRU 2 HOLES

R0.375

R0.250

6.25

SURFACES MUST BE
PARALLEL, FLAT,
SQUARE AND TRUE TO
EACH OTHER WITHIN
0.005 FIR.

MATERIAL: BRASS

16/ALL OVER

0.740

6.750

0.120   0.120

0.250 $^{+0.002}_{-0.000}$

0.240

0.500 $^{+0.000}_{-0.002}$

1x1 SWT
Blunt Fin BLI

FIN MOUNT 1"

128
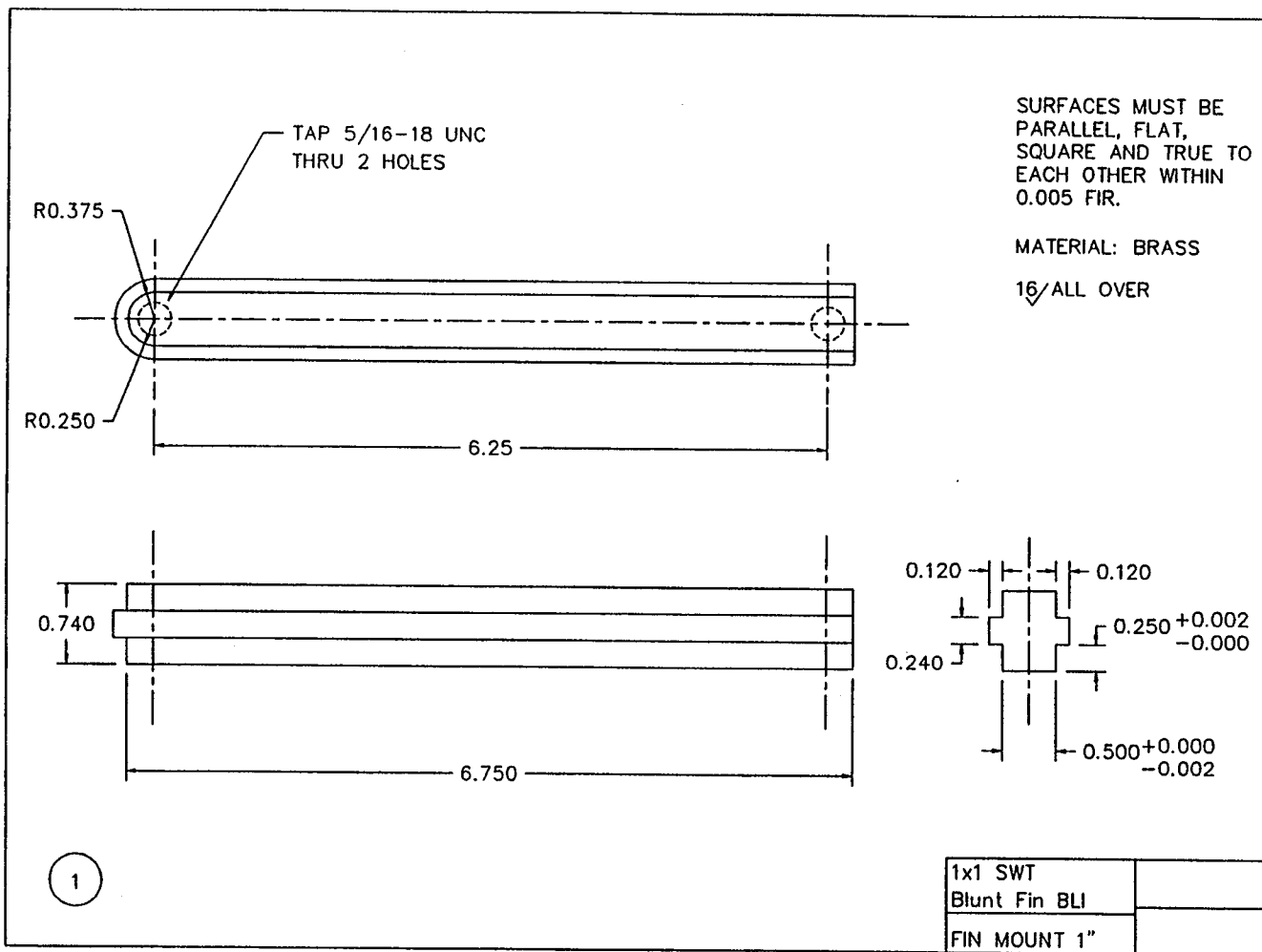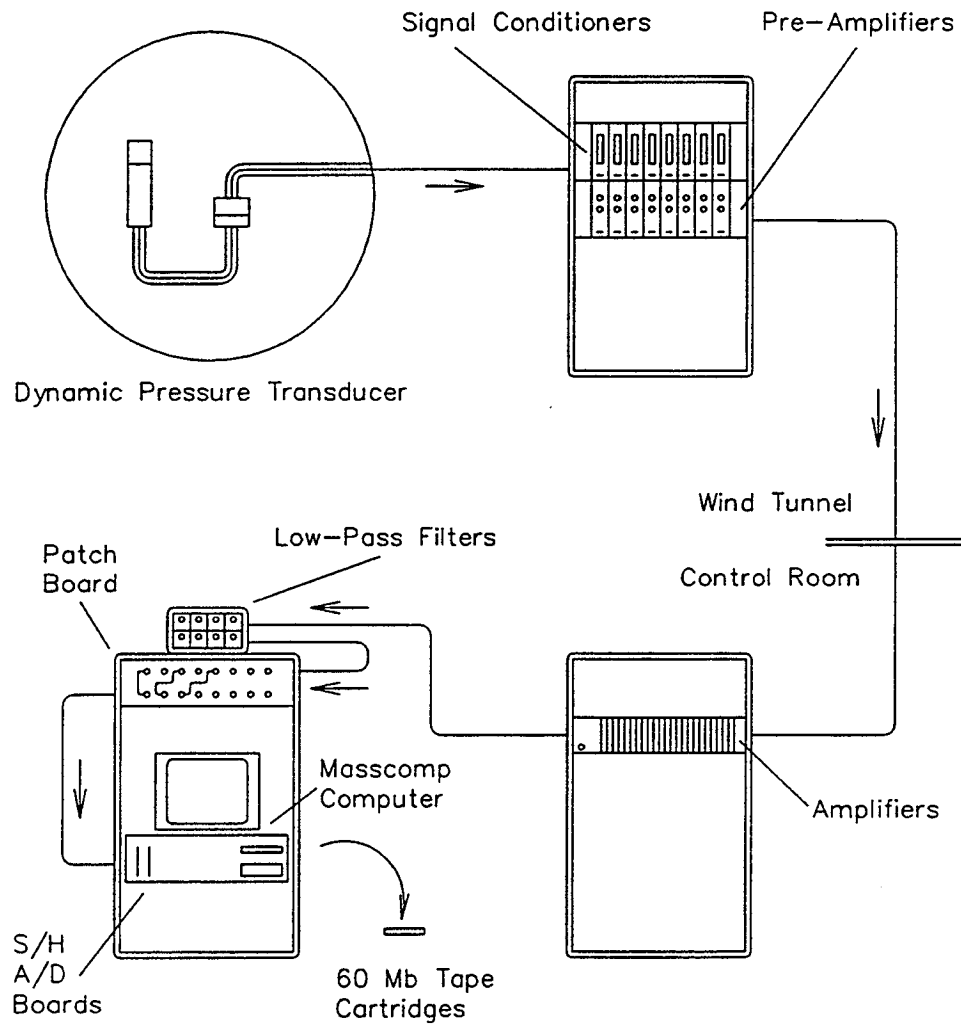
Figure 12   Dynamic Pressure Measurement Data Acquisition System

130

P(t) (psia) vs t (ms)
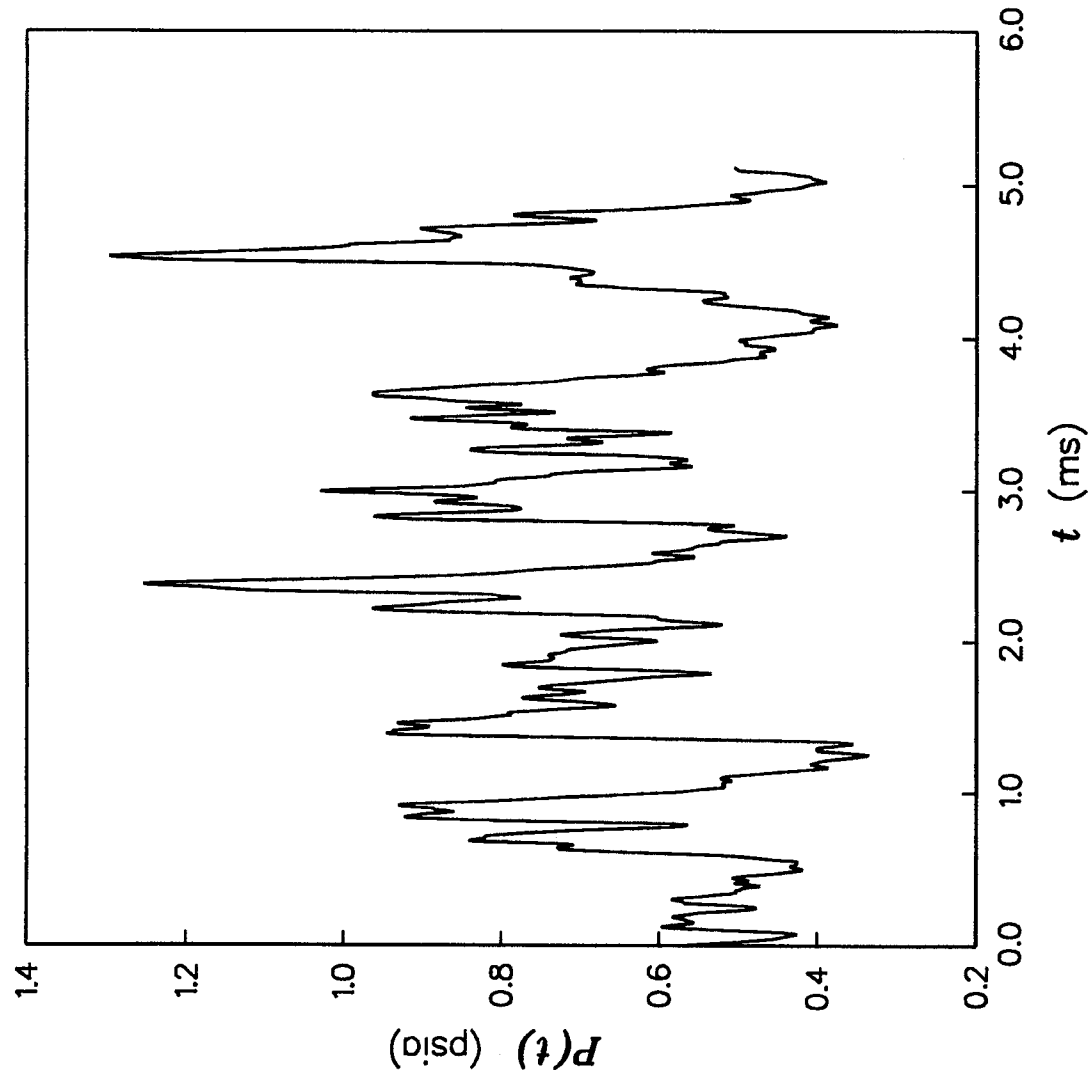
Figure 13   Example of a Dynamic Pressure Transducer Signal

131
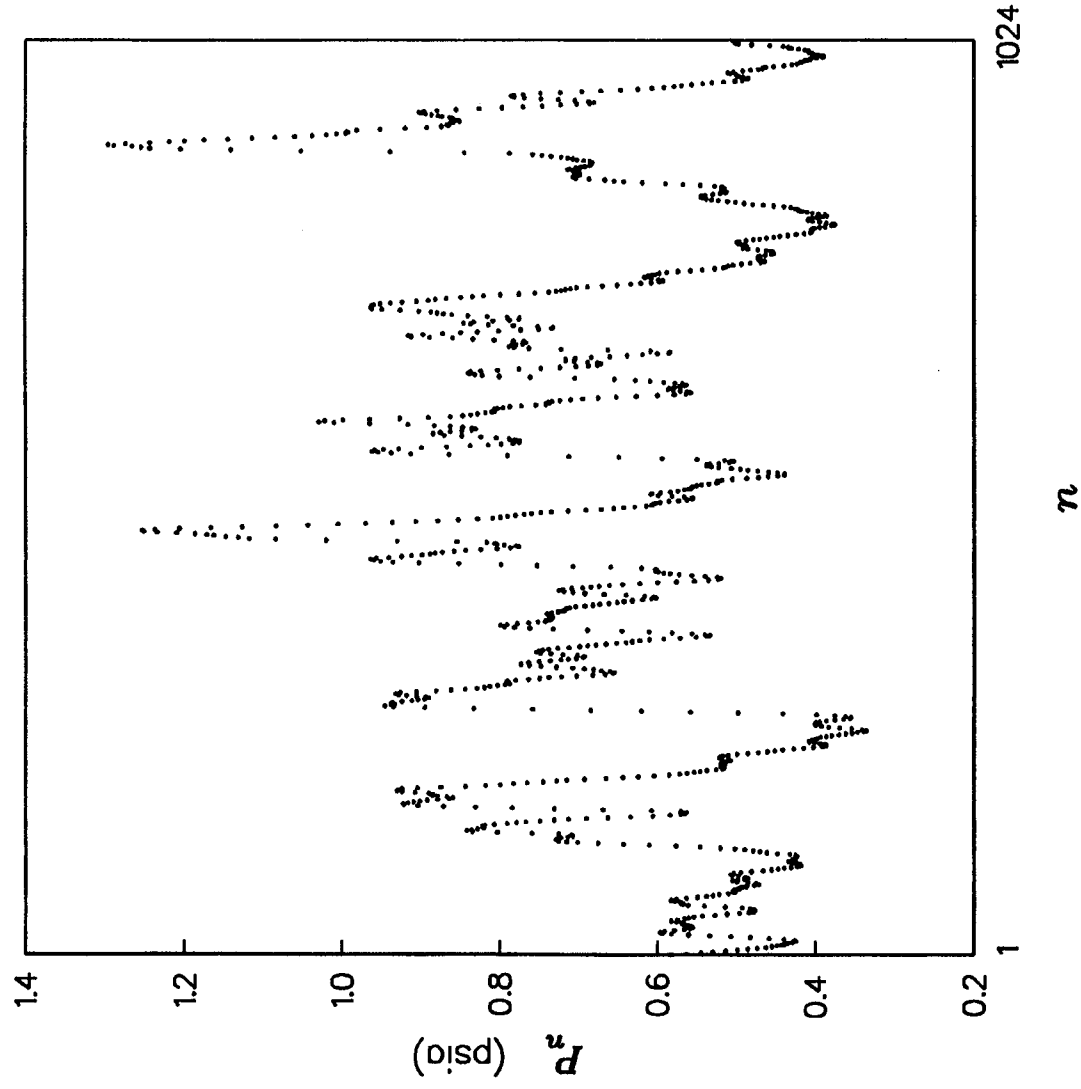
Figure 14   Discrete Data Representation of Dynamic Pressure
Transducer Signal
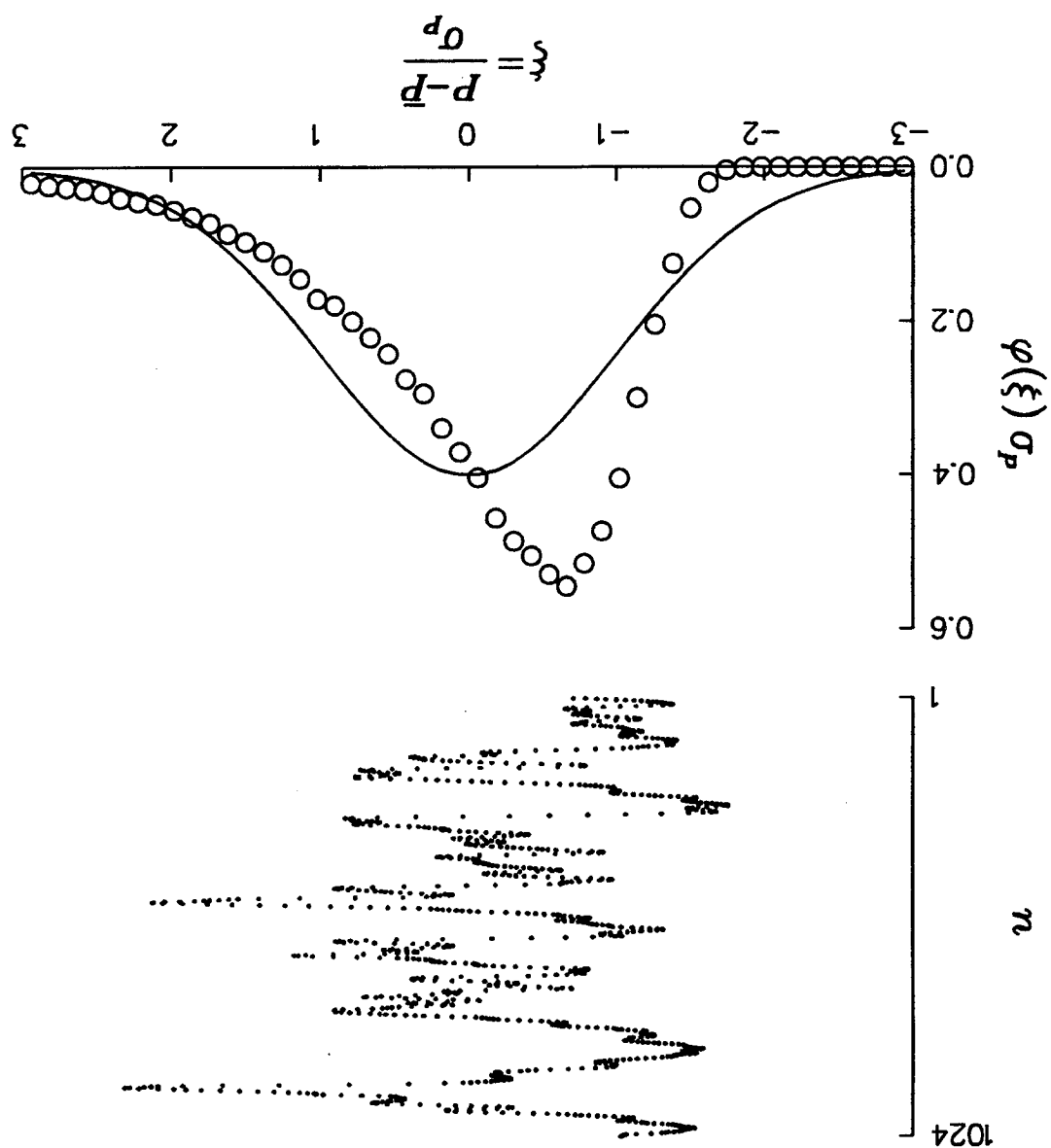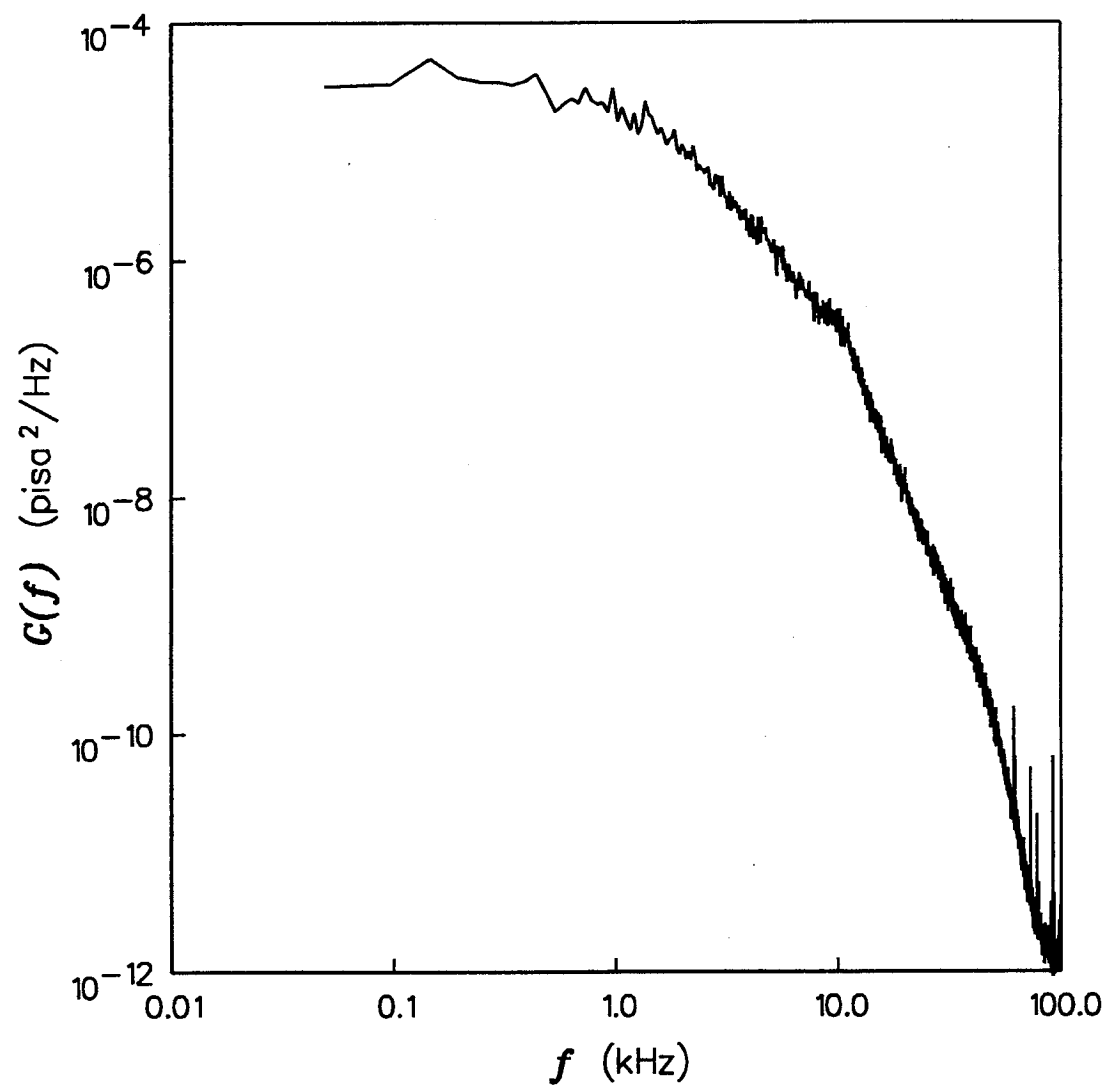
Figure 16   Example of a Power Spectral Density Function
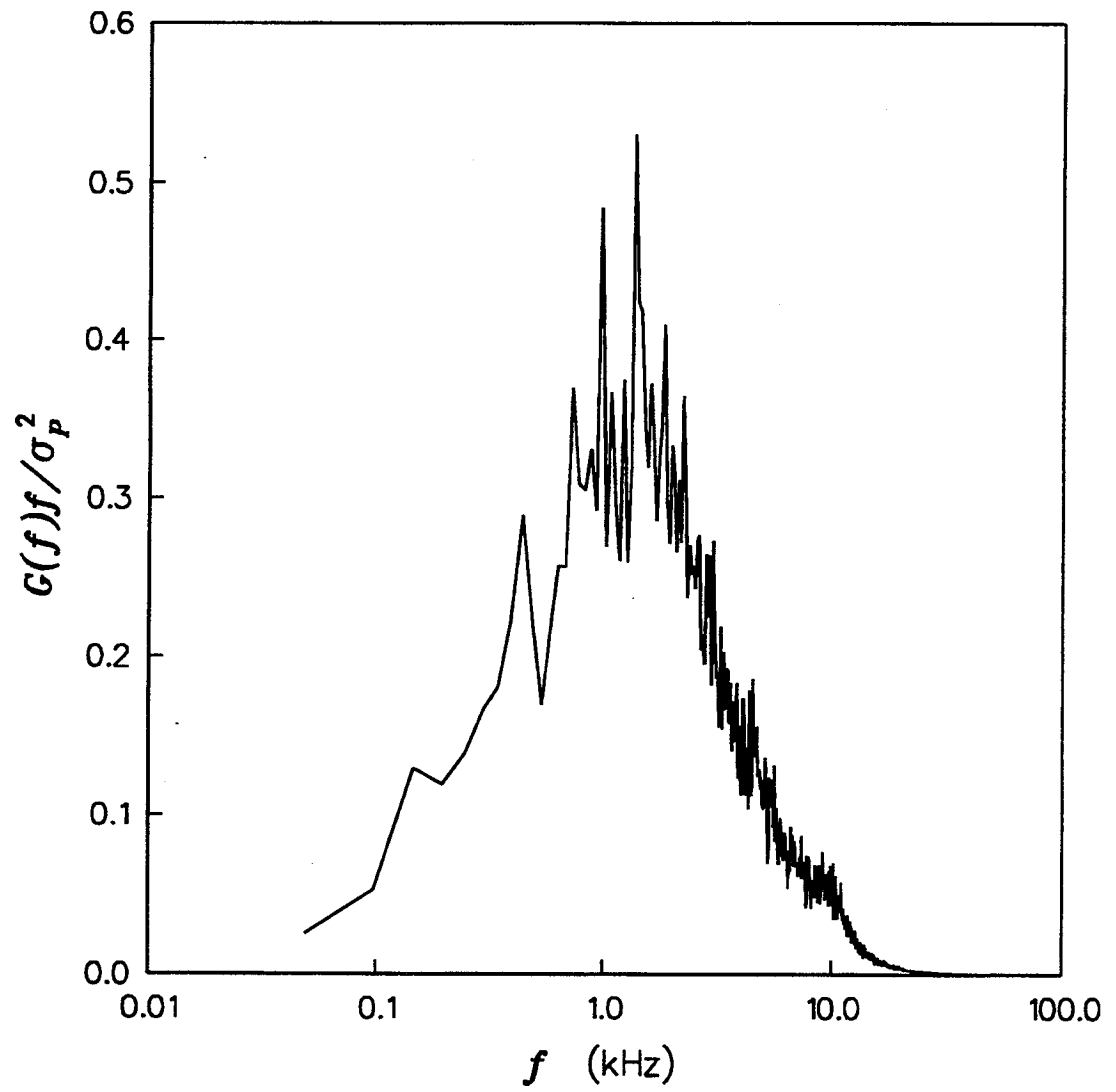
Figure 17   Example of a Normalized Power Spectral Density Function
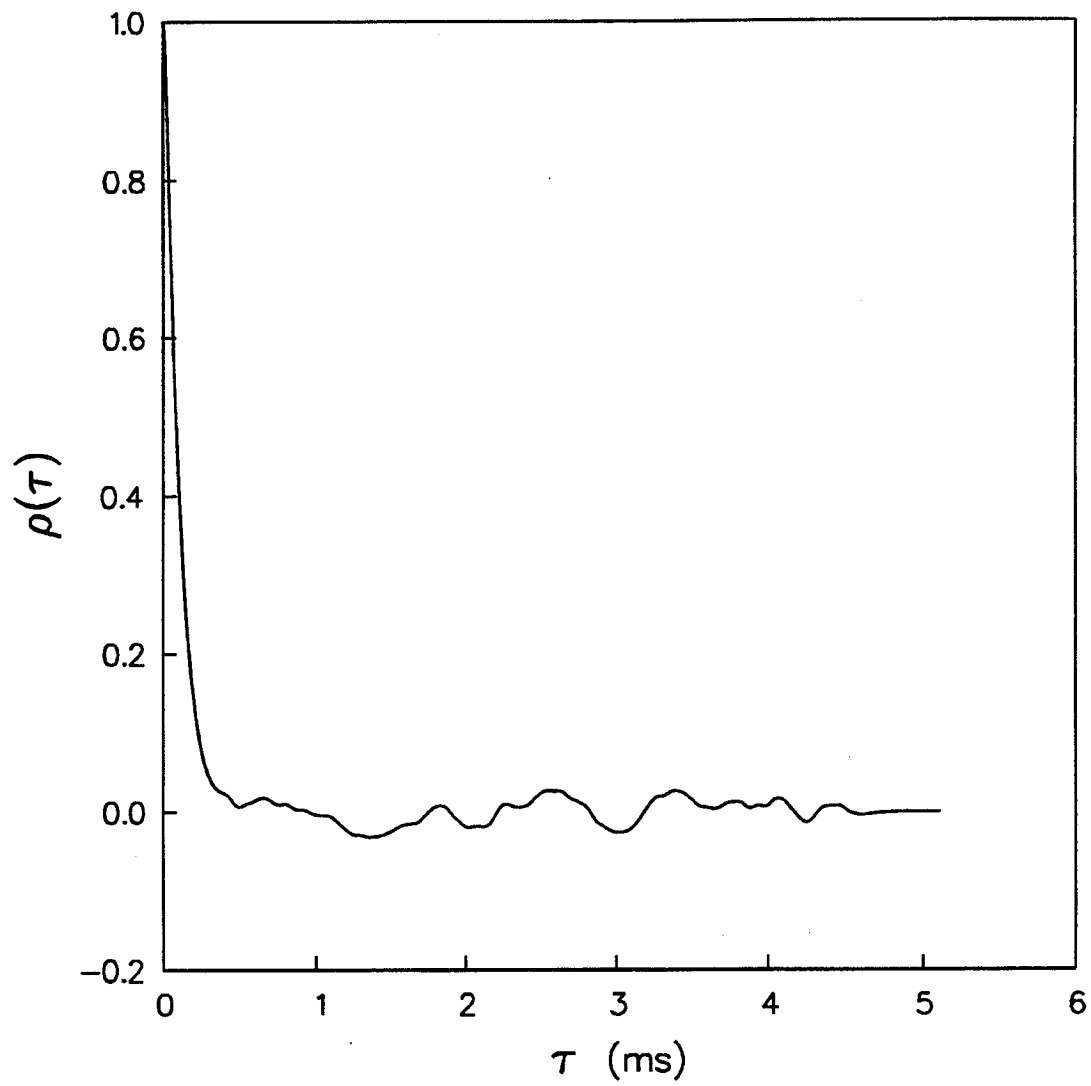
Figure 18   Example of an Autocorrelation Function

136
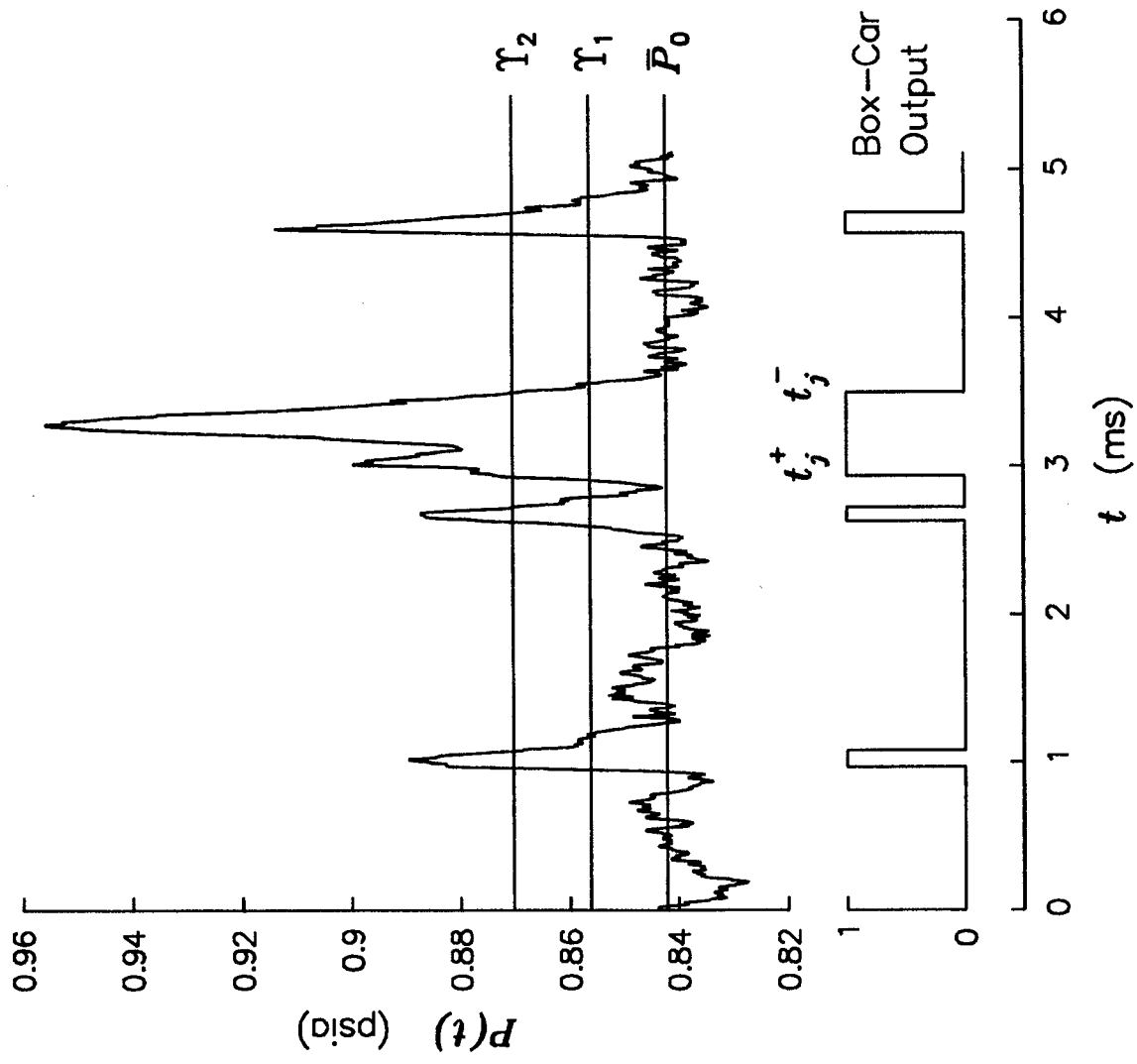
Figure 19   Example of a Box-Car Signal Constructed from a Two-
Threshold Algorithm
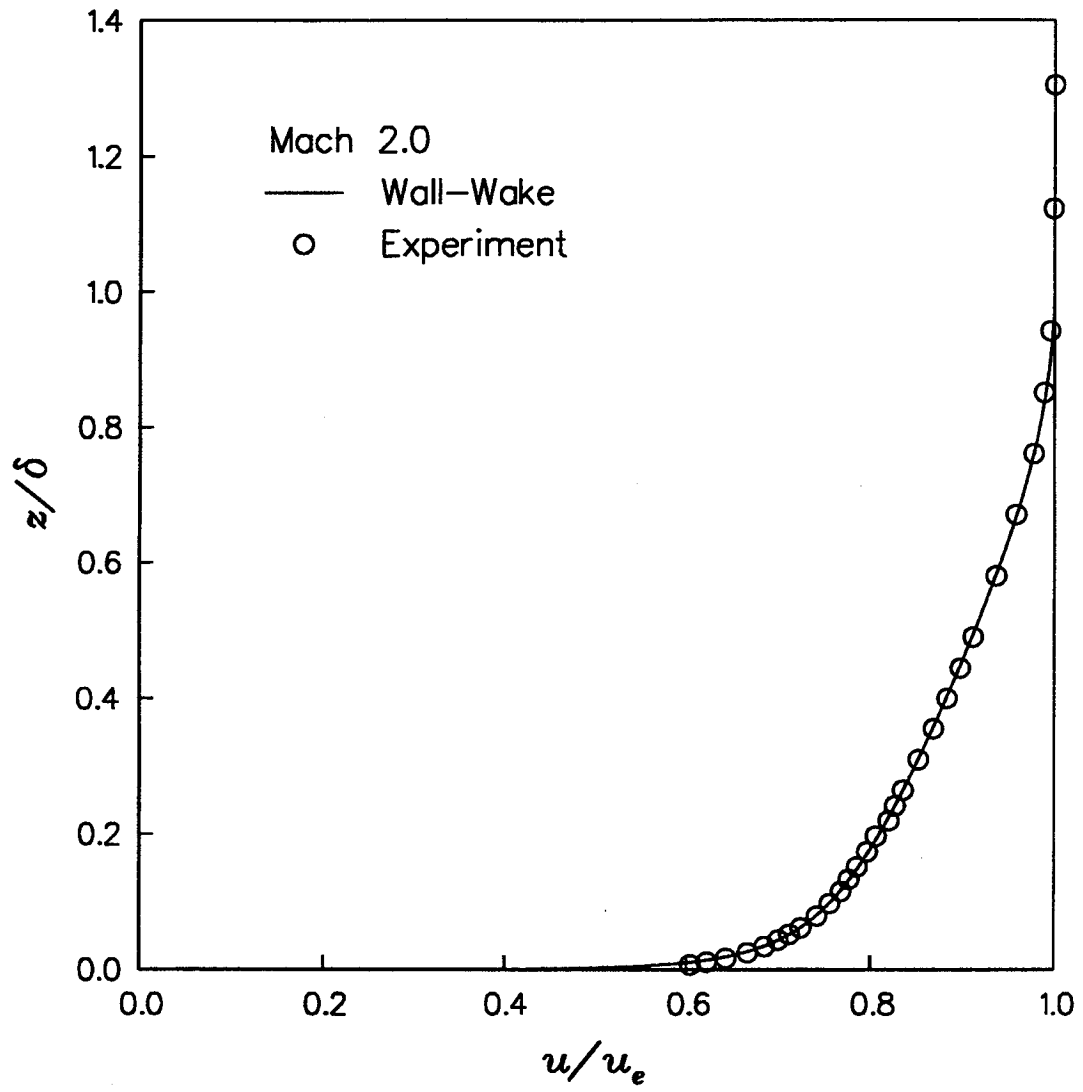
Figure 20   Mach 2.0 Incoming Boundary Layer Velocity Profile
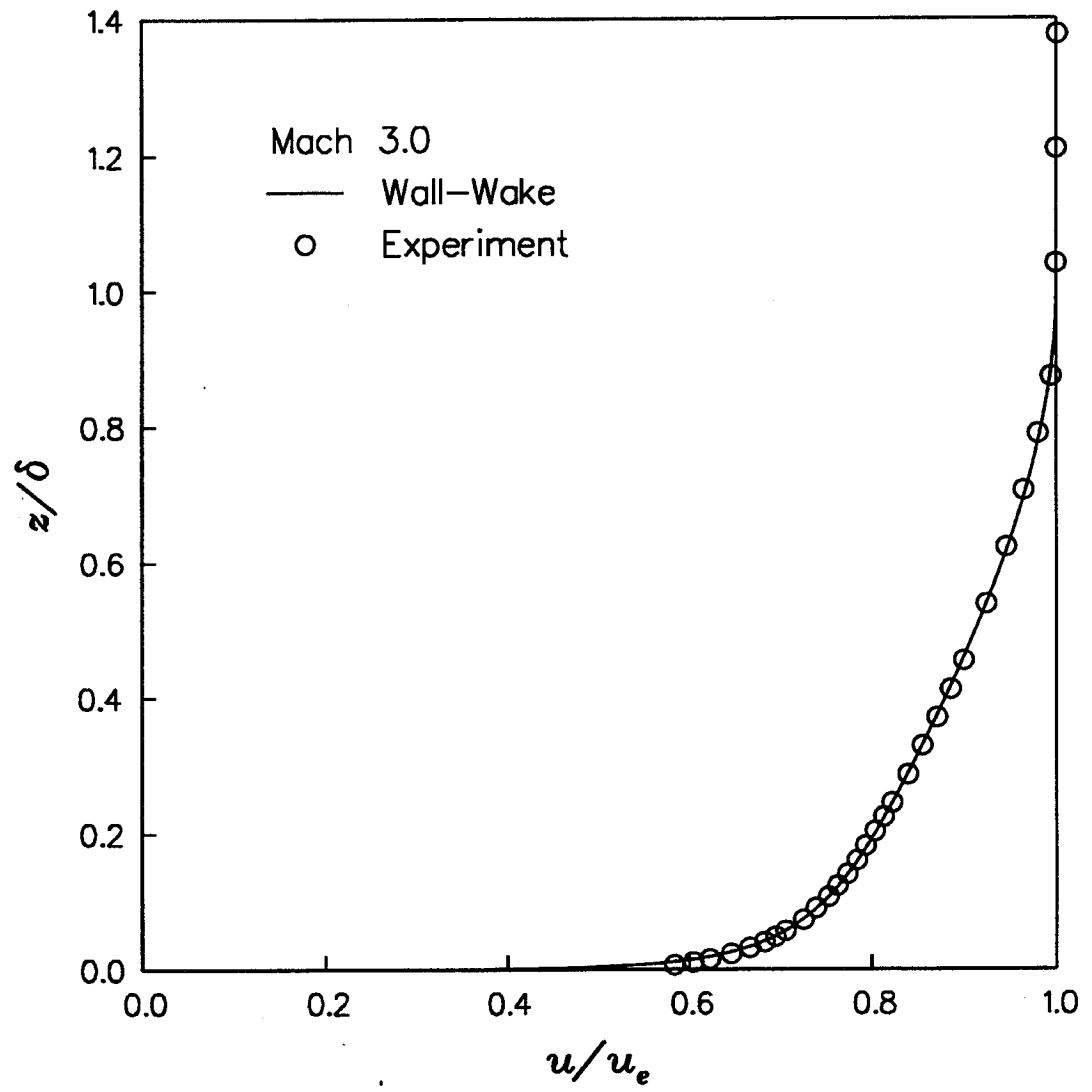
Figure 21   Mach 3.0 Incoming Boundary Layer Velocity Profile
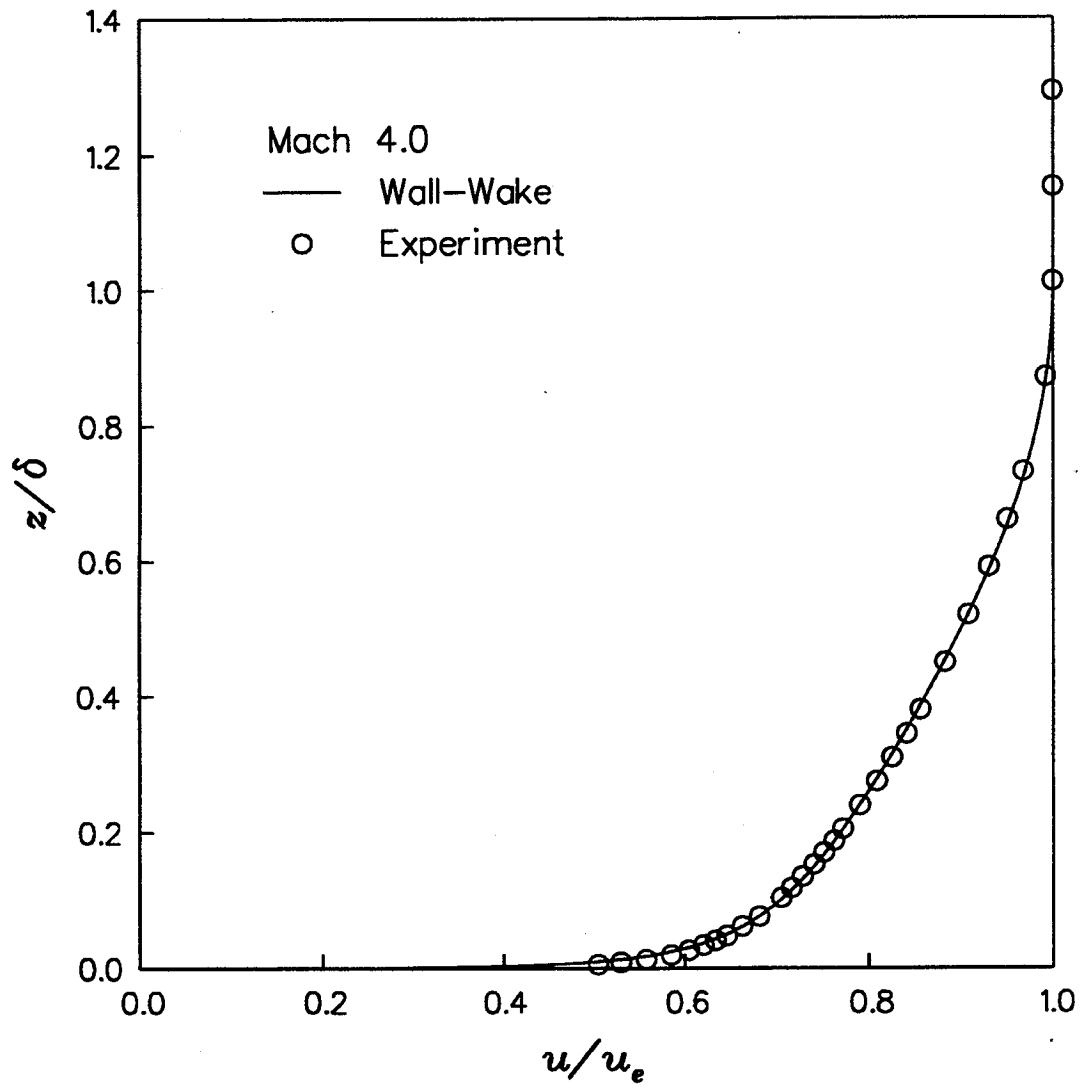
Figure 22   Mach 4.0 Incoming Boundary Layer Velocity Profile
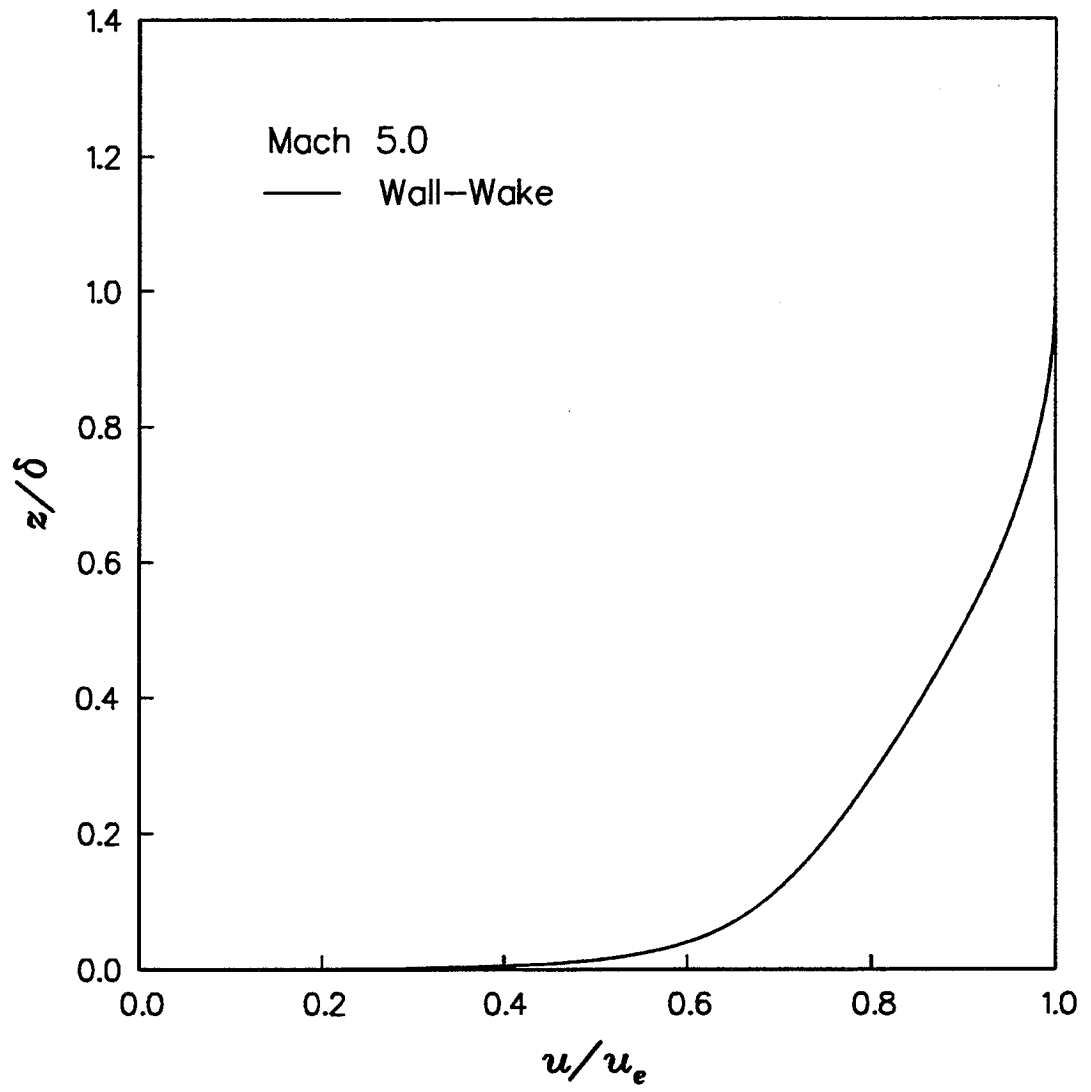
Figure 23   Mach 5.0 Incoming Boundary Layer Velocity Profile
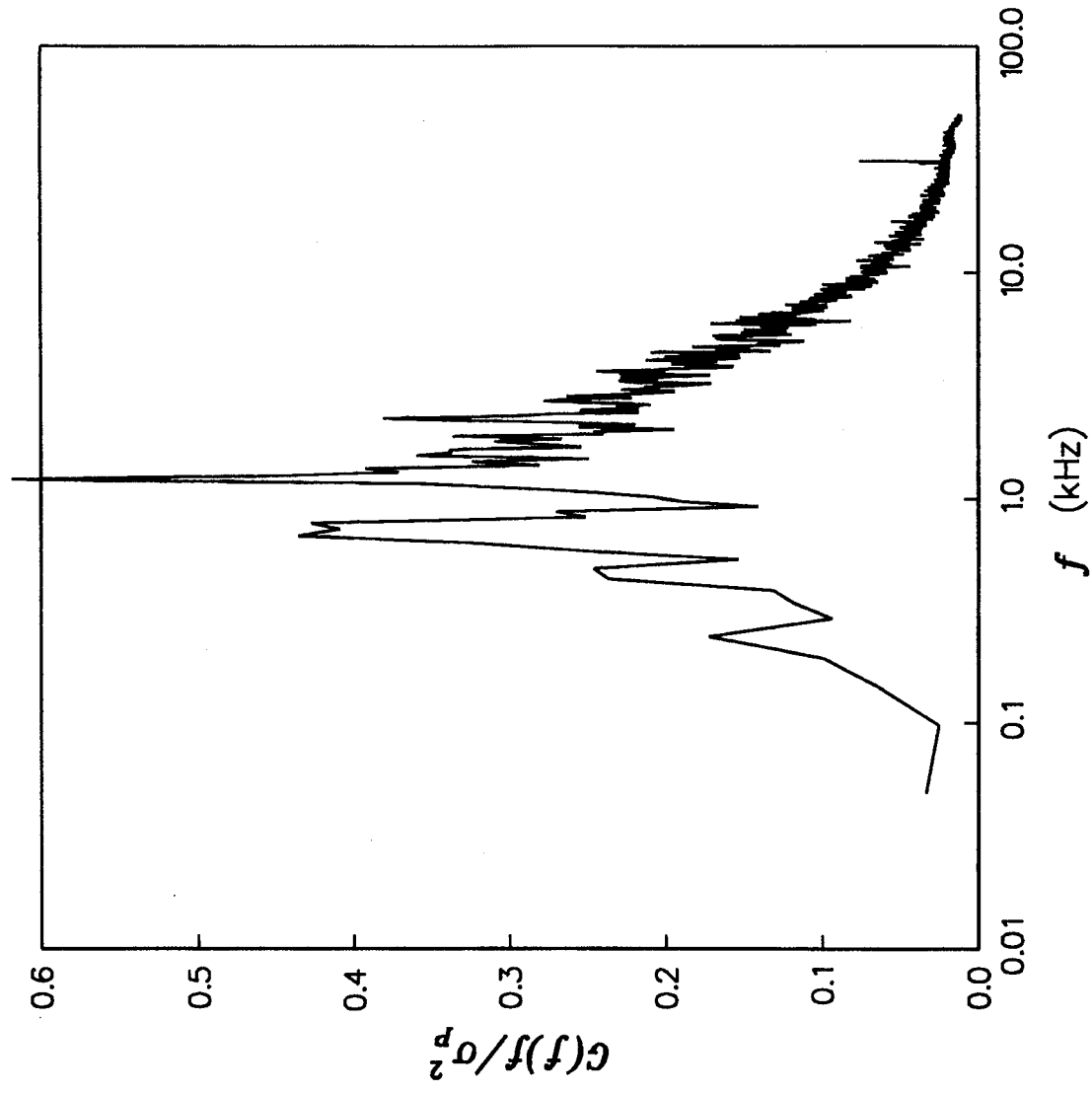
Figure 24   Mach 2.0 Incoming Boundary Layer Normalized Power
Spectral Density
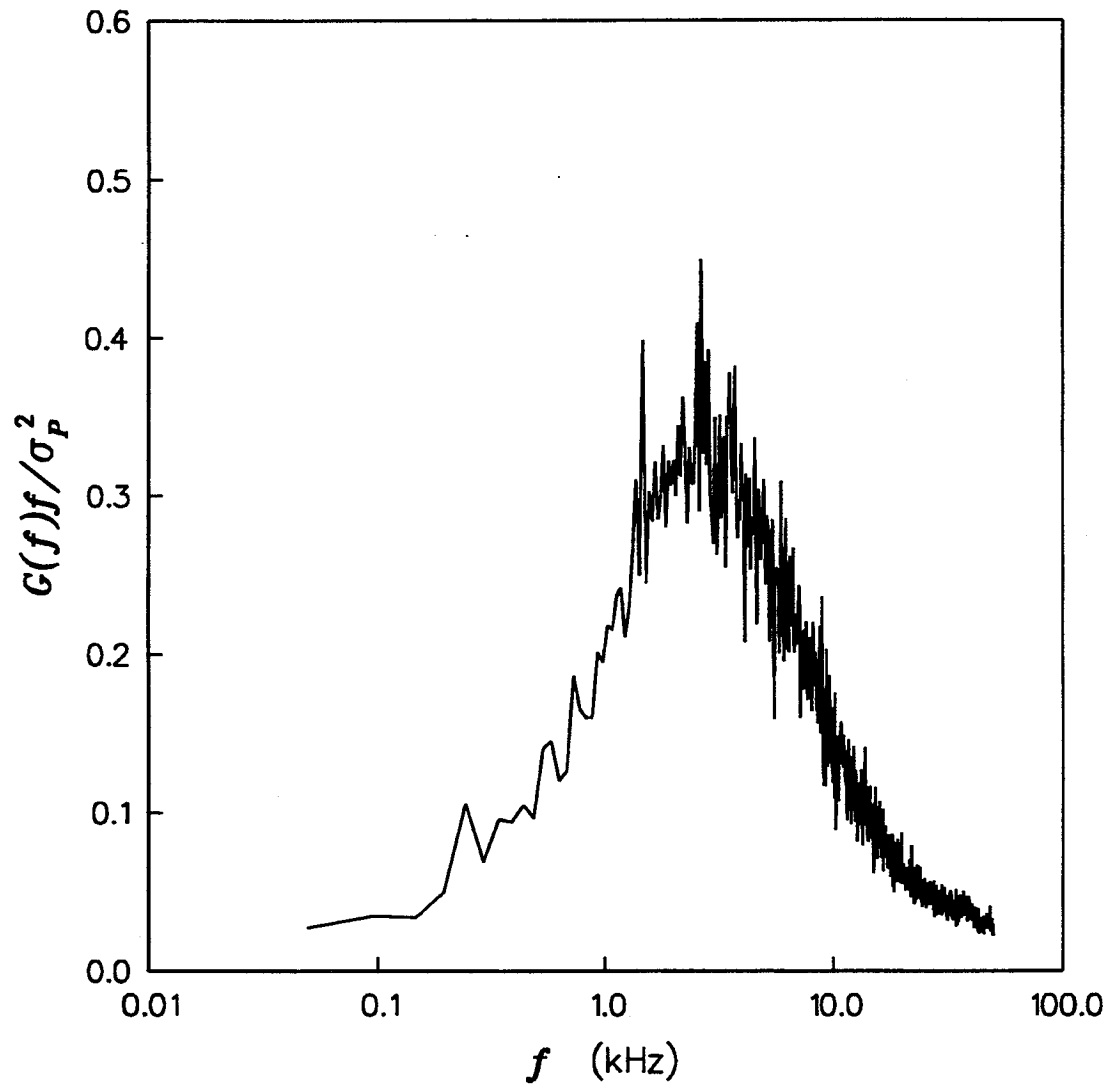
Figure 25   Mach 3.0 Incoming Boundary Layer Normalized Power
                 Spectral Density
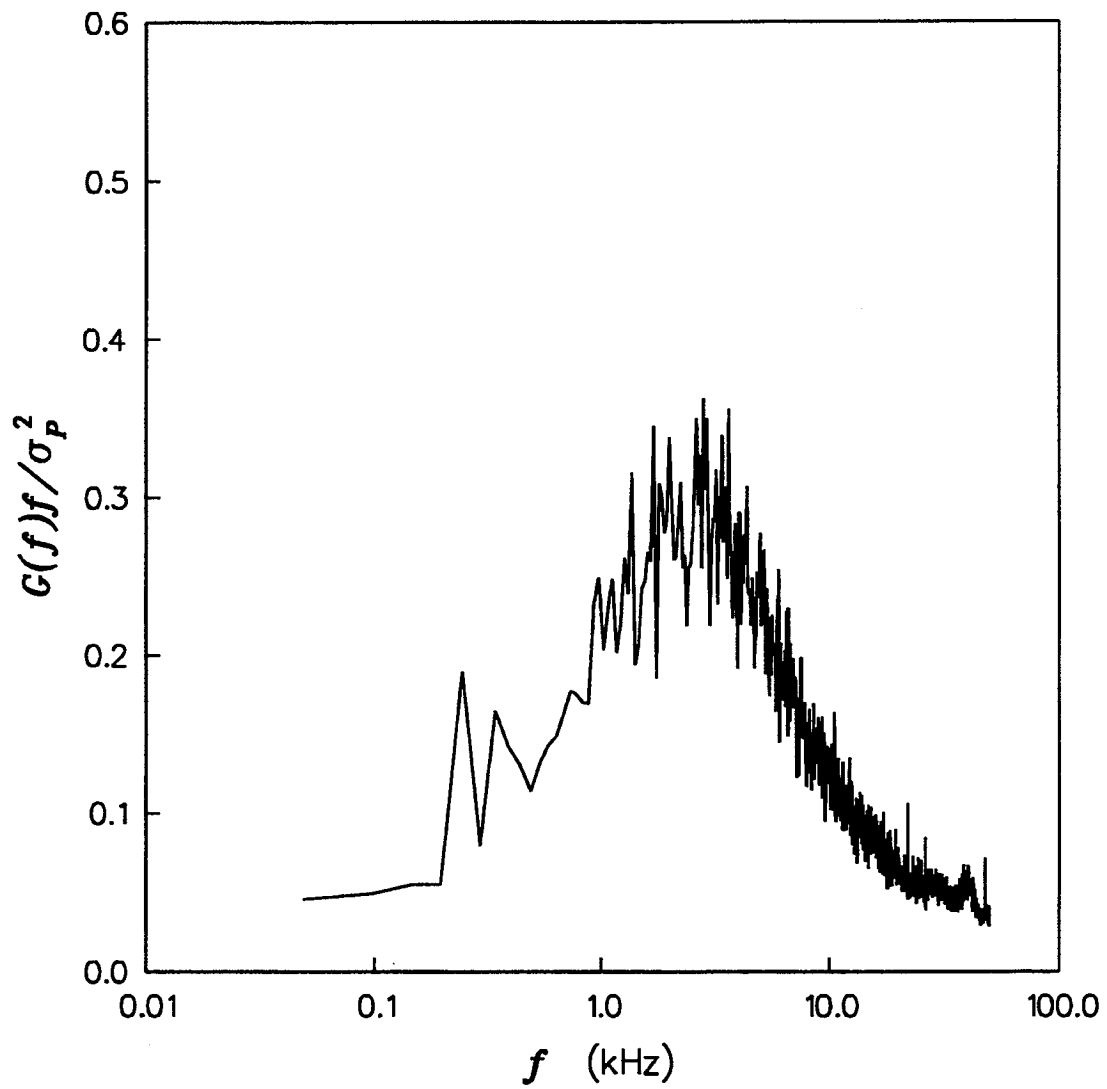
Figure 26   Mach 4.0 Incoming Boundary Layer Normalized Power
            Spectral Density
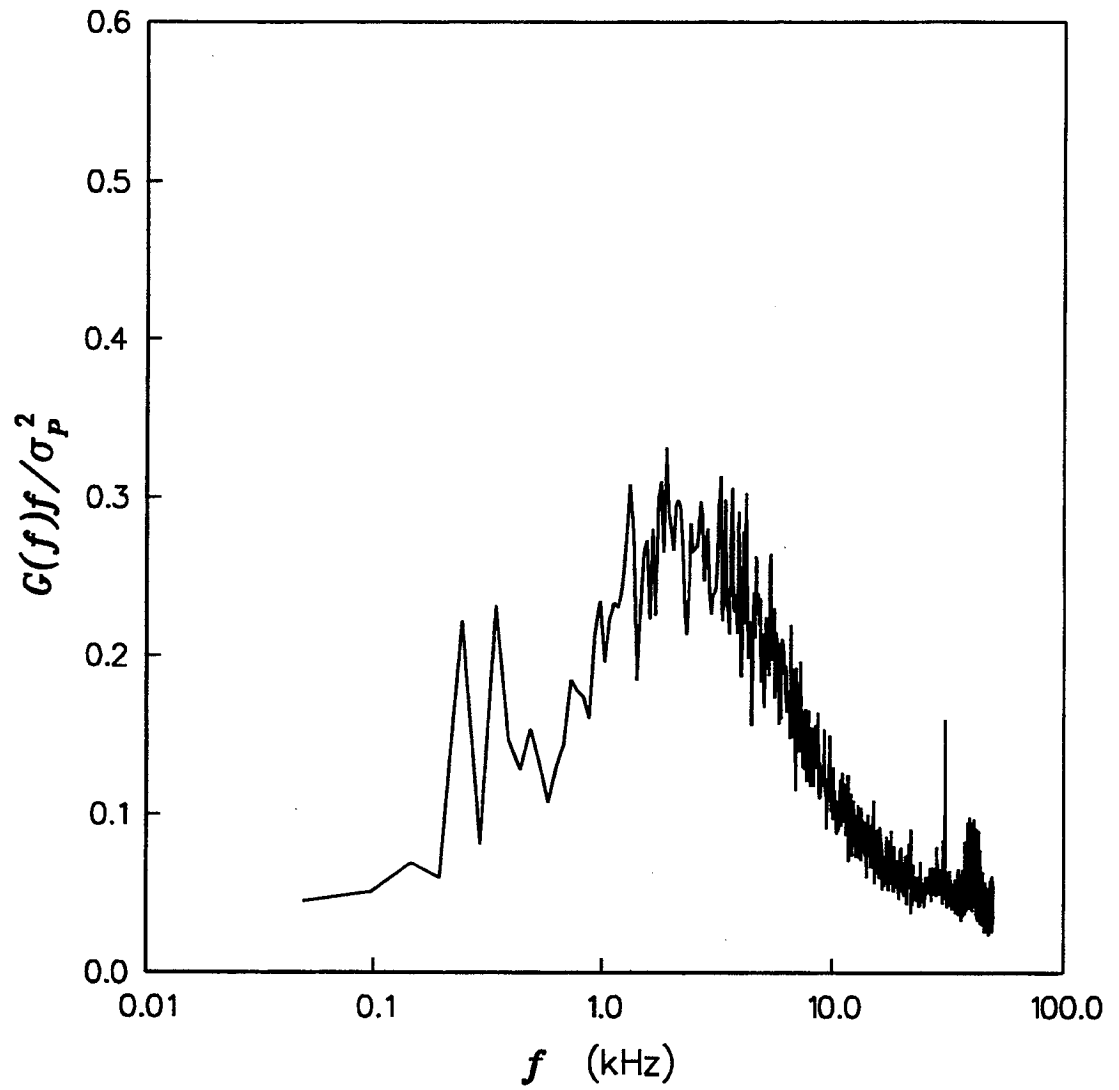
Figure 27   Mach 5.0 Incoming Boundary Layer Normalized Power
                   Spectral Density
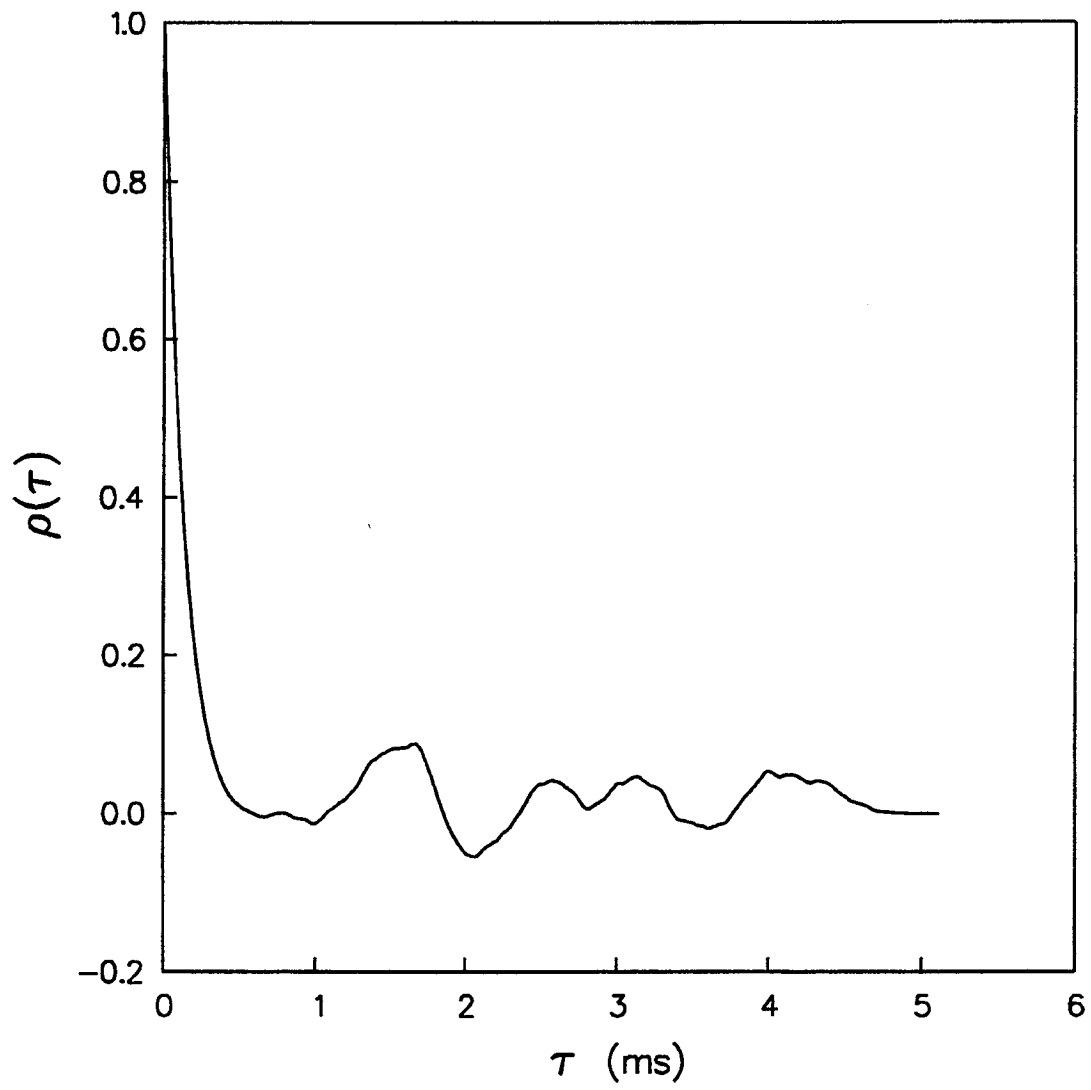
Figure 28   Mach 2.0 Incoming Boundary Layer Autocorrelation
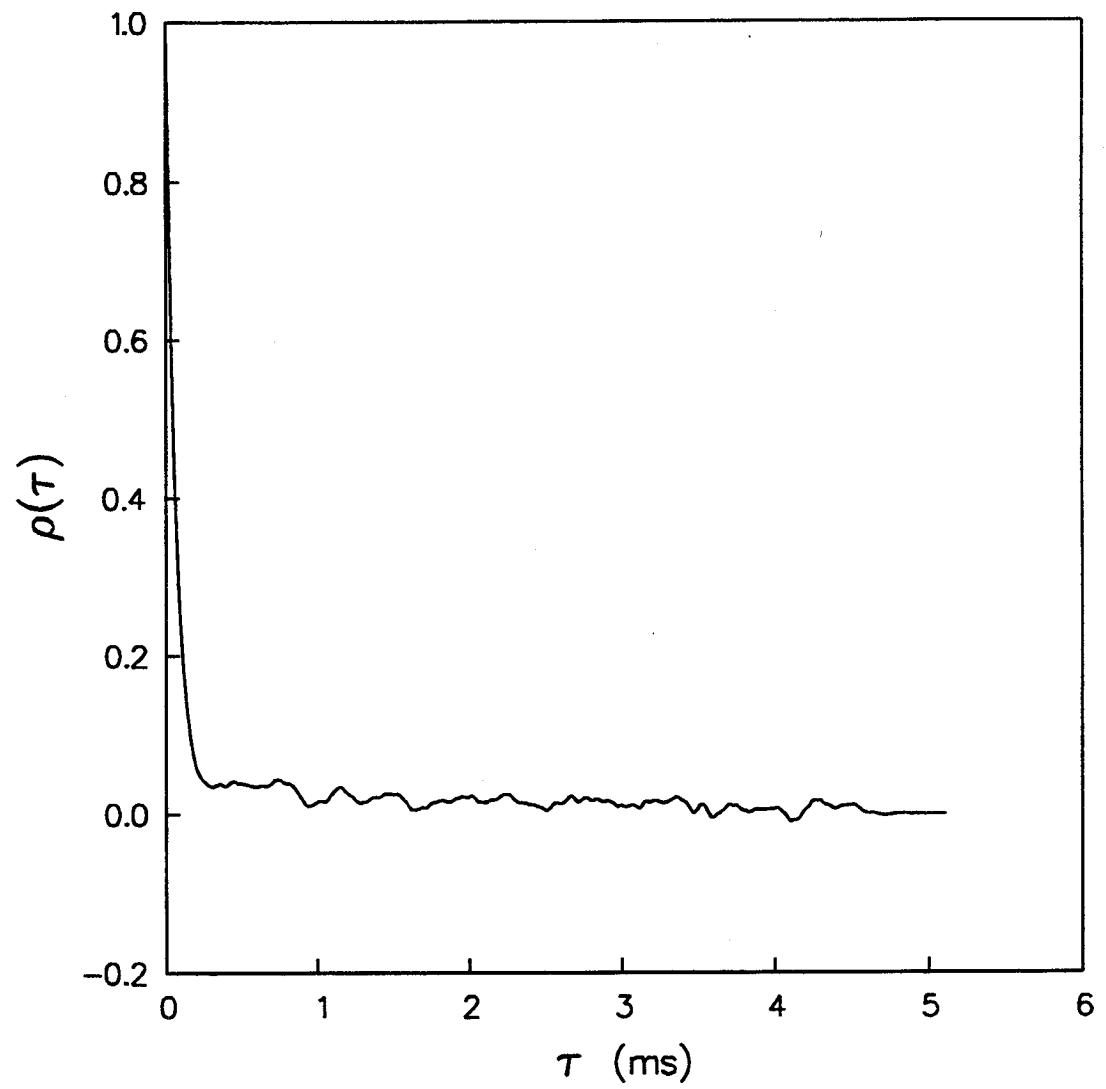
Figure 29   Mach 3.0 Incoming Boundary Layer Autocorrelation
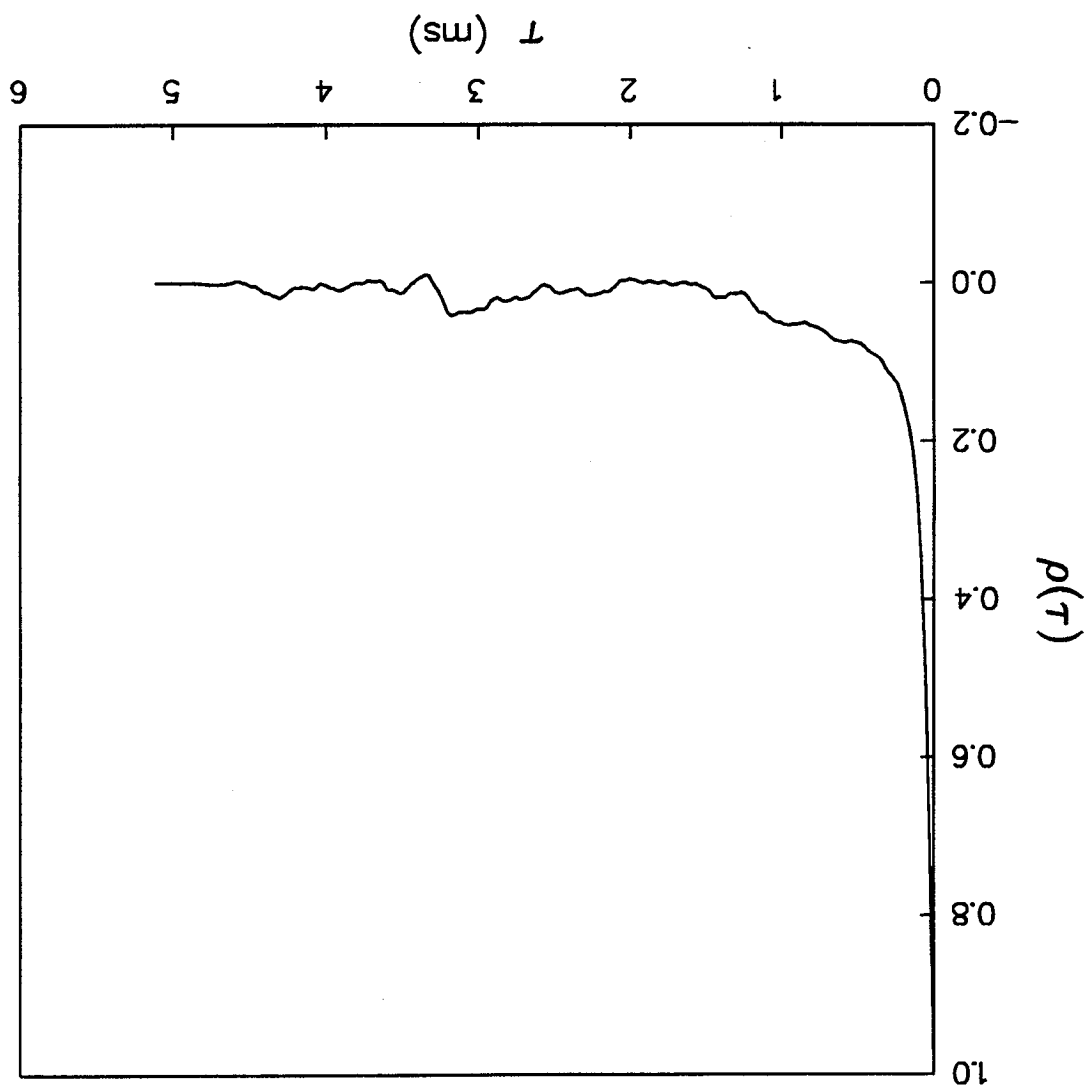
Figure 30   Mach 4.0 Incoming Boundary Layer Autocorrelation
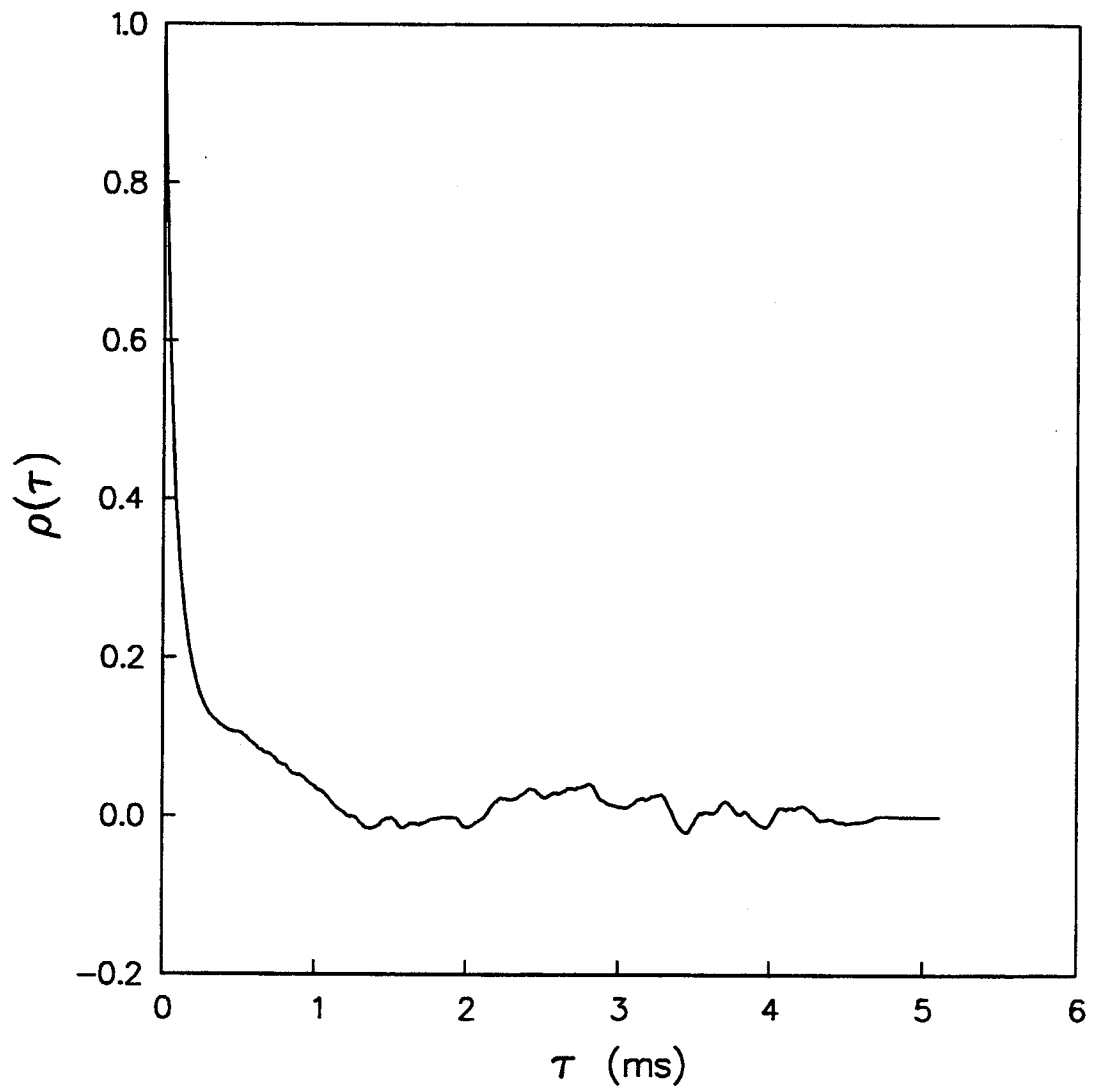
Figure 31   Mach 5.0 Incoming Boundary Layer Autocorrelation
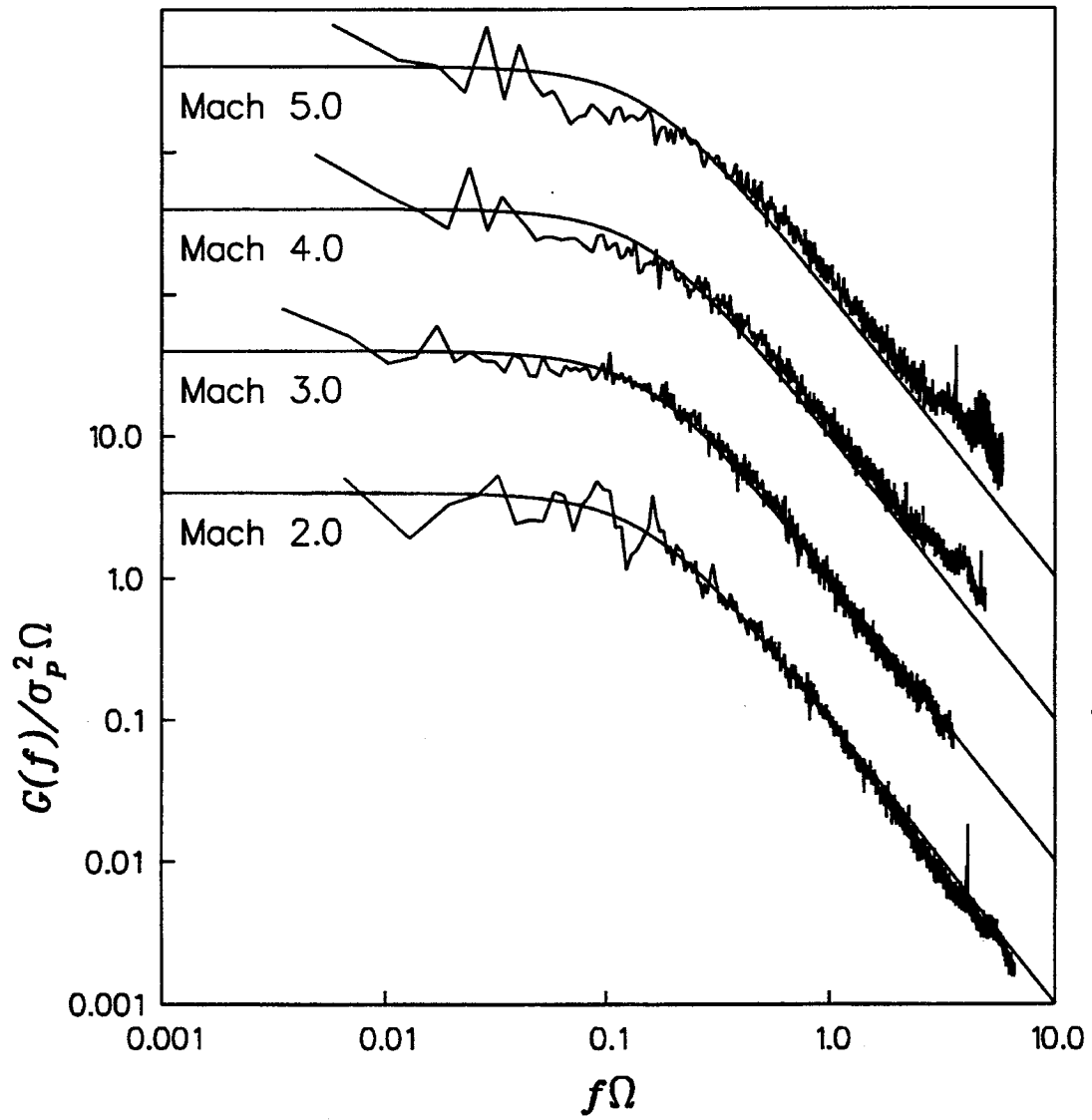
Figure 32   Comparison of Incoming Boundary Layer Power Spectral
                   Density Functions with Theory
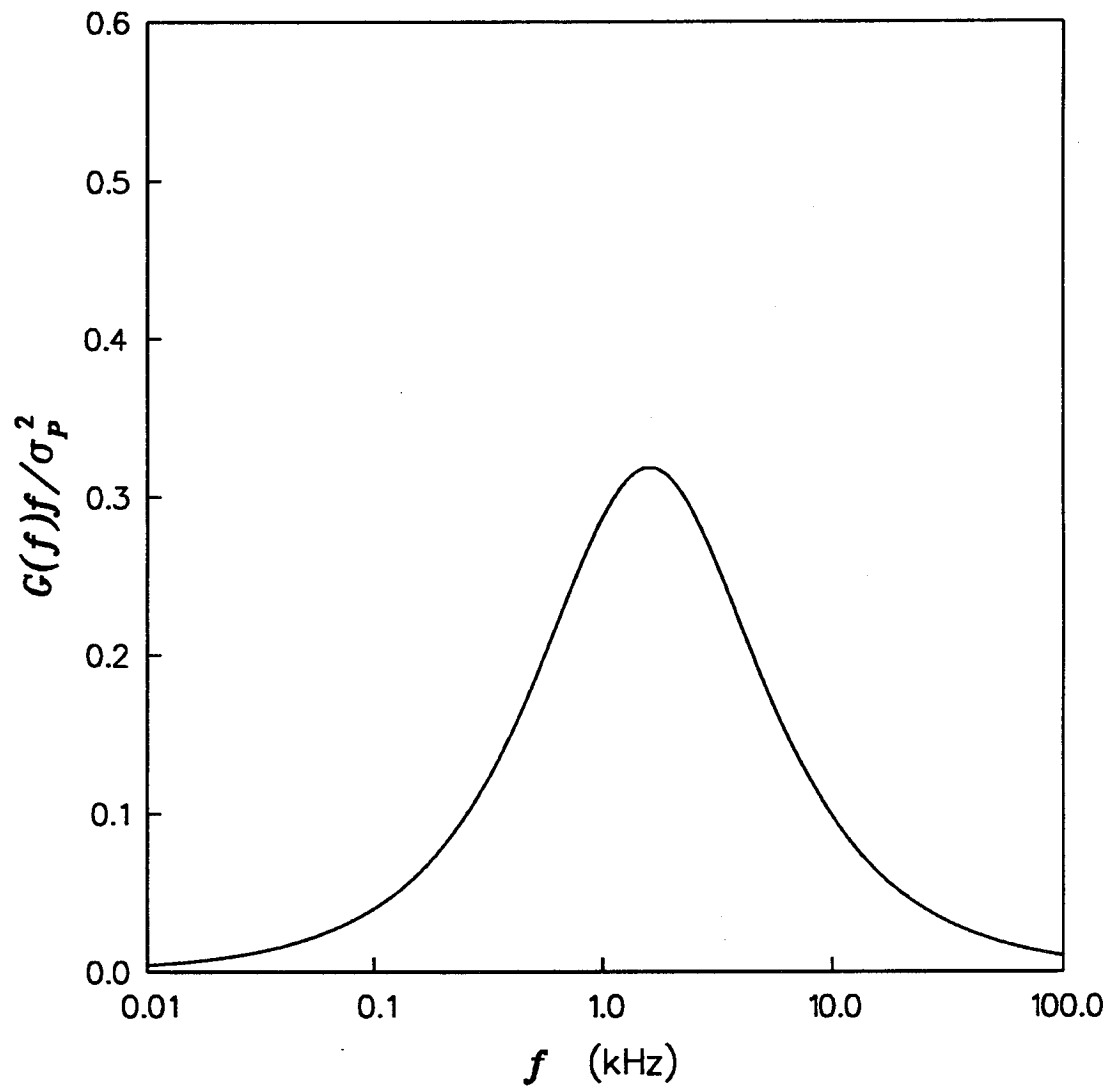
Figure 33   Theoretical Normalized Power Spectral Density Function for all Mach Numbers, $\Omega = 0.1$ ms
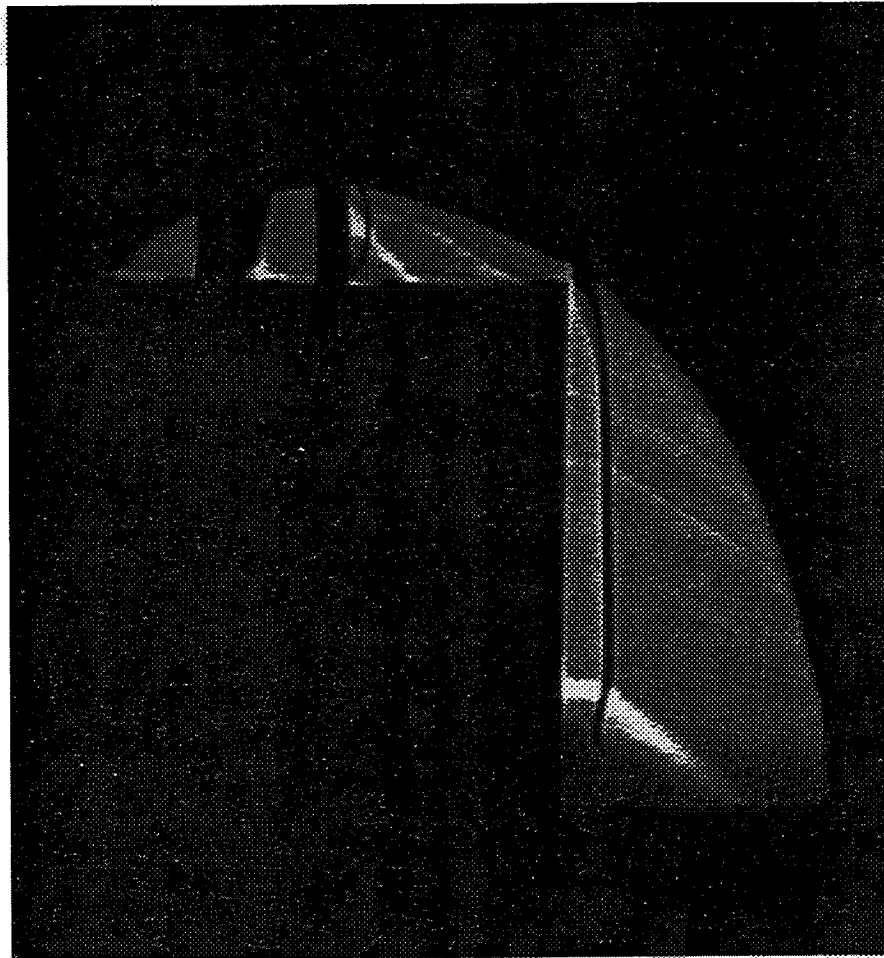
Figure 34   Mach 2.0 Interaction Schlieren Photograph
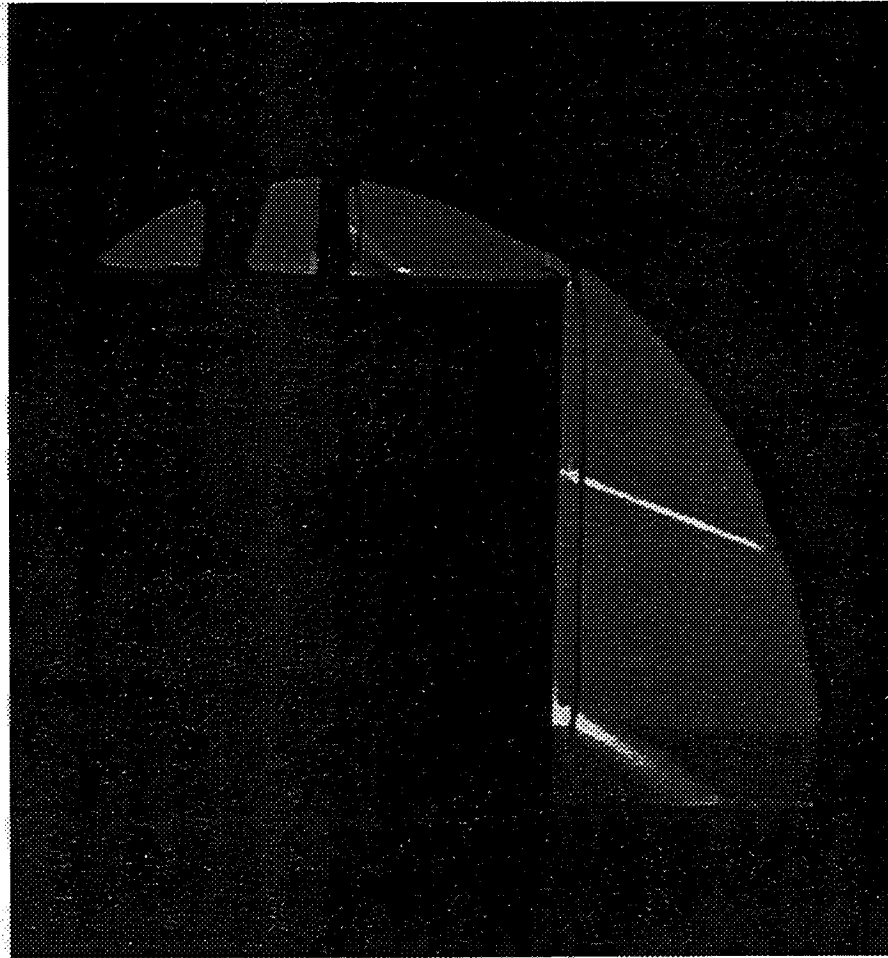
Figure 35   Mach 3.0 Interaction Schlieren Photograph
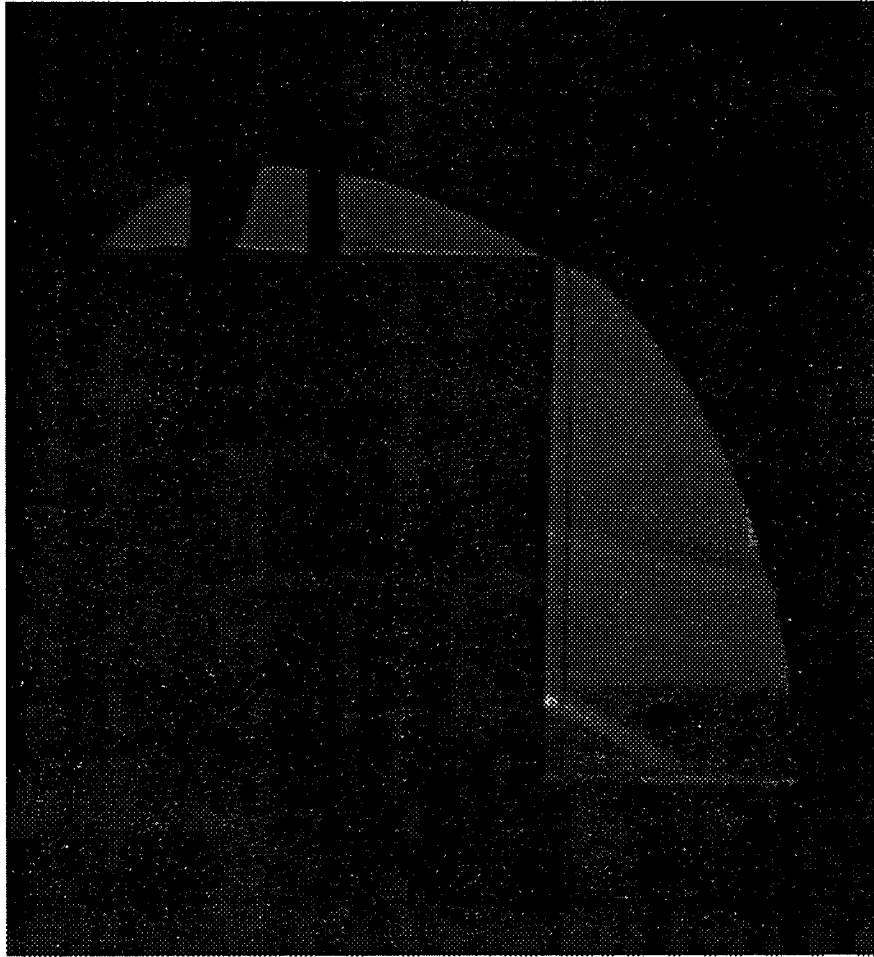
Figure 36   Mach 4.0 Interaction Schlieren Photograph
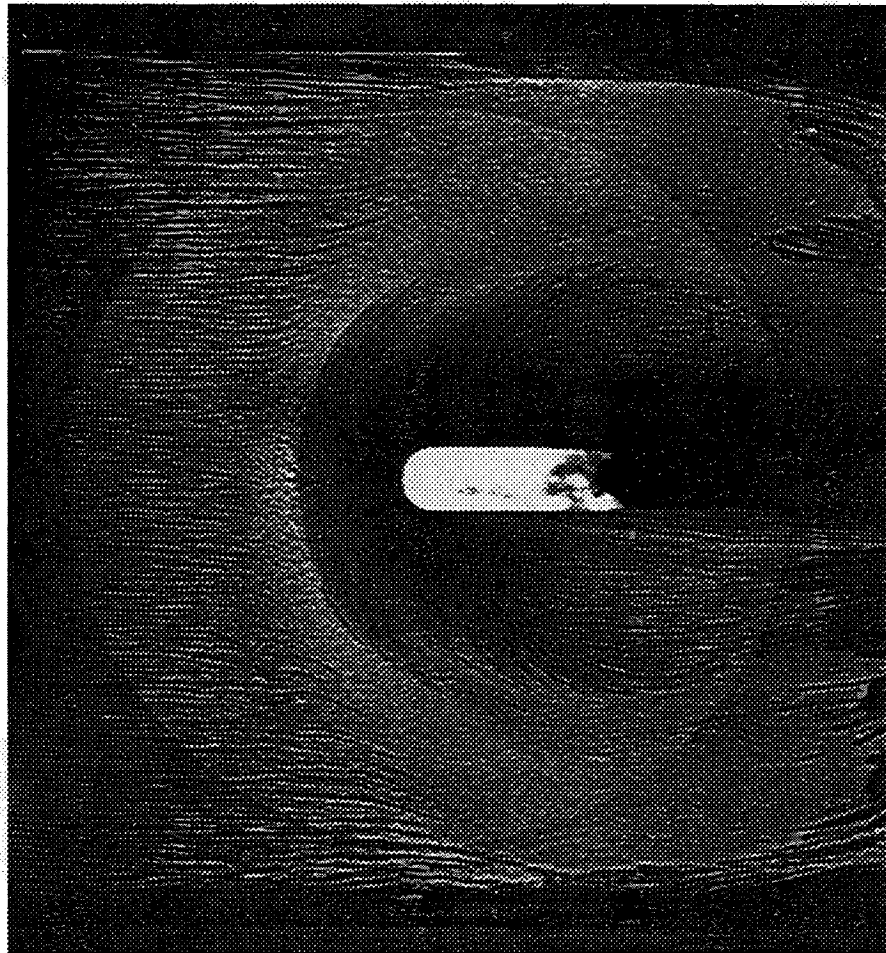
Figure 37   Mach 2.0 Interaction Surface Flow Visualization
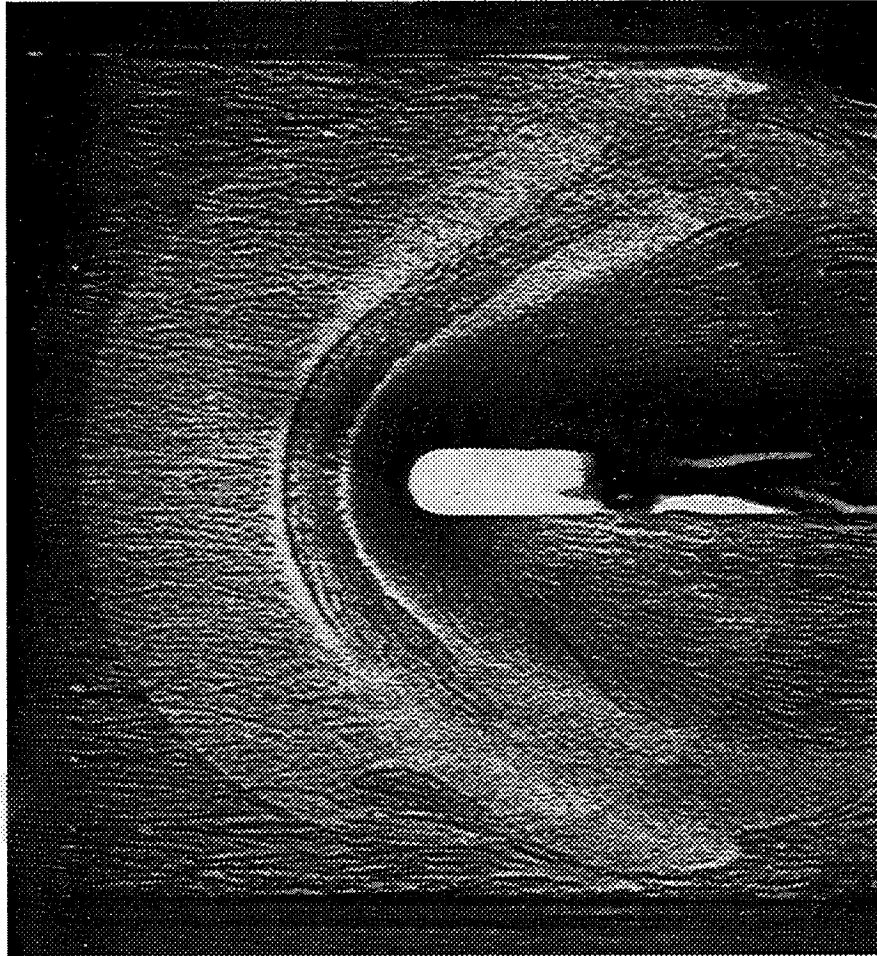
Figure 38   Mach 3.0 Interaction Surface Flow Visualization
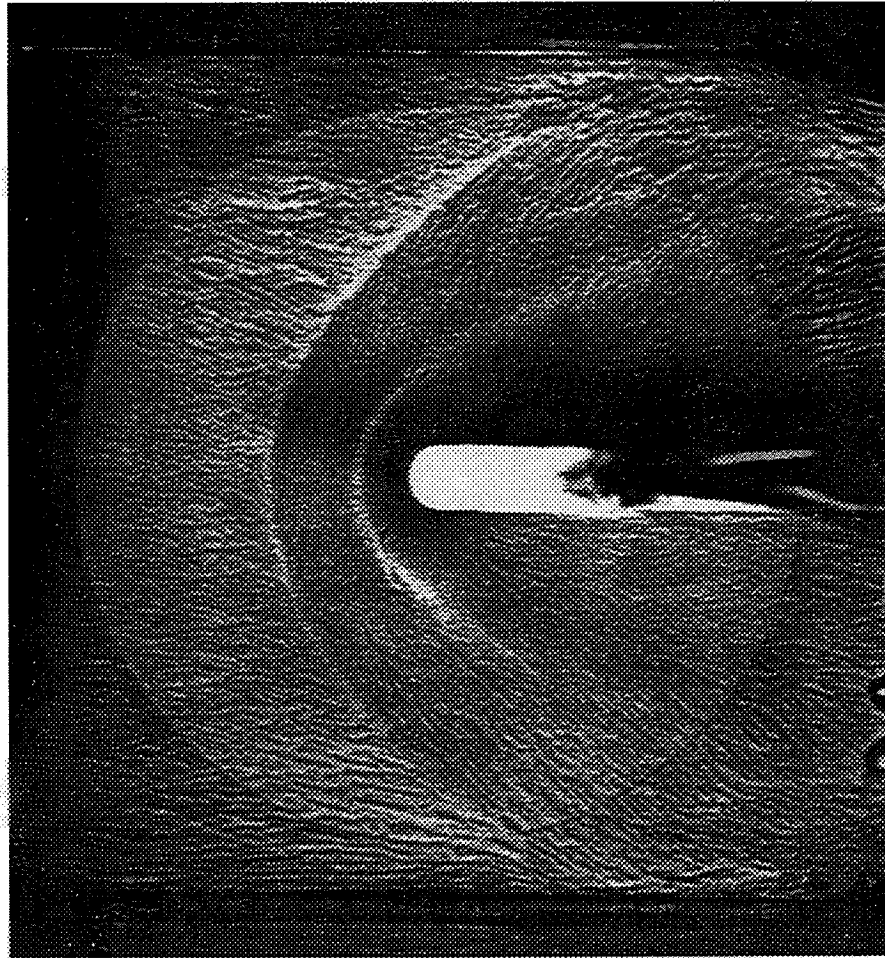
Figure 39   Mach 4.0 Interaction Surface Flow Visualization
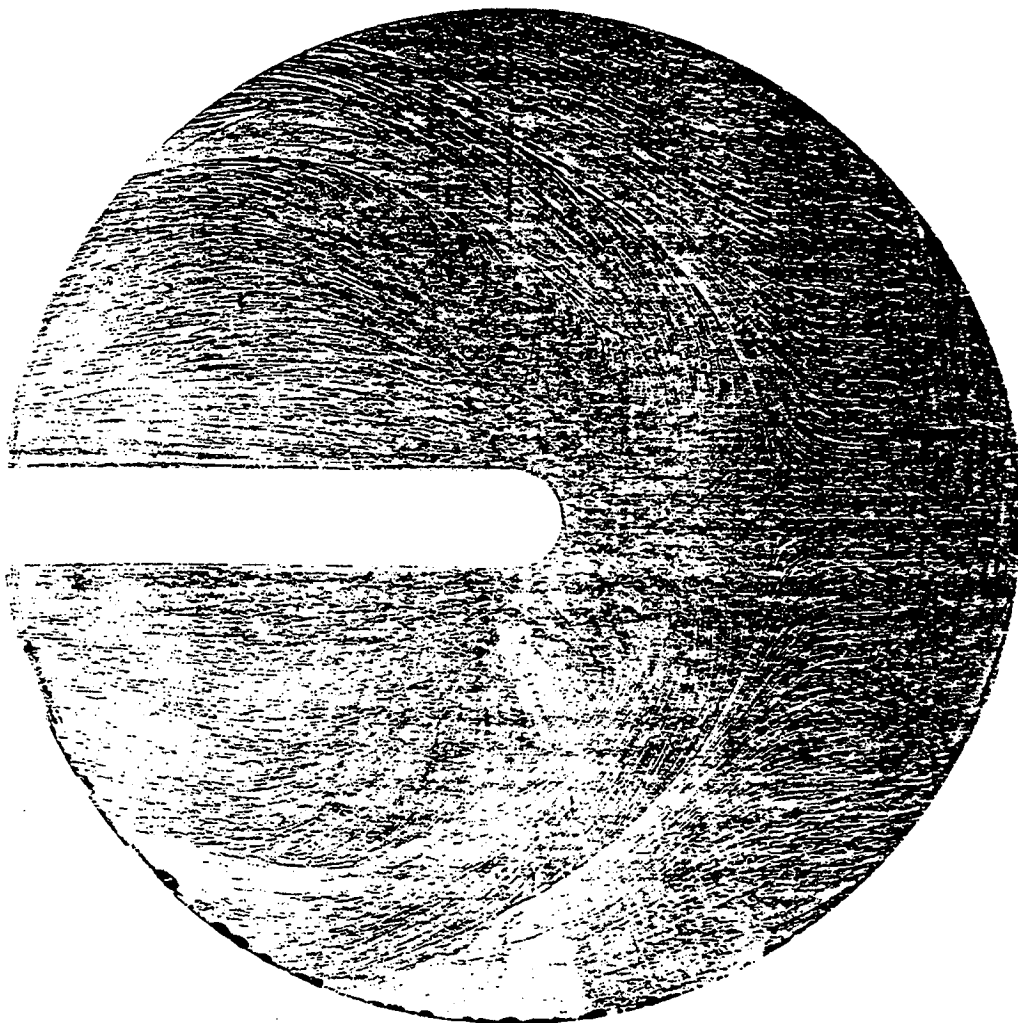
Figure 40   Mach 2.0 Interaction Surface Wall Shear Trace
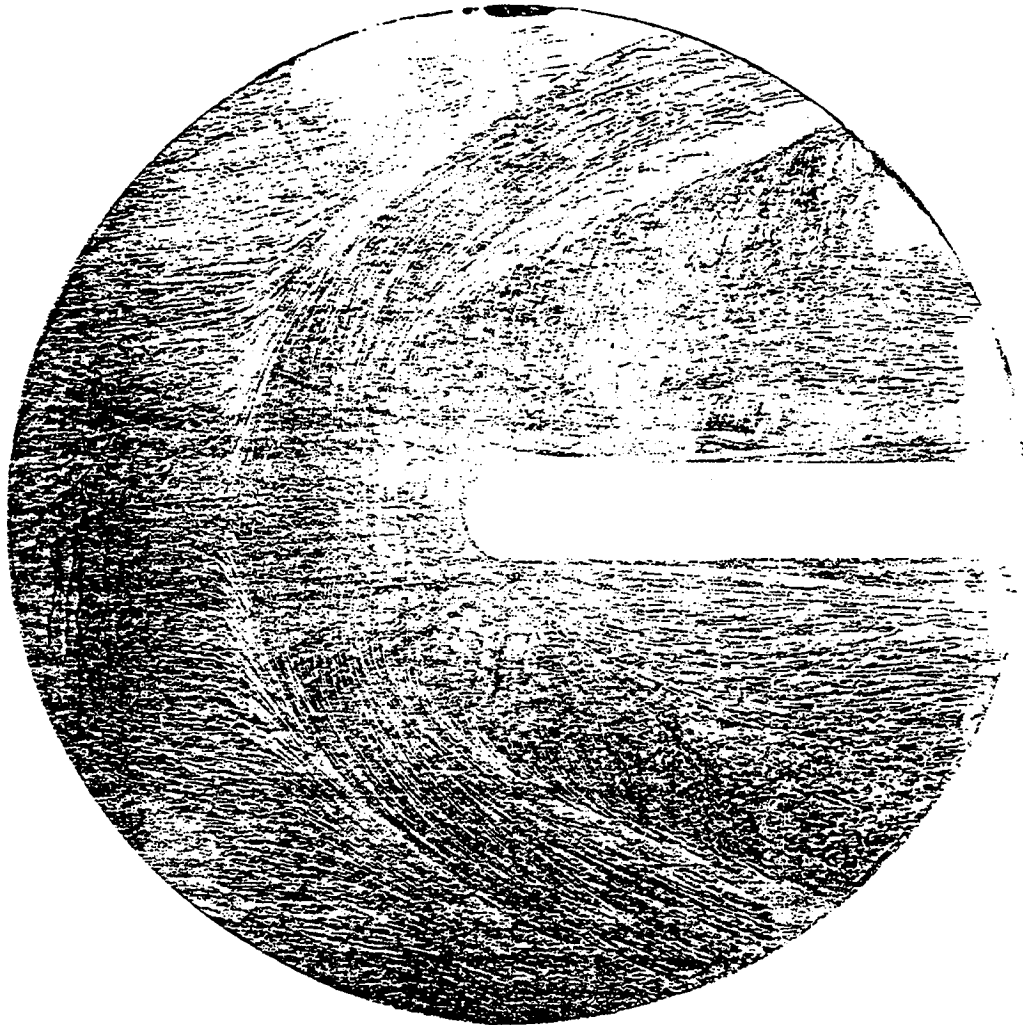
Figure 41   Mach 3.0 Interaction Surface Wall Shear Trace
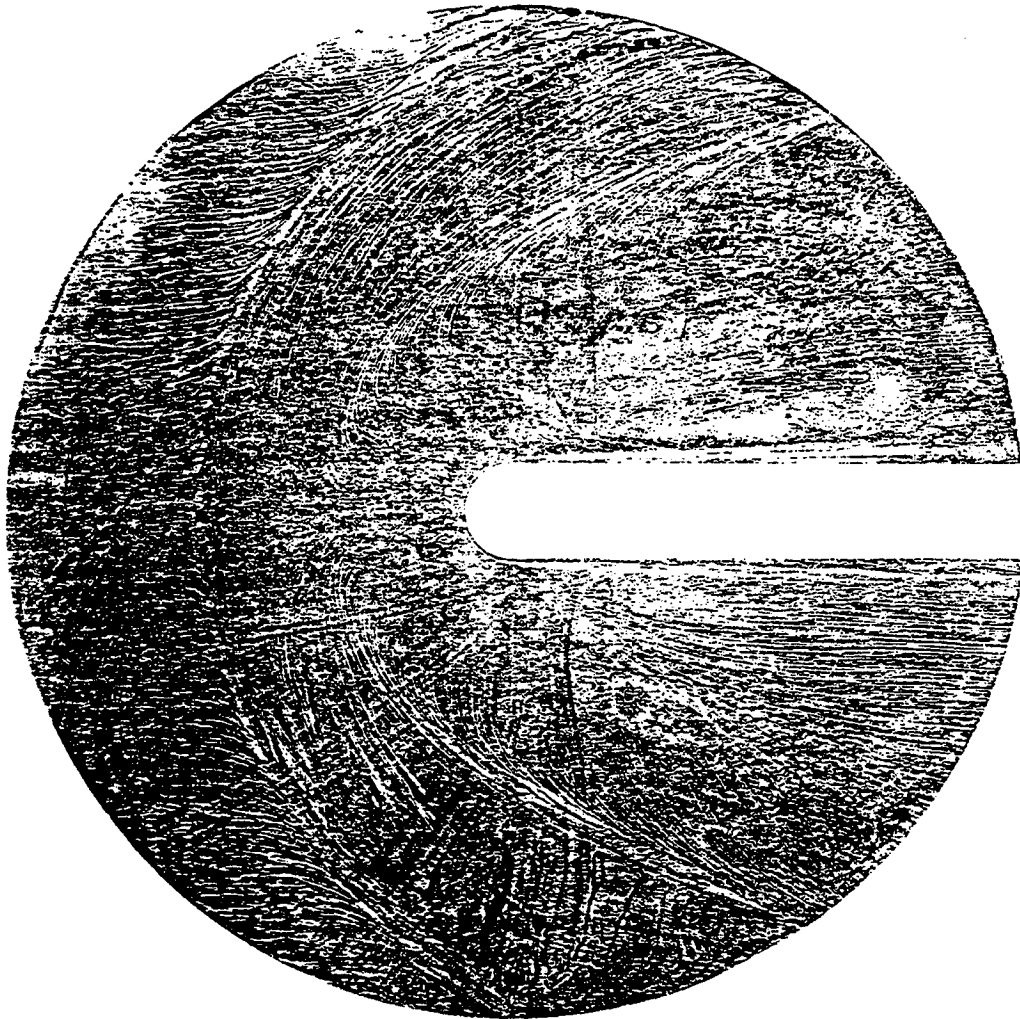
Figure 42   Mach 4.0 Interaction Surface Wall Shear Trace
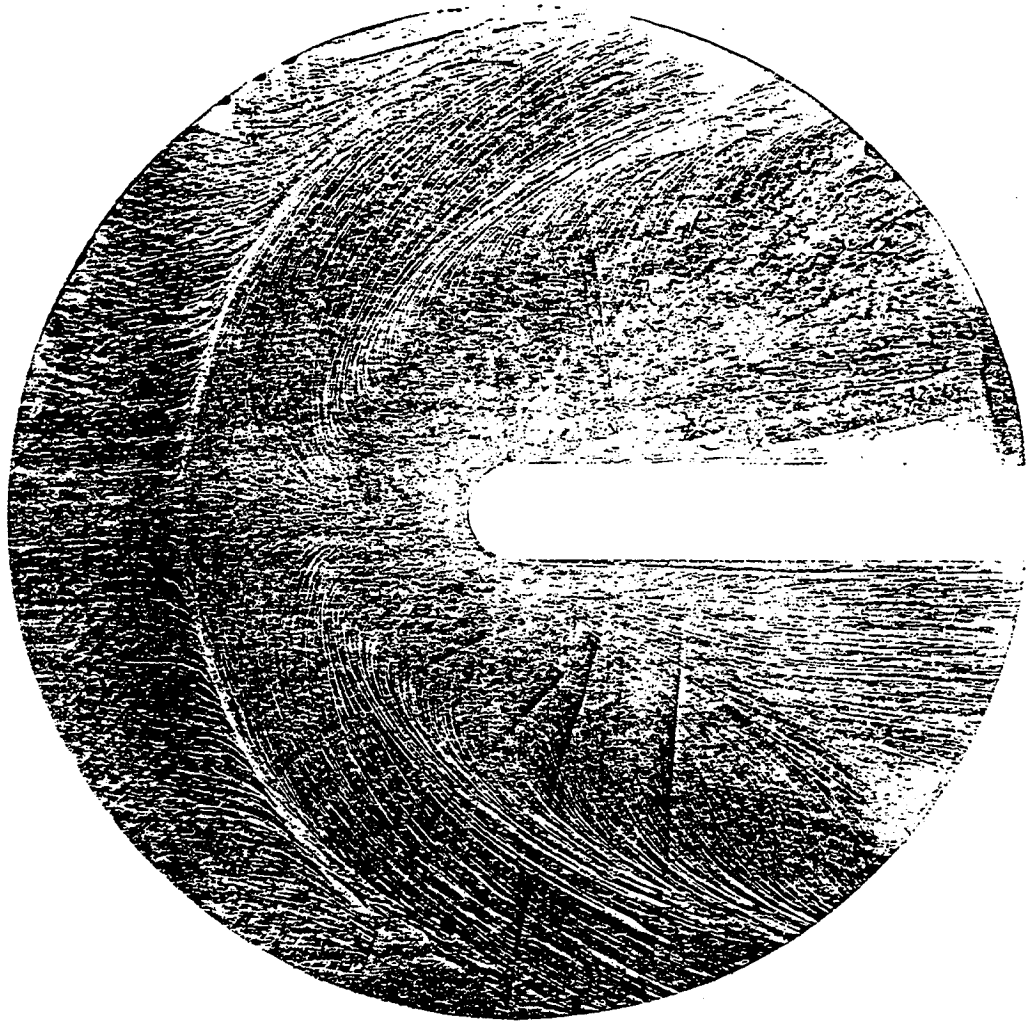
Figure 43   Mach 5.0 Interaction Surface Wall Shear Trace
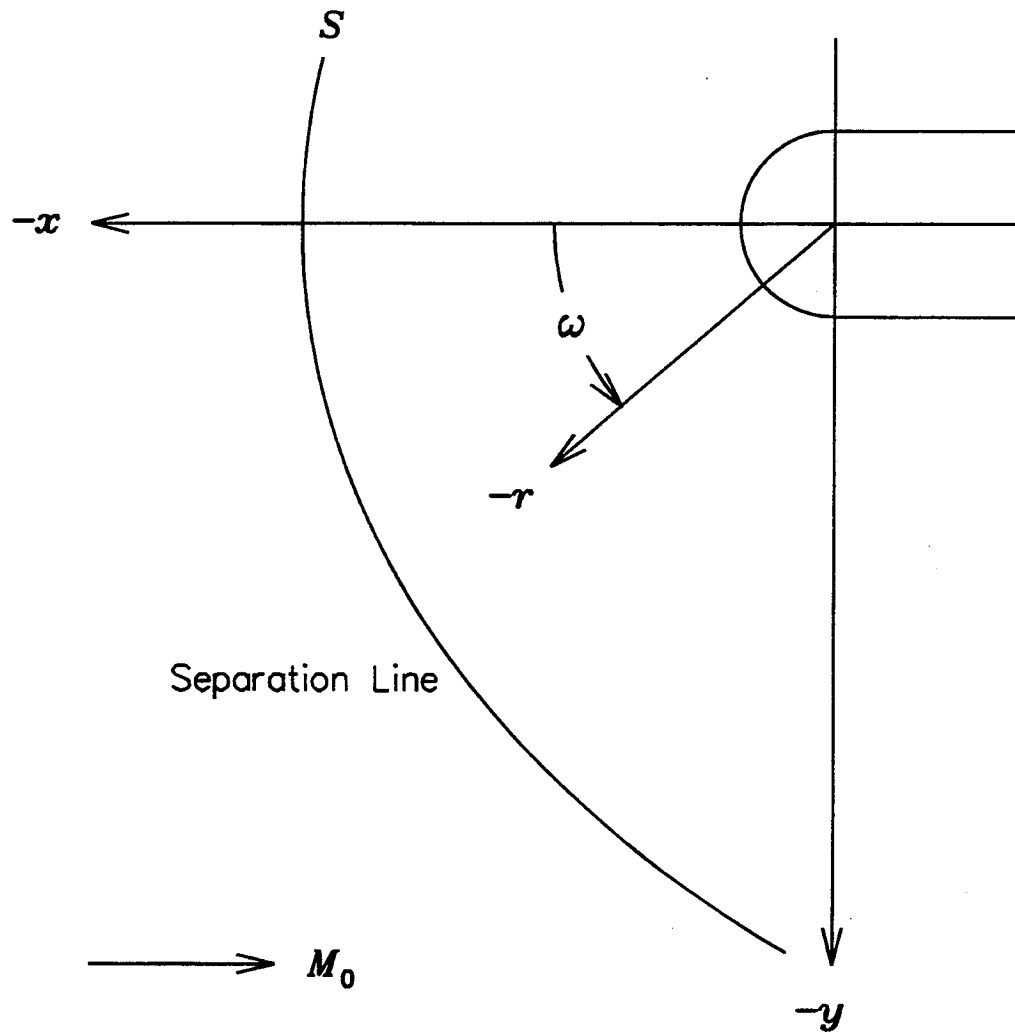
Figure 44   Interaction Region Polar Coordinate System
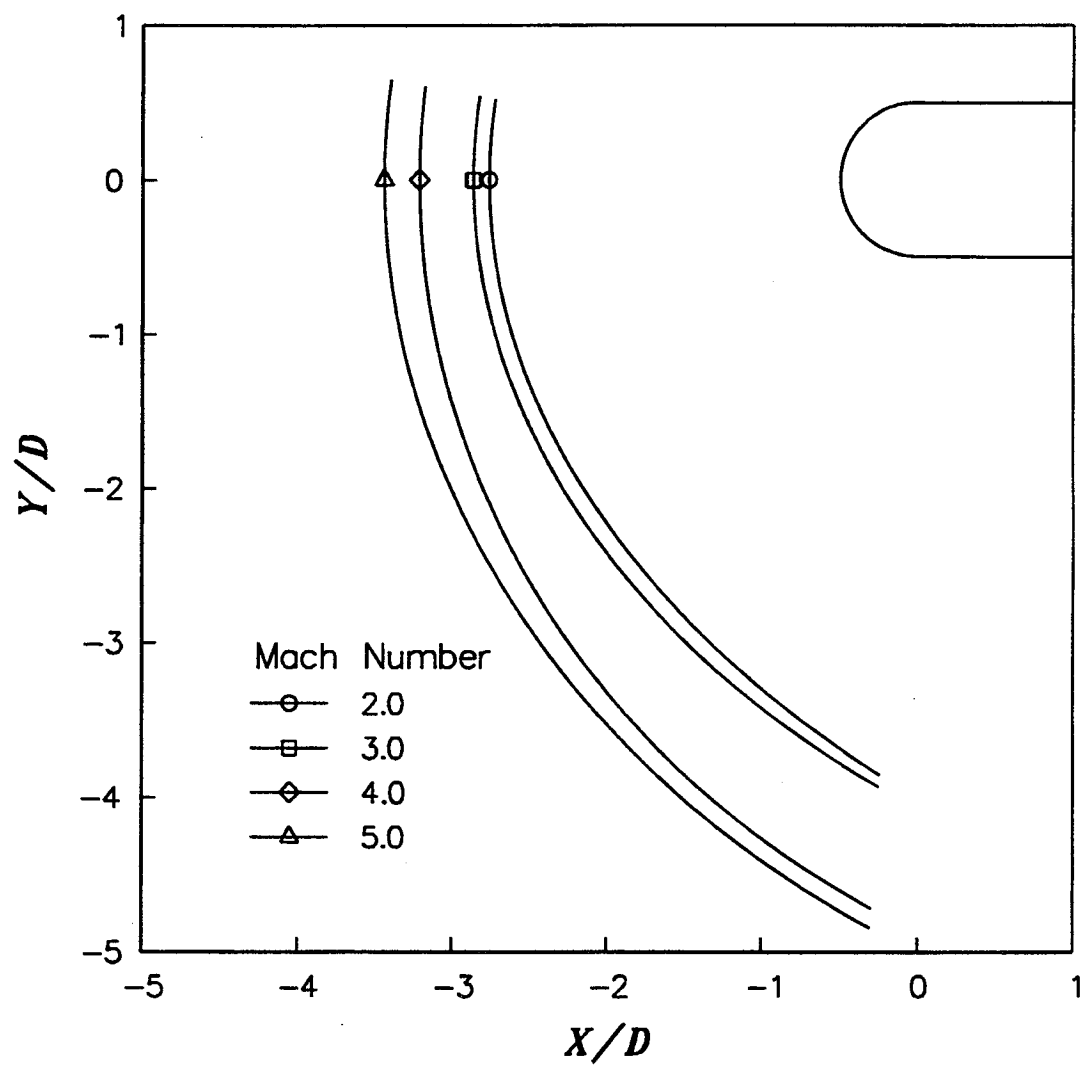
Figure 45   Separation Line Curve Fits
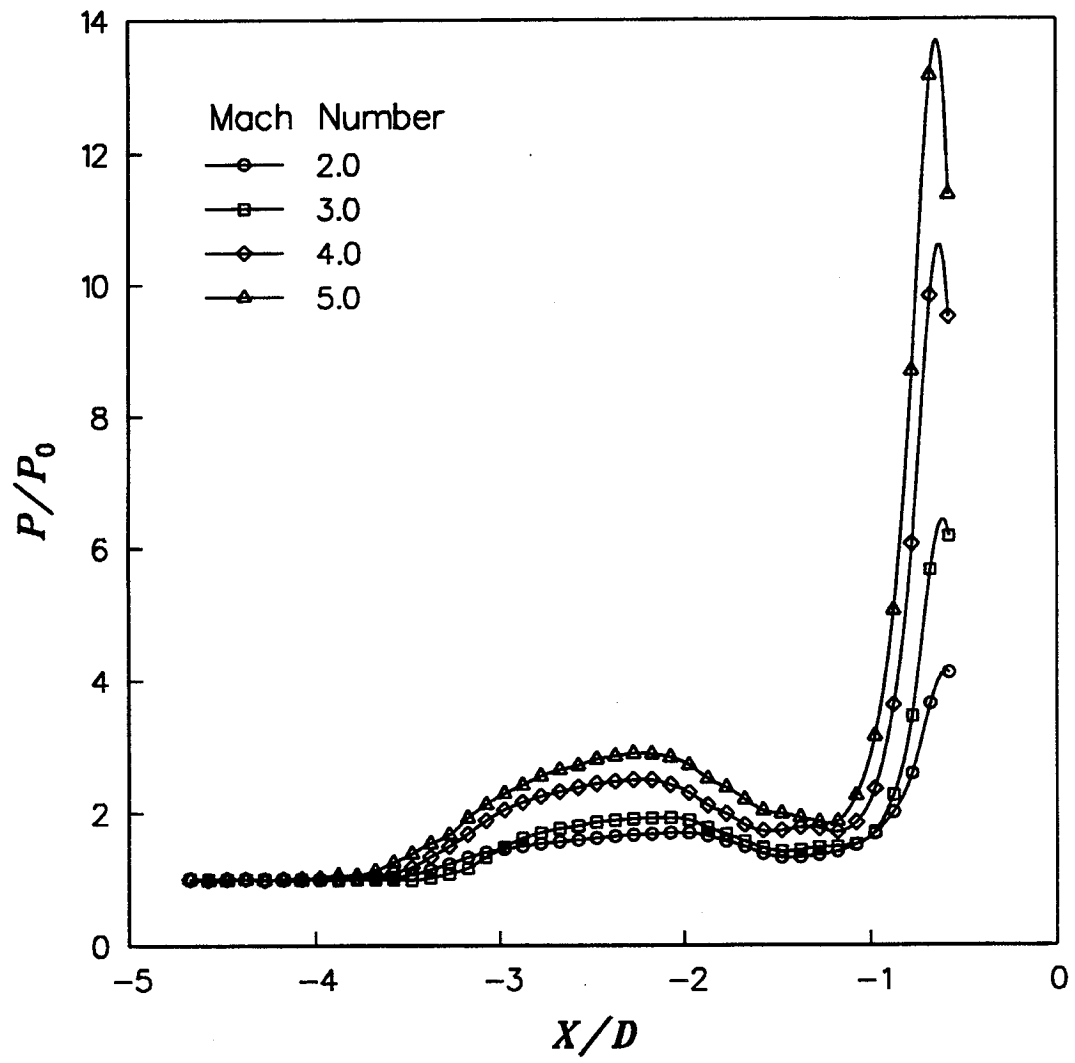
Figure 46   Centerline Static Pressures
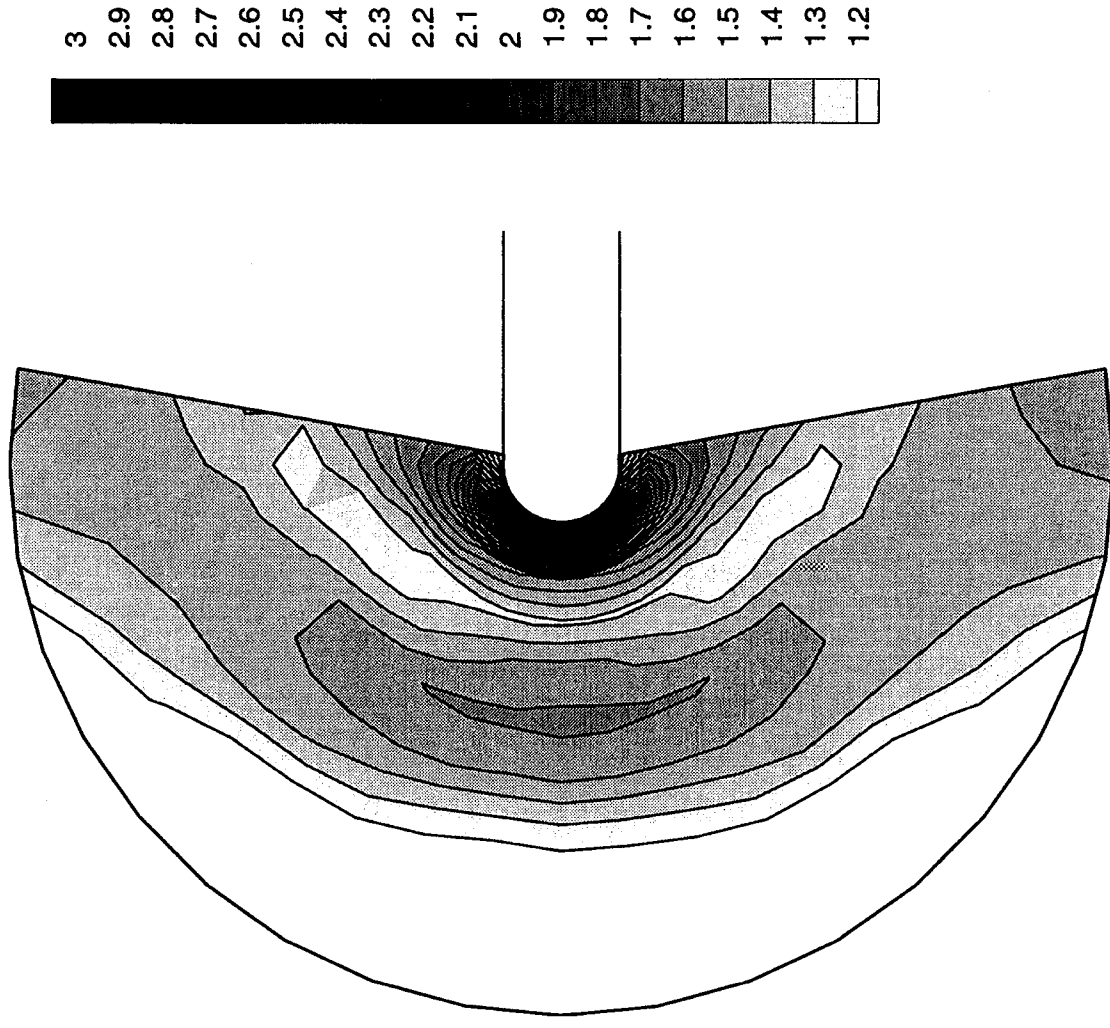
Figure 47   Mach 2.0 Static Pressure Countours P/P_0

164

3
2.9
2.8
2.7
2.6
2.5
2.4
2.3
2.2
2.1
2
1.9
1.8
1.7
1.6
1.5
1.4
1.3
1.2

165
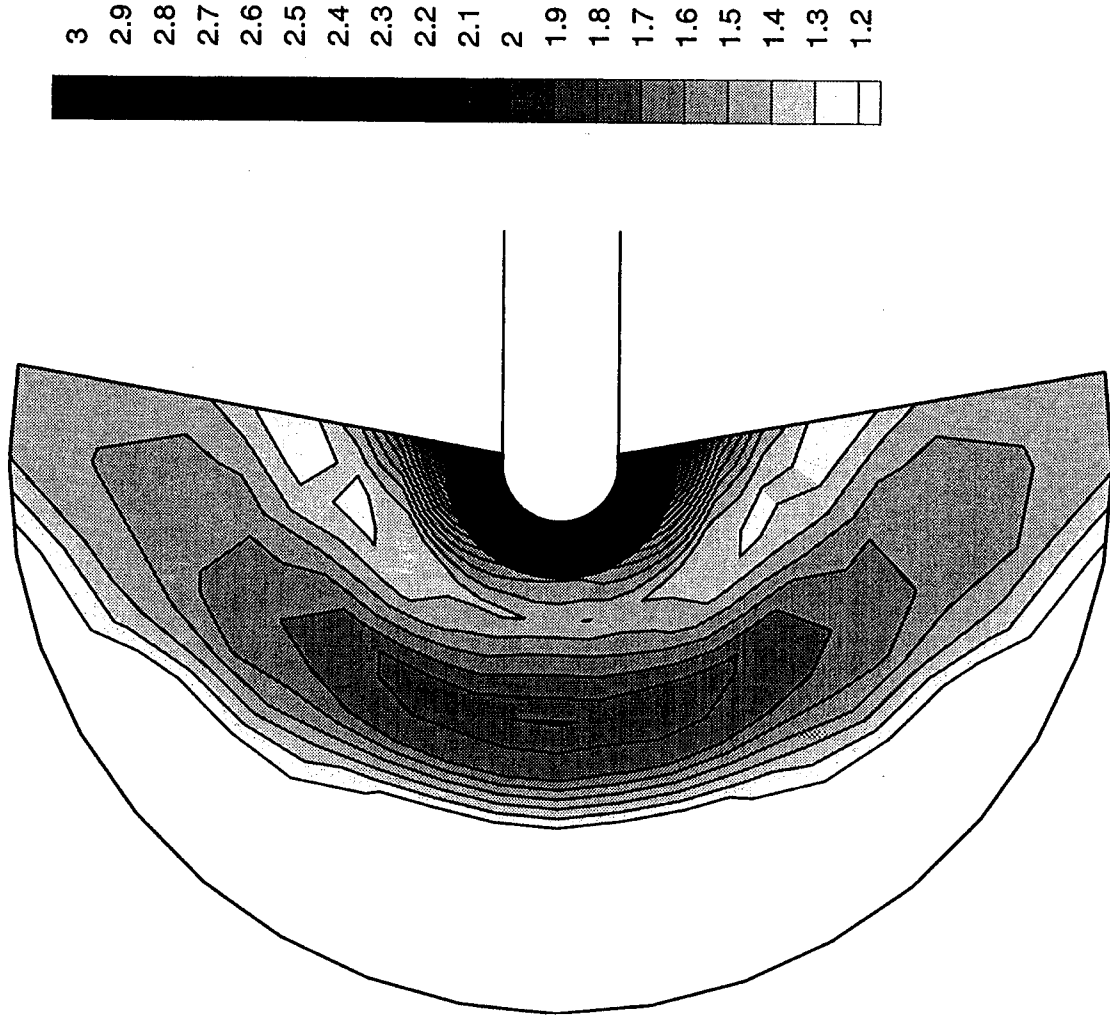
Figure 48   Mach 3.0 Static Pressure Countours P/P_0

166

3
2.9
2.8
2.7
2.6
2.5
2.4
2.3
2.2
2.1
2
1.9
1.8
1.7
1.6
1.5
1.4
1.3
1.2
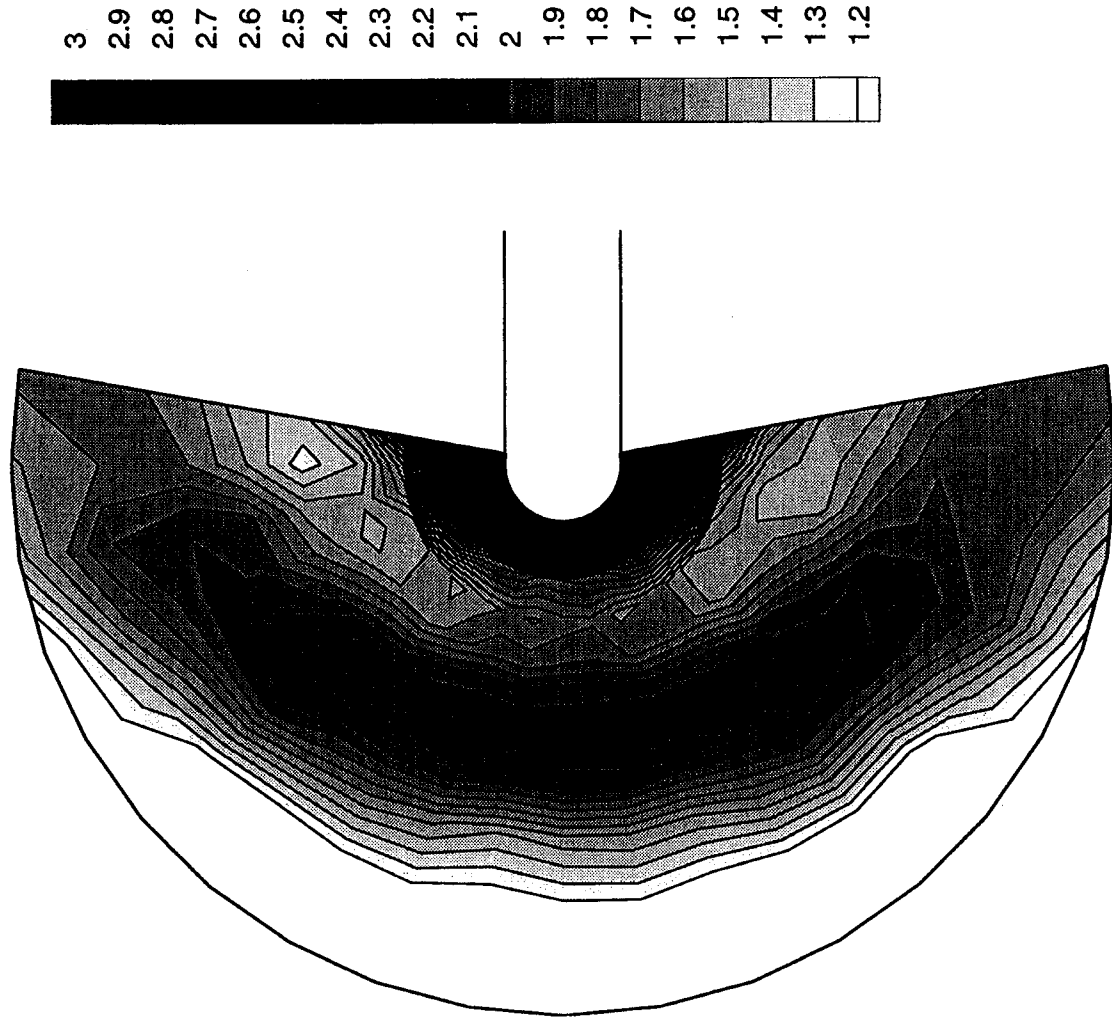
Figure 49   Mach 4.0 Static Pressure Countours P/P_0

167
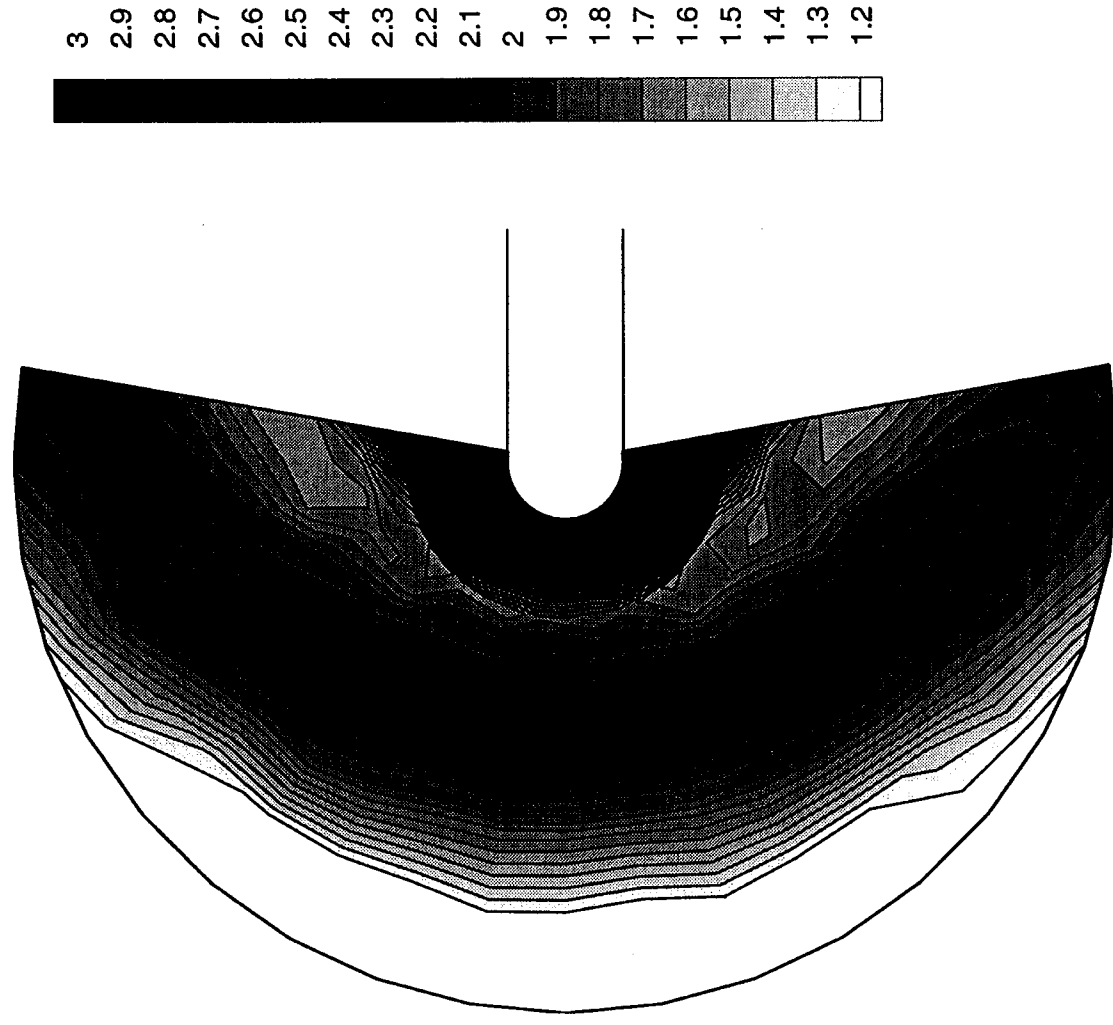
Mach 5.0 Static Pressure Countours P/P_0
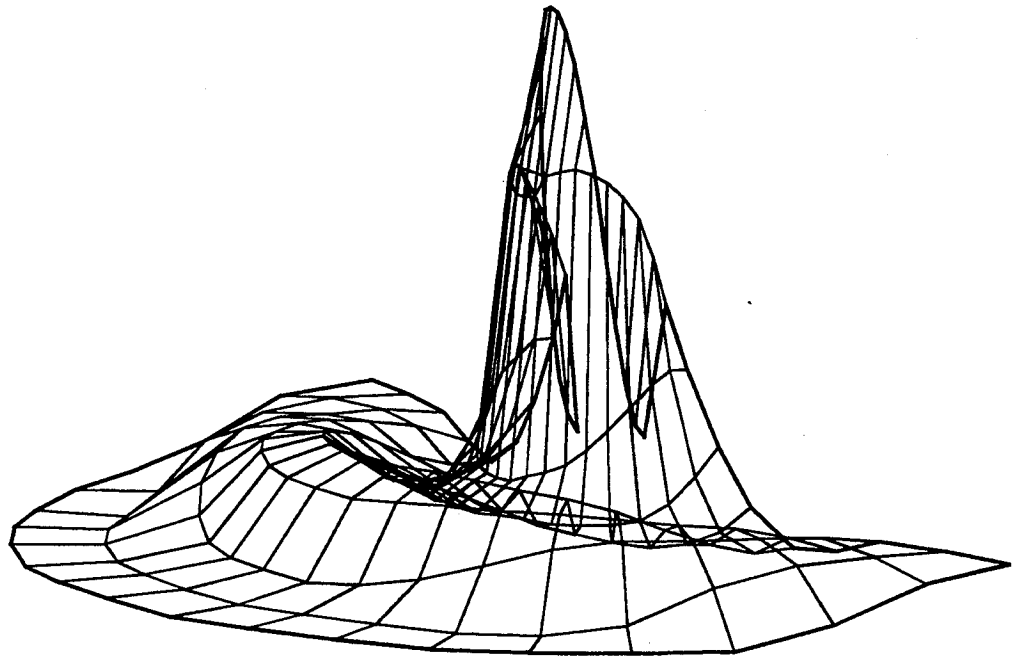
Figure 50

Figure 51   Mach 3.0 Static Pressure Mesh Plot
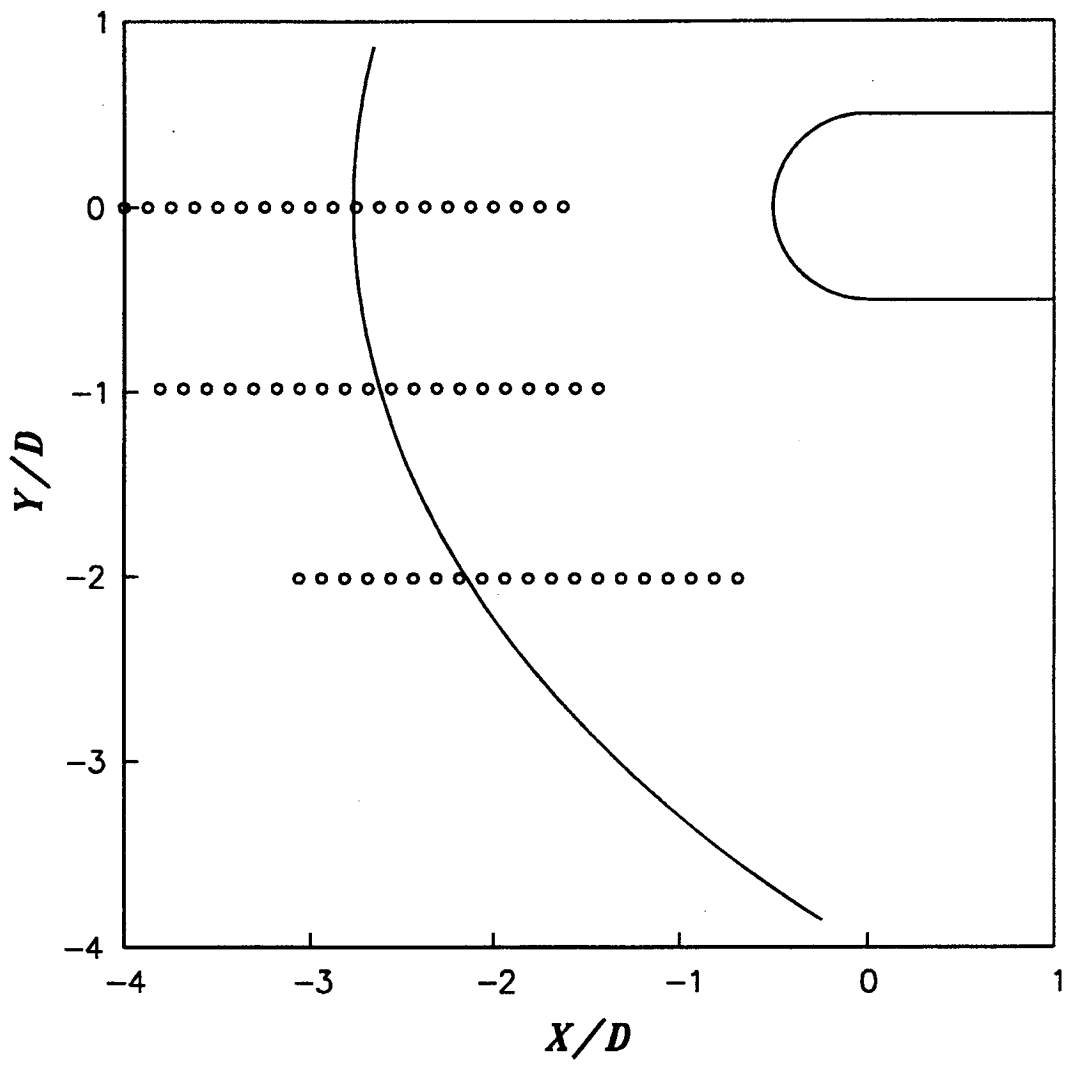
Figure 52   Mach 2.0 Dynamic Pressure Transducer Measurement
                   Locations
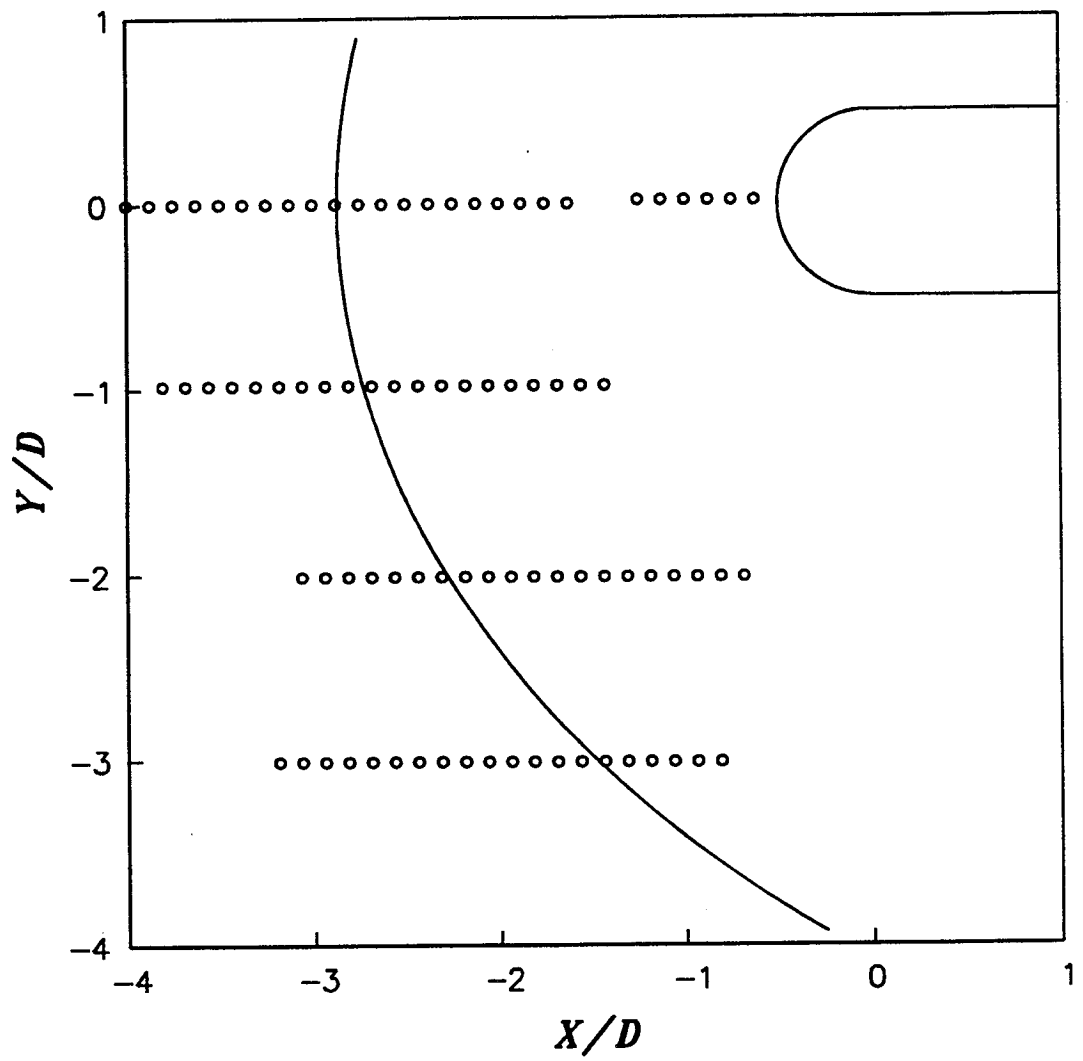
Figure 53   Mach 3.0 Dynamic Pressure Transducer Measurement
                   Locations
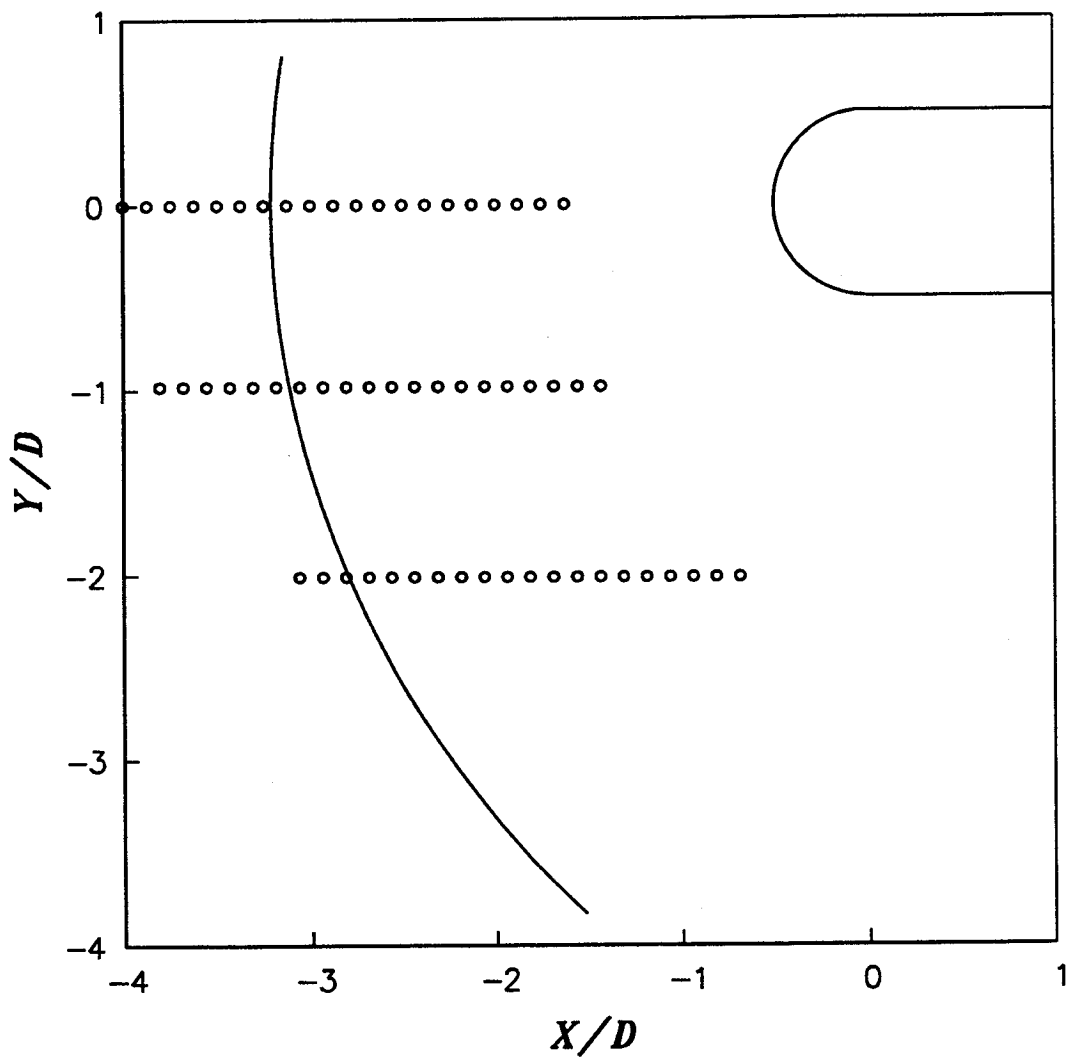
Figure 54   Mach 4.0 Dynamic Pressure Transducer Measurement
                   Locations
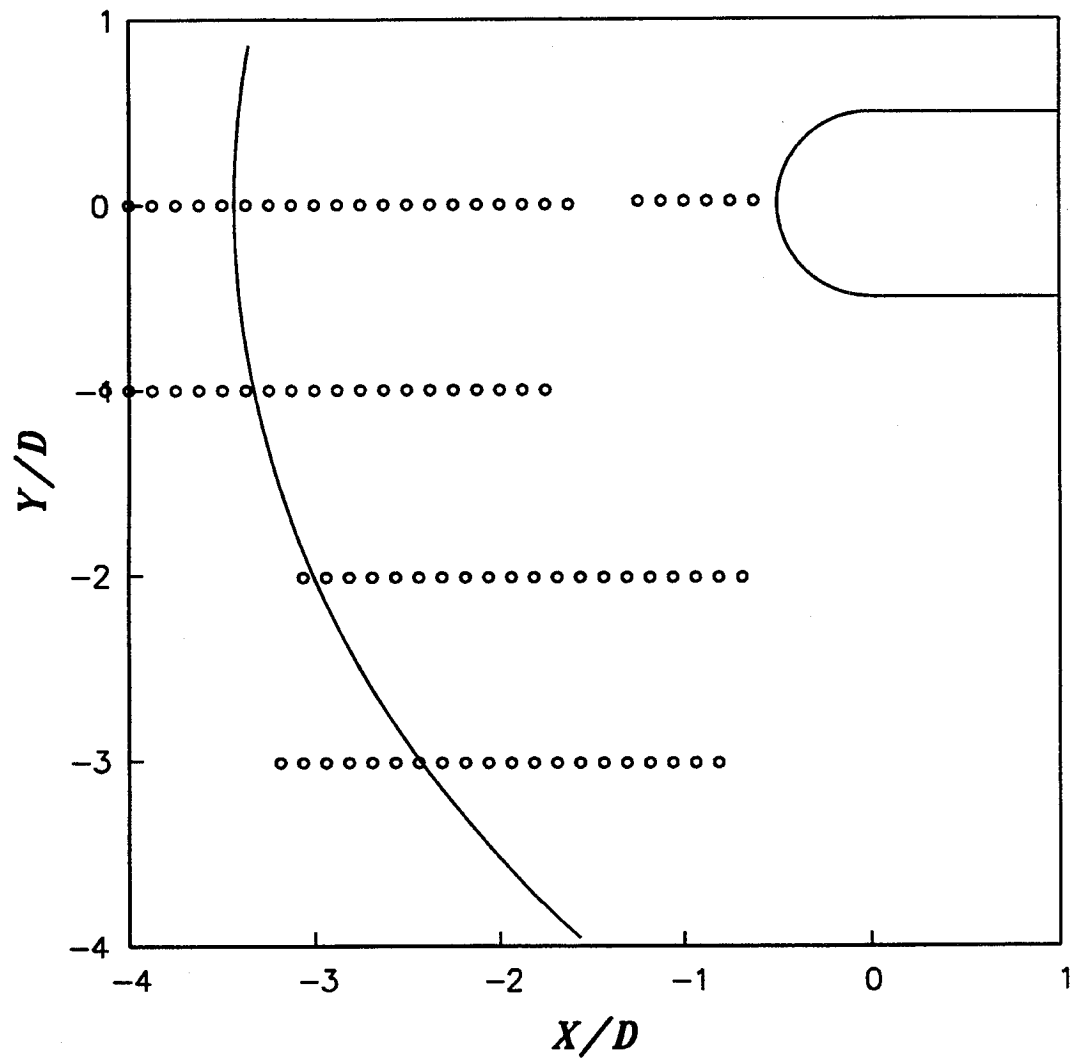
Figure 55   Mach 5.0 Dynamic Pressure Transducer Measurement
                   Locations
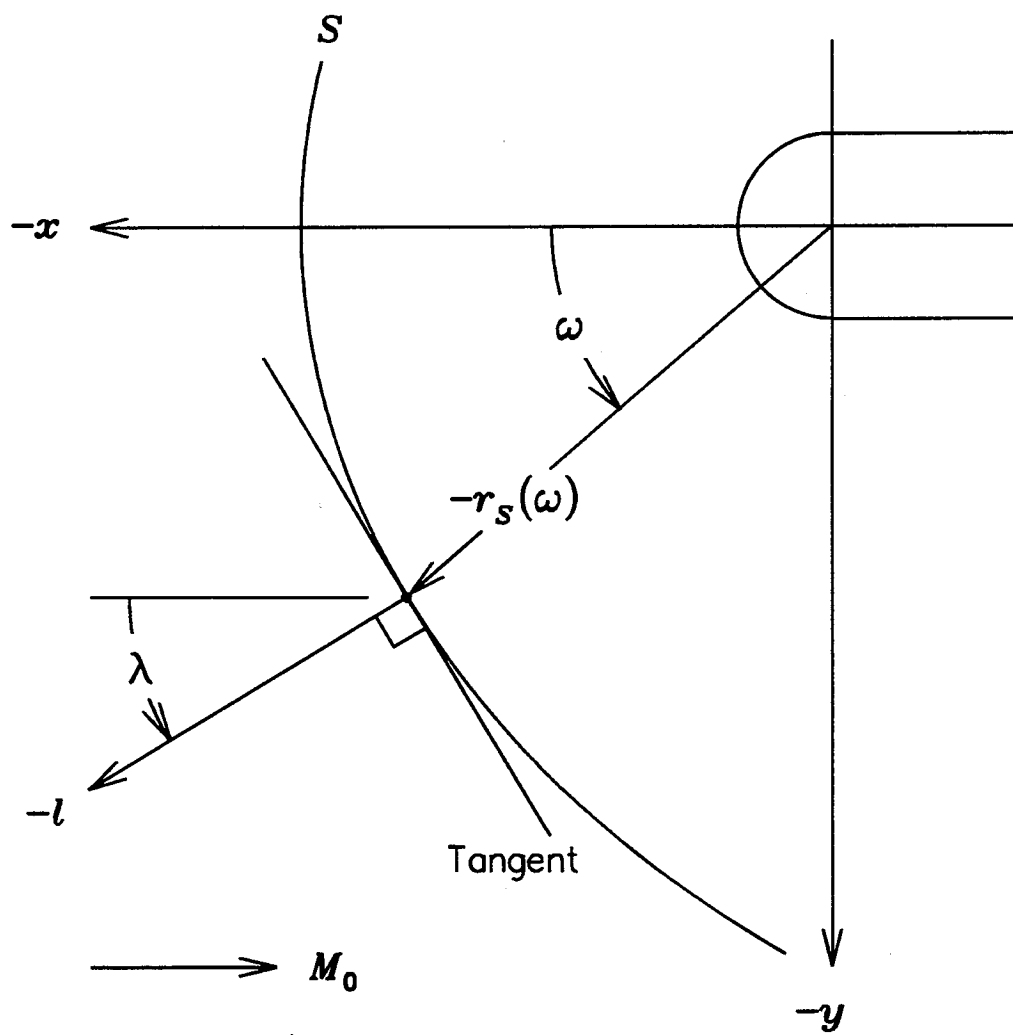
Figure 56   Interaction Region Orthonormal Coordinate System
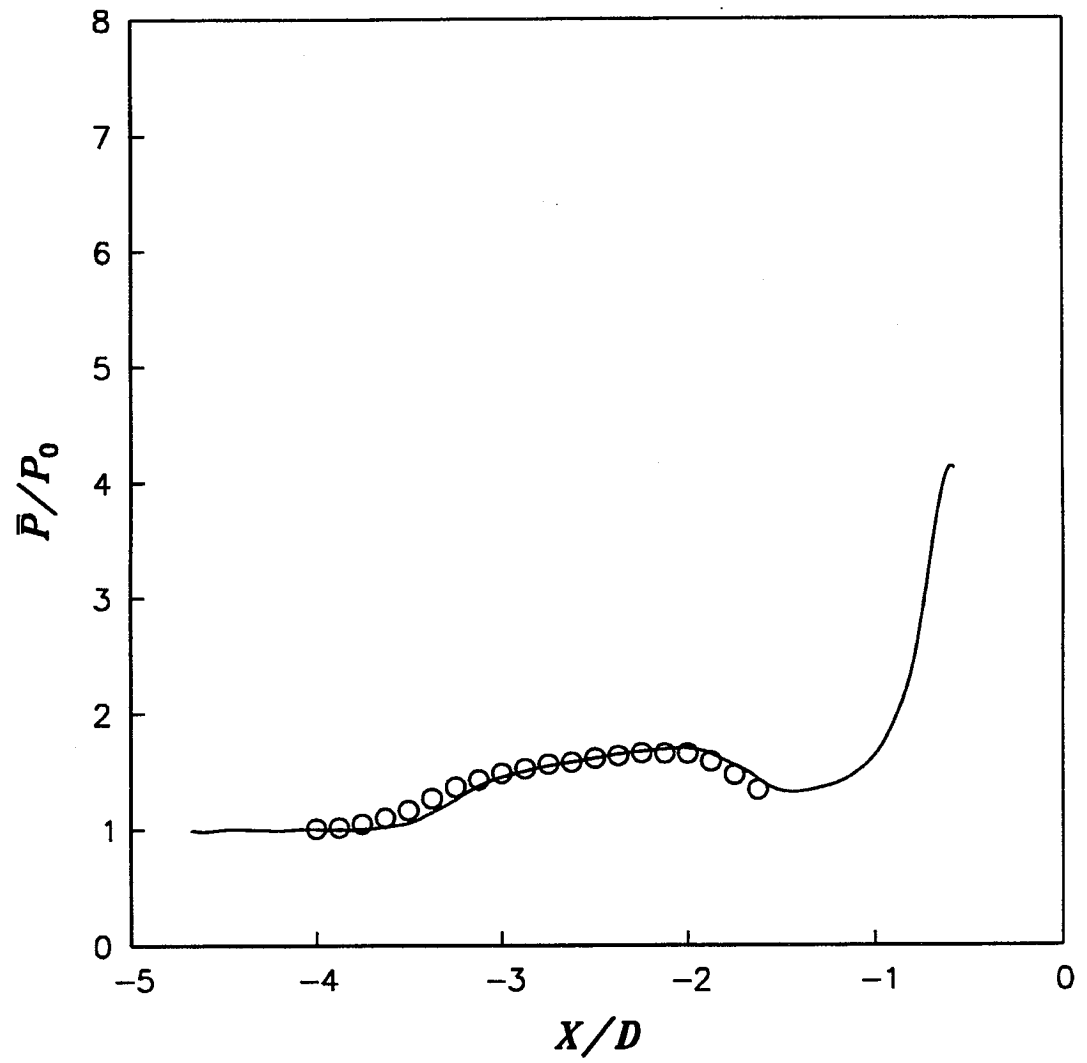
Figure 57   Mach 2.0 Centerline Mean Pressures
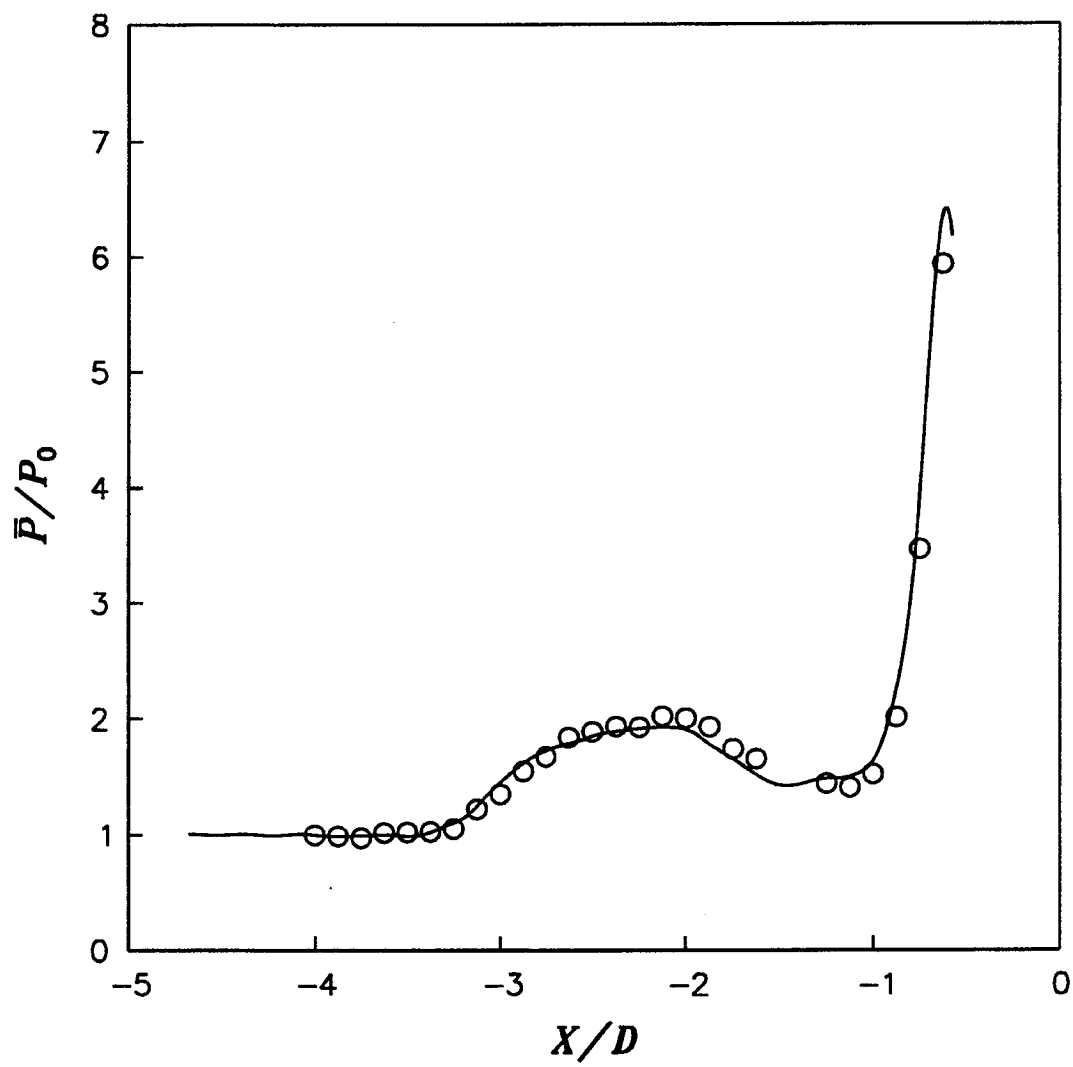
Figure 58   Mach 3.0 Centerline Mean Pressures
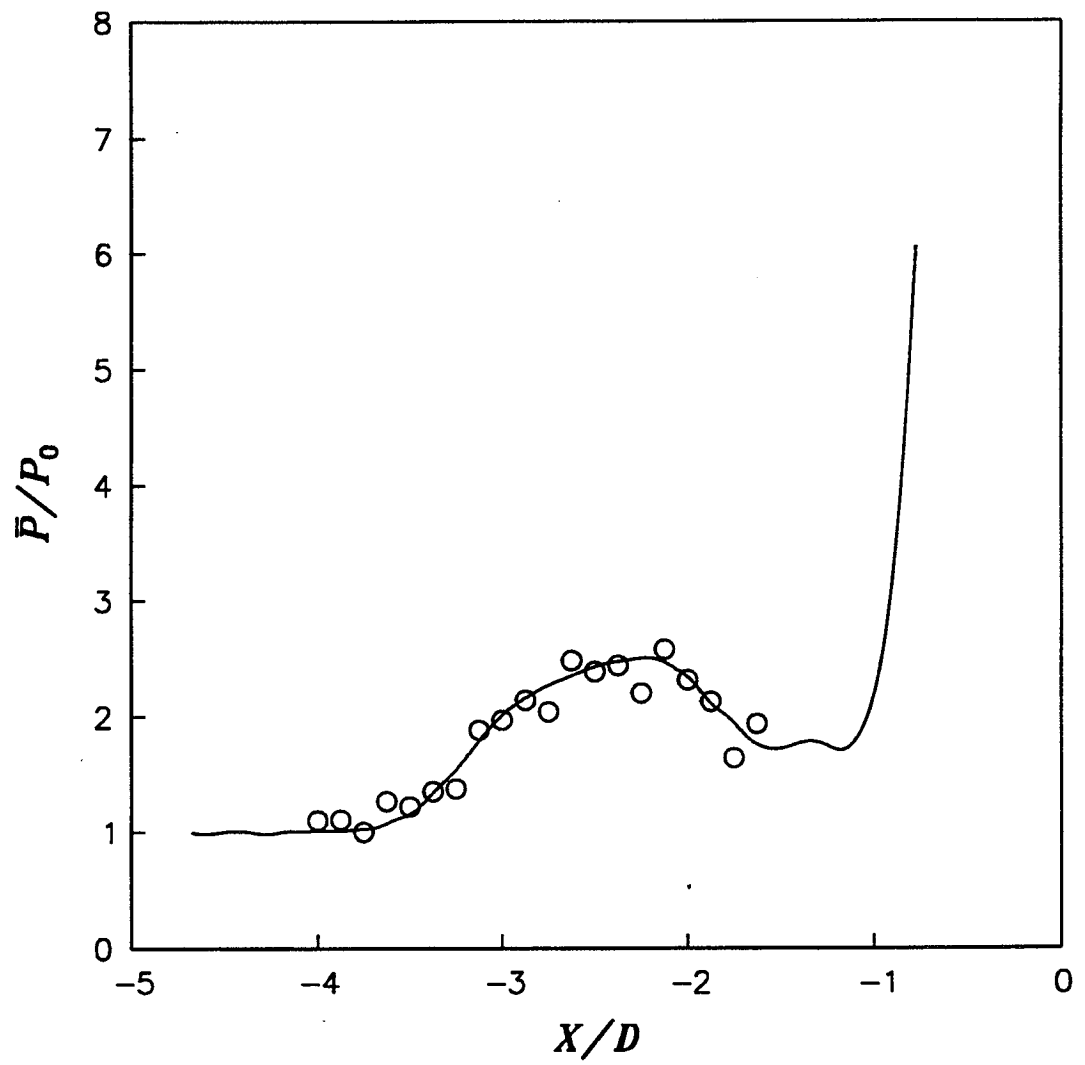
Figure 59   Mach 4.0 Centerline Mean Pressures
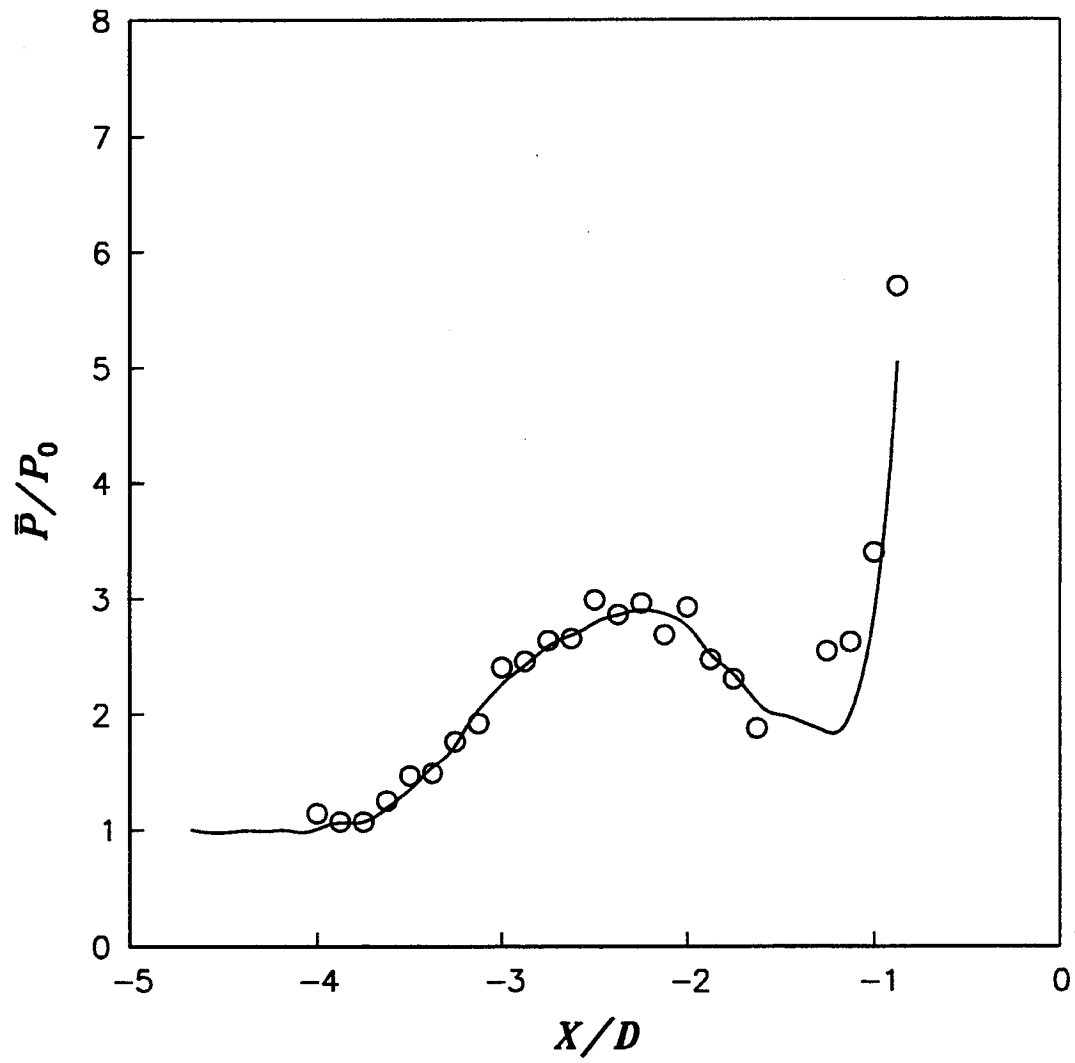
Figure 60   Mach 5.0 Centerline Mean Pressures
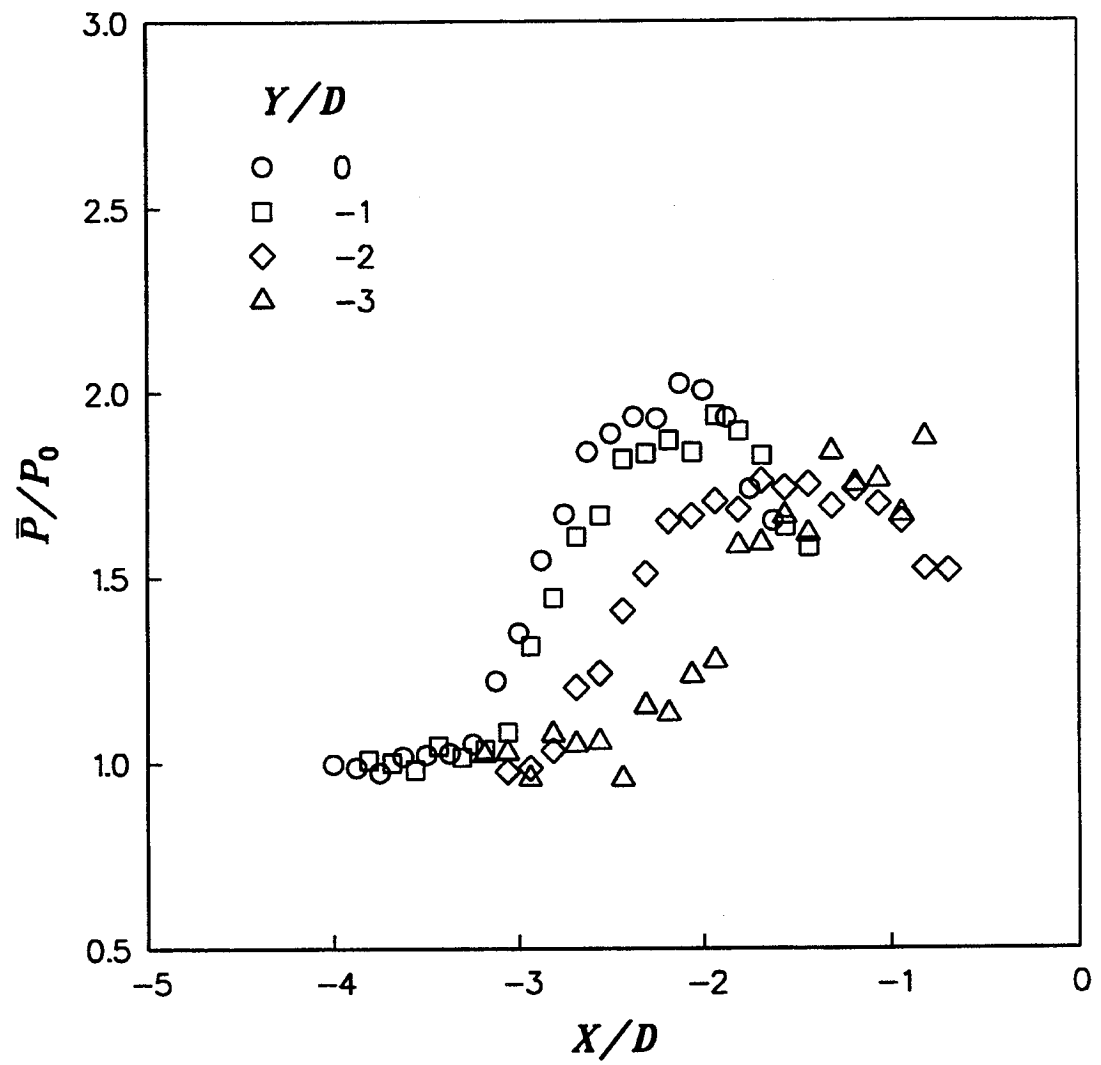
Figure 61   Mach 3.0 Mean Pressures
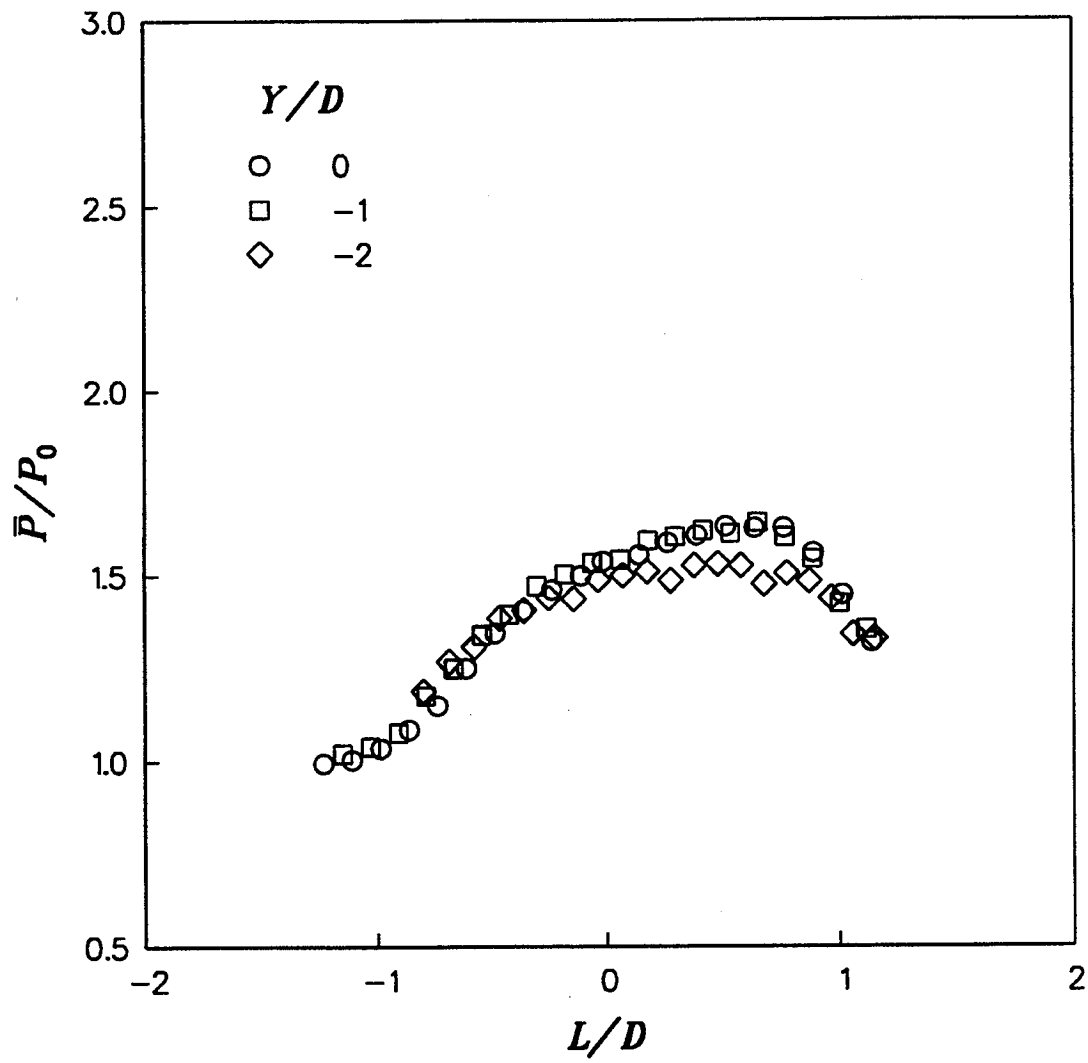
Figure 62   Mach 2.0 Mean Pressures
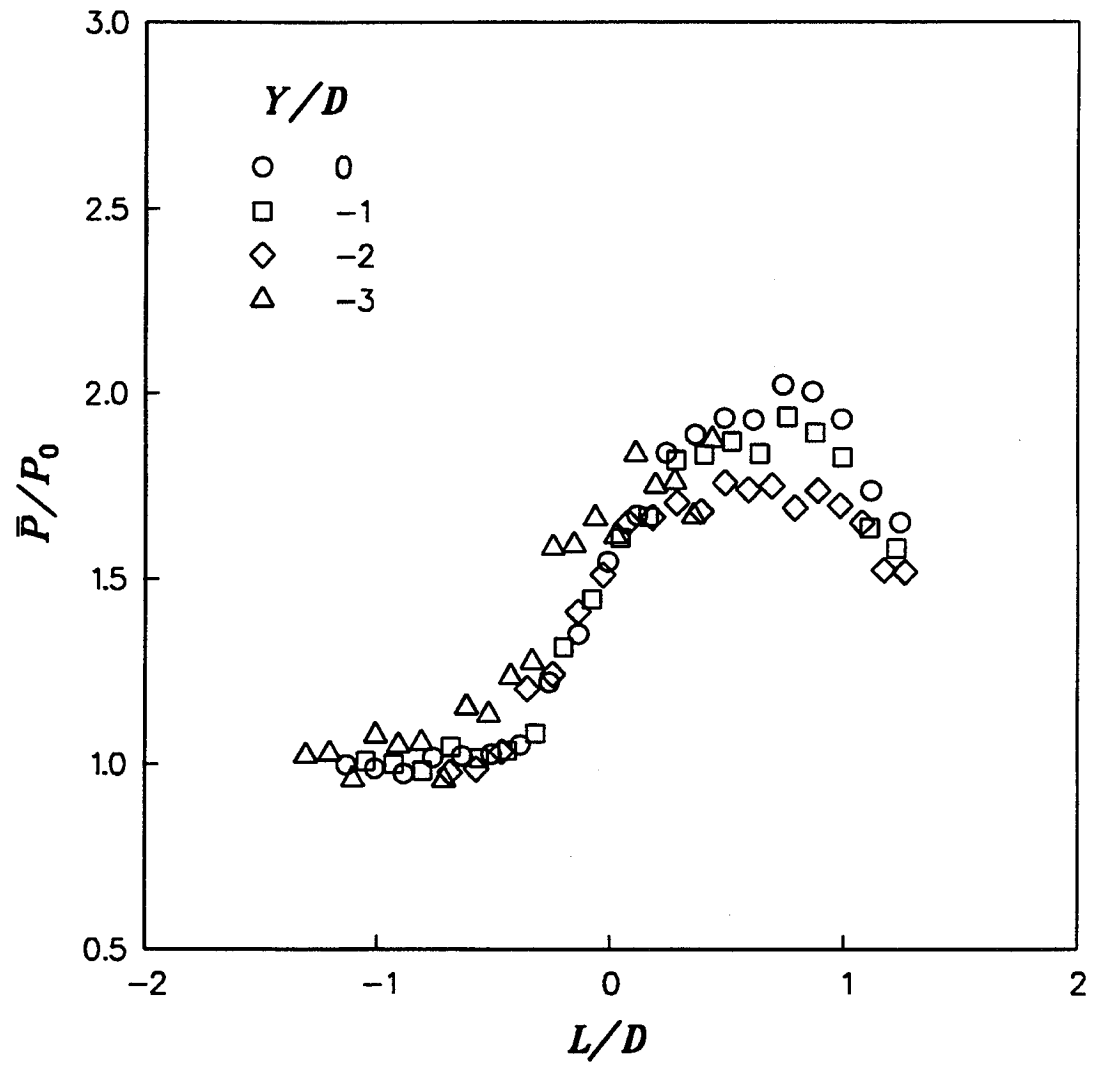
Figure 63   Mach 3.0 Mean Pressures
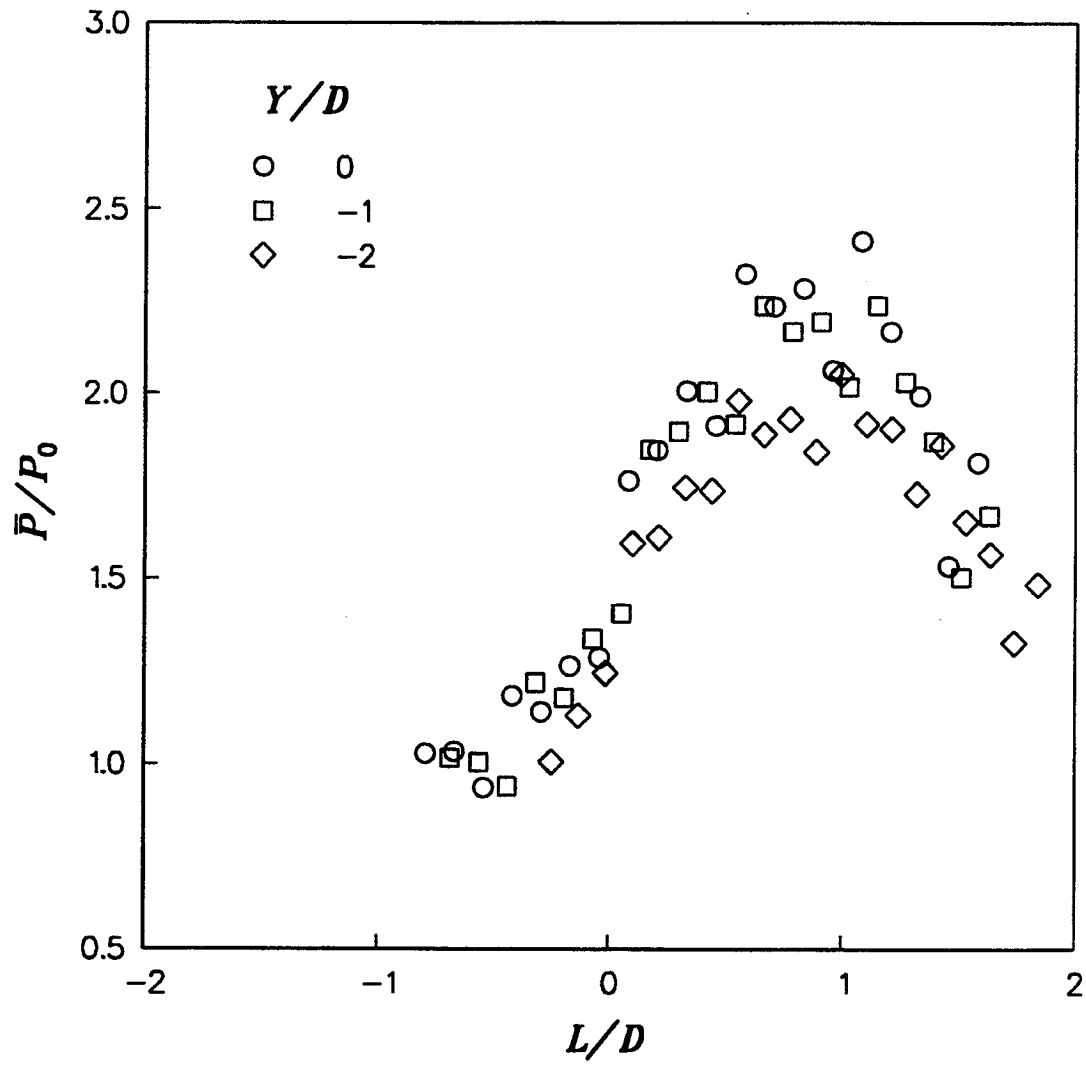
Figure 64   Mach 4.0 Mean Pressures
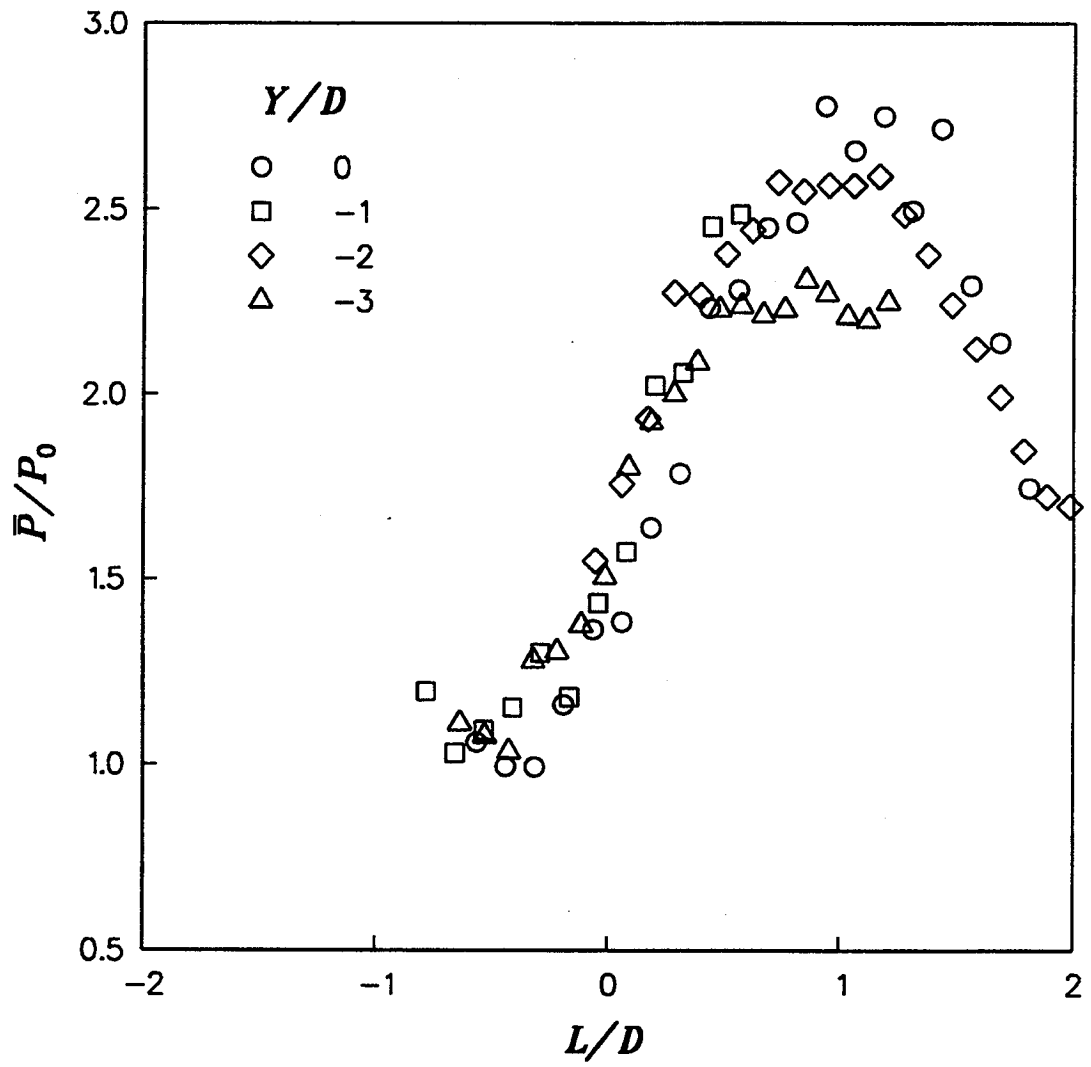
Figure 65   Mach 5.0 Mean Pressures
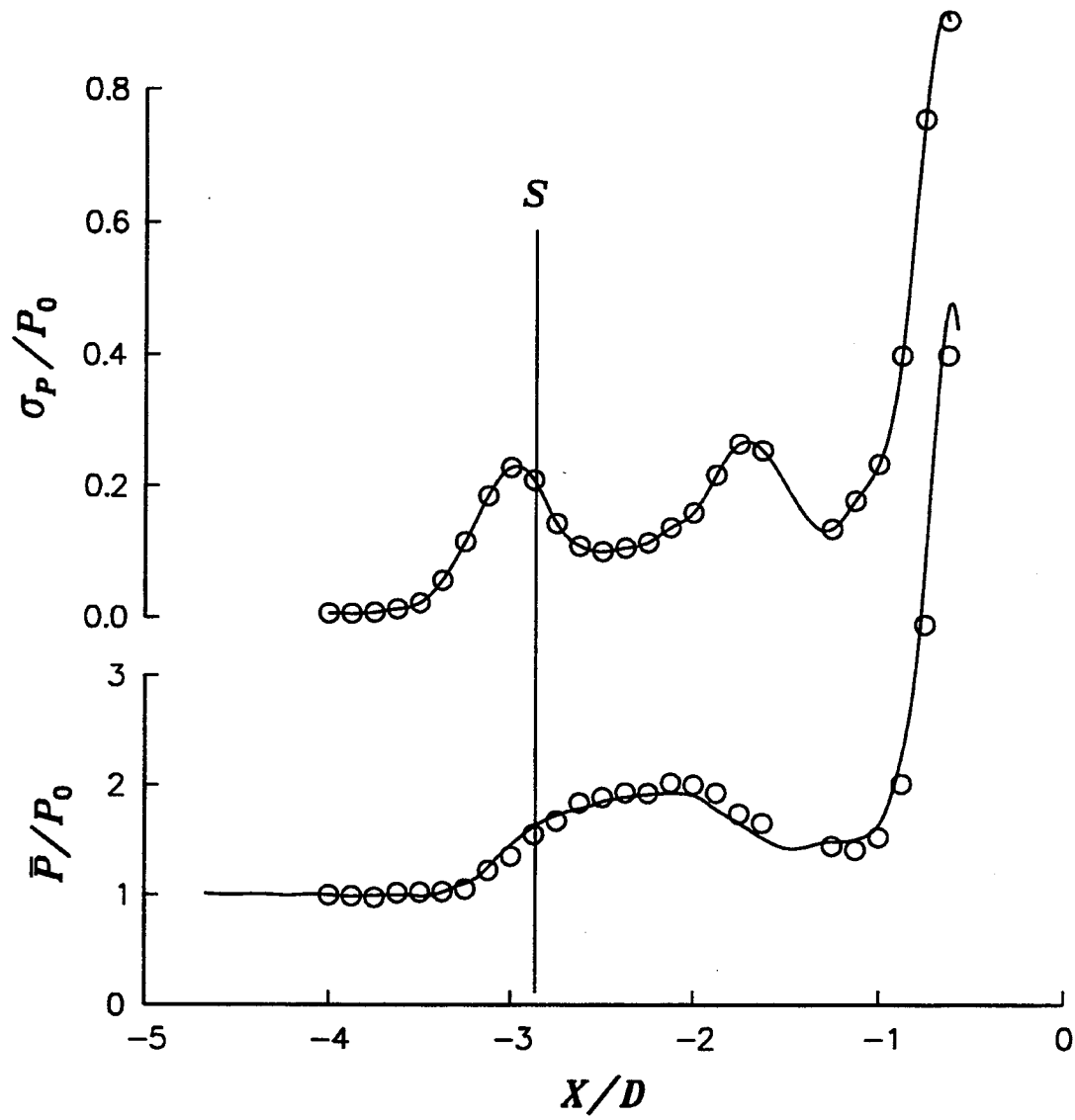
Figure 66   Mach 3.0 Centerline Comparison of Mean Pressures and
                   Standard Deviations
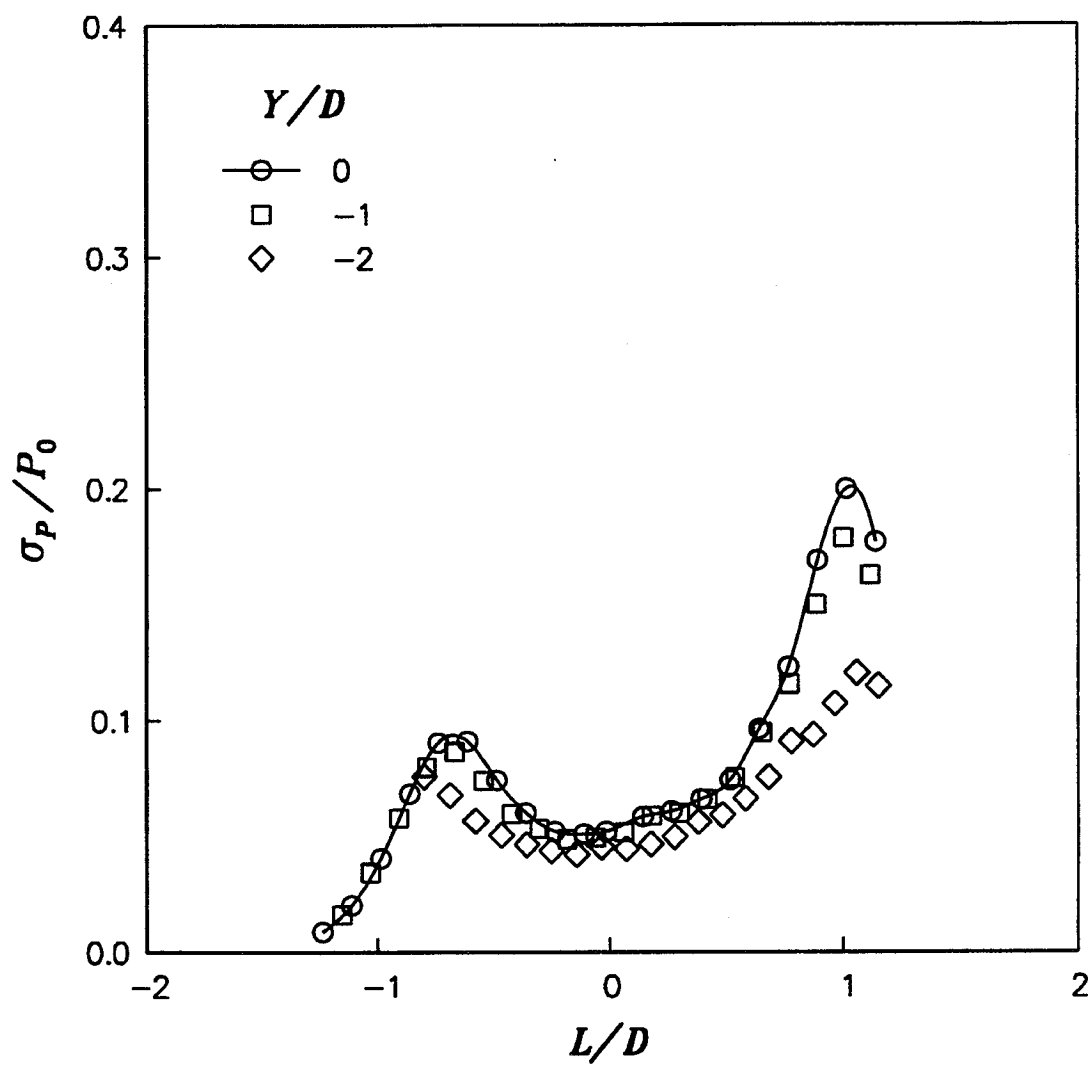
Figure 67   Mach 2.0 Standard Deviations
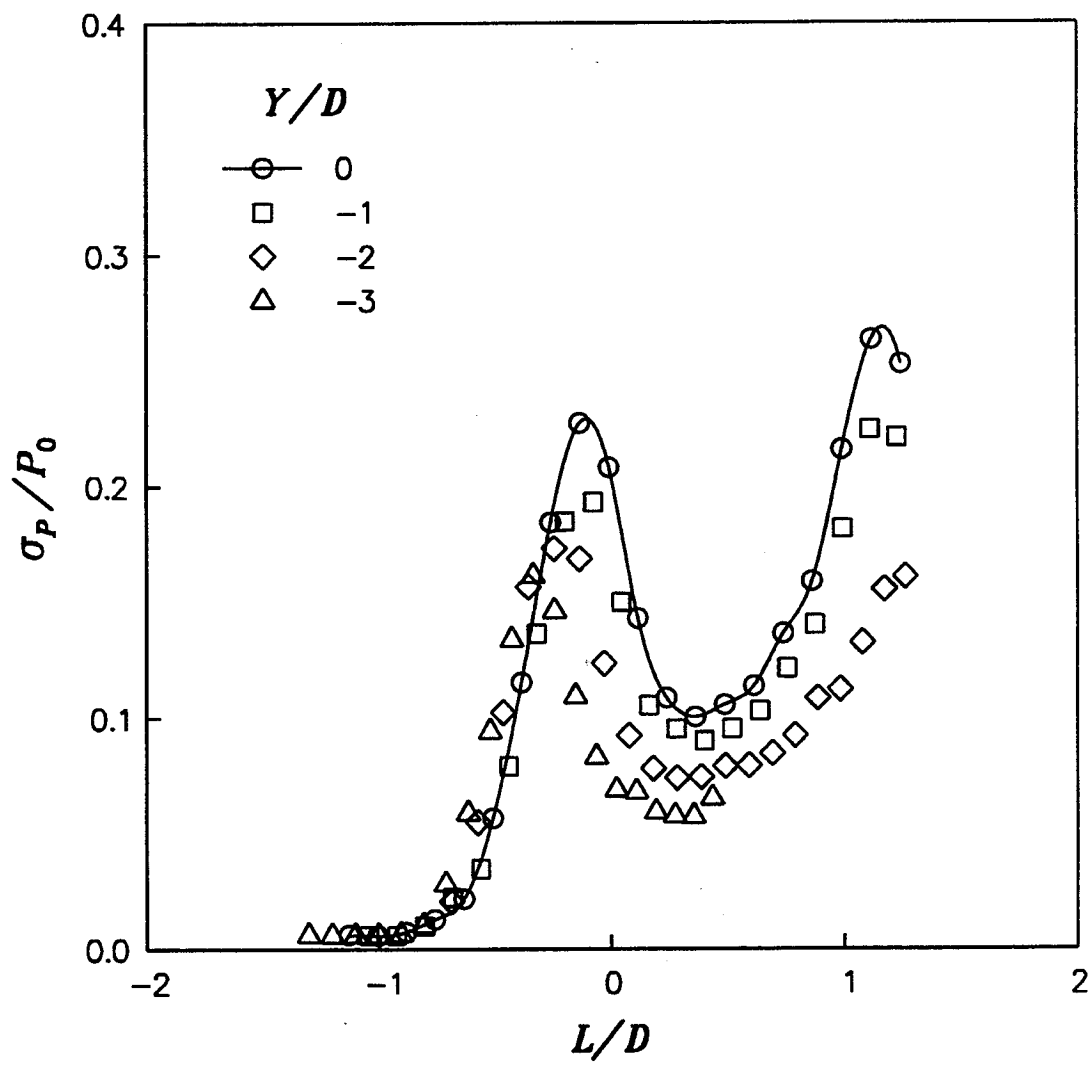
Figure 68   Mach 3.0 Standard Deviations
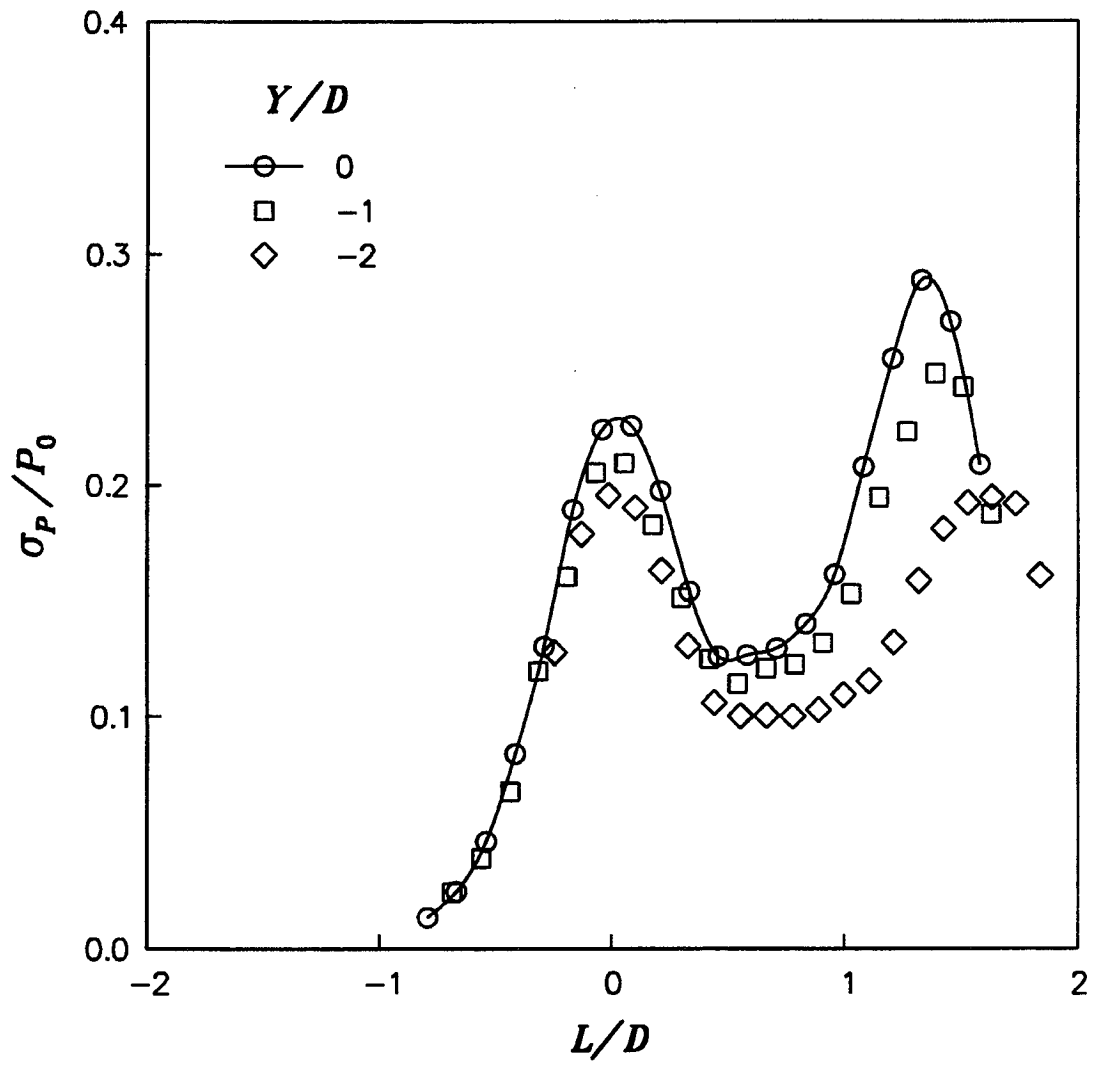
Figure 69   Mach 4.0 Standard Deviations
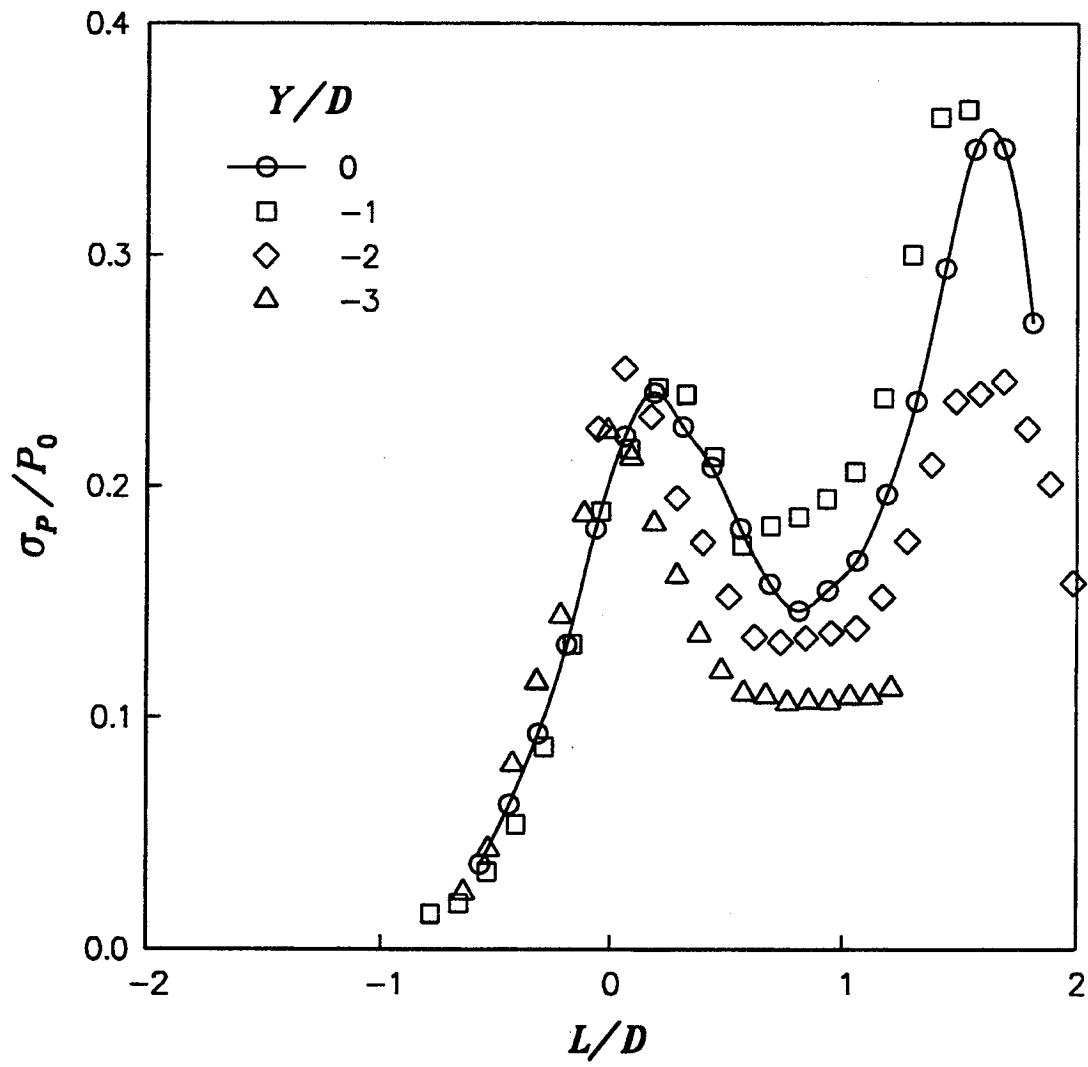
Figure 70   Mach 5.0 Standard Deviations
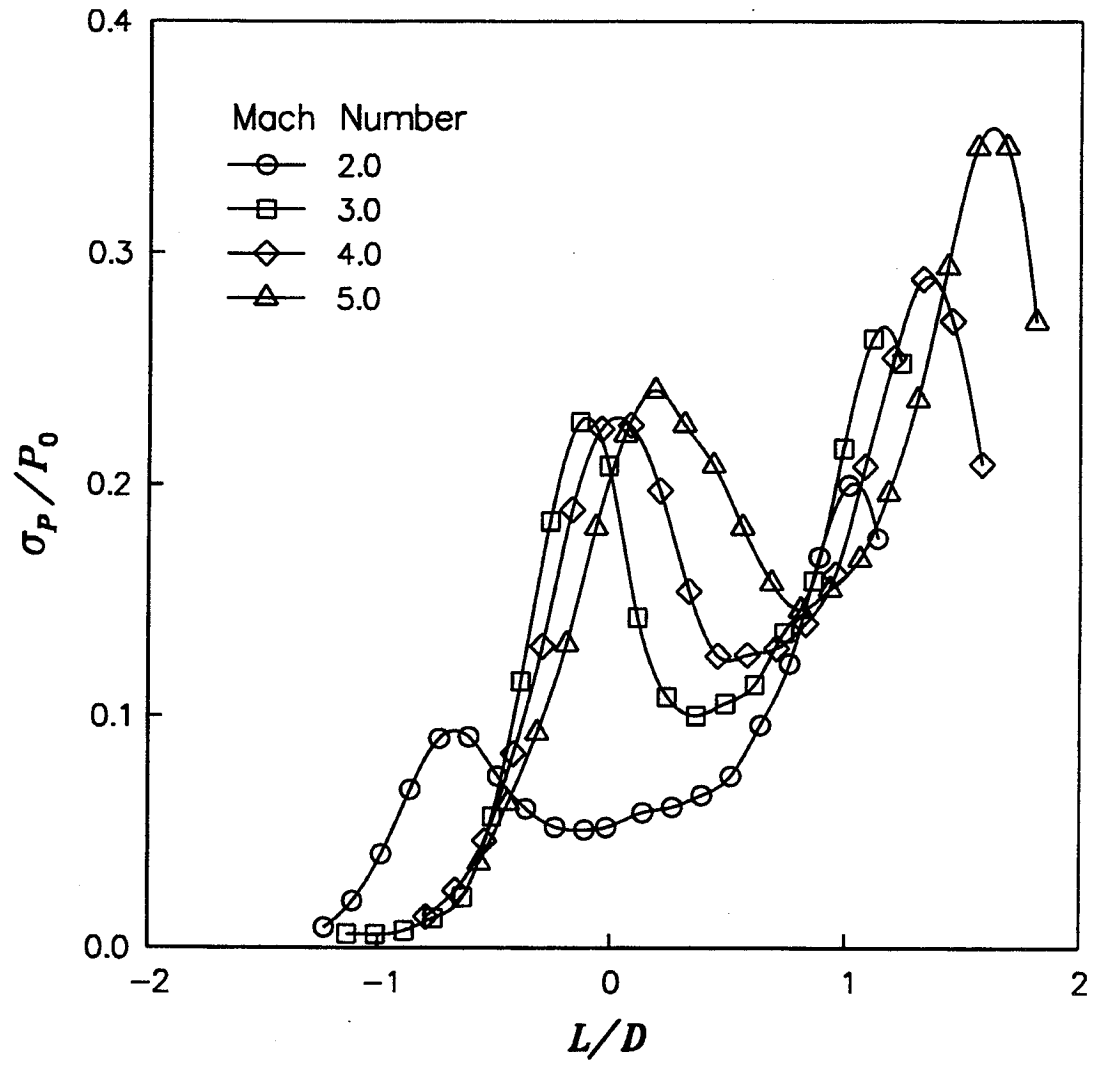
Figure 71   Centerline Standard Deviations
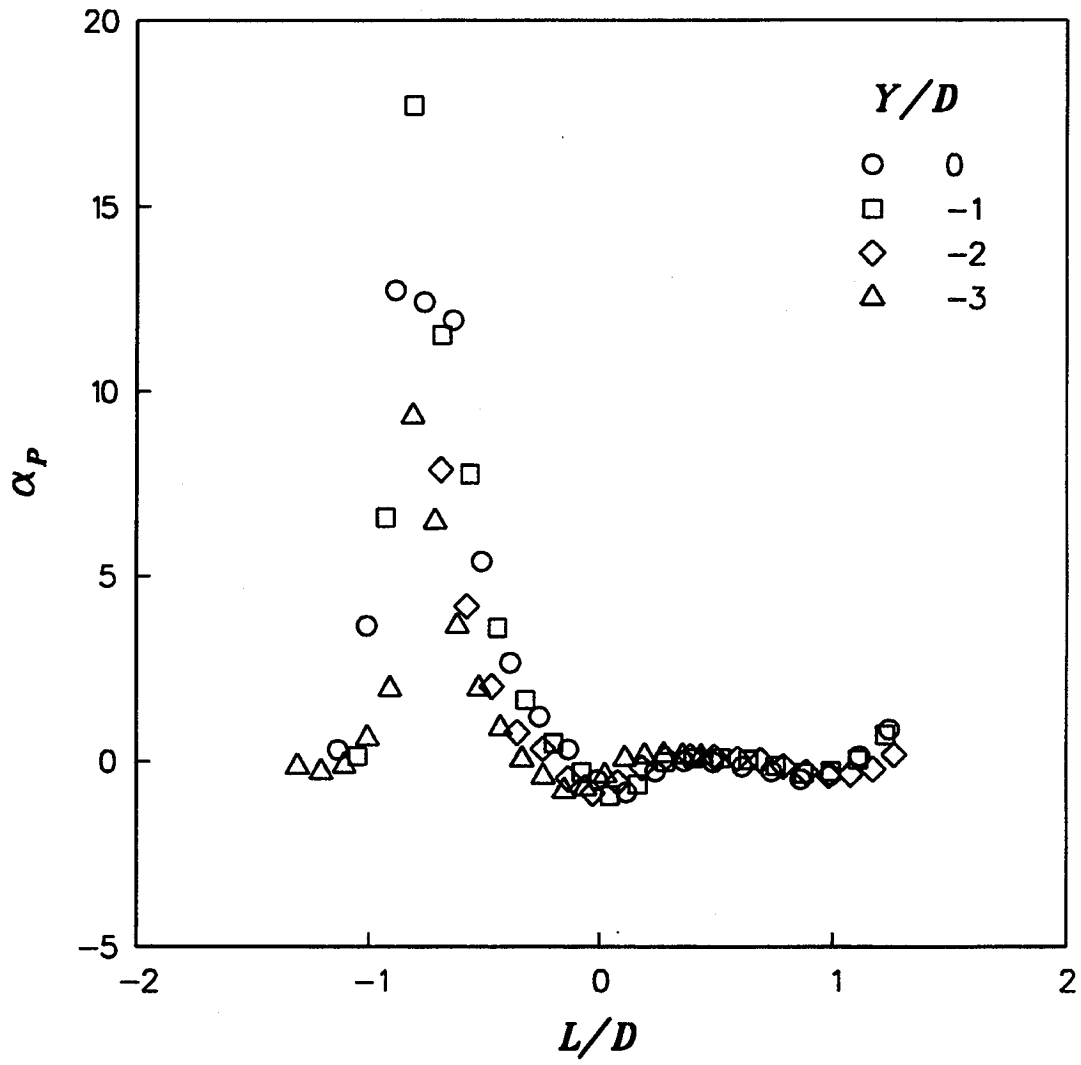
Figure 72   Mach 3.0 Skewness
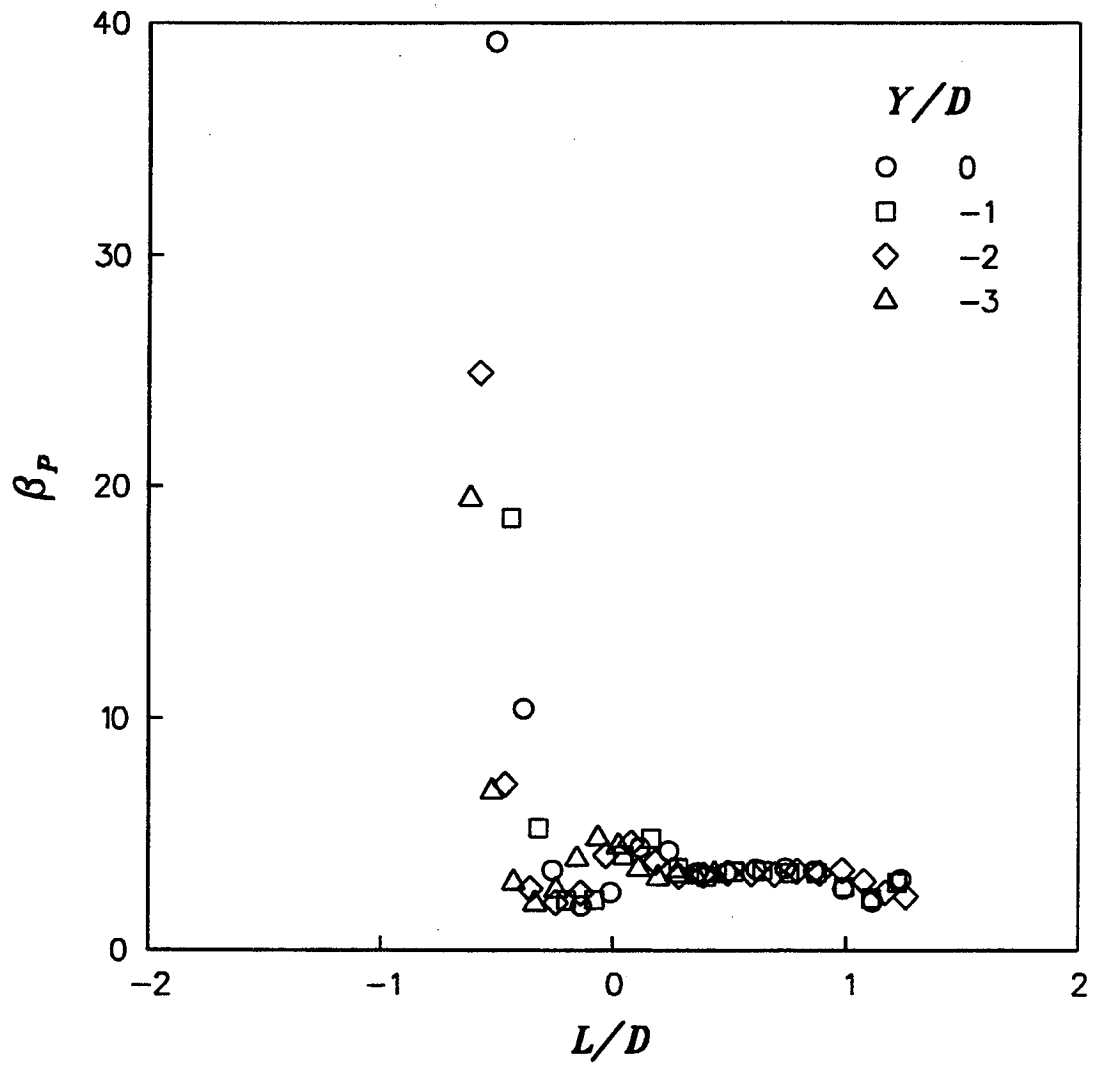
Figure 73   Mach 3.0 Kurtosis
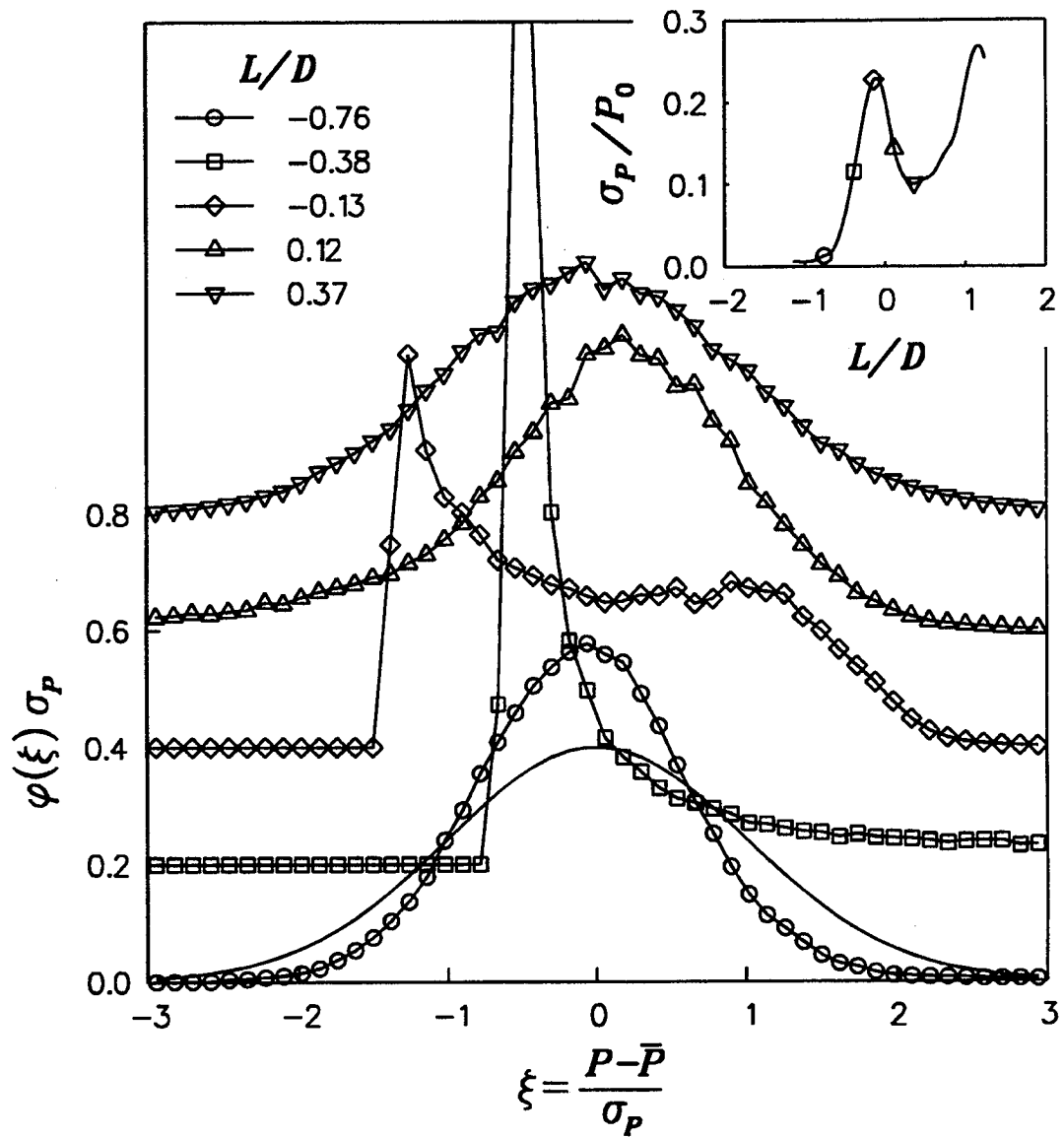
Figure 74   Mach 3.0 Probability Density Functions
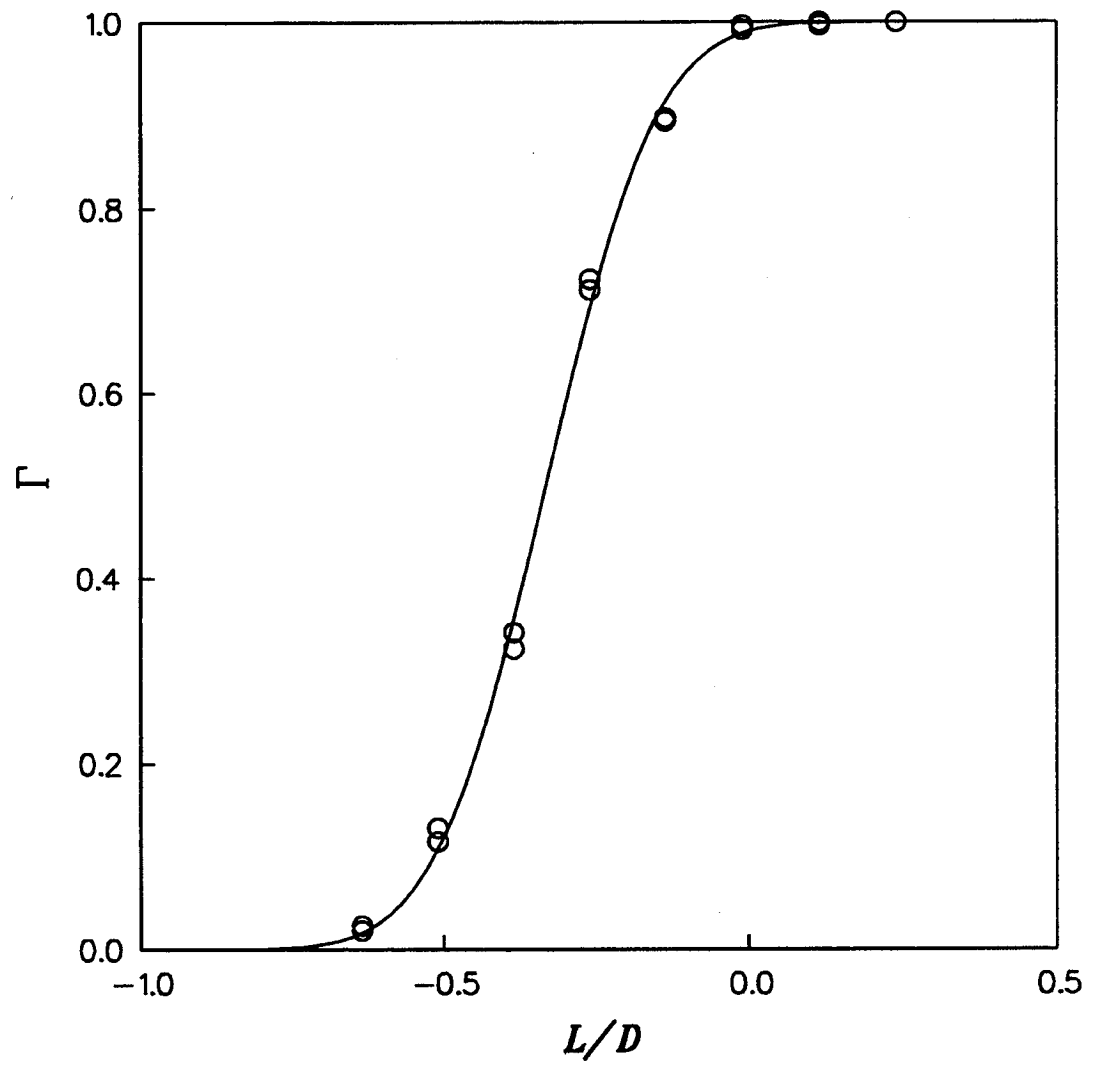
Figure 75   Mach 3.0 Centerline Intermittency Distribution
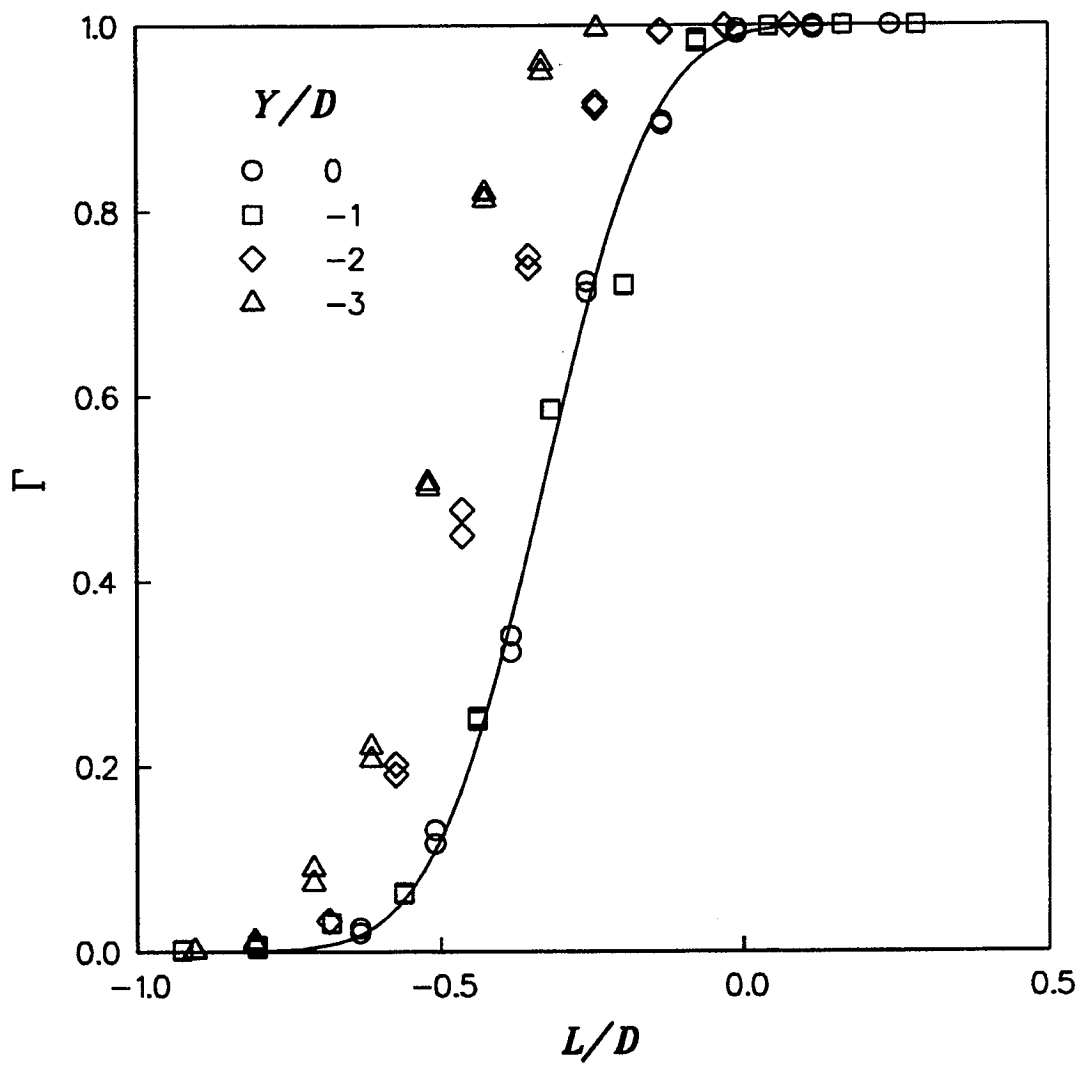
Figure 76　　　　　　Mach 3.0 Intermittency Distributions
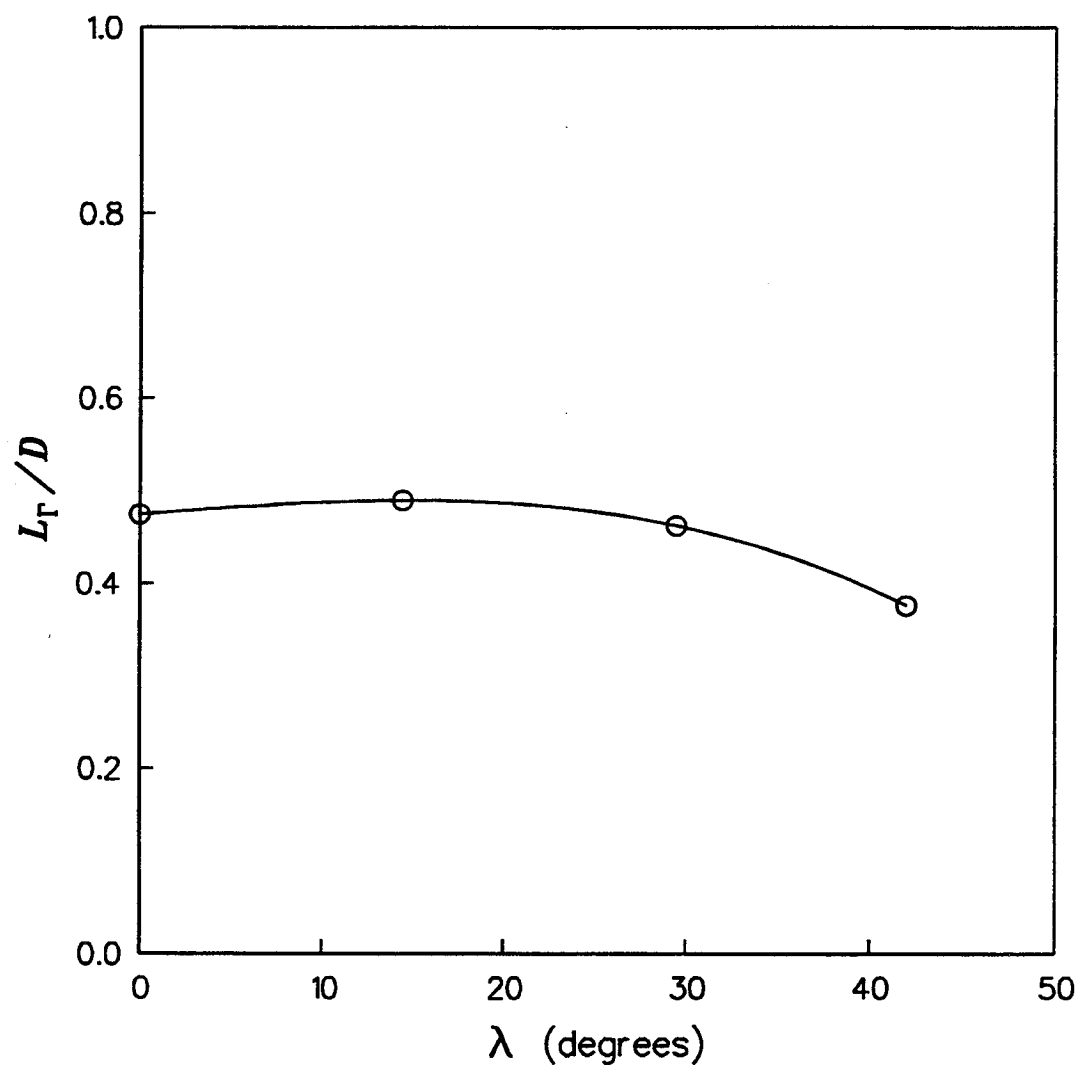
Figure 77   Mach 3.0 Intermittent Region Length
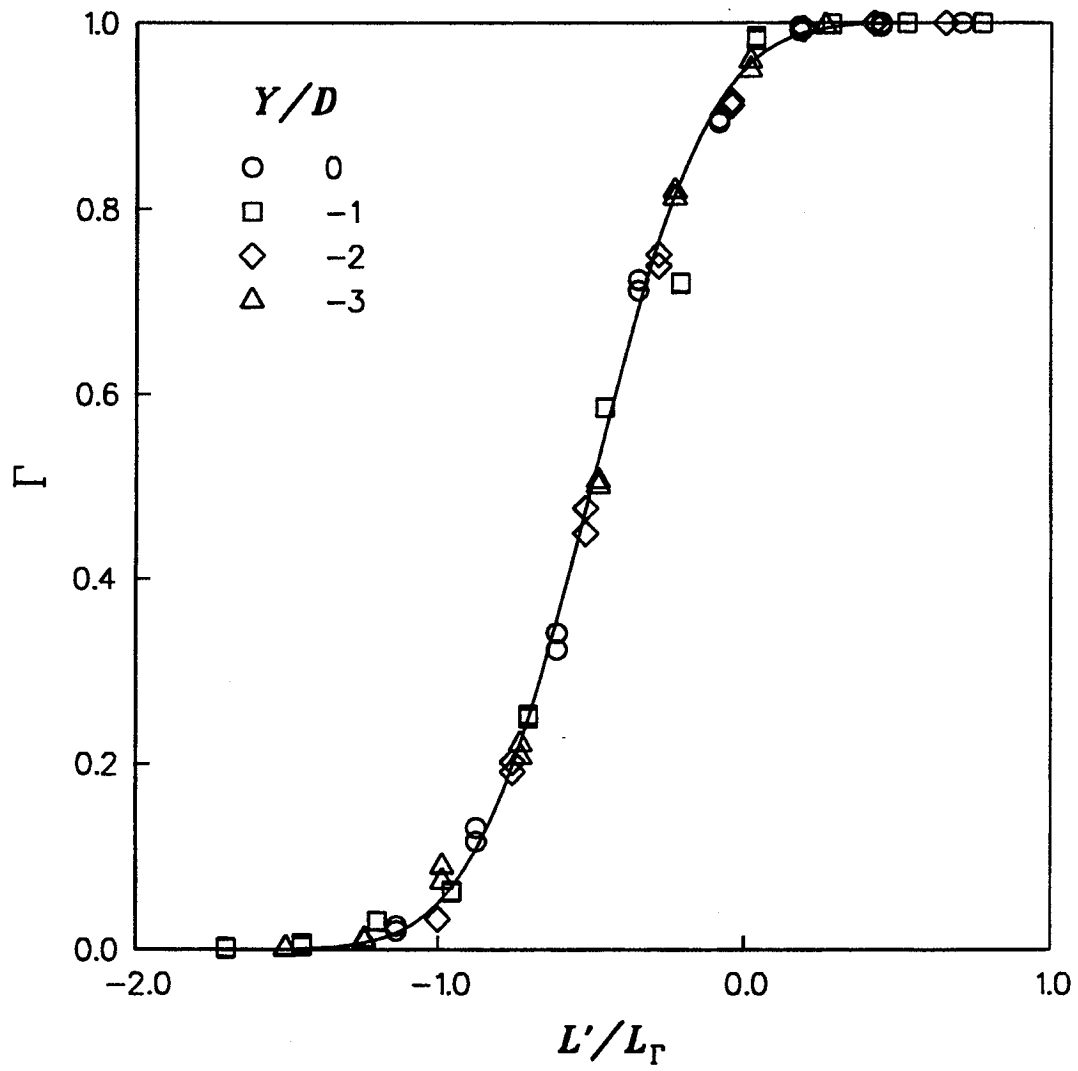
Figure 78   Mach 3.0 Intermittency Distribution Comparison
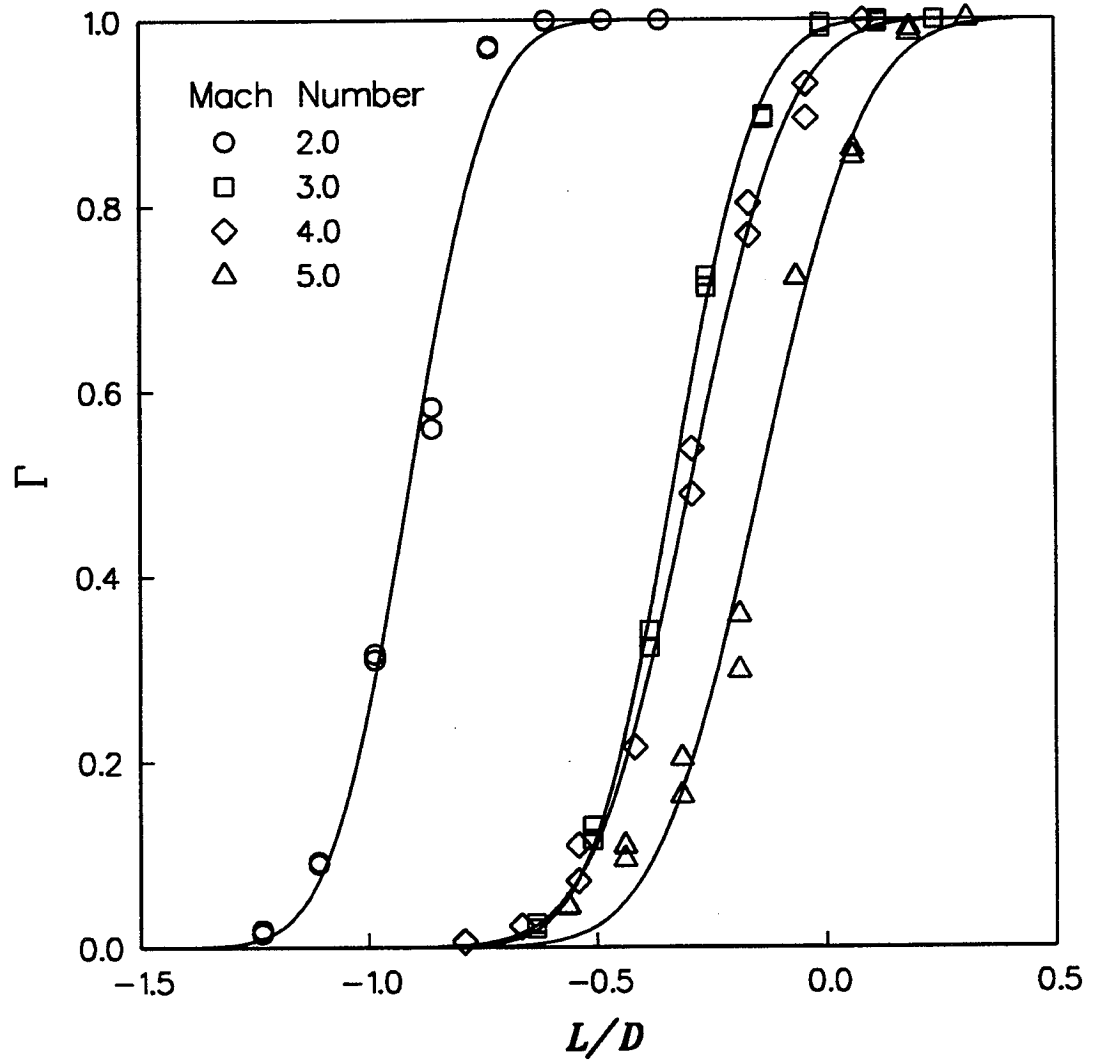
Figure 79   Centerline Intermittency Distributions
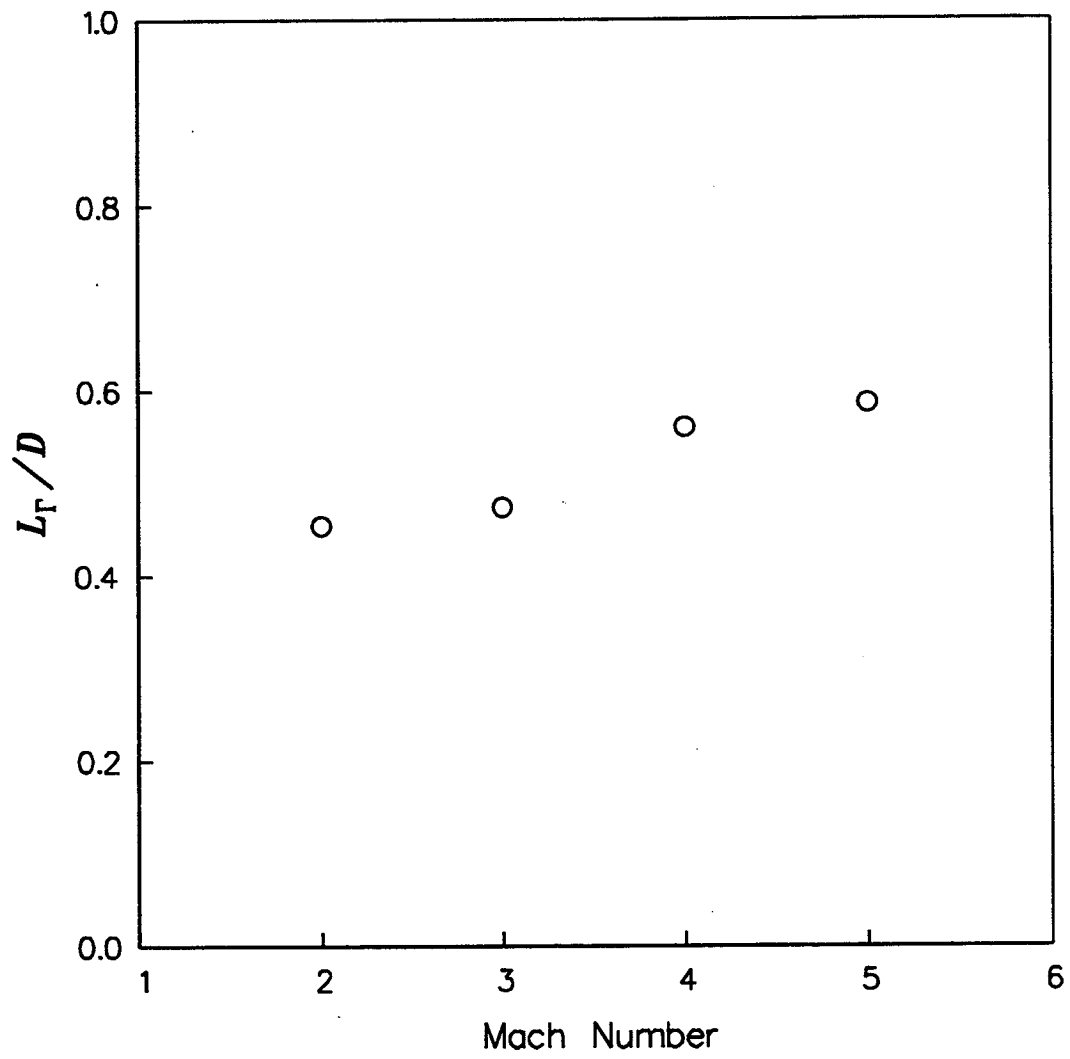
Figure 80   Centerline Intermittent Region Length
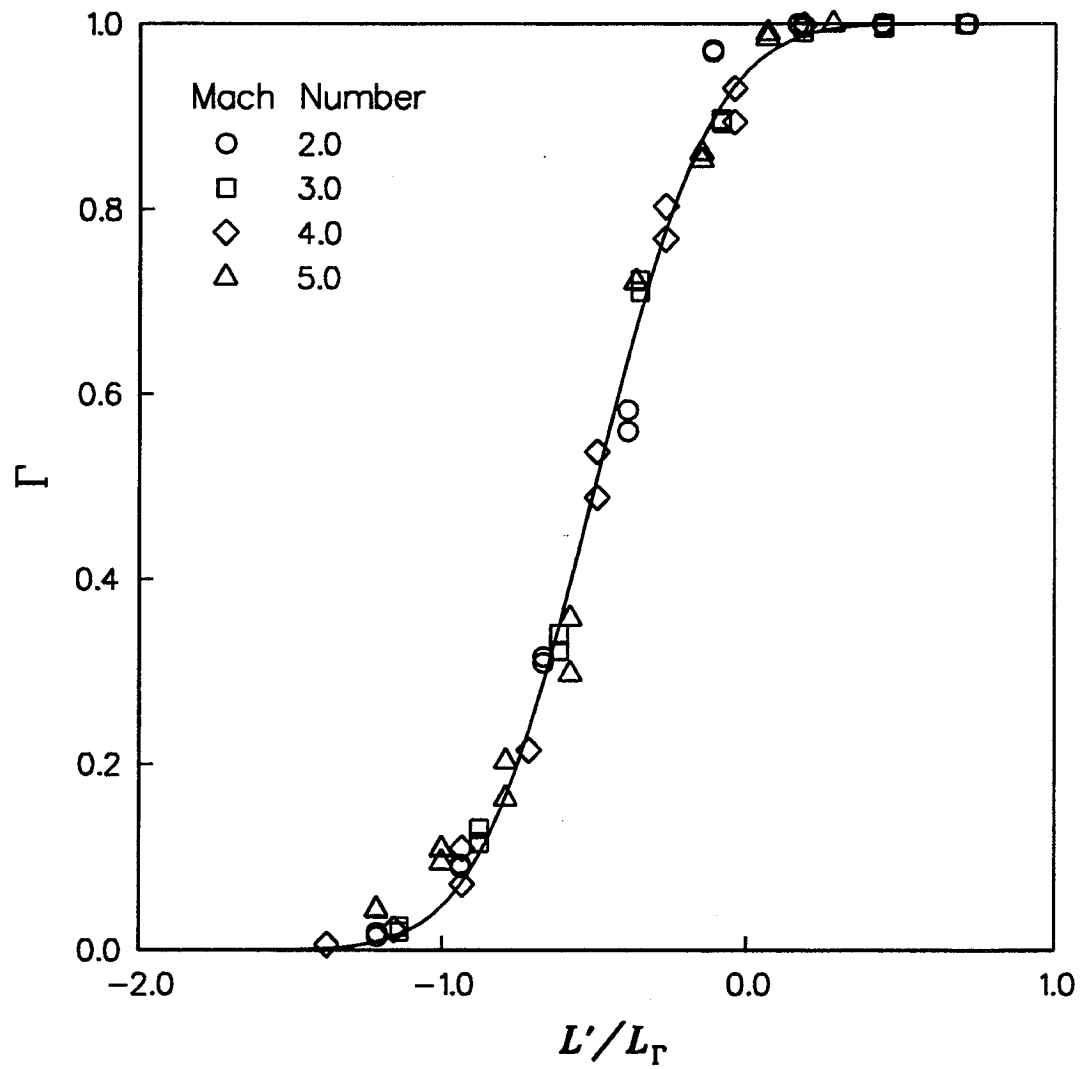
Figure 81   Centerline Intermittency Distribution Comparison
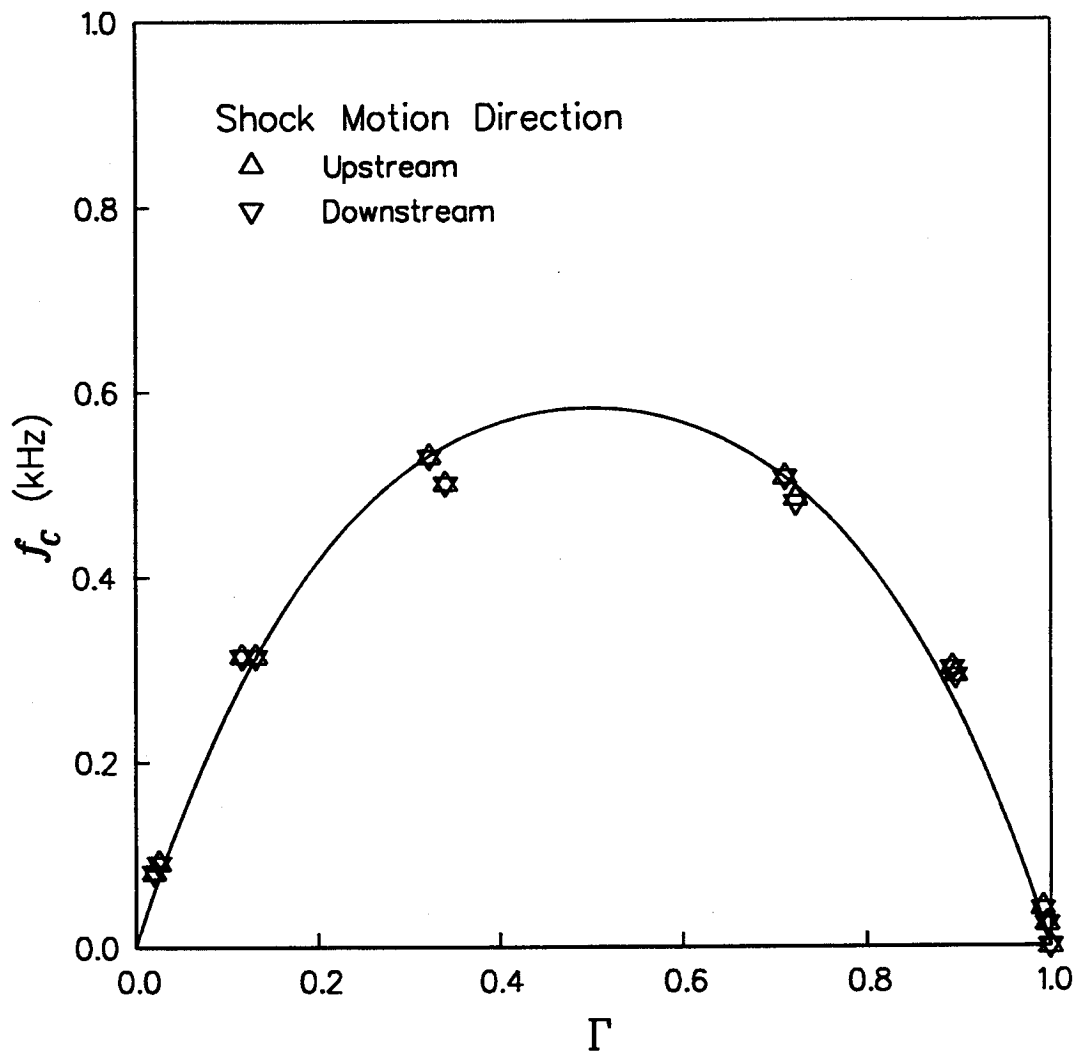
Figure 82   Mach 3.0 Centerline Zero-Crossing Frequency
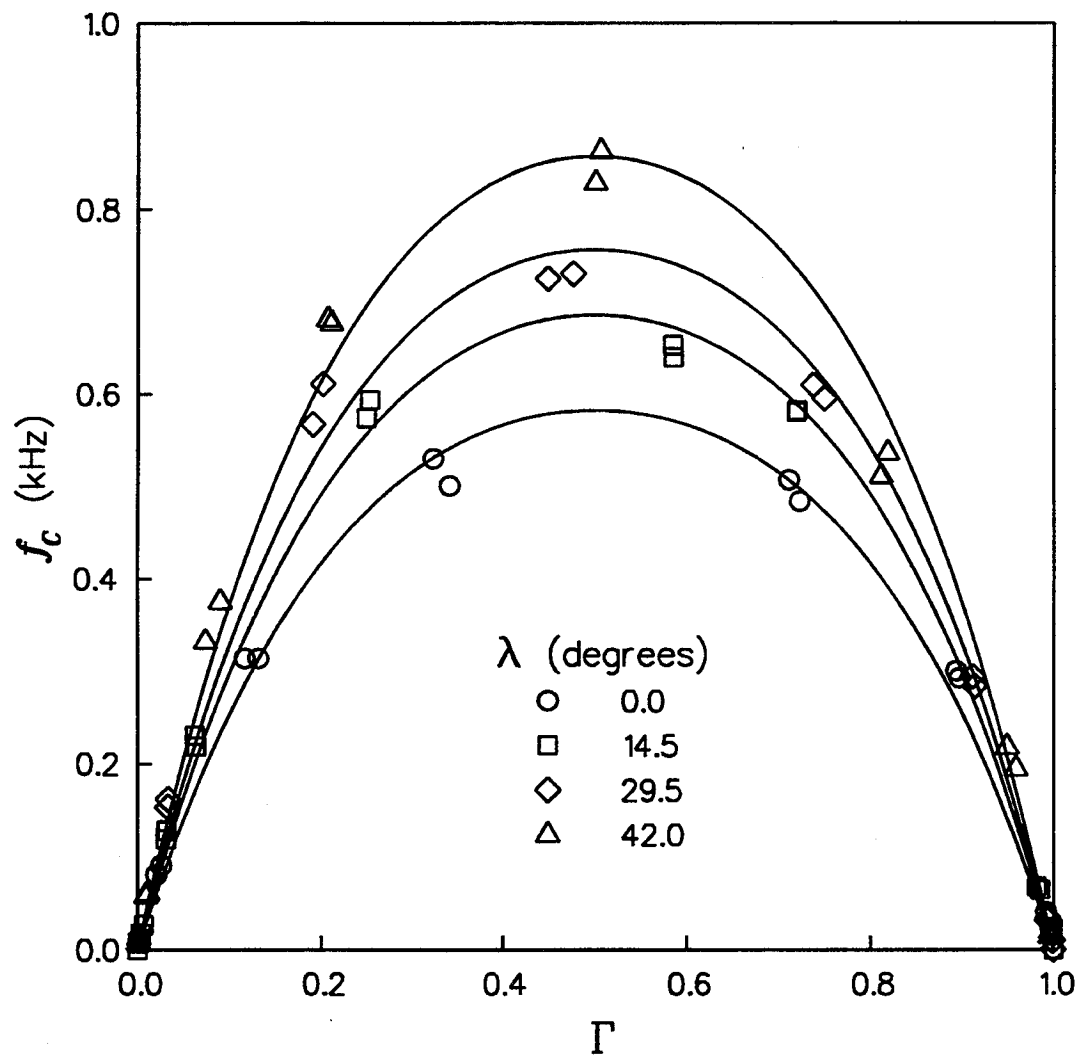
Figure 83   Mach 3.0 Zero-Crossing Frequencies
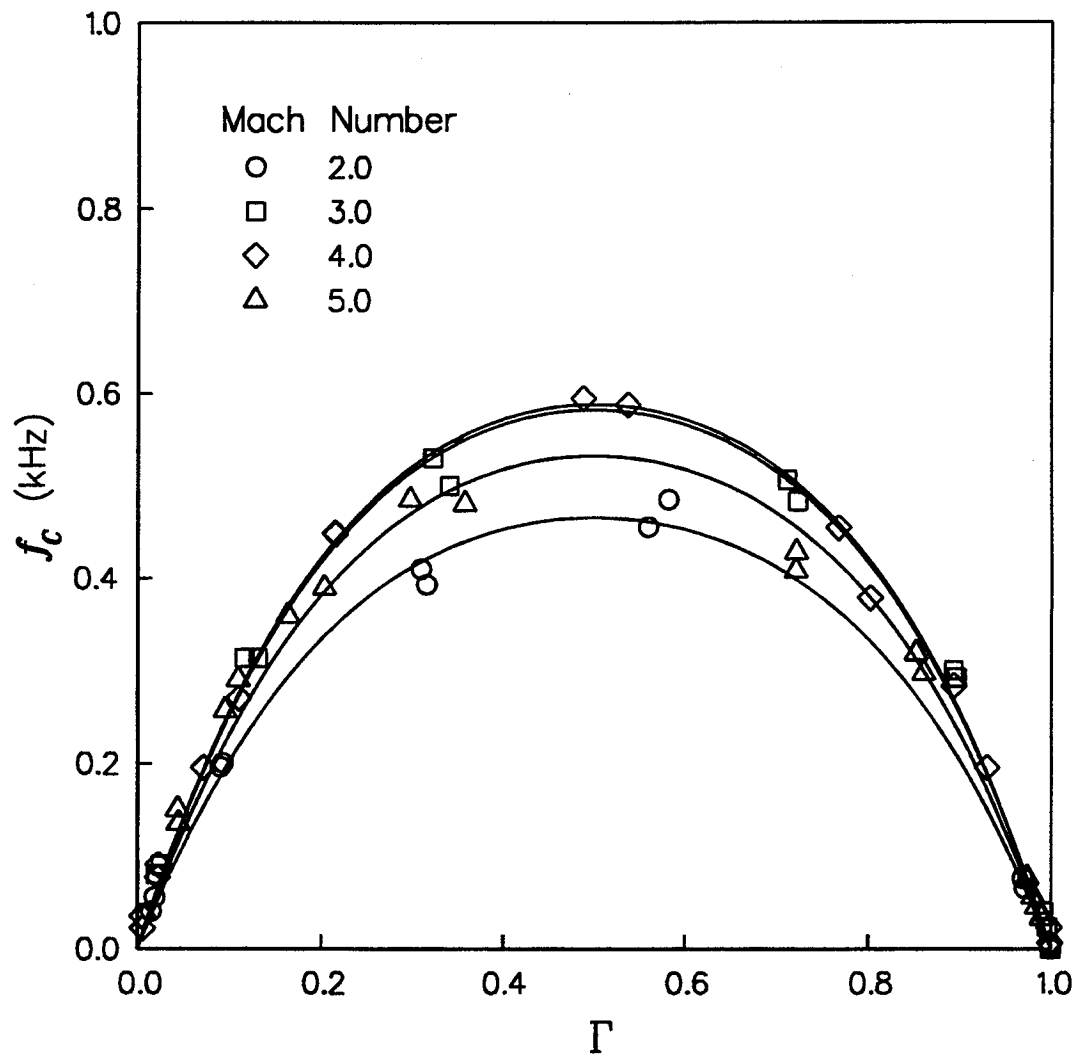
Figure 84   Centerline Zero-Crossing Frequencies
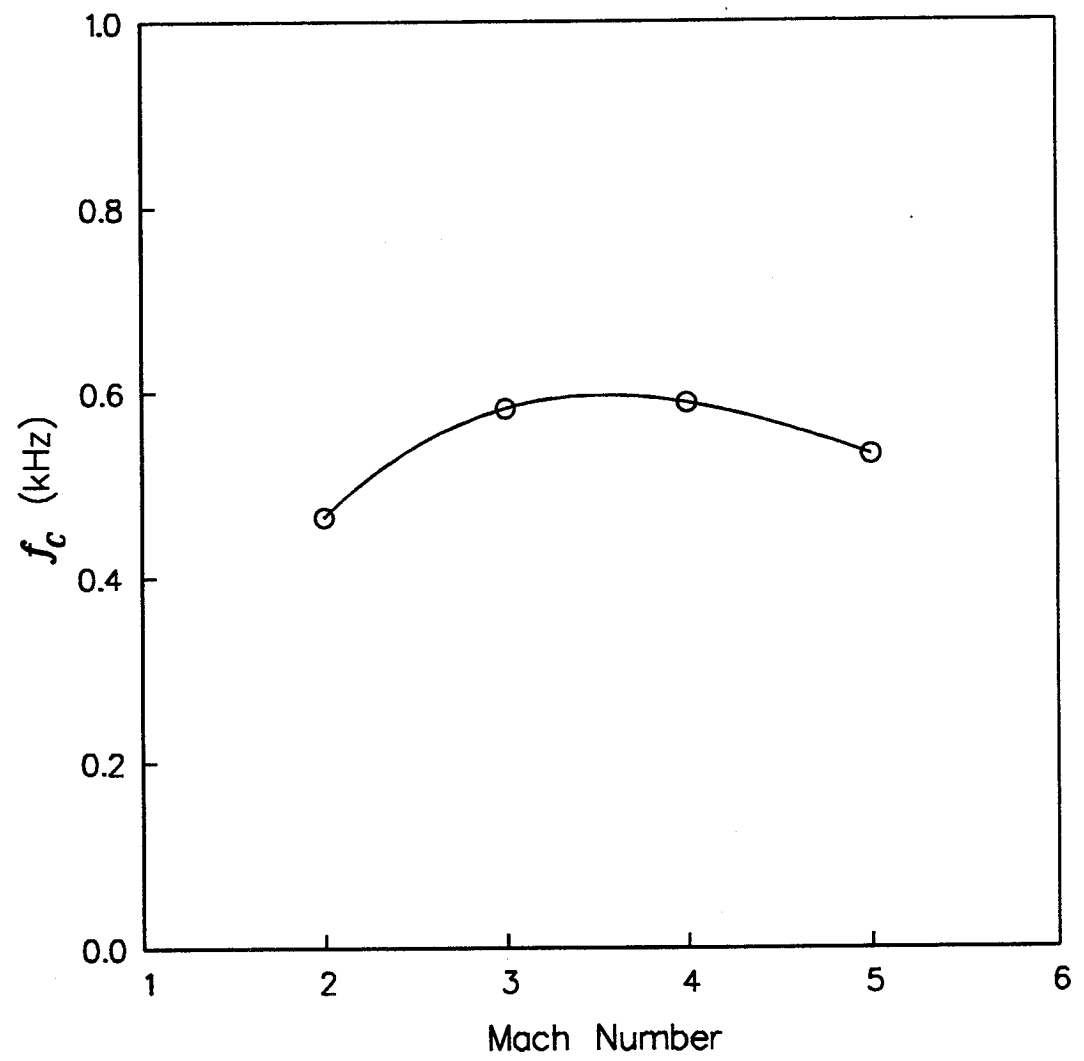
Figure 85   Centerline Maximum Zero-Crossing Frequency
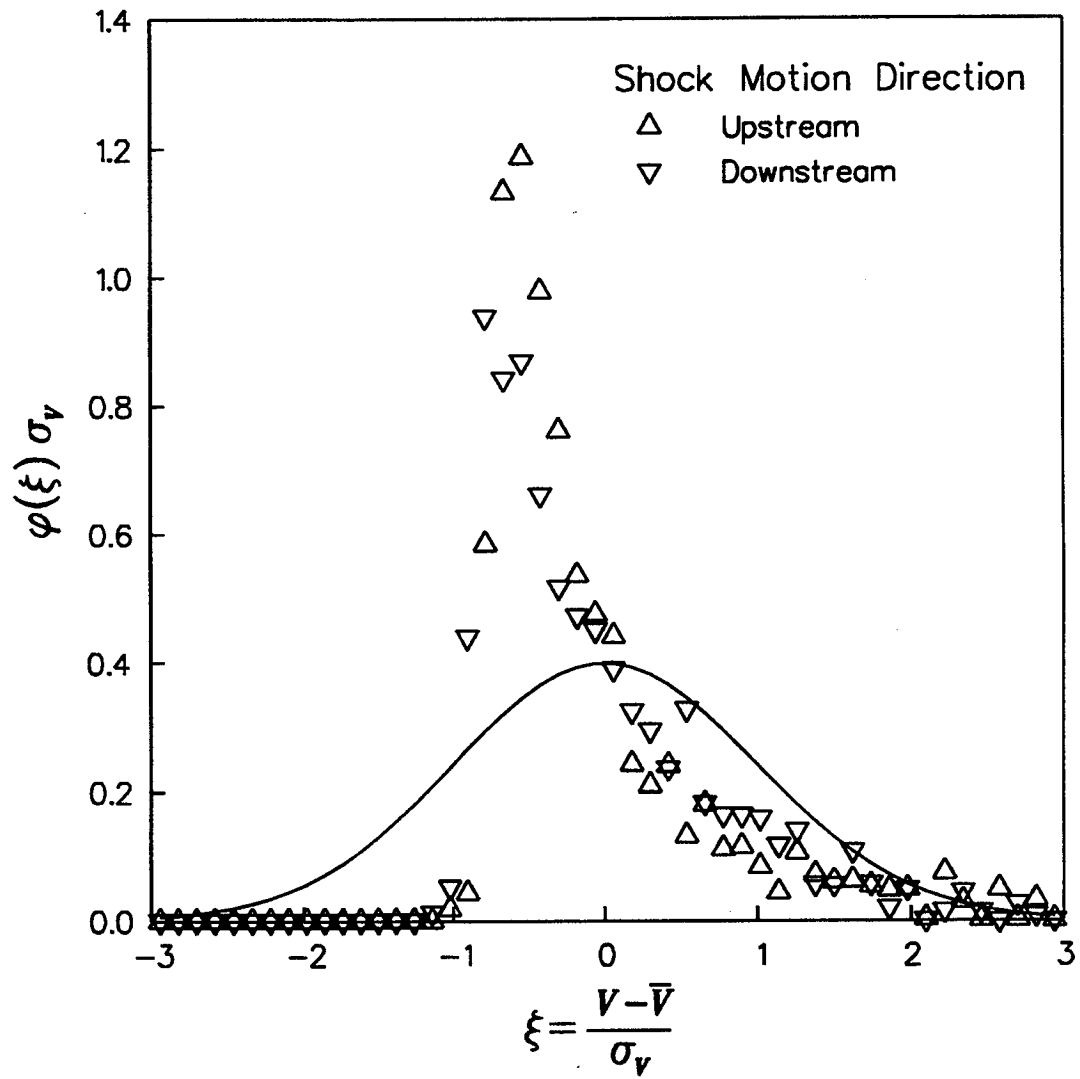
Figure 86   Mach 3.0 Centerline Shock Velocity Probability Density Functions
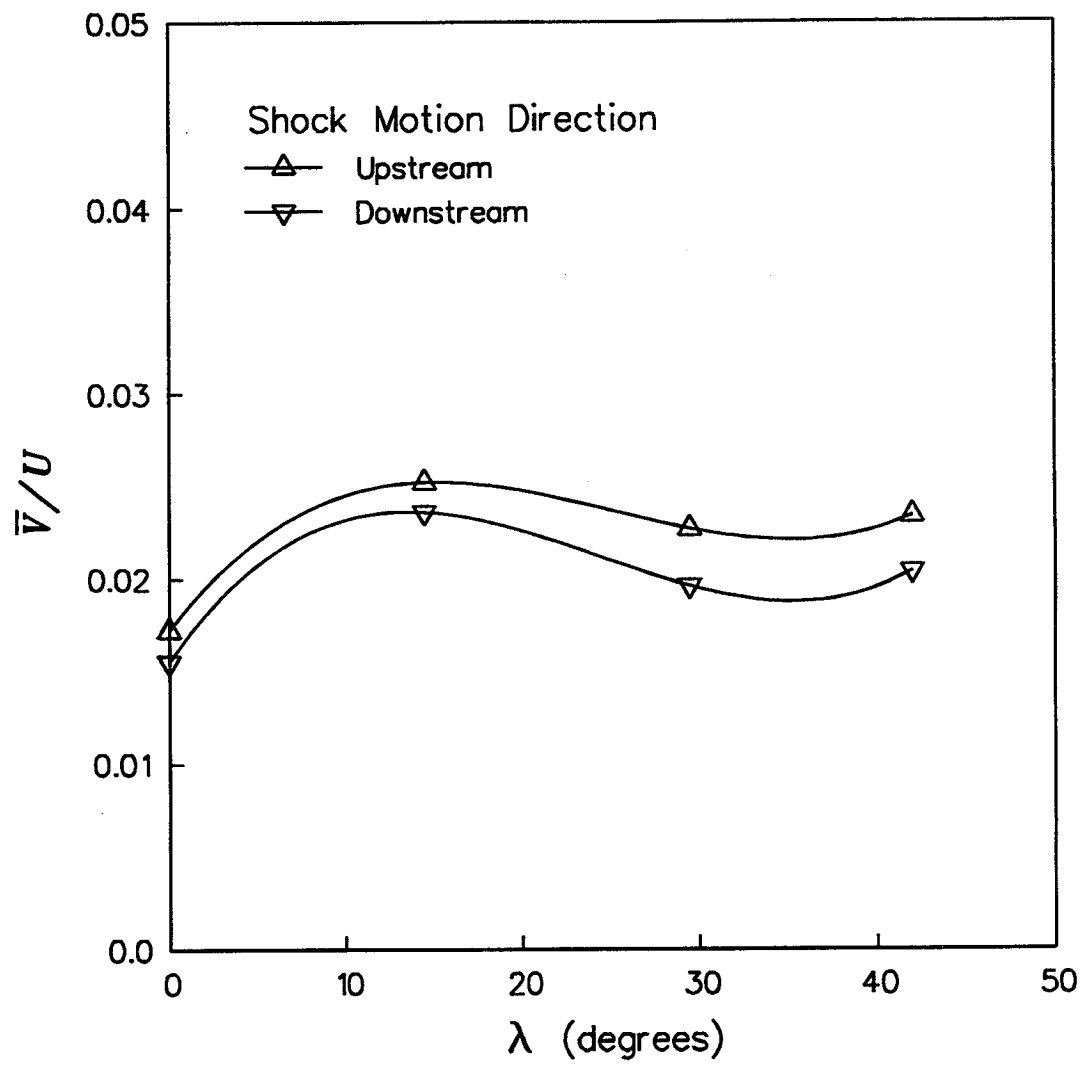
Figure 87   Mach 3.0 Mean Shock Velocity
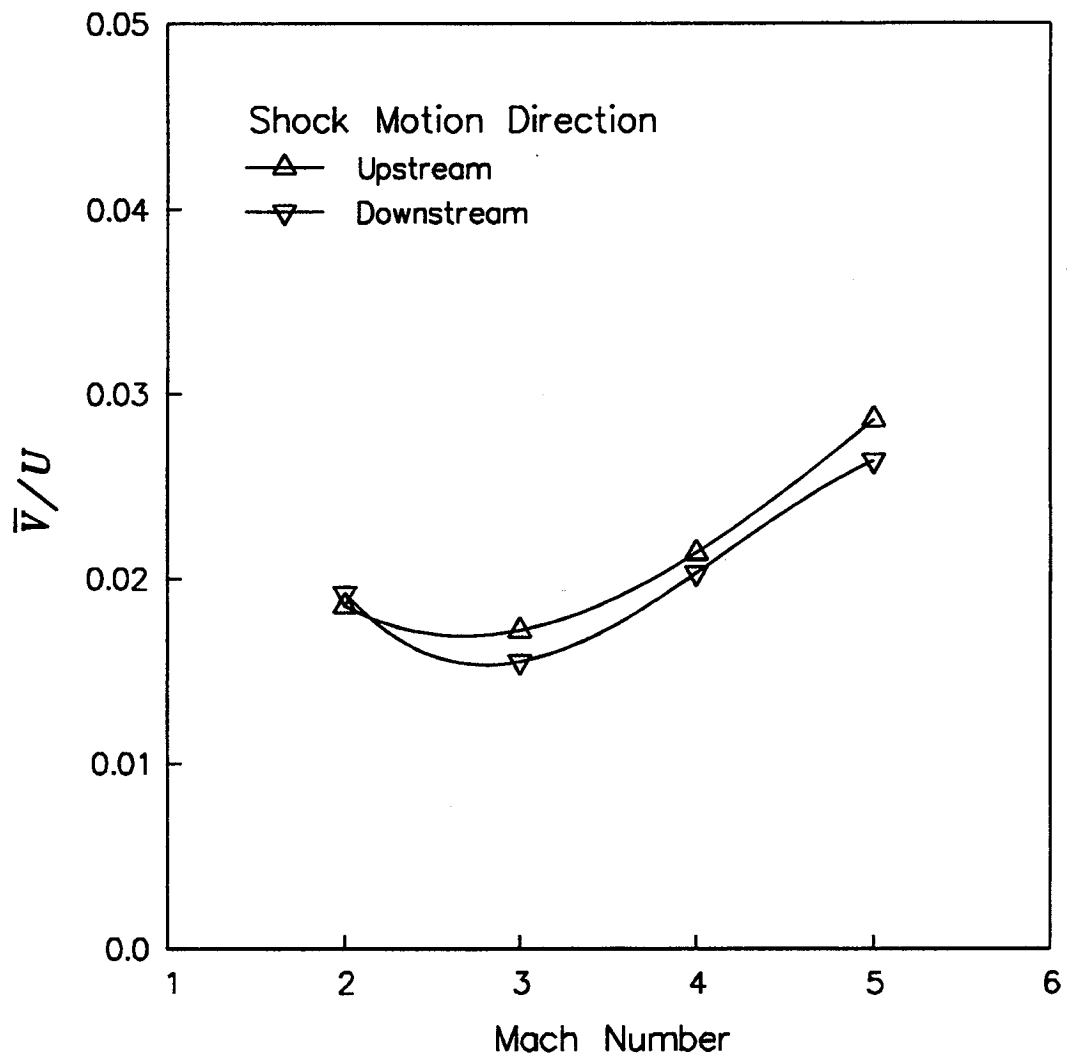
Figure 88   Centerline Mean Shock Velocity
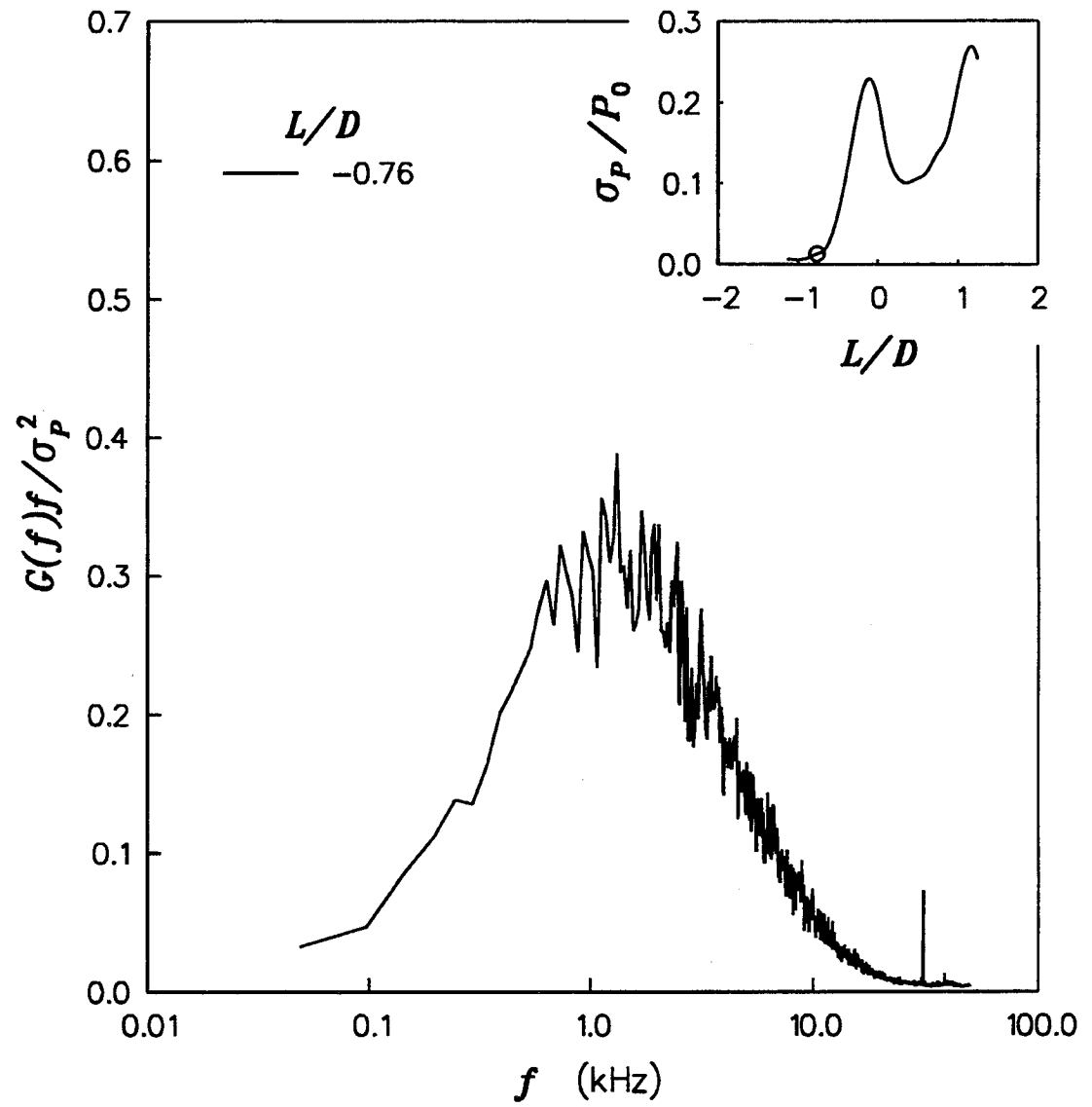
Figure 89   Mach 3.0 Centerline Power Spectra (1 of 5)
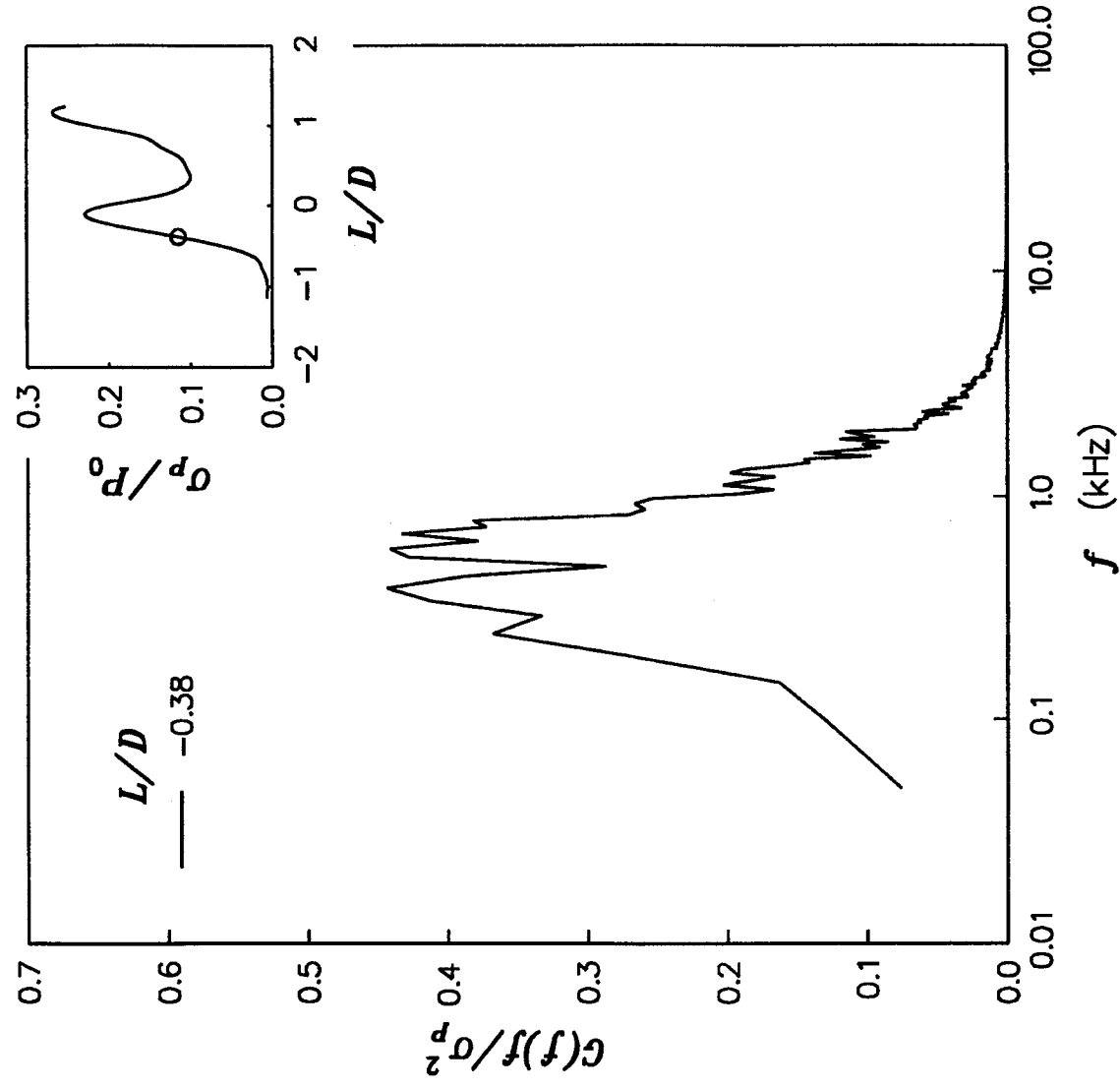
Figure 90   Mach 3.0 Centerline Power Spectra (2 of 5)
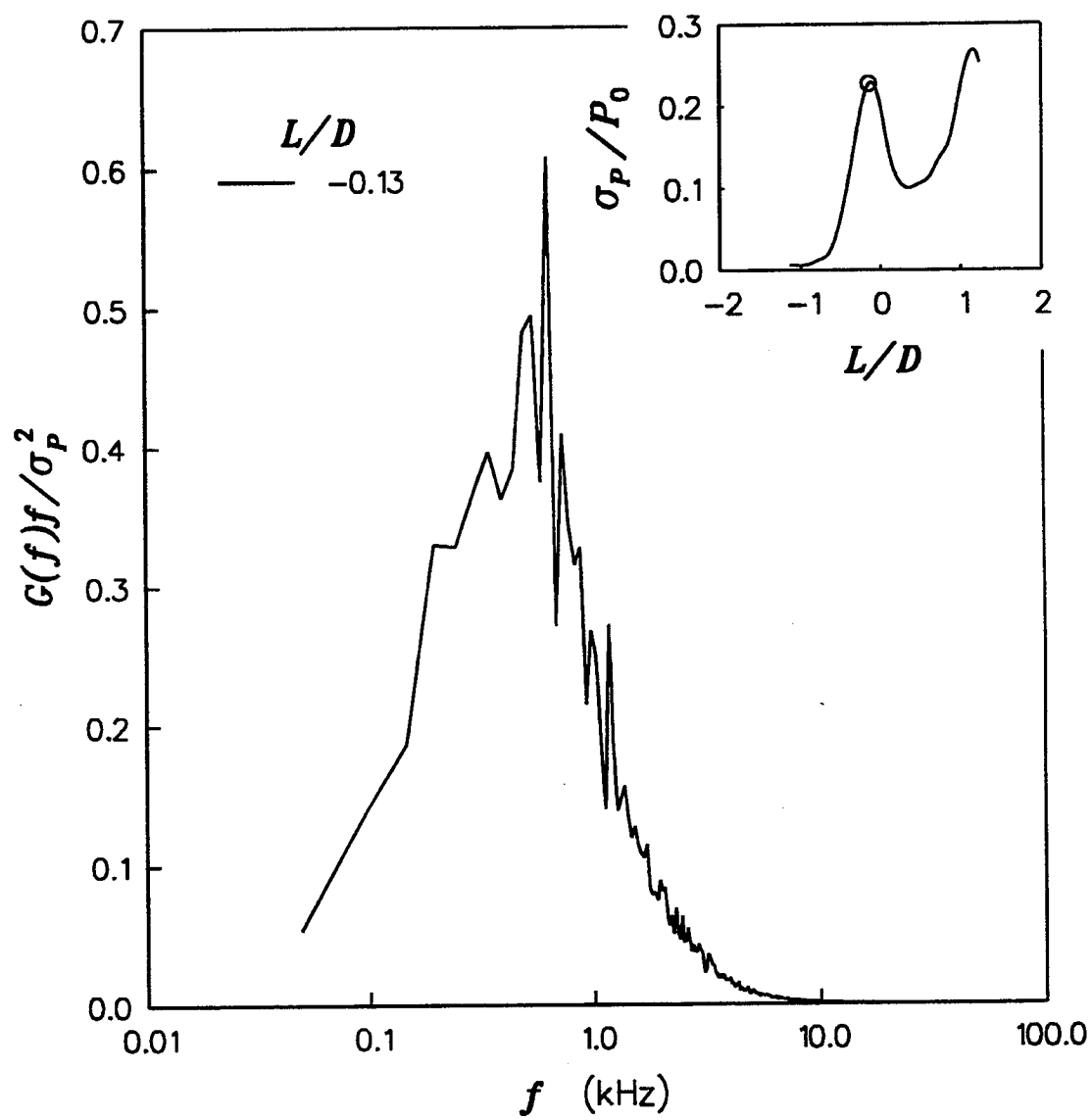
Figure 91   Mach 3.0 Centerline Power Spectra (3 of 5)
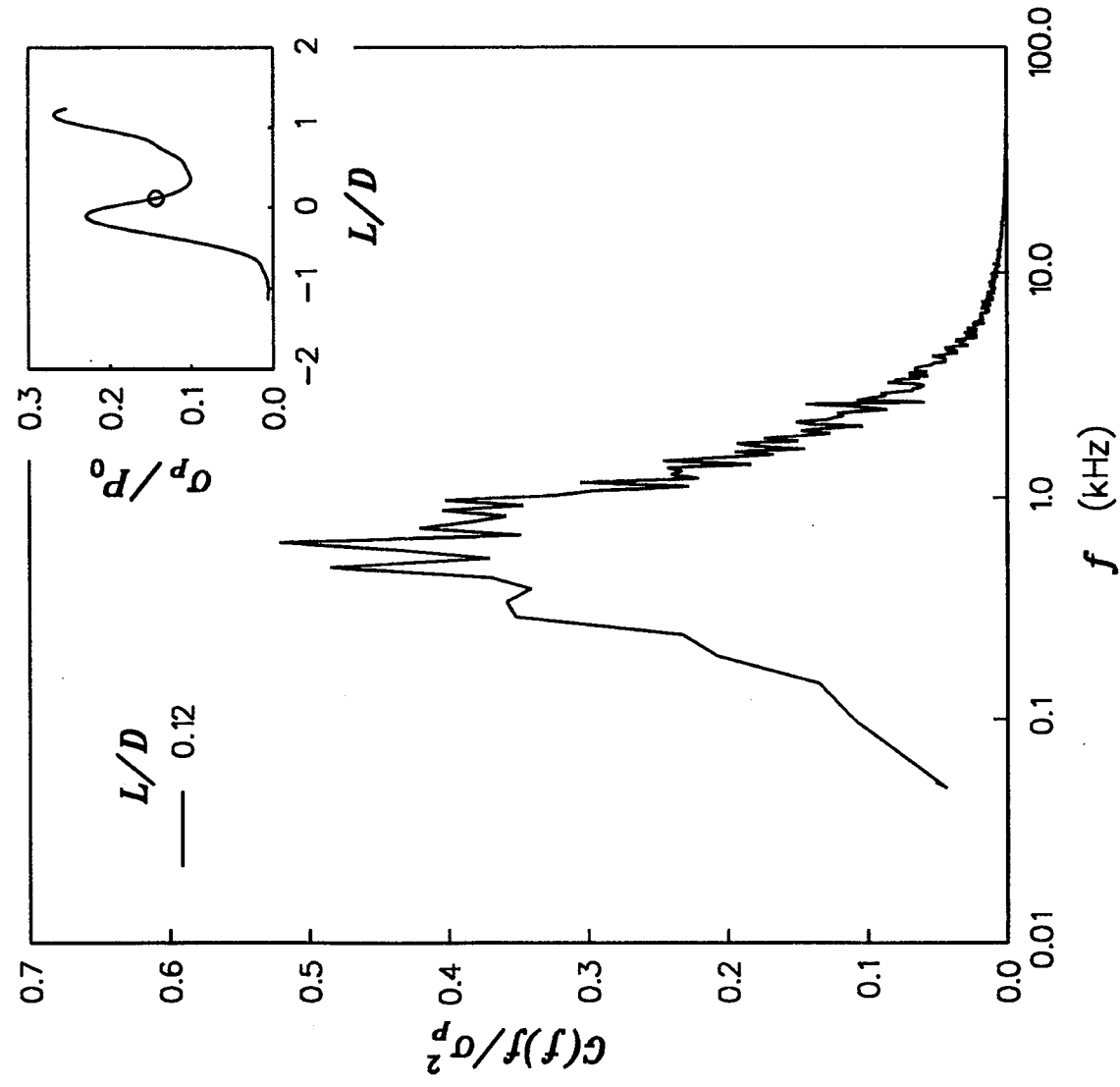
Figure 92   Mach 3.0 Centerline Power Spectra (4 of 5)

210
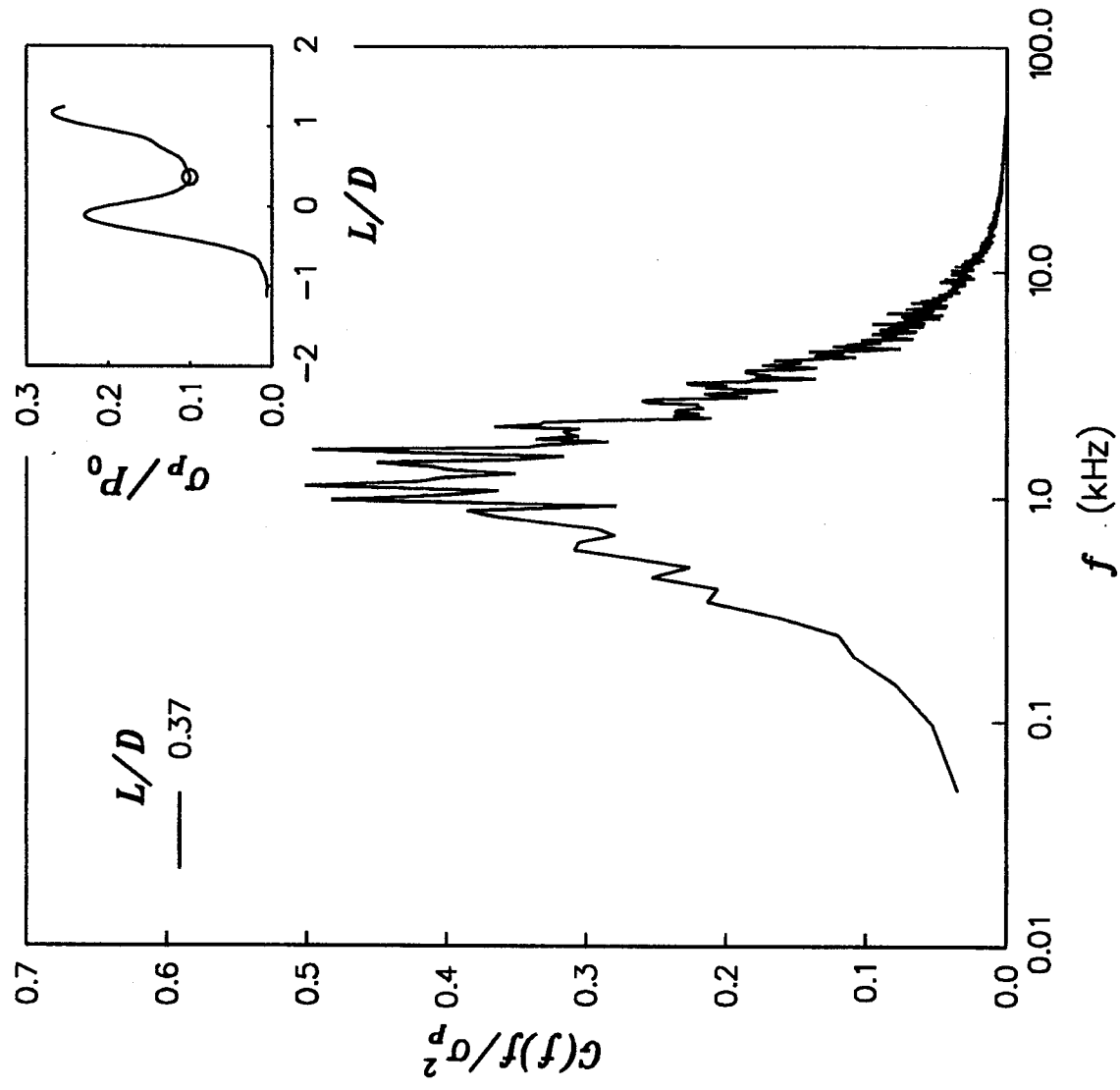
Figure 93   Mach 3.0 Centerline Power Spectra (5 of 5)
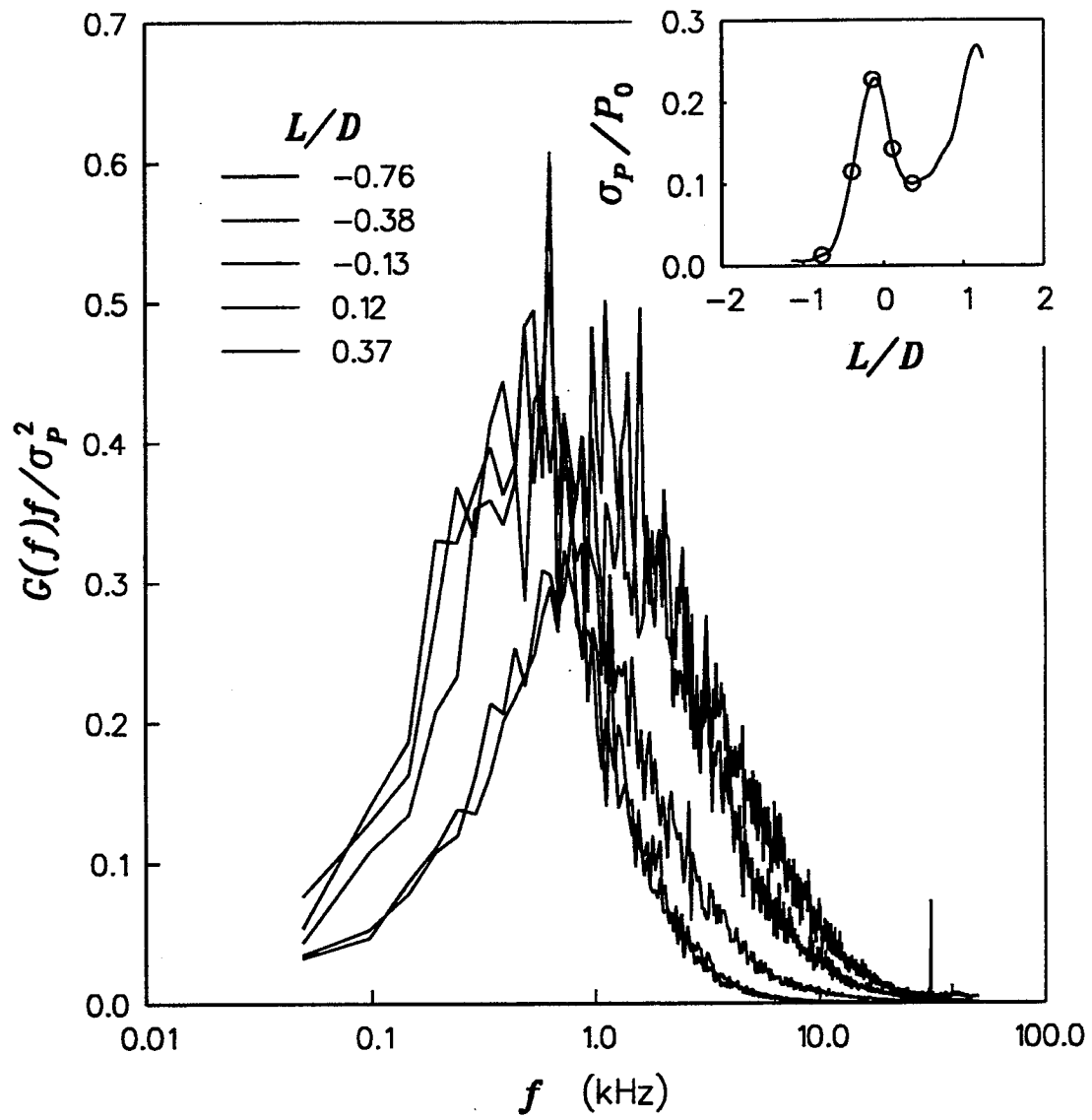
Figure 94   Mach 3.0 Centerline Power Spectra Comparison
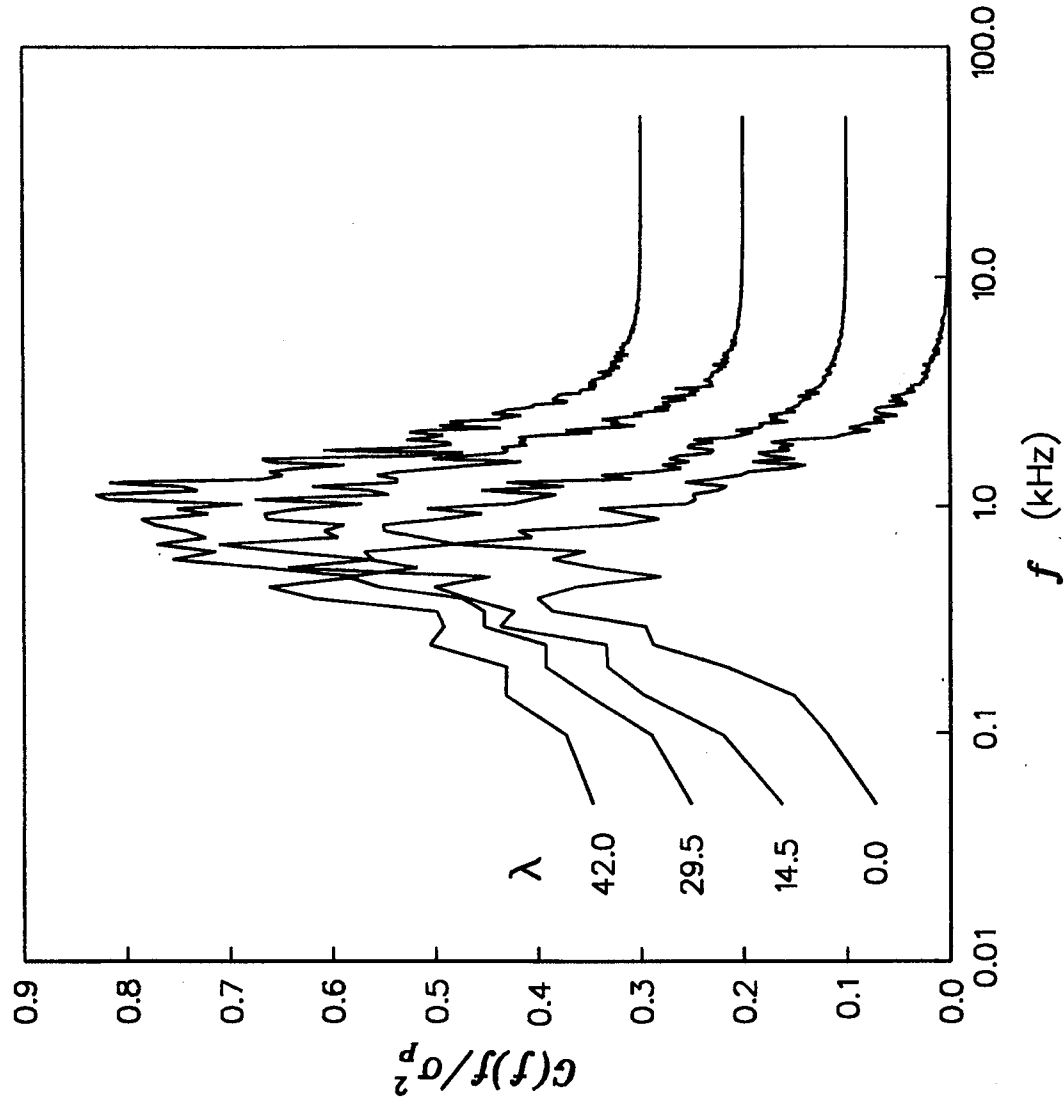
Figure 95   Mach 3.0 Power Spectra
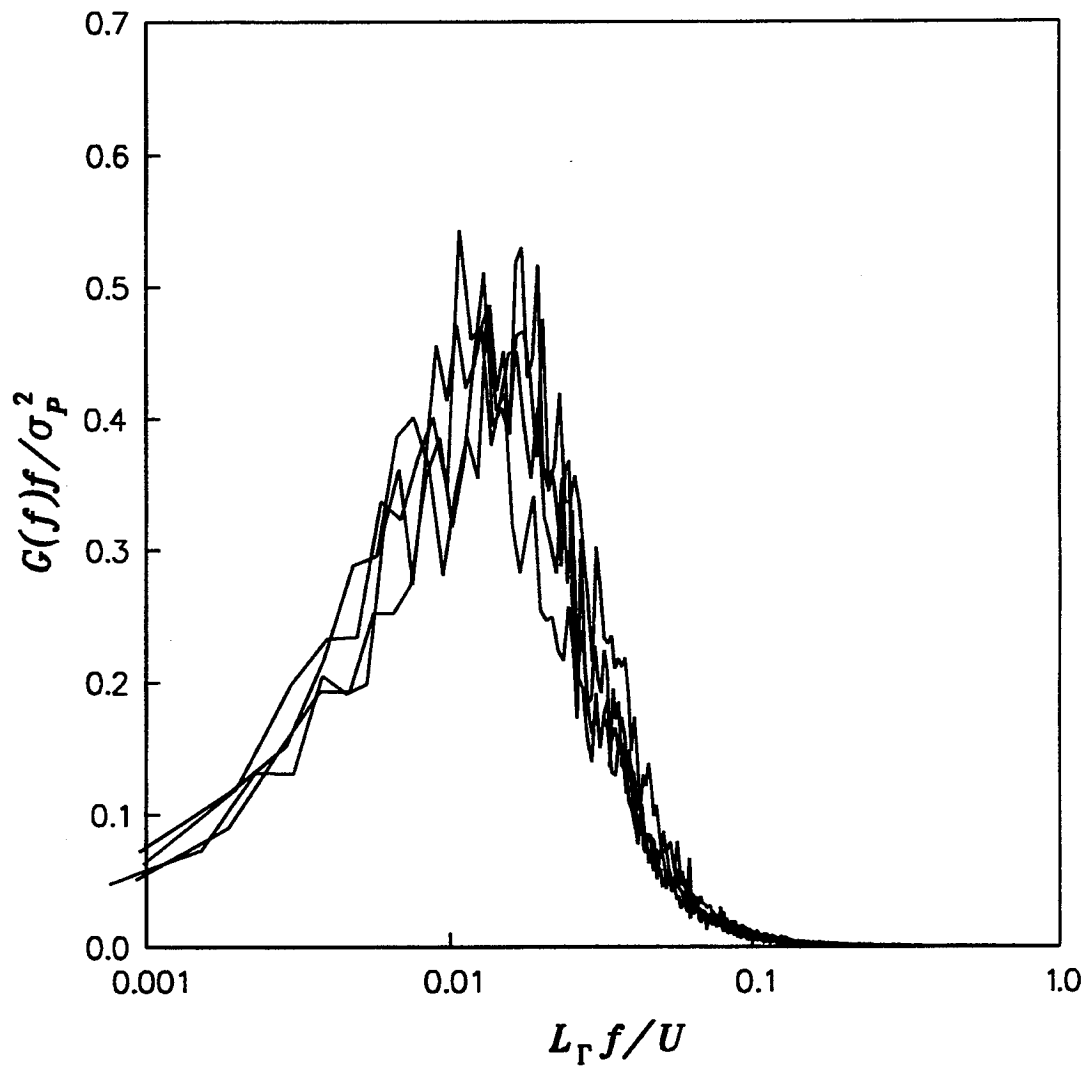
Figure 96   Mach 3.0 Power Spectra Comparison
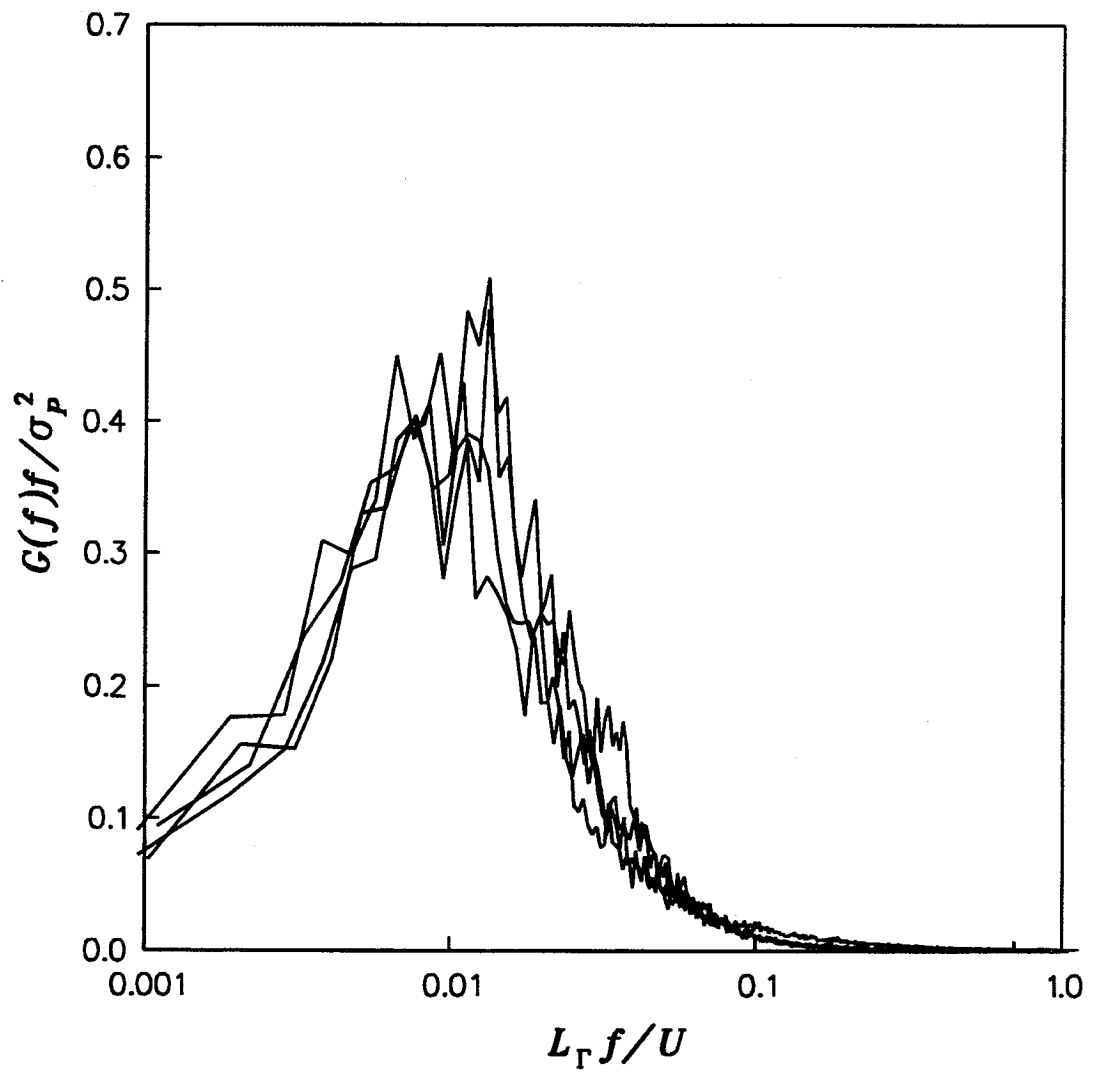
Figure 97   Centerline Power Spectra Comparison Mach Numbers 2.0, 3.0, 4.0, and 5.0
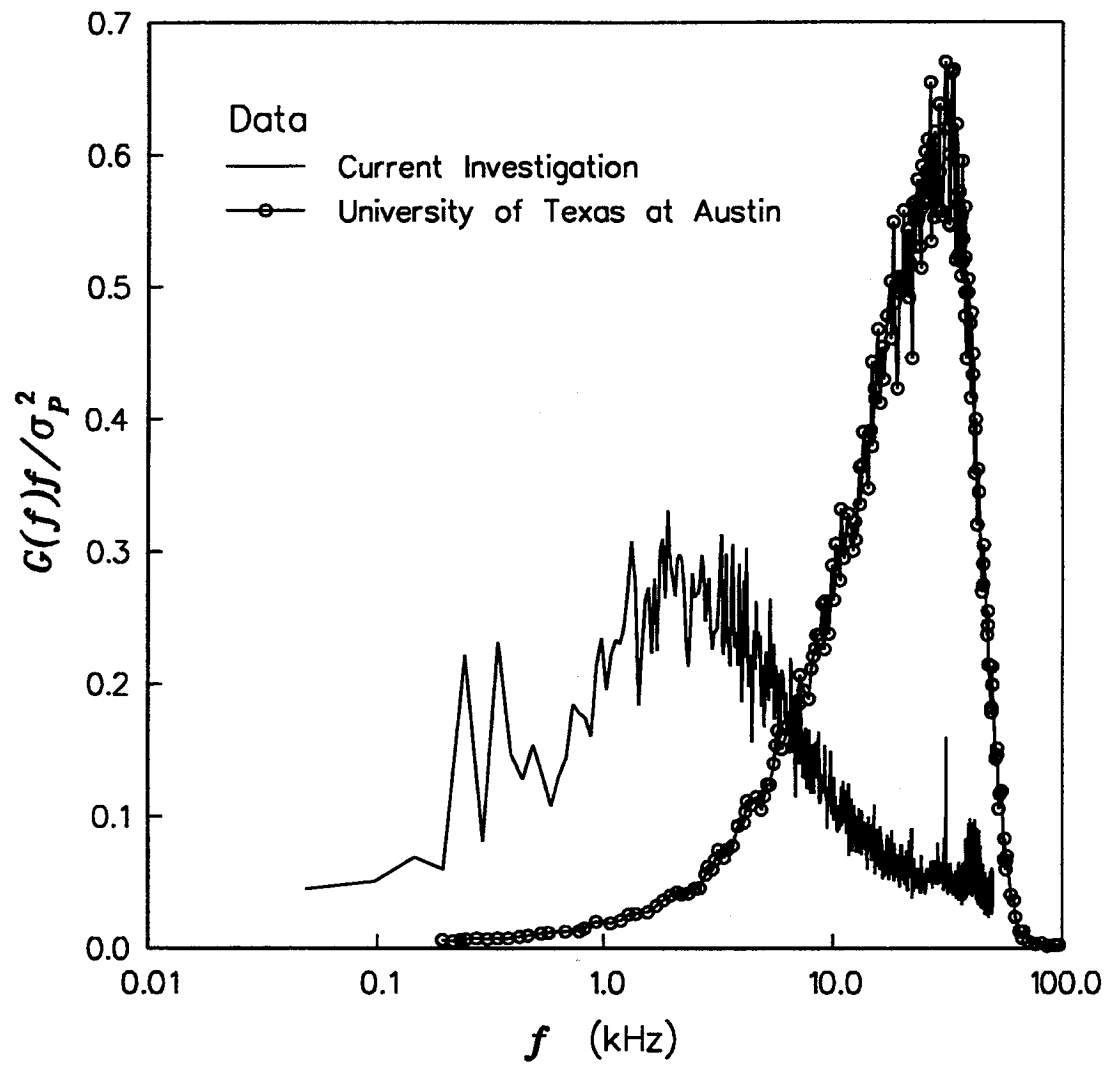
Figure 98   Mach 5.0 Incoming Boundary Layer Power Spectra
Comparison
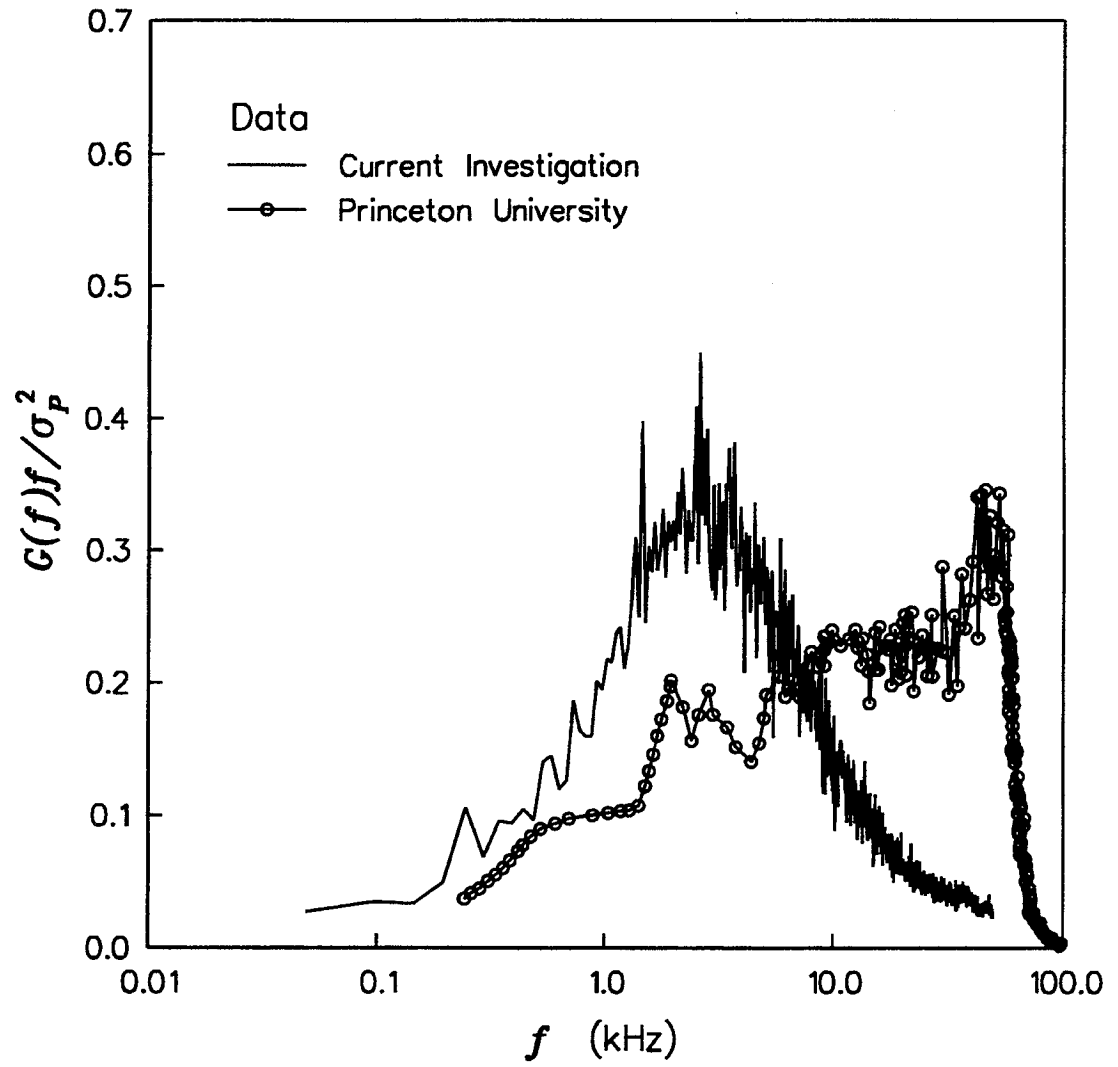
Figure 99   Mach 3.0 Incoming Boundary Layer Power Spectra
                   Comparison
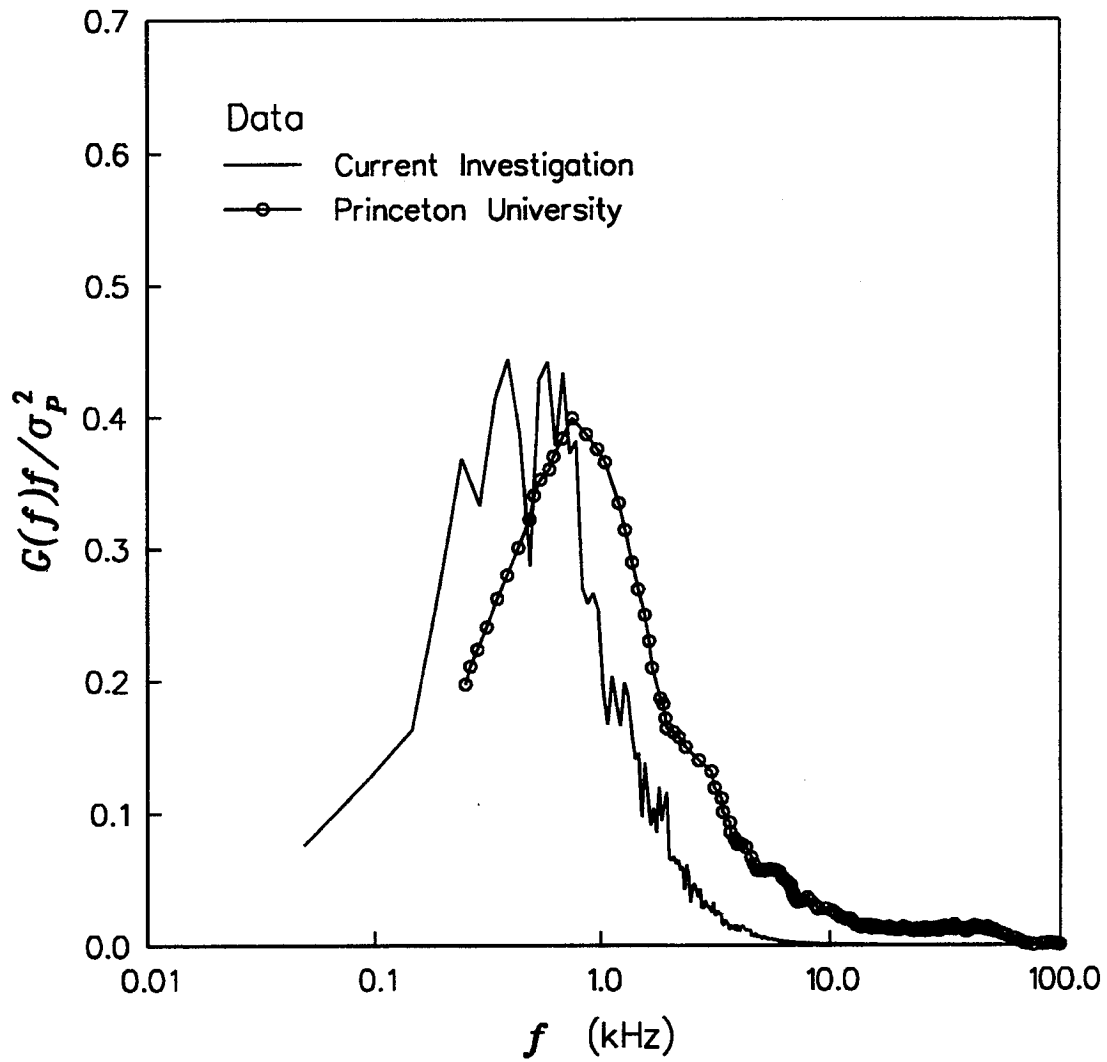
Figure 100   Mach 3.0 Intermittent Region Centerline Power Spectra
              Comparison
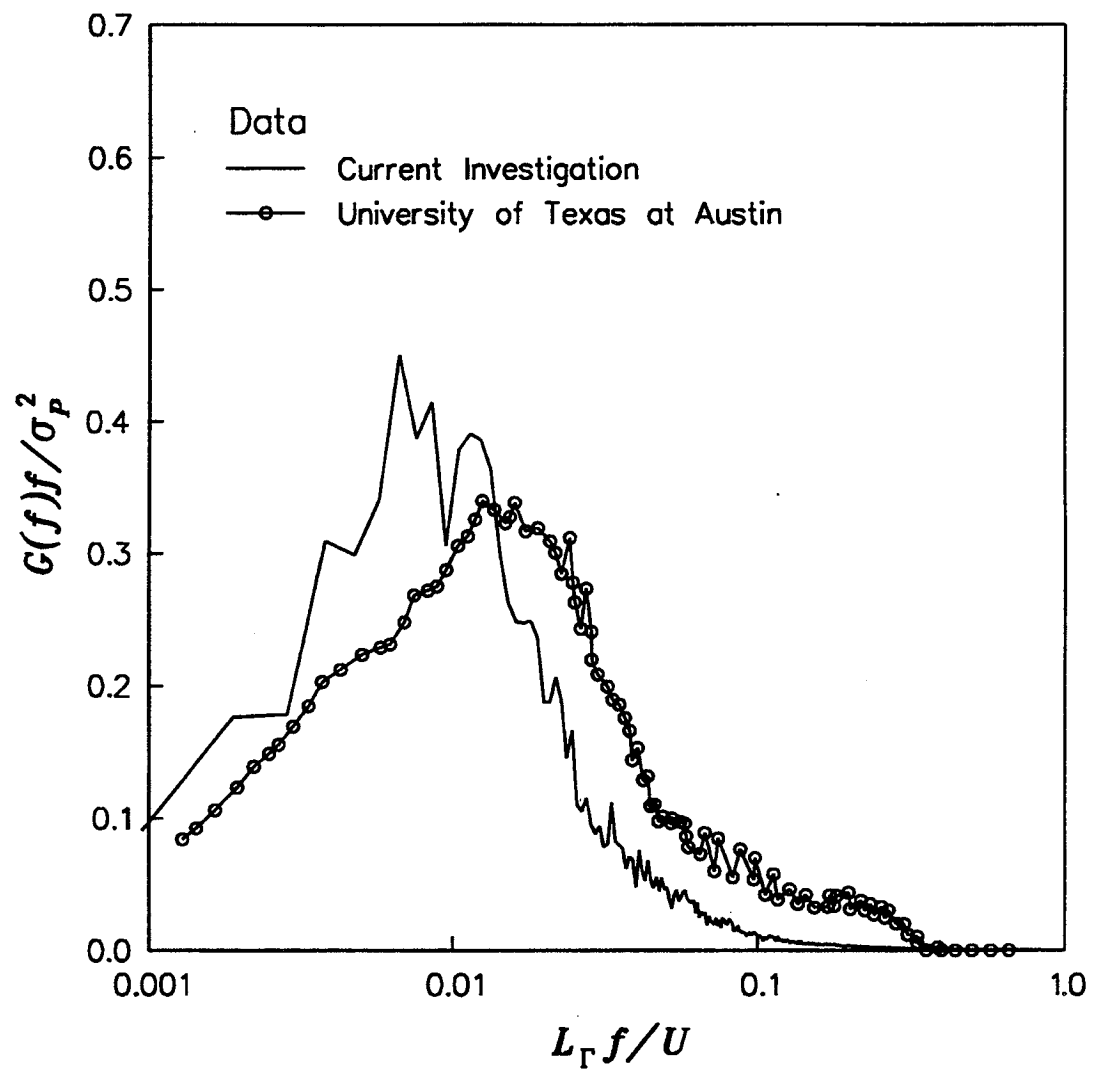
Figure 101   Mach 5.0 Intermittent Region Centerline Power Spectra Comparison
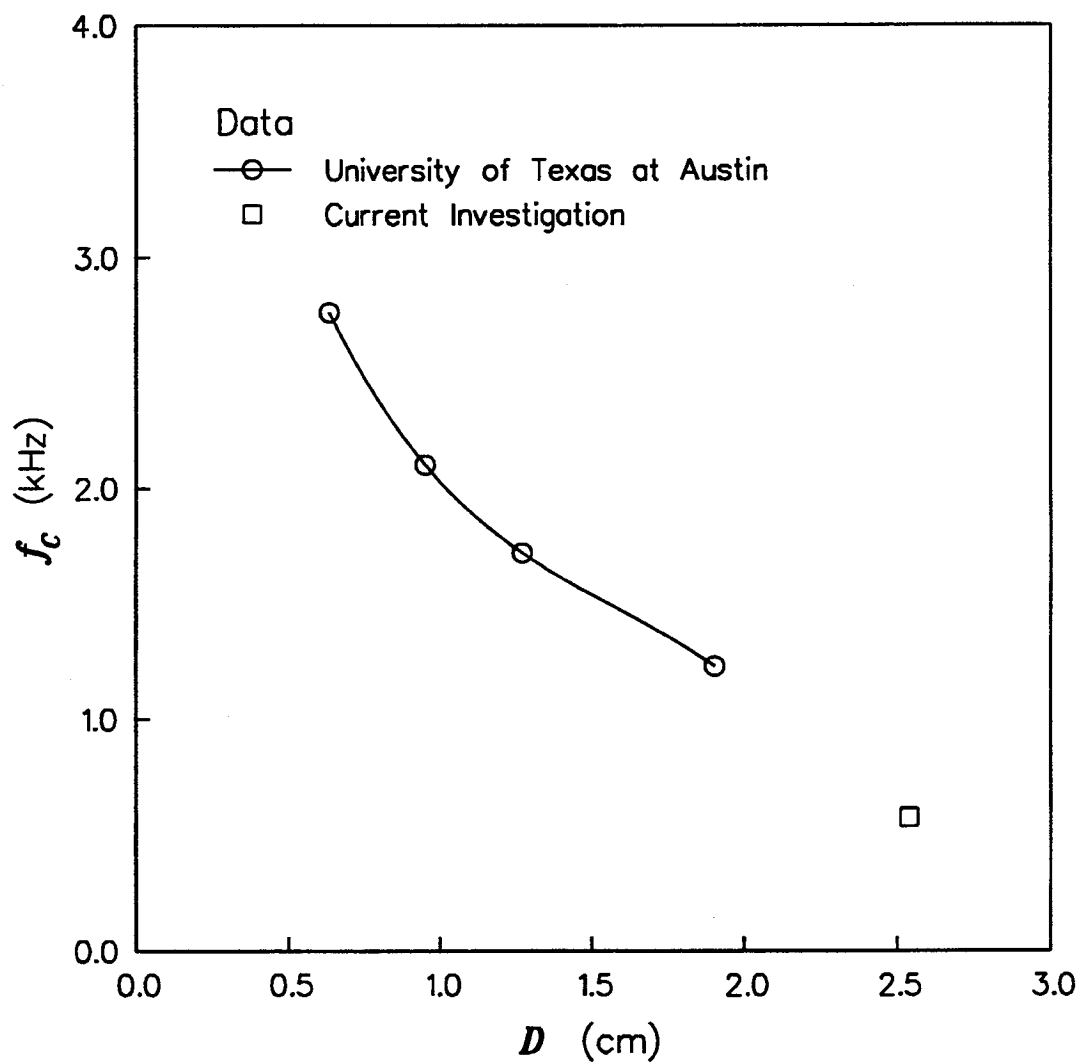
Figure 102   Mach 5.0 Centerline Maximum Zero-Crossing Frequency
Comparison
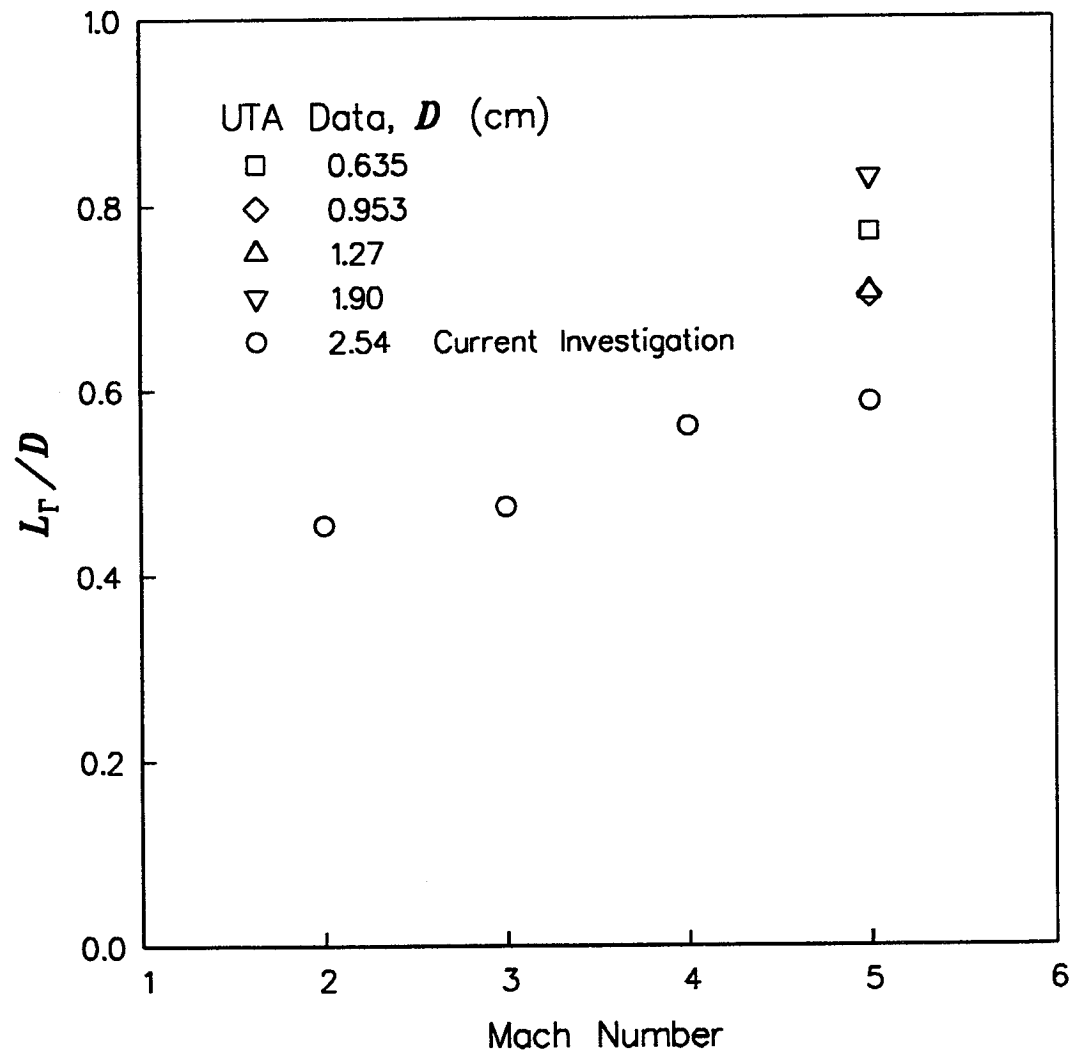
Figure 103   Centerline Intermittent Region Length Comparison
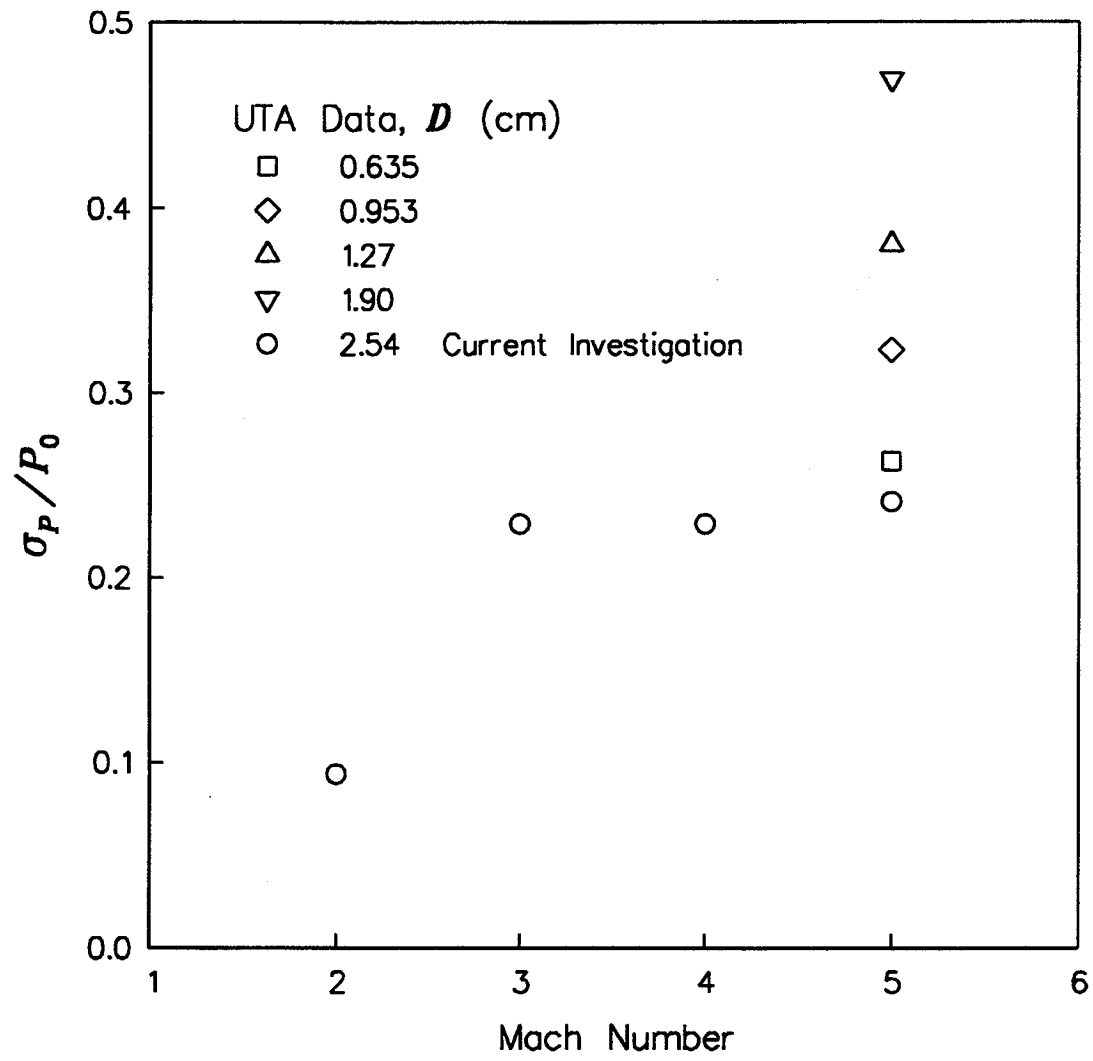
Figure 104   Centerline Maximum Standard Deviation Comparison
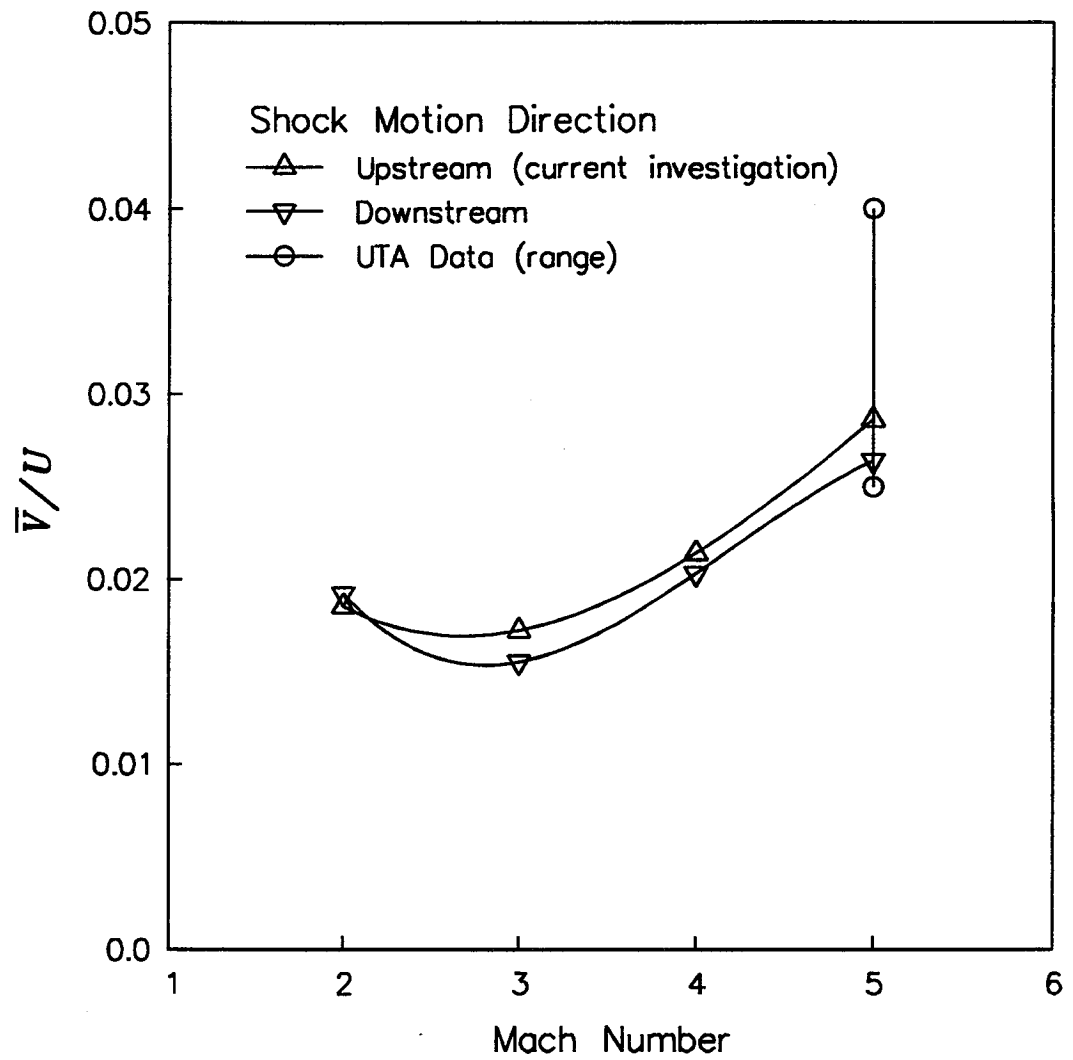
Figure 105   Centerline Mean Shock Velocity Comparison
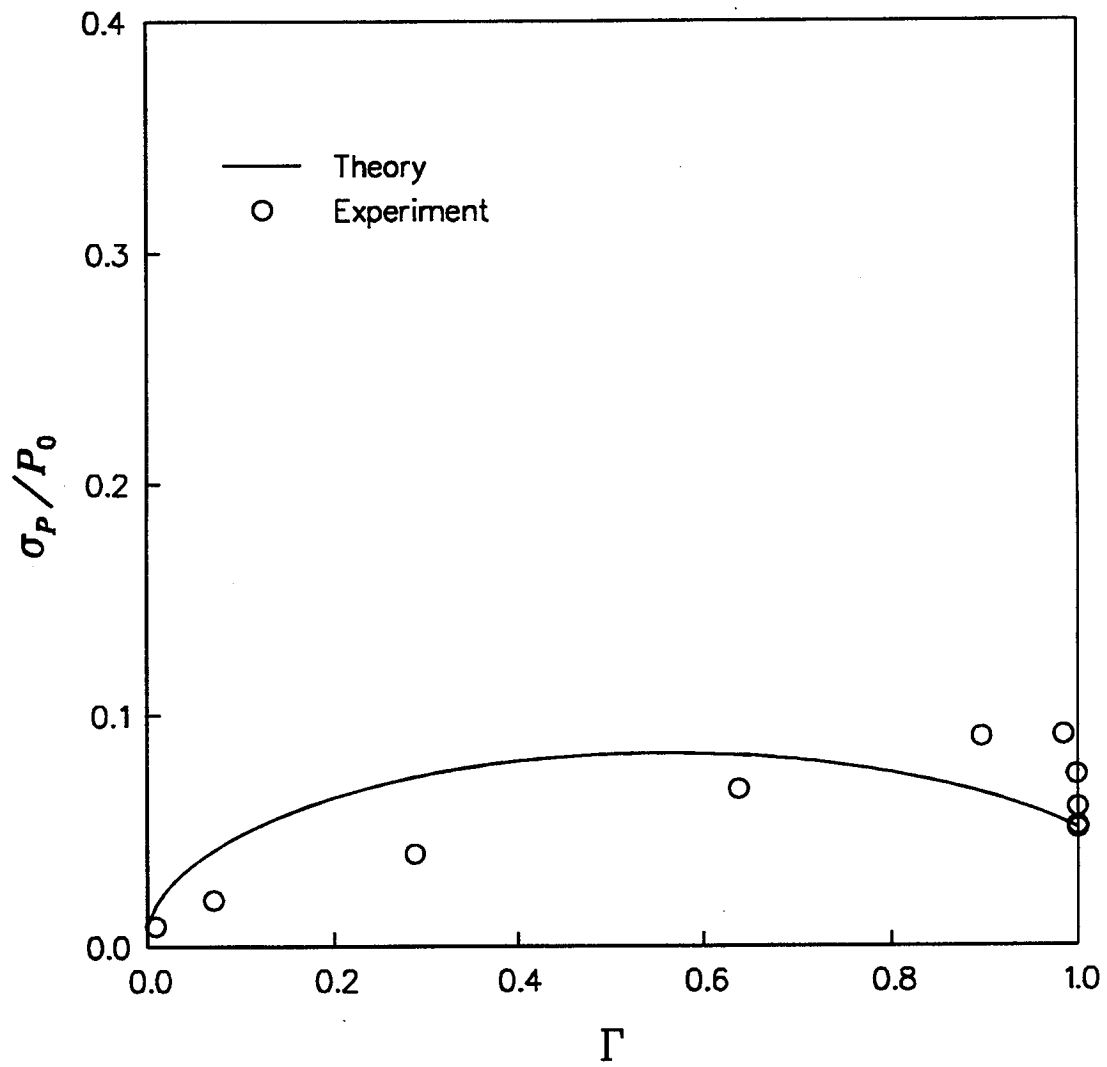
Figure 106   Mach 2.0 Centerline Standard Deviation Comparison with
              Theory
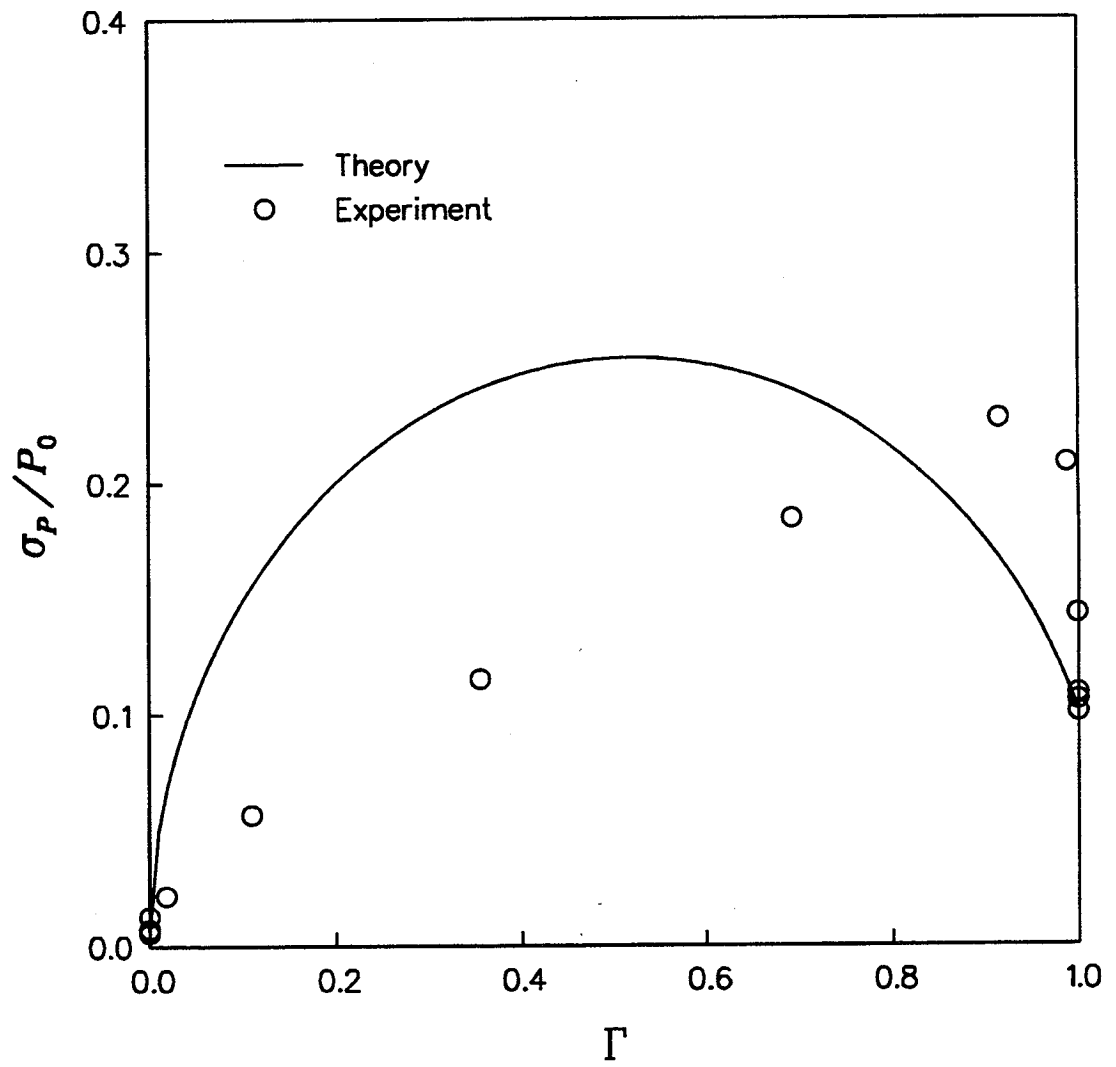
Figure 107   Mach 3.0 Centerline Standard Deviation Comparison with
                     Theory
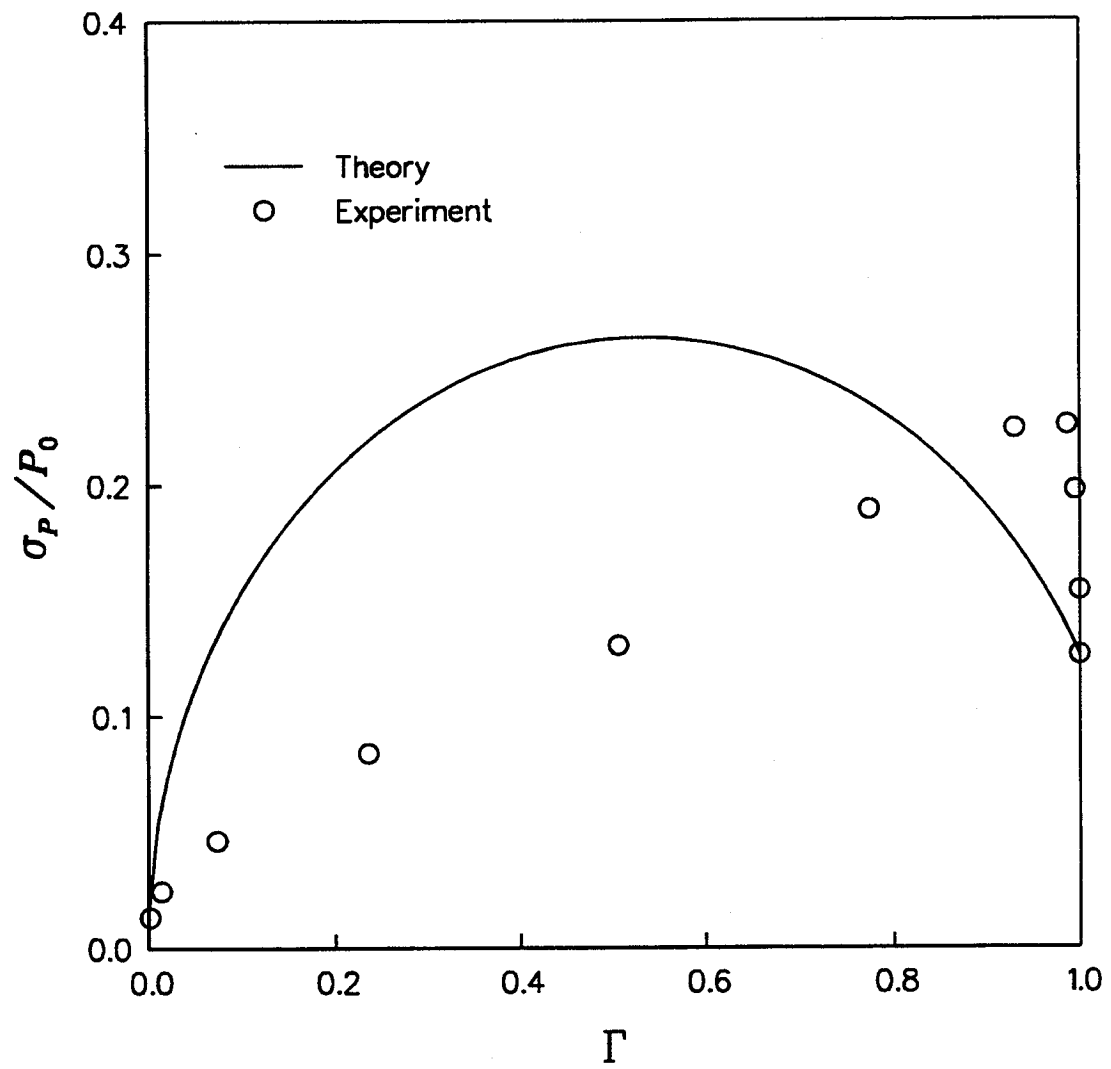
Figure 108   Mach 4.0 Centerline Standard Deviation Comparison with Theory
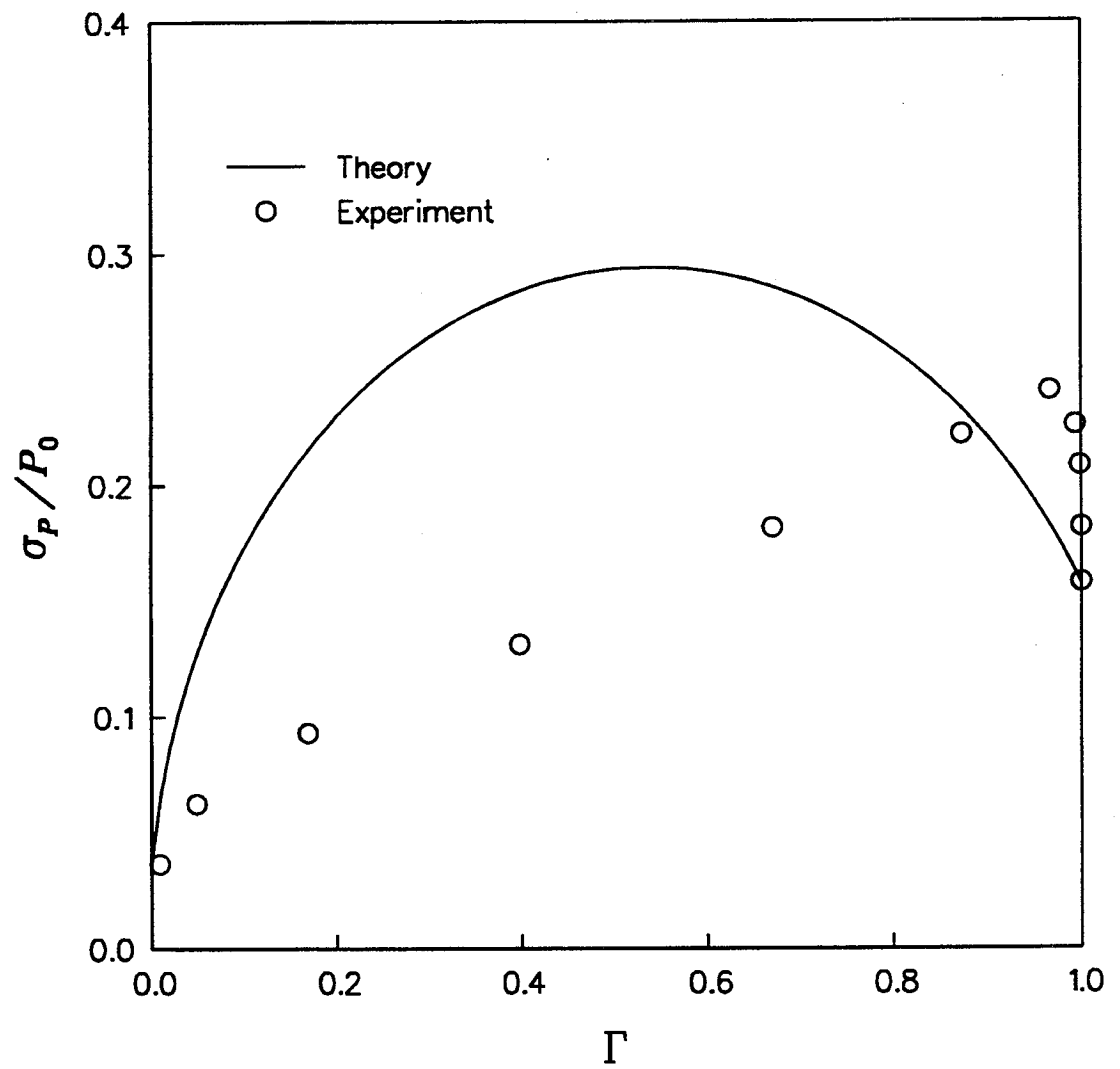
Figure 109   Mach 5.0 Centerline Standard Deviation Comparison with Theory
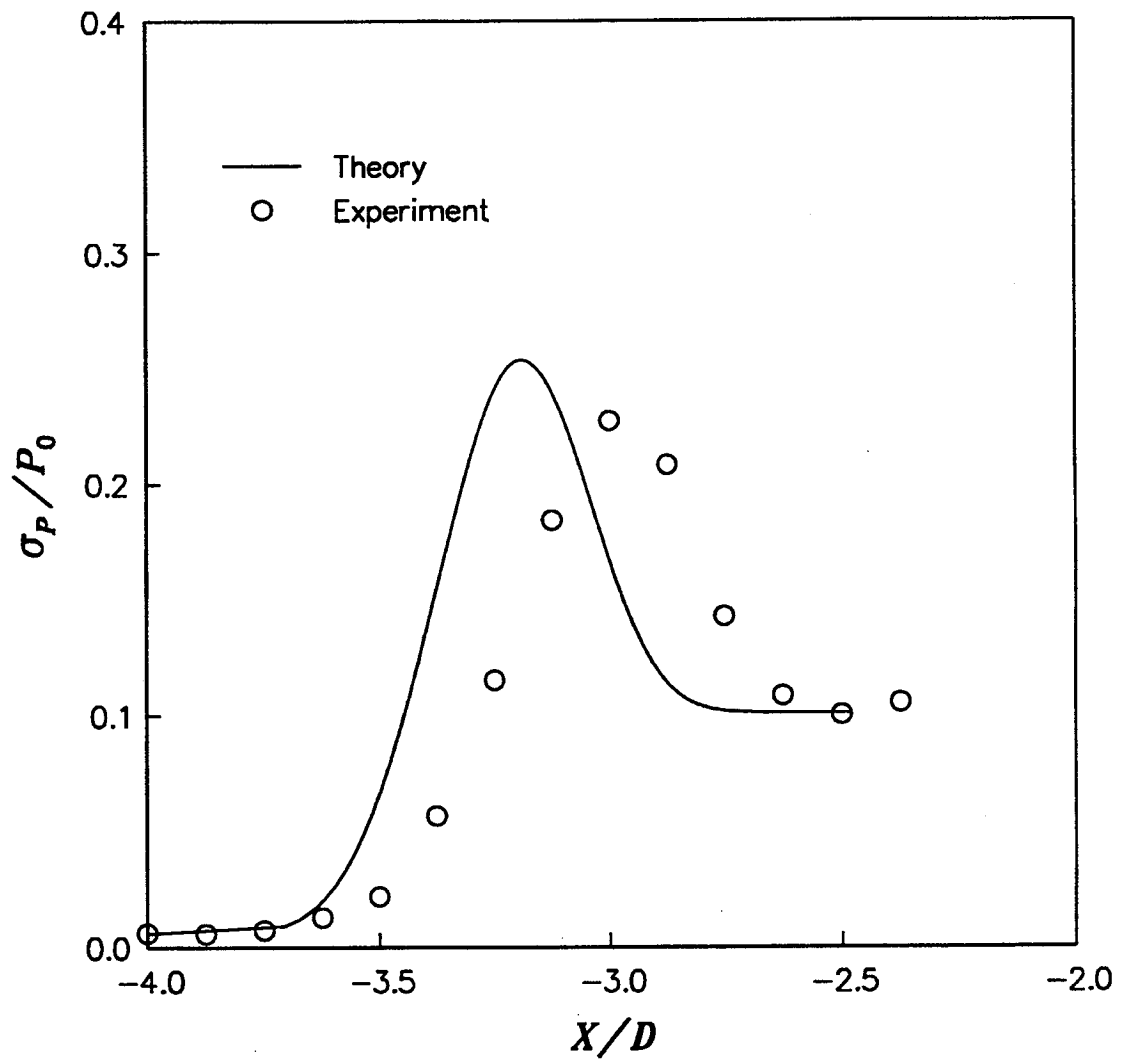
Figure 110   Mach 3.0 Centerline Standard Deviation Comparison with
                Theory in Spatial Coordinates
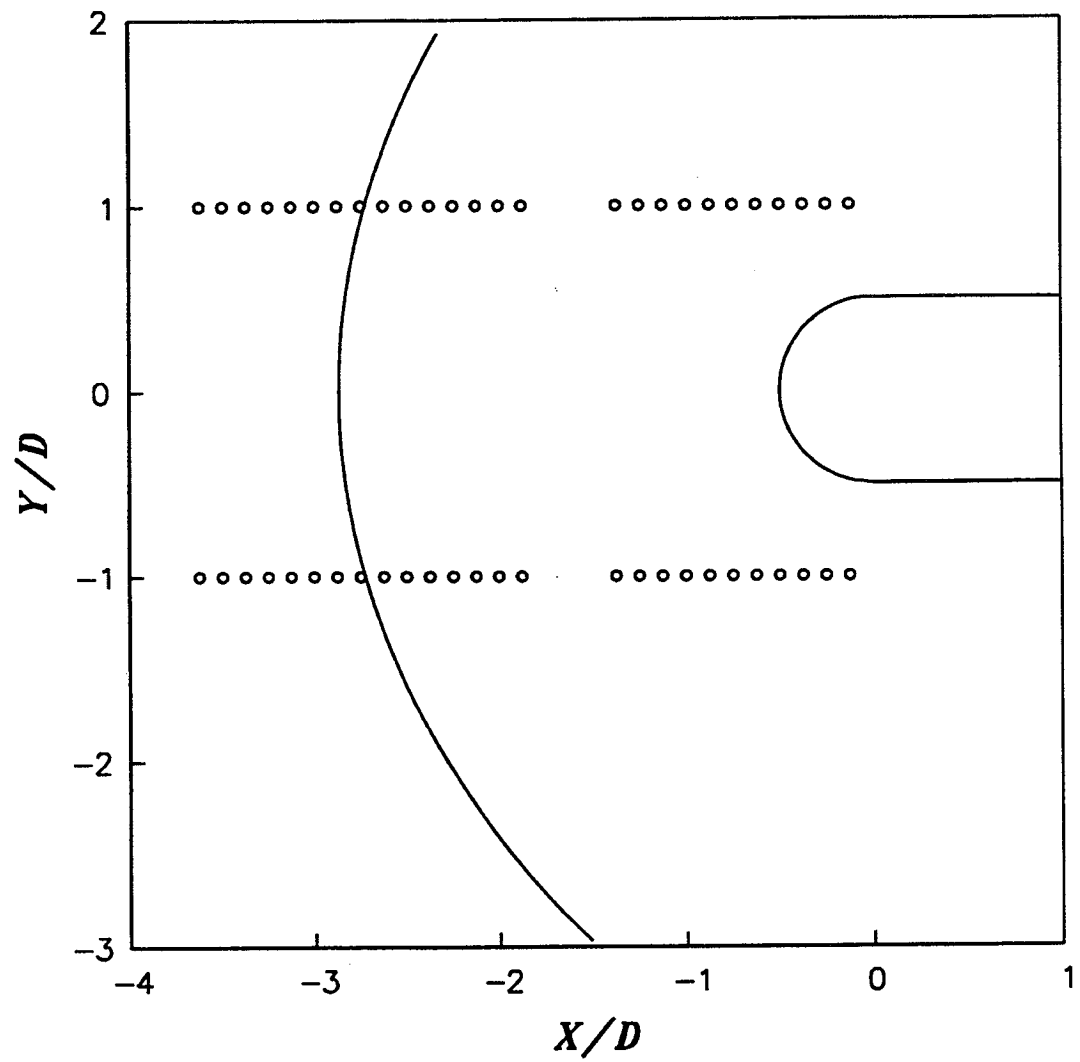
Figure 111   Mach 3.0 Dynamic Pressure Transducer Locations for Latteral Correlation Measurements
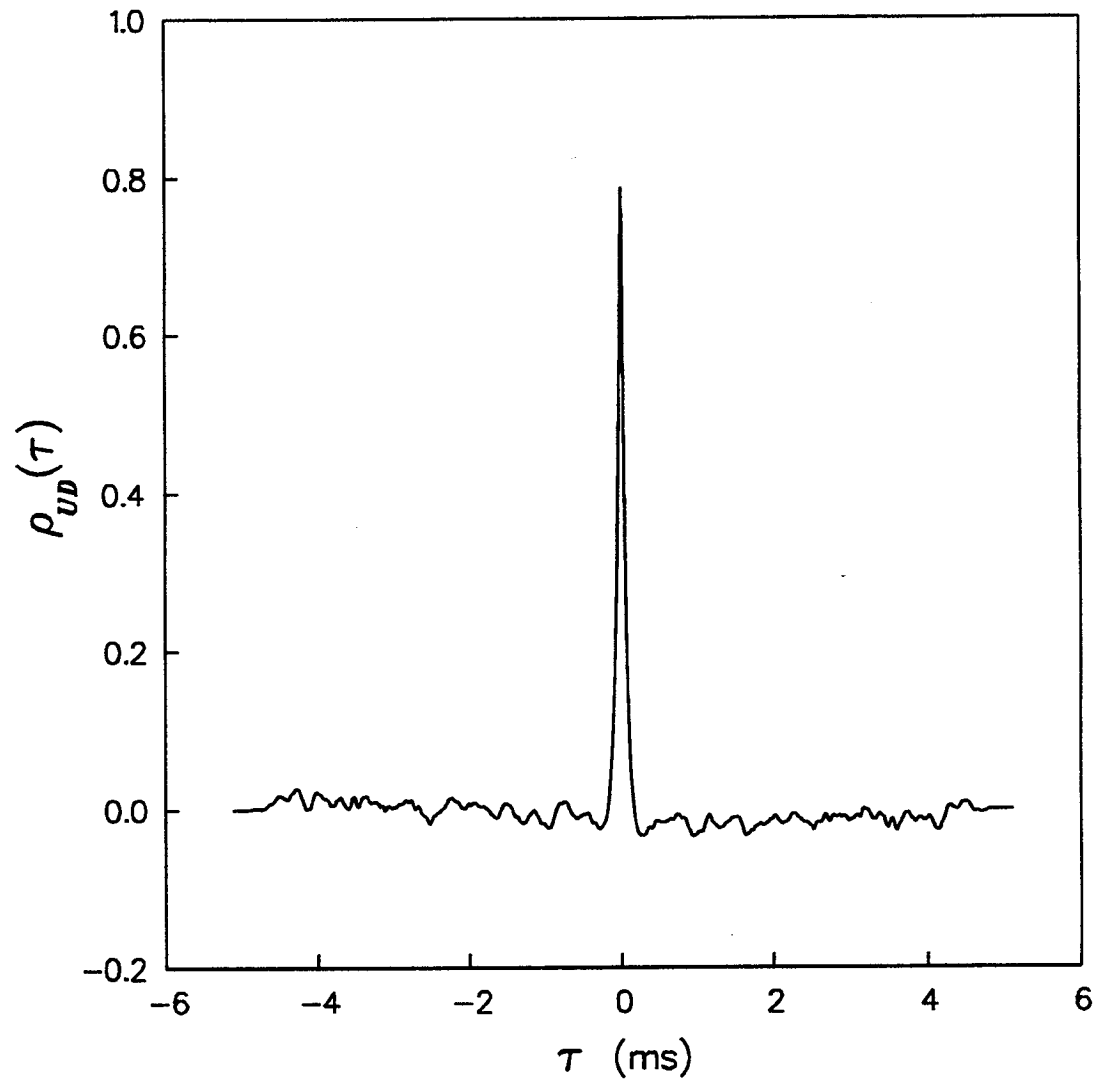
Figure 112   Mach 3.0 Incoming Boundary Layer Longitudinal Cross-Correlation
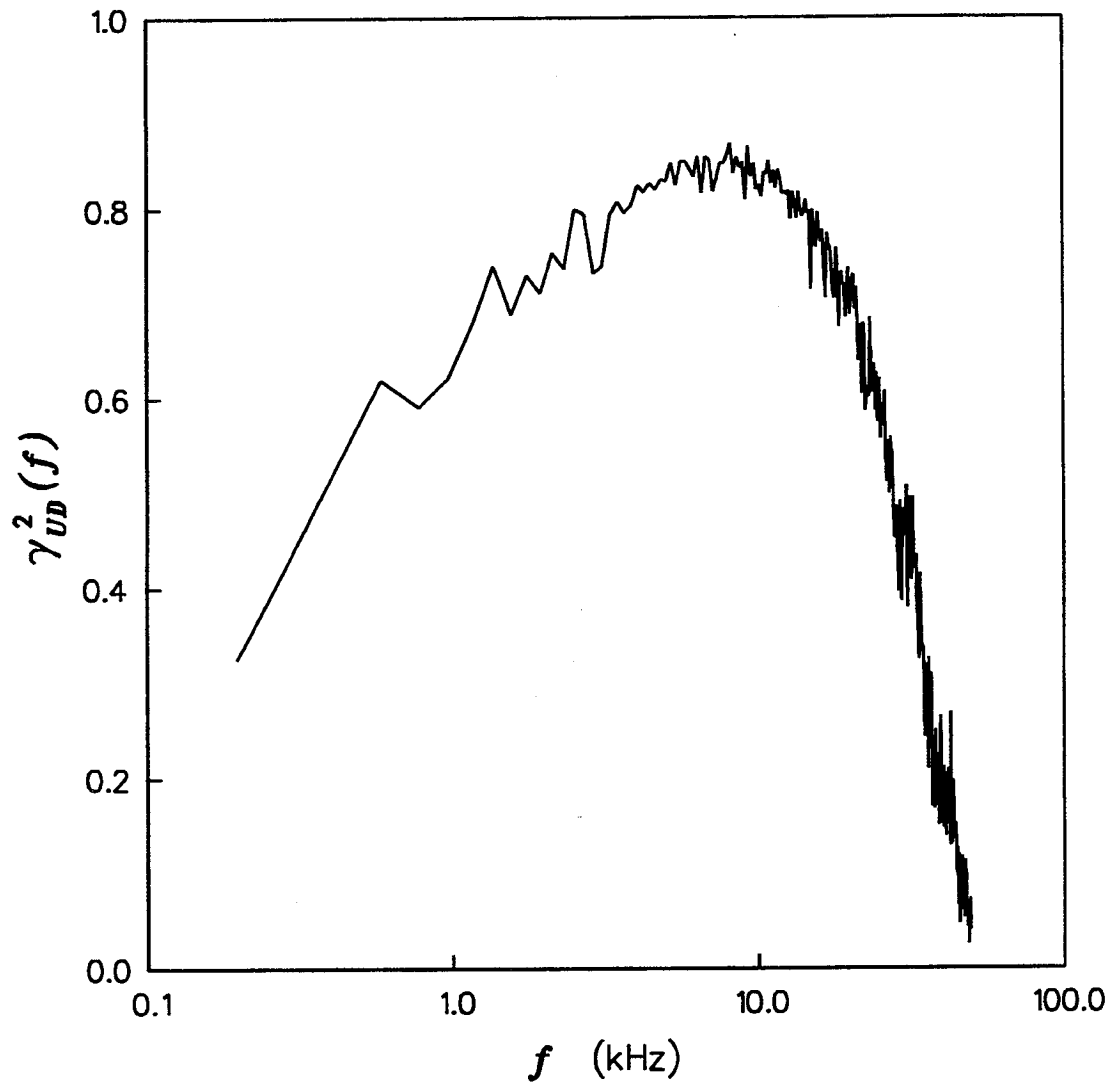
Figure 113 Mach 3.0 Incoming Boundary Layer Longitudinal Coherence Function
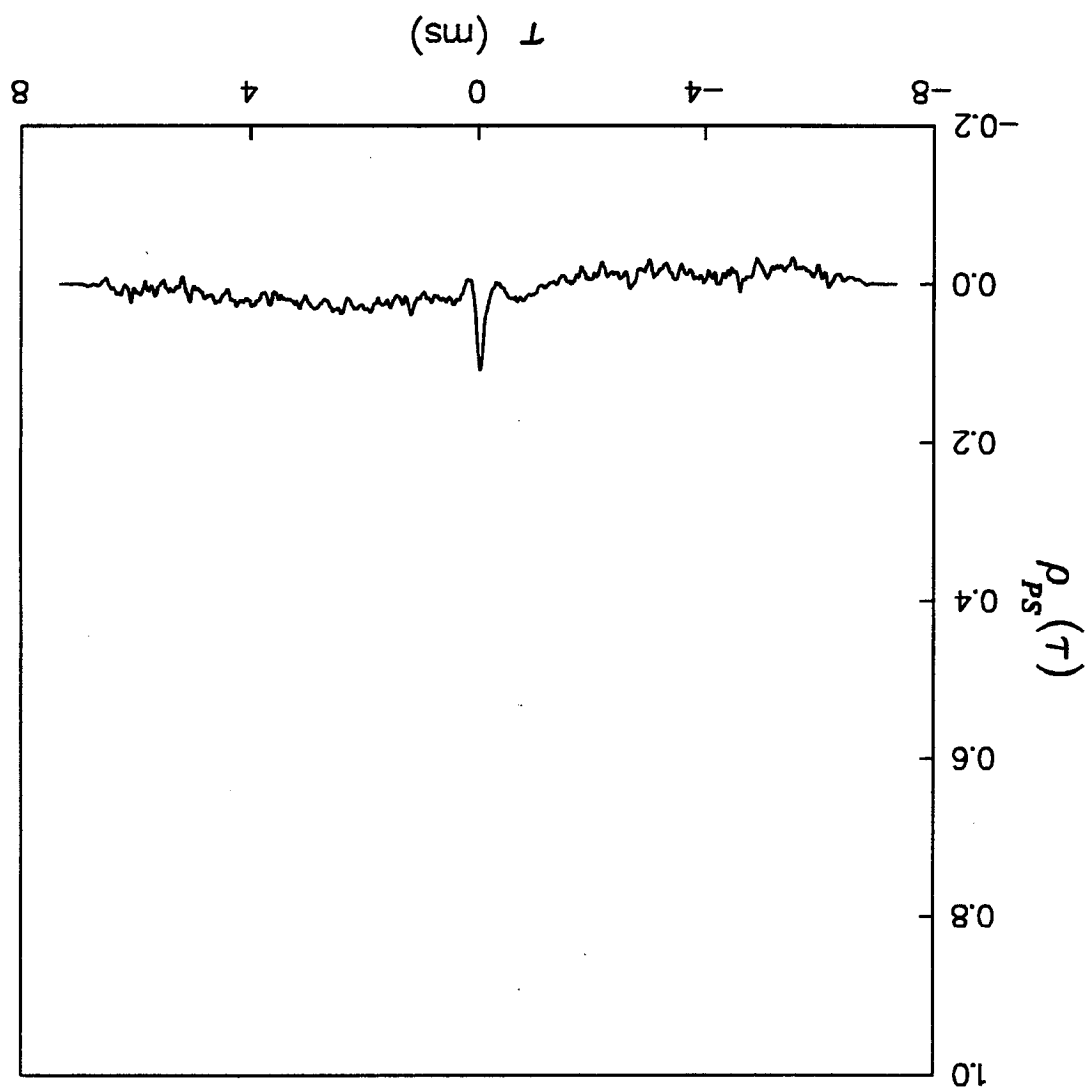
Mach 3.0 Incoming Boundary Layer Lateral Cross-Correlation
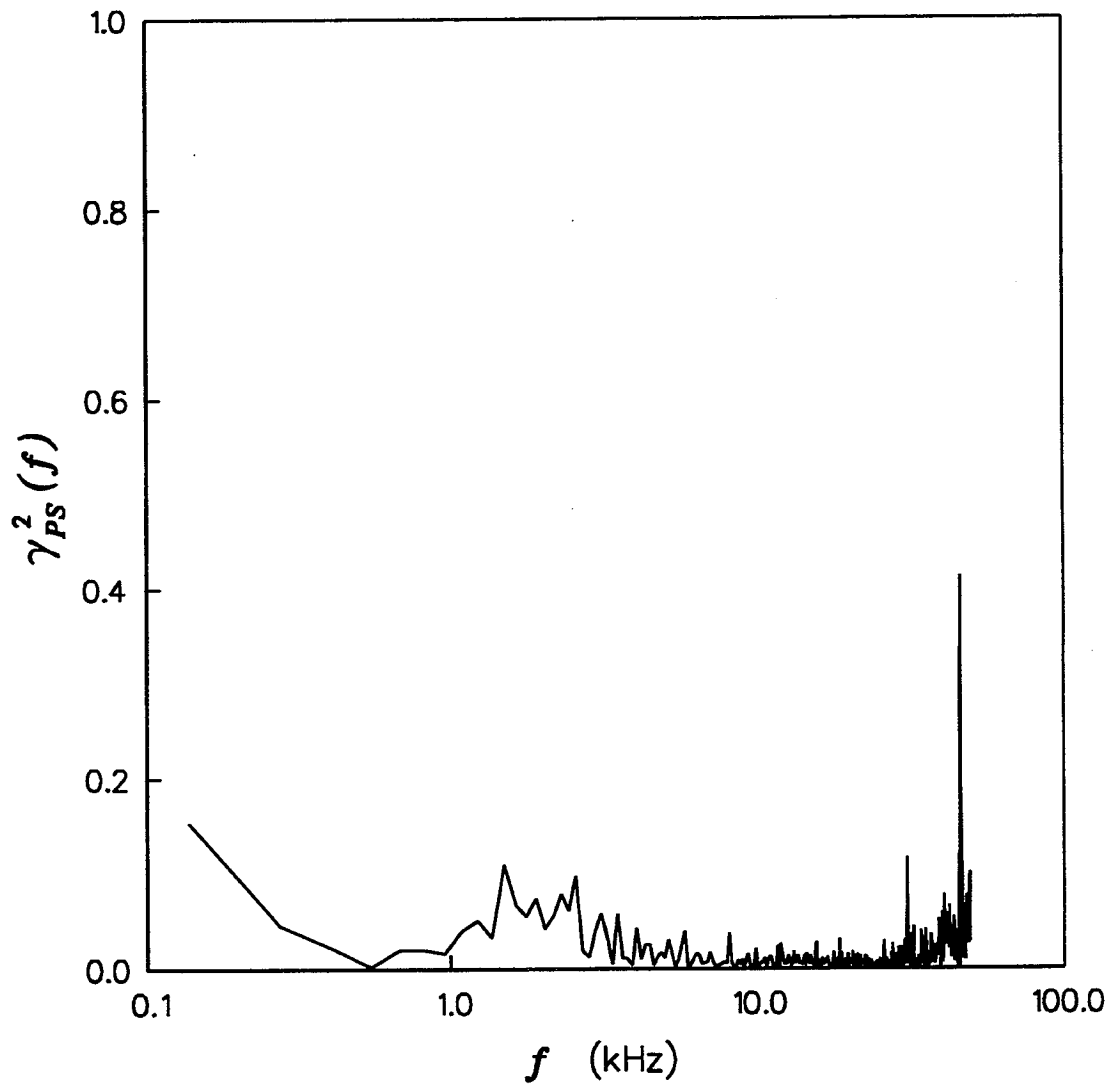
Figure 114

Figure 115   Mach 3.0 Incoming Boundary Layer Lateral Coherence
                    Function
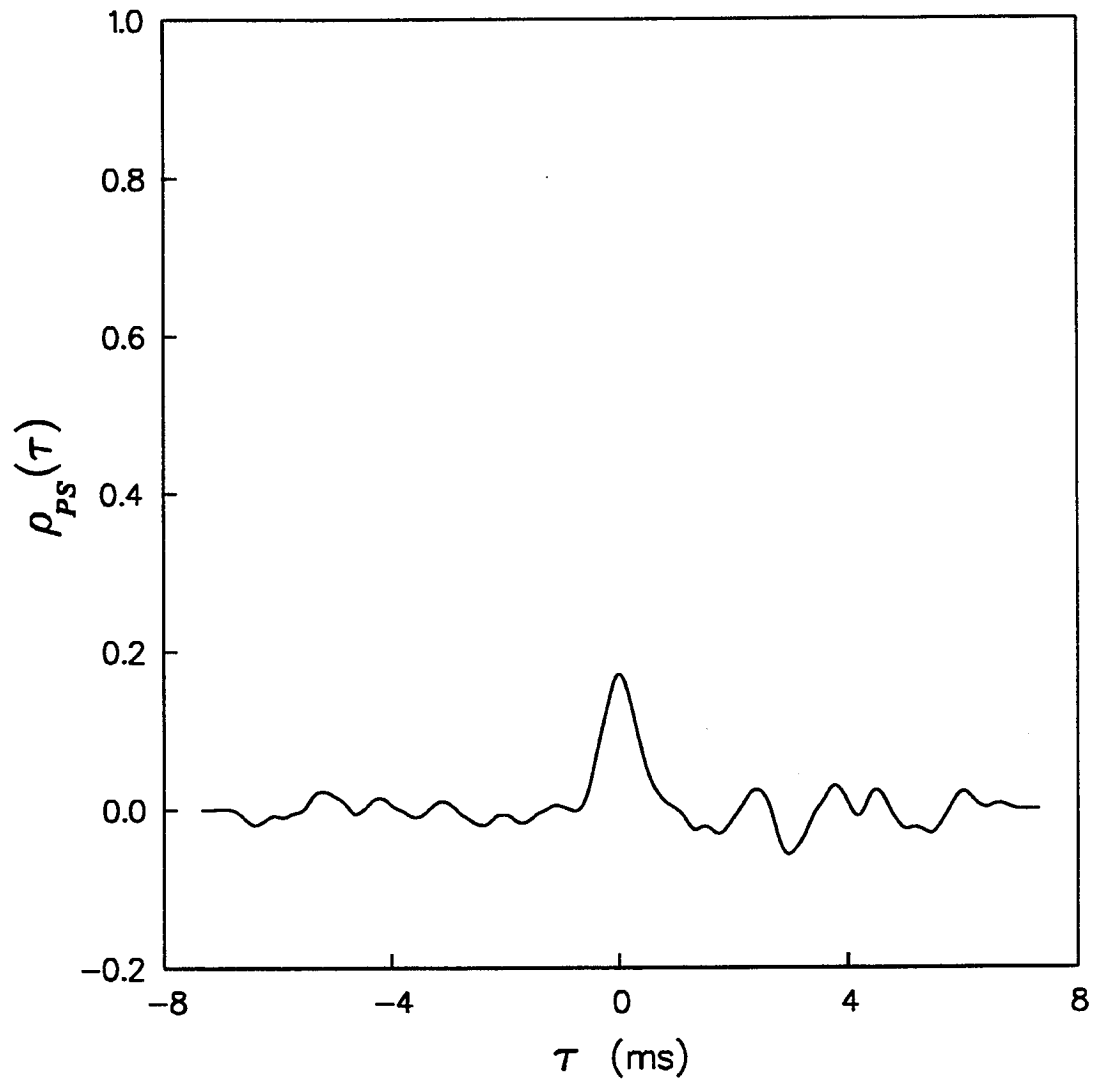
Figure 116   Mach 3.0 Intermittent Region Lateral Cross-Correlation
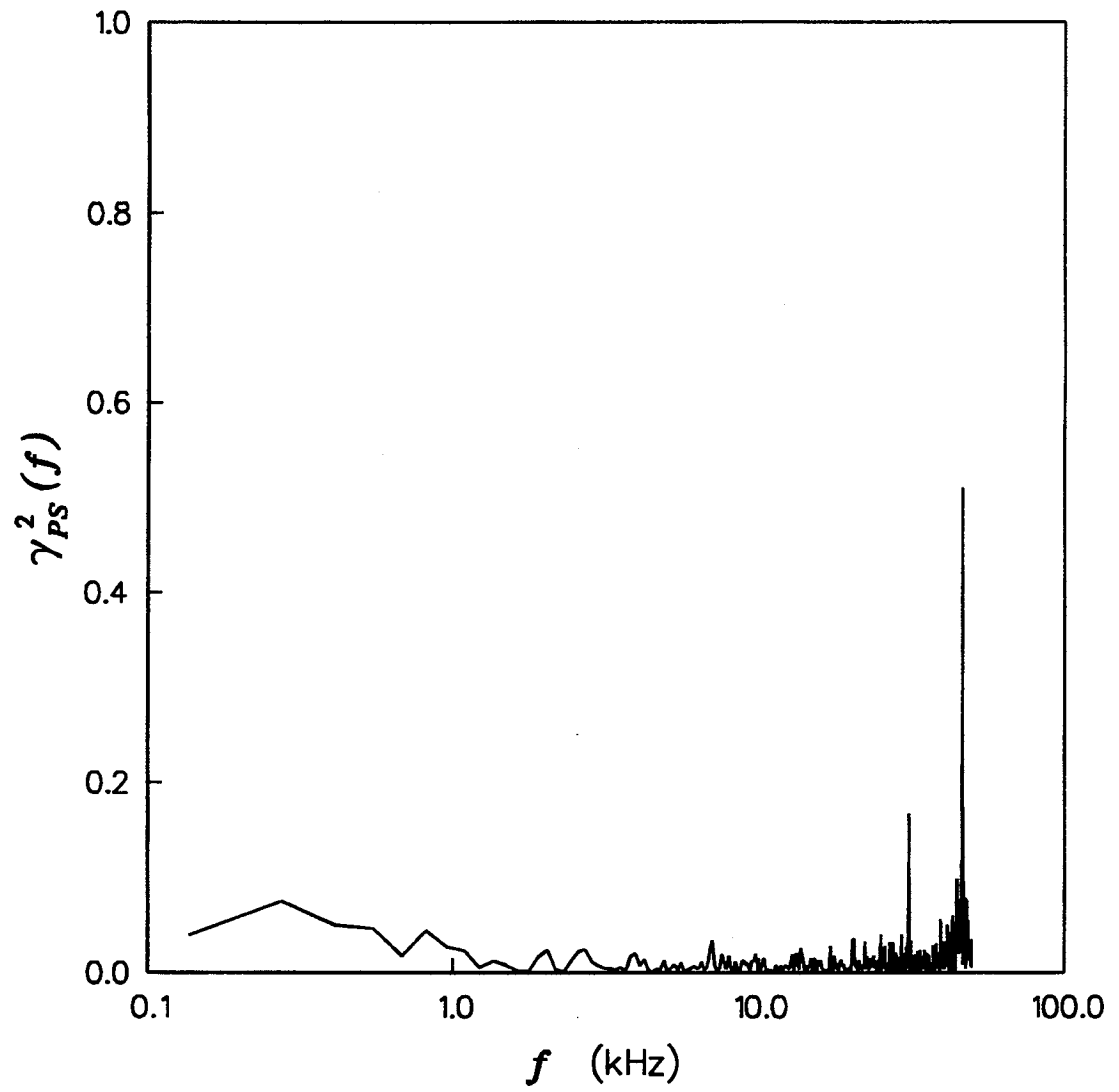
Figure 117   Mach 3.0 Intermittent Region Lateral Coherence Function
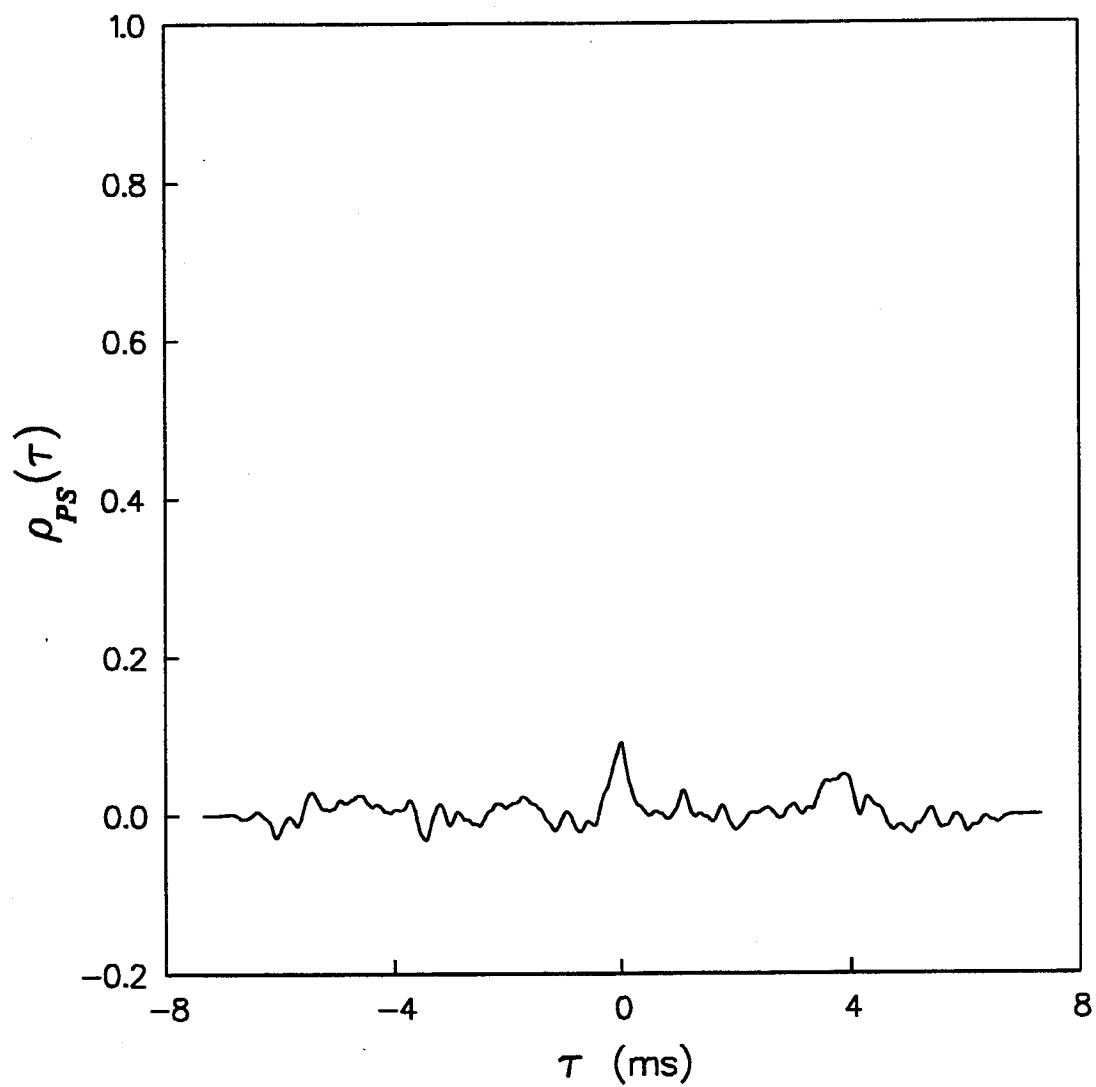
Figure 118   Mach 3.0 Separated Region Lateral Cross-Correlation
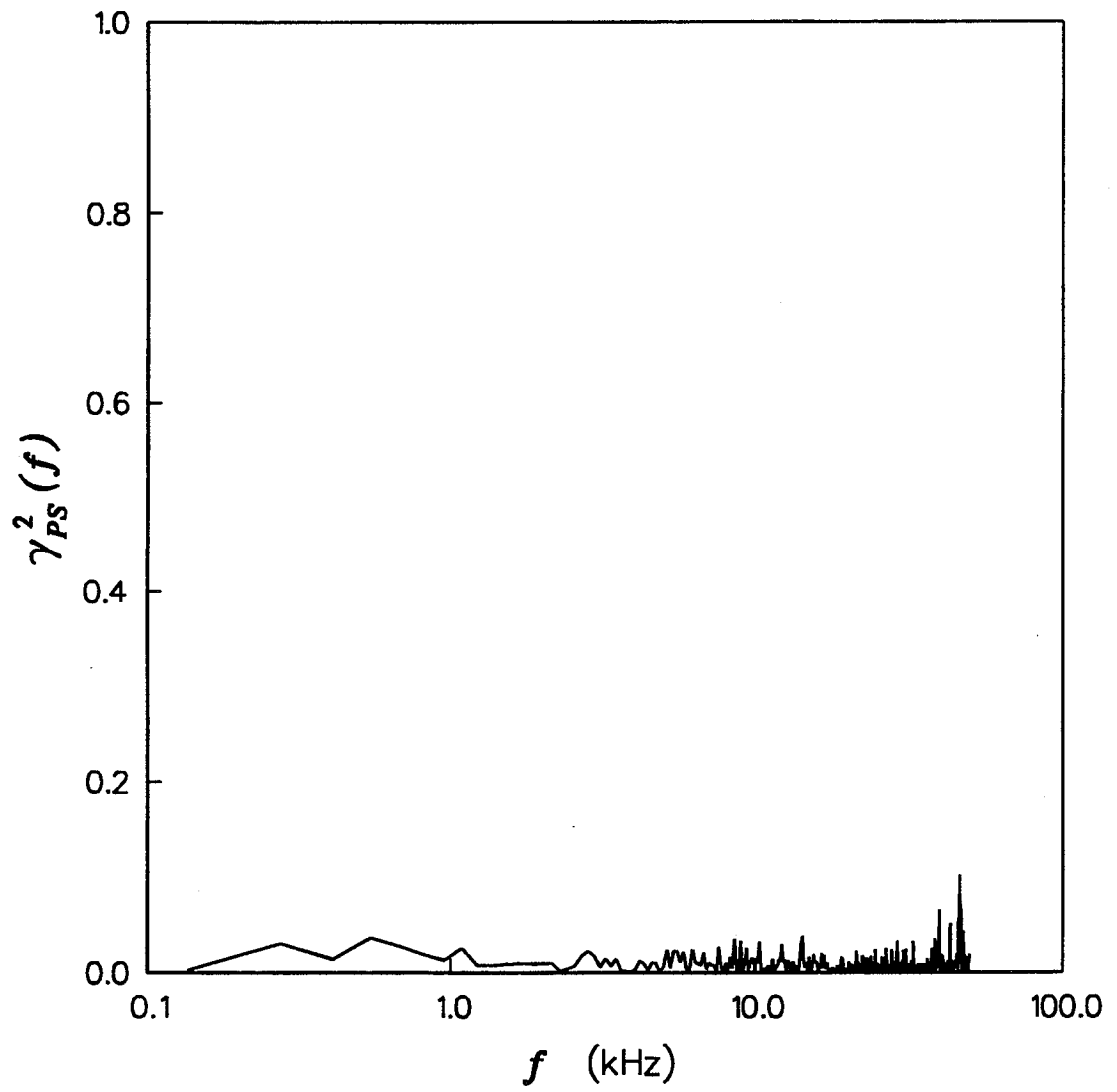
Figure 119   Mach 3.0 Separated Region Lateral Coherence Function

REPORT DOCUMENTATION PAGE

1. AGENCY USE ONLY (Leave blank)	2. REPORT DATE	3. REPORT TYPE AND DATES COVERED
	April 1997	Final Contractor Report

4. TITLE AND SUBTITLE

Experimental Investigation of Unsteady Shock Wave Turbulent Boundary Layer Interactions About a Blunt Fin

5. FUNDING NUMBERS

WU–523–36–13
C–NAS3–27186

6. AUTHOR(S)

Paul J. Barnhart and Isaac Greber

7. PERFORMING ORGANIZATION NAME(S) AND ADDRESS(ES)

NYMA Inc.
2001 Aerospace Parkway
Brook Park, Ohio 44142

8. PERFORMING ORGANIZATION REPORT NUMBER

E–10700

9. SPONSORING/MONITORING AGENCY NAME(S) AND ADDRESS(ES)

National Aeronautics and Space Administration
Lewis Research Center
Cleveland, Ohio 44135–3191

10. SPONSORING/MONITORING AGENCY REPORT NUMBER

NASA CR–202334

11. SUPPLEMENTARY NOTES

12a. DISTRIBUTION/AVAILABILITY STATEMENT

Unclassified - Unlimited
Subject Category 34

This publication is available from the NASA Center for AeroSpace Information, (301) 621–0390.

12b. DISTRIBUTION CODE

13. ABSTRACT (Maximum 200 words)

A series of experiments were performed to investigate the effects of Mach number variation on the characteristics of the unsteady shock wave/turbulent boundary layer interaction generated by a blunt fin. A single blunt fin hemicylindrical leading edge diameter size was used in all of the experiments which covered the Mach number range from 2.0 to 5.0. The measurements in this investigation included surface flow visualization, static and dynamic pressure measurements, both on centerline and off-centerline of the blunt fin axis. Surface flow visualization and static pressure measurement showed that the spatial extent of the shock wave/turbulent boundary layer interaction increased with increasing Mach number. The maximum static pressure, normalized by the incoming static pressure, measured at the peak location in the separated flow region ahead of the blunt fin was found to increase with increasing Mach number. The mean and standard deviations of the fluctuating pressure signals from the dynamic pressure transducers were found to collapse to self-similar distributions as a function of the distance perpendicular to the separation line. The standard deviation of the pressure signals showed initial peaked distribution, with the maximum standard deviation point corresponding to the location of the separation line at Mach number 3.0 to 5.0. At Mach 2.0 the maximum standard deviation point was found to occur significantly upstream of the separation line. The intermittency distributions of the separation shock wave motion were found to be self-similar profiles for all Mach numbers. The intermittent region length was found to increase with Mach number and decrease with interaction sweepback angle. For Mach numbers 3.0 to 5.0 the separation line was found to correspond to high intermittencies, or equivalently to the downstream locus of the separation shock wave motion. The Mach 2.0 tests, however, showed that the intermittent region occurs significantly upstream of the separation line. Power spectral densities measured in the intermittent regions were found to have self-similar frequency distributions when compared as functions of a Strouhal number for all Mach numbers and interaction sweepback angles. The maximum zero-crossing frequencies were found to correspond with the peak frequencies in the power spectra measured in the intermittent region.

14. SUBJECT TERMS

Shock wave turbulent boundary layer interactions; Unsteady separation shock wave motion; Dynamic pressure measurements

15. NUMBER OF PAGES

245

16. PRICE CODE

A11

17. SECURITY CLASSIFICATION OF REPORT	18. SECURITY CLASSIFICATION OF THIS PAGE	19. SECURITY CLASSIFICATION OF ABSTRACT	20. LIMITATION OF ABSTRACT
Unclassified	Unclassified	Unclassified	